SURFACE MODIFICATION OF MULTI-WALLED CARBON NANOTUBES DIRECTLY GROWN ON A STAINLESS STEEL MESH FOR ENERGY STORAGE AND CONVERSION

Elmira Pajootan

Department of Chemical Engineering

McGill University

Montréal, Québec, Canada

April 2022

A thesis submitted to McGill University in partial fulfillment of the requirements of the degree of Doctor of Philosophy

Abstract

Direct alkaline methanol fuel cells (DAMFCs) are electrical energy conversion systems emerging to address the energy shortage and meet sustainability goals. Fuel cells (FCs) are highly efficient, offering continuous operation as long as fuel is fed to the system. However, the commercialization of FCs faces many challenges because of the need for highly stable, low-cost and efficient electrocatalyst materials for anode and cathode electrodes. The current state-of-the-art commercially available anode and cathode material is platinum-supported carbon (Pt/C). However, the slow oxygen reduction kinetics at the cathode, poor stability of the Pt electrocatalyst, and the sluggish methanol electro-oxidation on the surface of Pt and its deactivation by carbon monoxide byproduct require high Pt loadings and more expensive catalyst with reduced cell efficiency. The main objective of this PhD project was to develop and characterize 3D porous Pt-based electrodes with low loading for both anodic and cathodic reactions in DAMFCs, with the goal of achieving high electrocatalytic activity and high stability.

The 3D porous Pt-based electrodes were synthesized first by a binder-free growth of multi-walled carbon nanotubes (MWCNTs) on the surface of stainless steel mesh (SS) using the chemical vapor deposition (CVD) method. Then, Pt nanostructures were deposited on the grown MWCNTs using a solvent-free and binder-free pulsed laser ablation/deposition (PLA or PLD) technique.

The shape, size distribution, and crystalline structure of the Pt nanoparticles were investigated using transmission electron microscopy (TEM). The morphology of the nanoparticle thin films on the surface of MWCNTs was studied by scanning electron microscopy (SEM), and energy dispersive X-ray spectroscopy (EDS) was used for elemental analysis. The surface elemental composition and the chemical state of the electrocatalyst were evaluated by X-ray photoelectron spectroscopy (XPS). Moreover, the X-ray diffraction (XRD) pattern was used to determine the crystalline structure of the synthesized electrocatalysts.

To study the electrocatalytic behavior and stability of the synthesized anode and cathode, cyclic voltammetry (CV), linear sweep voltammetry (LSV), chronoamperometry (CA), and electrochemical impedance spectroscopy (EIS) measurements were performed in a three-electrode cell, a rotating disk electrode (RDE), and a gas diffusion electrode (GDE) setup. We first optimized the growth of MWCNTs on SS mesh using the CVD method to obtain uniform forest-like structures on the SS with minimum MWCNTs structural defects. Achieving high electrochemical

capacitive behavior was indicative of MWCNTs providing high surface area. A radiofrequency (RF) plasma with two different gas mixtures of $Ar/C_2H_6/O_2$ and $Ar/C_2H_6/N_2$ was additionally applied to functionalize the MWCNTs with oxygen- and nitrogen-containing functional groups with the aim to increase the capacitance of the electrodes. An RF power level of 20 W with the $Ar/C_2H_6/O_2$ gas mixture for 15 min achieved the highest capacitance of the electrodes.

The forest-like MWCNTs grown on SS were used as support material for the deposition of Pt nanostructures using PLA. The influence of laser pulse energy and background gas pressure on Pt nanostructure characteristics was studied. Results showed that uniform and dense nanoparticle thin films at low pressure to highly porous granular coatings at higher pressure were deposited on MWCNTs. A mechanism was proposed for nanoparticle formation in the gas phase. A positive shift in the Pt 4f7/2 binding energies at lower PLA pressure and laser energy observed by XPS was linked to the formation of smaller Pt nanoparticles. In the RDE setup, all Pt/MWCNT/SS electrocatalysts yielded a higher specific oxygen reduction reaction (ORR) activity than the commercial Pt/C electrocatalyst. The Pt/MWCNT/SS electrode with the lowest Pt loading of 14.2 $\mu g\ cm^{-2}$ and the highest surface area of 69.9 $m^2 g^{-1}_{Pt}$ yielded the highest ORR specific activity in the gas diffusion setup.

Next, Pt nanoparticle thin films were deposited on MWCNTs grown on SS using the PLA setup at different background gas pressures and different PLA durations. The synthesized electrocatalysts were evaluated for the methanol oxidation reaction (MOR) in an alkaline medium. The PLA conditions were optimized systematically, intending to reach the highest methanol oxidation current while maintaining the structural integrity of the electrodes. The MOR current was related to the Pt loading and electrochemically active surface area. The most robust electrocatalyst, obtained with PLA at 10^{-5} Torr for 5 min, outperformed the commercial Pt/C with similar Pt loading while exhibiting better structural stability.

Finally, the ORR activity of the Pt-based electrocatalyst was further improved by the deposition of titanium oxynitride (TiO_xN_y) thin films prior to the deposition of Pt nanoparticles. The PLA procedure was coupled with radiofrequency plasma to deposit TiO_xN_y with different morphologies and chemical compositions on MWCNTs. High-speed imaging of the laser-induced plasma expansion demonstrated that the nanoparticle deposition rate increased at higher RF plasma power levels, changing the morphology and increasing the oxygen content of the TiO_xN_y coatings. In addition, the deposition of Pt improved the ORR current density and stability.

Abrégé

Les piles à combustible alcalines directes au méthanol (DAMFC) sont des systèmes de conversion d'énergie électrique qui émergent pour faire face à la pénurie d'énergie et atteindre les objectifs de durabilité. Les piles à combustible sont très efficaces, offrant un fonctionnement continu tant que le carburant est alimenté dans le système. Cependant, la commercialisation des PAC est confrontée à de nombreux défis dans la production de matériaux électrocatalyseurs hautement stables, peu coûteux et efficaces pour les anodes et cathodes. Le matériau commercial d'anode et de cathode le plus courant est le platine déposé sur le carbone (Pt/C). Cependant, la cinétique lente de réduction de l'oxygène à la cathode et la faible stabilité de l'électrocatalyseur de Pt, l'électro-oxydation lente du méthanol à la surface du Pt et sa désactivation par le sous-produit de monoxyde de carbone conduisent à une charge élevée et à un catalyseur plus coûteux avec une efficacité réduite.

L'objectif principal de cette thèse était de développer et de caractériser des électrodes 3D poreuses à base de platine pour les réactions anodiques et cathodiques, atteignant une activité électrocatalytique élevée et une stabilité élevée à faible charge en Pt. Les électrodes 3D poreuses à base de Pt ont d'abord été synthétisées par une croissance sans liant de nanotubes de carbone à parois multiples (MWCNT) sur la surface d'un treillis en acier inoxydable (SS) en utilisant la méthode de dépôt chimique en phase vapeur (CVD). Ensuite, des nanostructures de Pt ont été déposées sur les MWCNT à l'aide d'une technique d'ablation/dépôt laser pulsé sans solvant et sans liant (ALP ou DLP).

La forme, la distribution de taille et la structure cristalline des nanoparticules de Pt ont été étudiées à l'aide de la microscopie électronique à transmission (MET). La morphologie des films minces de nanoparticules à la surface des MWCNT a été étudiée par microscopie électronique à balayage (MEB) et spectroscopie de rayons X à dispersion d'énergie (SDE) pour l'analyse élémentaire. La composition chimique de la surface et la structure chimique ont été évalués par spectroscopie photoélectronique à rayons X (SPX). De plus, la diffraction des rayons X (DRX) a été utilisé pour déterminer la structure cristalline des électrocatalyseurs. Pour étudier le comportement électrocatalytique et la stabilité de l'anode et de la cathode, des mesures par voltamétrie cyclique (VC), voltamétrie à balayage linéaire (VBL), chronoampérométrie (CA) et spectroscopie d'impédance électrochimique (SIE) ont été réalisés à l'aide d'une cellule à trois

électrodes, également d'une cellule à électrode à disque tournant (EDT) et d'une configuration d'électrode à diffusion de gaz (EDG).

Nous avons d'abord optimisé la croissance des MWCNT sur le maillage SS en utilisant la méthode CVD pour obtenir une structure uniforme de type forêt sur le SS avec un minimum de défauts structurels. L'obtention d'un comportement capacitif électrochimique était révélatrice de la croissance des MWCNT fournissant une surface spécifique élevée. Un plasma radio-fréquentiel (RF) dans deux mélanges gazeux d'$Ar/C_2H_6/O_2$ et $Ar/C_2H_6/N_2$ a également été appliqué pour fonctionalisation chimique des MWCNT avec des groupes fonctionnels contenant de l'oxygène et de l'azote dans le but d'augmenter la capacité des électrodes. Un niveau de puissance RF de 20 W utilisant le mélange gazeux $Ar/C_2H_6/O_2$ pendant 15 min a permi d'atteindre la capacité la plus élevée des électrodes.

Les MWCNT de type forêt cultivées sur SS ont été utilisés comme matériau support pour le dépôt de nanostructures de Pt à l'aide d'ALP. L'influence de l'énergie des impulsions laser et de la pression du gaz sur les caractéristiques des nanostructures de Pt a été étudiée. Les résultats ont montré que des couches minces uniformes et denses de nanoparticules sont formées à basse pression alors que des couches granulaires hautement poreuses sont formées à haute pression. Un mécanisme a été proposé pour la formation de nanoparticules en phase gazeuse. Un changement positif dans les énergies de liaison Pt 4f7/2 à une pression de chambre et énergie des pulses laser inférieures a été observé par SPX et associé à la formation de nanoparticules de Pt plus petites. Dans la configuration EDT, tous les électrocatalyseurs Pt/MWCNT/SS ont donné lieu à une activité de réaction de réduction spécifique de l'oxygène (RRO) plus élevée que l'électrocatalyseur Pt/C commercial. L'électrode Pt/MWCNT/SS avec la charge de Pt la plus faible et la surface la plus élevée a produit l'activité spécifique RRO la plus élevée dans la configuration de diffusion de gaz. Ensuite, des films minces de nanoparticules de Pt ont été déposés sur les MWCNT sur SS en utilisant la configuration l'ALP à différentes pressions de gaz et différentes durées de déposition. Les électrocatalyseurs synthétisés ont été évalués pour la réaction d'oxydation du méthanol (ROM) dans les DAMFC. Les conditions de déposition ont été optimisées systématiquement dans le but d'atteindre le courant d'oxydation du méthanol le plus élevé tout en maintenant l'intégrité structurelle des électrodes. Il a été observé que le courant ROM ont lié à la charge de Pt et à la surface électrochimiquement active. L'électrocatalyseur le plus robuste, obtenu par ALP à 10^{-5}

Torr pendant 5 min, a surpassé le Pt/C commercial avec une charge de Pt similaire tout en présentant une meilleure stabilité structurelle.

Enfin, l'activité RRO de l'électrocatalyseur à base de Pt a été encore améliorée par le dépôt de couches minces d'oxynitrure de titane (TiO_xN_y) avant le dépôt de nanoparticules de Pt. La procédure ALP a été couplée à un plasma radio-fréquence pour déposer le TiO_xN_y avec différentes morphologies et compositions chimiques sur des MWCNT. L'imagerie rapide de l'expansion du plasma induite par l'addition laser a démontré que le taux de déposition de nanoparticules augmentait à des niveaux de puissance plasma RF plus élevés, modifiant la morphologie et augmentant la teneur en oxygène des revêtements TiO_xN_y. De plus, le dépôt de Pt a amélioré la densité et la stabilité du courant RRO.

Acknowledgements

I would like to begin by thanking my incredible supervisors, Dr. Sylvain Coulombe and Dr. Sasha Omanovic. You continually provided guidance, encouragement, direction, and the freedom to work independently. You trusted me and gave me the opportunity to co-supervise and train undergraduate and graduate students and collaborate in many projects, which made me a stronger scientist. I will always be grateful to you.

I would like to thank my husband, Mehdi Rahimdokht. I am fortunate to have you by my side. The sacrifices you made are immeasurable. I sincerely thank my mother, brother, father, and grandmother for their love and support. Being away from you was one of the most challenging tasks I had to accomplish.

I would like to acknowledge the help of Dr. Jean-Luc Meunier, Dr. Ali Seifitokaldani, Dr. Jan Kopyscinski, and Dr. Pascal Hubert for answering my questions, providing equipment and collaborating with me on different projects.

Thank you, Frank Caporuscio, for all your pleasant chats, precious time and help during my studies. Thank you Andrew Golsztajn, Gerald Lepkyj, Ranjan Roy, Lisa Volpato, Louise Miller-Aspin, Anna Jean Pollock, and the rest of the chemical engineering staff for all your tremendous help.

I would like to thank my “PhD girls”, Dr. Elena and Dr. Jennifer. I am grateful for having you in my life, and thanks for all your love and support. Mohammad and Hanie, my journey at McGill after COVID-19 pandemic was blessed by knowing you. I am thankful for your friendship and making my final PhD years incredibly pleasant. I thank Ladan, Navid, Farnaz, Sara, and Heidi for having your support and friendship. Haniye, thank you for helping me with all those beautiful schematics. Mahdi and Roger, I am thrilled to have worked with you, enjoying our many scientific conversations.

I would like to thank the CPPE group: Lynn, Dante F, Dante SP, Steven, Phil, Larissa, Adya, Mathew, Felipe, Pablo, Robyn, Mohsen and Jasmin. I thank the Electrochemistry/Corrosion group: Emmanuel, Jeff, Deepak, Ahmad, Mahmoud, Xingge, Nancy, Satria, and Aqeel. In the end, I would like to thank Sammie, Jonathan, Gareth, Sogol, Minnan, Muyang, and Michael for assisting me with my PhD project.

Table of Contents

List of Figures

List of Figures (Supporting Information)

List of Tables

List of Tables (Supporting Information)

List of Equations/Reactions

Nomenclature

ADT	Accelerated Durability Test
BE	Binding Energy
BP	Backing Paper
C	Capacitance
CA	Chronoamperometry
CDC	Charging-Discharging Curves
C_{dl}	Total capacitance of the double-layer interface, F
C_e	Electrode Capacitance
CE	Counter Electrode
C_F	Faradaic Capacitance
CN	Coordination Number
CNT	Carbon Nanotubes
C_s	Specific Capacitance
CP	Carbon Paper
CPPE	Catalytic Plasma Process Laboratory
CV	Cyclic Voltammetry
CVD	Chemical Vapor Deposition
DAMFCs	Direct Alkaline Methanol Fuel Cells
DMFCs	Direct Methanol Fuel Cells
ECSA	Electrochemical Active Surface Area
EDLC	Electric Double-Layer Capacitance
EDS	Energy-Dispersive X-Ray Spectroscopy
EIS	Electrochemical Impedance Spectroscopy
ESR	Equivalent Series Resistance
f-MWCNT	Functionalized Multi-Walled Carbon Nanotubes
GC	Glassy Carbon
GCD	Galvanostatic Charge Discharge
GDE	Gas Diffusion Electrode
HC	Hybrid Capacitor

IHP	Inner Helmholtz Plane
LSV	Linear Sweep Voltammetry
MA	Mass Activity
MEA	Membrane Electrode Assembly
MOR	Methanol Oxidation Reaction
MWCNT	Multi-Walled Carbon Nanotubes
OHP	Outer Helmholtz Plane
ORR	Oxygen Reduction Reaction
PC	Pseudo-capacitor
PLA	Pulsed Laser Ablation
PLD	Pulsed Laser Deposition
RDE	Rotating Disk Electrode
RE	Reference Electrode
RF	Radiofrequency
RF-PAPLD	Radiofrequency Plasma-Assisted Pulsed Laser Deposition
SA	Specific Activity
SCCM	Standard Cubic Centimeter per Minute
SC	Supercapacitor
SEM	Scanning Electron Microscopy
SS	Stainless Steel
RHE	Reference Hydrogen Electrode
t-CVD	Thermal Chemical Vapor Deposition
TEM	Transition Electron Microscopy
WE	Working Electrode
Wt%	Weight Percent Ratio
XPS	X-Ray Photoelectron Spectroscopy

Chapter 1

1. Introduction

1.1 Overview

Human beings have always searched for potential energy sources to meet their needs. “Energy” is originally from two Greek words: “en+ergos”, meaning “at work” or “in action” [1]. Humankind has experienced three industrial revolutions, each triggered by radical innovations: the development of a two-cylinder steam engine by James Watt in the 1760s, the discovery of the internal combustion engine and electric generator at the end of the 19th century, and the construction of the first computer in the 1940s. However, the undesirable outcome of these inventions, such as environmental pollution, carbon dioxide (CO_2) emissions and associated global warming, irreversible climate change and increased frequency and magnitude of natural disasters, are mainly because of the direct consumption of fossil fuels intensified by the rapid growth of the world population [2]. The level of atmospheric CO_2 in 2021 has reached 417 ppm, which has observed a 50% increase since the beginning of industrialization. The consumption of fossil fuels alone produced 9.8 ± 0.5 Gtons of carbon in 2014, forcing the world to look for alternatives to fossil fuels, such as wind, solar, hydro, geothermal, nuclear, tidal energy, biodiesel and biogases. Energy storage and conversion technologies are highly demanded due to the intermittency of renewable energy sources [3, 4].

Supercapacitors (SCs) as energy storage devices have attracted much attention because of their high specific power and moderate energy densities, suitable for a wide range of applications from electric cars to portable electronics, specifically flexible electronic devices. Carbon-based materials, metal oxides, and conductive polymers are being widely investigated as supercapacitor electrode materials. Multi-walled carbon nanotubes (MWCNTs)-based electrodes are promising candidates for these applications owing to their high electrical conductivity, high specific surface area and chemical inertness, facilitating the electrical double-layer charging, resulting in high power density and long lifetime. However, the low energy density of MWCNT-based

supercapacitor devices, their hydrophobicity and high agglomeration tendency, and the use of additives such as binders in electrode manufacturing processes reducing their surface area, can limit their performance.

On the other hand, fuel cells (FCs), as a green and environmentally friendly technology, seems to be one of the most proper systems to provide efficient and continuous energy conversion. Fuel cells are advantageous due to producing no or less pollution, being quiet with no moving parts, having fuel flexibility, wide application range, and high thermodynamic efficiency. However, low-temperature FCs suffer from immature hydrogen infrastructure, high cost and difficulties in producing, storing, and transporting pure green hydrogen gas. Therefore, many researchers are interested in the development of direct methanol fuel cells (DMFCs) for portable applications. Moreover, direct alkaline methanol fuel cells (DAMFCs) have higher kinetics of methanol electro-oxidation. However, the expensive and complex main FC parts (electrode, catalyst and membrane, i.e. the membrane-electrode-assembly) need extensive improvement to achieve low-cost, efficient and durable energy conversion [5]. Consequently, ongoing research is undertaken to improve fuel cells' components to promote their performance, and according to Scopus, Canada has been among the top 5 countries interested in using nanostructured materials in FCs since 2002 [6]. The main disadvantages of the commercially available Pt-based electrocatalyst, which is the material used in DMFC/DAMFC, are inadequate stability, low poisoning tolerance by methanol oxidation reaction byproducts, or oxygen reduction reaction intermediates, which requires higher Pt loadings to compensate for the activity loss during the anodic and cathodic reactions.

In this context, this PhD thesis presents a binder-free dry approach toward synthesizing electrode materials for SCs and DAMFCs. In this regard, chemical vapor deposition (CVD) was used to directly grow MWCNTs on a flexible stainless steel (SS) mesh without using any binder materials, providing a 3D porous skeleton with high electrical conductivity and large surface area. The synthesized material is used for supercapacitor electrodes and as electrocatalyst support for DAMFC electrodes. A radiofrequency (RF) plasma was used to functionalize the surface of MWCNTs in a dry, moderate experimental condition, preserving the 3D structure of the electrodes to achieve high capacitance for SC application. The solvent-free and byproduct-free pulsed laser ablation/deposition (PLA or PLD) method was employed to synthesize and deposit Pt-based nanostructures on the 3D porous MWCNTs grown on the SS. The synthesized 3D porous nanostructured electrode materials were tested for DAMFC application, demonstrating improved

activity, stability and low Pt loadings. Moreover, this project contributes toward making stable electrode materials with the potential of removing the carbon paper backing and current collector from fuel cell components.

1.2 Objectives

One of the research directions in improving the performance of supercapacitors and DAMFCs is the design of the active electrode materials. For the former, the focus is on developing electrodes with high electrical conductivity, large specific surface area, high capacitance and long cyclability; for the latter, the focus is on designing efficient, low-cost, low loading, and stable electrocatalysts promoting the performance and lifetime of fuel cells. Therefore, the main objective of this PhD thesis was to synthesize (*i*) high-capacitance MWCNT-based supercapacitor electrodes using the radiofrequency plasma functionalization, and (*ii*) Pt/MWCNT-based electrocatalysts with improved intrinsic and extrinsic characteristics by pulsed laser ablation/deposition technique to enhance the efficiency, durability, and reduce the overall cost of direct alkaline fuel cells by lowering Pt loading. The following specific objectives were defined to accomplish the main goal of this project:

1. Optimization of the growth of multi-walled carbon nanotubes (MWCNTs) on stainless steel meshes using a chemical vapor deposition (CVD) method to develop a 3D structure, with high electrical conductivity and large surface area, to be used for supercapacitor and direct alkaline fuel cell electrode material.
2. Oxygen and nitrogen functionalization of MWCNTs using a radiofrequency plasma functionalization technique to improve their capacitive behavior as supercapacitor electrodes.
3. Deposition of Pt nanoparticle thin films on MWCNT with different morphologies and loadings *via* the pulsed laser ablation/deposition (PLA or PLD) technique.
4. Determination of the relationships between PLA conditions and the structure of the electrocatalysts, and understanding the mechanism of nanoparticle formation during PLA.

5. Systematic optimization of the synthesis conditions of Pt nanoparticle thin films to achieve the highest electrocatalytic activity toward the oxygen reduction reaction (ORR) in alkaline fuel cells.

6. Investigation of the best PLA operating conditions for the deposition of Pt nanoparticle thin films on MWCNTs to achieve the highest electrocatalytic activity toward the methanol oxidation reaction (MOR) in direct alkaline methanol fuel cells.

7. Synthesis of titanium oxynitride (TiO_xN_y) thin films on MWCNTs using the combination of PLD and radiofrequency (RF) plasma.

8. Investigation and understanding of the RF plasma and laser-induced plasma interactions resulting in different morphologies and chemical composition of TiO_xN_y.
9. Deposition of Pt nanoparticles on the TiO_xN_y-covered MWCNTs as a more active and stable electrocatalyst for the ORR.

1.3 Thesis Structure

This dissertation is a manuscript-based thesis prepared following the McGill University Graduate and Postdoctoral Studies (GPS) guidelines and regulations to fulfill the requirements for a doctorate degree. This thesis is comprised of 8 chapters.

Chapter 1 is the introductory section emphasizing the importance of this research, followed by the objectives of the thesis.

Chapter 2 provides a comprehensive background and literature review related to supercapacitors and fuel cells, their working principles, and the importance and synthesis of electrocatalyst materials.

Chapter 3 presents the methodology and experimental procedures used to carry out the experiments.

The four manuscripts fulfilling the objectives of this thesis are presented in Chapters 4 to 7. These manuscripts are either published or currently going through the review process in peer-reviewed journals.

Chapter 4 is titled “Plasma-Functionalized Multi-walled Carbon Nanotubes Directly Grown on Stainless Steel Meshes as Supercapacitor Electrodes”, fulfilling the first and second objectives of this thesis to optimize the growth of MWCNTs on stainless steel meshes by CVD and to oxygen and nitrogen functionalize of MWCNTs using a radiofrequency plasma functionalization technique to improve their capacitive behavior.

Chapter 5, entitled “Controllable Dry Synthesis of Binder-Free Nanostructured Platinum Electrocatalysts Supported on Multi-Walled Carbon Nanotubes and their Performance in the Oxygen Reduction Reaction”, represents the work to achieve objectives 3, 4, and 5 to deposit different Pt nanoparticle thin films on MWCNT under different PLA/PLD conditions and optimize the synthesis conditions to achieve the highest electrocatalytic activity and stability for ORR in alkaline fuel cells.

Chapter 6, entitled “Two-Step Dry Synthesis of Binderless 3D Low Pt-Loading Electrocatalysts for Direct Alkaline Methanol Fuel Cell Anodes”, is written to accomplish objective 6 to achieve the highest electrocatalytic activity toward MOR in direct alkaline methanol fuel cells by optimizing the PLA operating conditions for the deposition of Pt nanoparticle thin films on MWCNTs.

Chapter 7, with the title “Radiofrequency Plasma-Assisted Pulsed Laser Deposited Pt/TiO_xN_y Coatings on Multi-walled Carbon Nanotubes as Gas Diffusion Electrodes for the Oxygen Reduction Reaction”, describes the work toward fulfilling objectives 7, 8, and 9 to synthesize TiO_xN_y and Pt-coated TiO_xN_y thin films on MWCNTs using the combination of PLD and RF plasma and evaluate their electrocatalytic activity for ORR.

Finally, in Chapter 8, a summary of the main findings and contributions to knowledge drawn from this project and the recommendations for future work are presented.

In Appendix A, all my collaborative projects closely related to my thesis and conference contributions during my PhD studies are listed.

Chapter 2

2. Literature Review

This chapter presents the fundamentals of supercapacitors and their electrode materials and reviews the fuel cells principles, the electrocatalyst materials and their synthesis routes.

2.1 Fundamentals of Electrochemical Supercapacitors

The rapid technological development and population growth after the Industrial Revolution have increased the energy demand, thus requiring the deployment of environmentally-friendly technologies based on renewable energy sources to sustain human activities. The electrical energy can be stored in electrochemical systems *via* two different mechanisms; indirectly by the charge released from Faradaic oxidation and reduction reactions at the electrode materials (e.g. in batteries), and directly by non-Faradaic electrostatic charge storage at the electrode/electrolyte interface (e.g. in electrochemical capacitors). Due to the irreversibility of the charge-discharge processes in batteries and the redox kinetics, they have a limited lifetime and power density, but high energy densities. However, capacitors are known to have unlimited recyclability because no chemical changes occur. Nevertheless, a disadvantage of capacitors is their low energy density [7, 8].

The electrochemical capacitors, called supercapacitors (SCs) or ultra-capacitors, are energy storage systems that, unlike batteries, can be used over a wide temperature range (−40 to 85°C) and for a significantly larger number of charging/discharging cycles. Supercapacitors have high power densities, but their energy density is lower than batteries. Similar to capacitors, supercapacitors can demonstrate a longer lifespan than batteries because the electrode materials do not undergo a phase or chemical changes during the charge-discharge processes. Figure 2-1(a) illustrates the charge-discharge behavior of supercapacitors and batteries. For *ideal* supercapacitors, the voltage varies linearly with time, while in batteries, the voltage remains almost

constant over a long time. In Figure 2-1(a), t_c is the charge and t_d is the discharge time, V_w is the voltage of the supercapacitor or the open-circuit voltage of the battery, V_{max} and V_{min} are the maximum and minimum voltages at the end of the charge-discharge, and ESR is the equivalent series resistance [8-11].

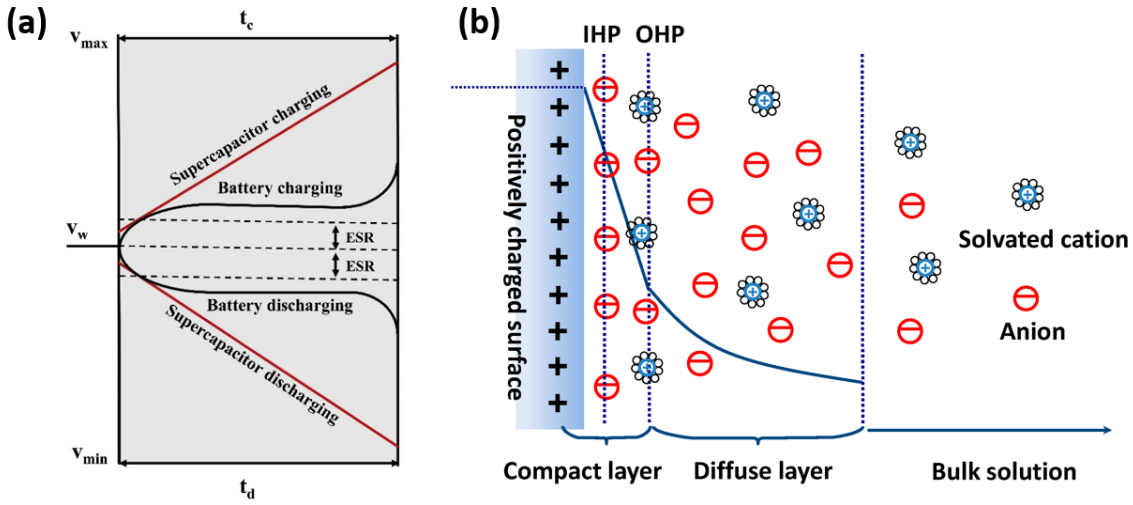

Figure 2-1. (a) Charge-discharge for batteries and supercapacitors, and (b) the electrical double layer at the electrode/electrolyte interface [8, 9].

2.1.1 Charge Storage Mechanism in Supercapacitors

Supercapacitors can be categorized into three types based on the charge-storage mechanism: (i) electrical double-layer capacitors (EDLCs), (ii) pseudo-capacitors (PCs), and (iii) hybrid capacitors (HCs).

In EDLCs, the charge is stored based on non-faradaic processes, in which by applying potential at the supercapacitor electrodes, an electrical double layer is formed at the electrode surface (Figure 2-1(b)), which Helmholtz first described. The electrolyte ions are electrostatically attracted to the electrode/electrolyte interface to compensate for the opposite electrode charge. Two ion regions of compact and a diffuse layer are formed. The specifically adsorbed ions constitute the inner Helmholtz plane (IHP), while the outer Helmholtz plane (OHP) is characterized by the solvated counter-ions. The diffuse layer extending to the bulk electrolyte contains the distributed ions. In EDLCs, no reaction occurs at the electrode interface; instead, the rearrangement of charges results in the current flow. The porous carbonaceous materials are mostly used in EDLCs.

However, they exhibit low capacitance and energy density since the presence of pores can limit the accessibility of the electrolyte to the electrode surface.

In PCs, charge storage is due to fast reversible redox (Faradaic) reactions at the electrode surface, usually involving the outer and sub-outer region of the electrode. The pseudo-capacitive behavior depends on the electrode's surface chemical composition, surface area and electrolyte type. Transition metal oxides like ruthenium oxide and nickel oxide and conducting polymers, such as polyaniline and polypyrrole, exhibit pseudo-capacitive behavior. The combination of EDLCs and pseudo-capacitors is called hybrid capacitors (HCs), which benefit from both charge storage mechanisms, resulting in an improved supercapacitive performance [12, 13].

2.1.2 Supercapacitor History and Market

Supercapacitors emerged in the 1970s and 1980s. Researchers in many American and European countries, including South Korea, Russia, and Japan, studied and developed SCs. The concept of double-layer capacitance was stated by Helmholtz in 1853; however, the use of this type of capacitors as energy storage devices took many decades. The double-layer carbon-based condenser was first patented by Standard Oil Company Sohio in 1968, and NEC produced SCs using this patent in 1979. The demand for SCs is globally rising, especially for hybrid SC/battery or SC/fuel cell systems for many different applications, including medical equipment, military equipment, and transportation. With the enhancement in the performance of SCs, the global market of SCs reached 117 billion CAD in 2020 [13].

2.1.3 Supercapacitor Electrode Material

Carbon-based materials, including activated carbons, carbon foams, carbon nanotubes (CNTs), and graphene, are extensively used as SC electrode materials, owing to their favorable physical and chemical properties, such as low cost, electrical conductivity, chemical inertness, large specific area, and variety of forms (powders, fibers, sheets, and tubes). As mentioned earlier, activated carbons are used in EDLCs because of their high specific surface area. Moreover, CNTs are of particular importance in developing SC electrodes due to their high electrical conductivity and large specific surface area with highly porous tubular structure. Nonetheless, CNTs have a smaller specific surface area (surface area per mass) compared to activated carbon and are

hydrophobic, resulting in low energy density when used as SC electrodes. Also, entangled and agglomerated CNTs possess lower specific surface area and are their surface is less accessible to ions than when they are vertically aligned [12, 14].

In order to develop high-capacitance CNT-based SCs, research is focused on improving their specific surface area, wettability, and adding the pseudo-capacitance charge storage mechanism to the EDL. This goal can be achieved by adding electrically conductive polymers or transition metal oxides to CNTs or providing redox-active oxygen- and nitrogen-containing functional groups on the surface of CNTs [12]. More explanations about the functionalization of CNTs are given in Section 2.4.5.

2.2 Fundamentals of Fuel Cells

2.2.1 Fuel Cell History

Sir William Grove and Christian Friedrich Schönbein were the first inventors of fuel cells who illustrated its fundamentals and principle in the 1830s. Later, Friedrich Wilhelm Ostwald mentioned that they have a theoretical efficiency of nearly 100% and can be used as energy conversion systems based on the direct conversion of chemical energy into electrical energy [1, 15]. Table 2-1 reports a brief history of fuel cells development.

Table 2-1. Fuel cells history in brief [16-18]

Invention	**Inventor**	**Year**
The principle of fuel cells was demonstrated.	Sir William Grove and Christian Friedrich Schönbein (in independent research)	1838
Fuel cell gained its actual name. A hydrogen fuel cell that produced 6 A ft^{-2} at 0.73 V was constructed.	Ludwig Mond and Charles Langer	1889
The relationship between different components of a fuel cell (electrodes, electrolyte, oxidizing and reducing agents, anions and cations) was experimentally determined.	Friedrich Wilhelm Ostwald	1890s

Extensive research was performed on high-temperature fuel cells with molten silver as the electrolyte and a unit that used clay and metal oxides as a solid electrolyte.	Emil Baur	1920s
The first model of an alkaline electrolyte fuel cell was constructed.	Francis Thomas Bacon	1932
The first vehicle using an alkaline fuel cell with a 40-cell stack capable of 5 kW was built.	Francis Thomas Bacon	1959
The polymer electrolyte membrane (PEM) fuel cell was invented by General Electric.	Thomas Grubb and Leonard Niedrach	1960s
The first fuel cell technology was successfully applied in NASA's spacecraft.	—	1960-70s
The oil crisis fostered the development of alternative technologies, including phosphoric acid fuel cells.	—	1970s
US navy used fuel cells in their submarines.	—	1980s
Large stationary fuel cells were developed for commercial and industrial applications.	—	1990s
Ballard breakthrough: Further development of PEM, and using fuel cells for wider applications than spacecraft.	Ballard Power Systems	1990s
Early commercialization of fuel cells	—	2000

2.2.2 Fuel Cell Operation

A fuel cell is an electrochemical device (galvanic cell) that converts the free energy of hydrogen or hydrocarbon oxidation reaction directly into an electrical current without combustion, while fuel and oxidant are fed to the system [15, 18]. Fuel cells are not limited by the Carnot efficiency, and they benefit from a relatively high combined efficiency (electric/heat). Their other advantages include low emissions and silent operation with few if any moving parts, making them durable and scalable [19, 20]. In contrast to batteries, a fuel cell produces electricity as long as the fuels are fed continuously to the system. However, the high cost of FCs' components is the main barrier to their broader commercialization [20].

Figure 2-2 shows that all fuel cells consist of three essential parts; the anode, the cathode, and the electrolyte, which can be a solid membrane or a liquid. When solid membranes are used as

electrolytes, the thickness of this assembly, referred to as the membrane electrode assembly (MEA), is generally smaller than 1 mm. The active layer is a part of the anode and cathode containing the electrocatalyst material active for the redox reactions occurring on the surface of the electrocatalyst. The MEA is usually sandwiched between porous backings (with adequate electronic and heat conductivity, fluid flow permeability, mechanical stability, and wettability) and flow distributors.

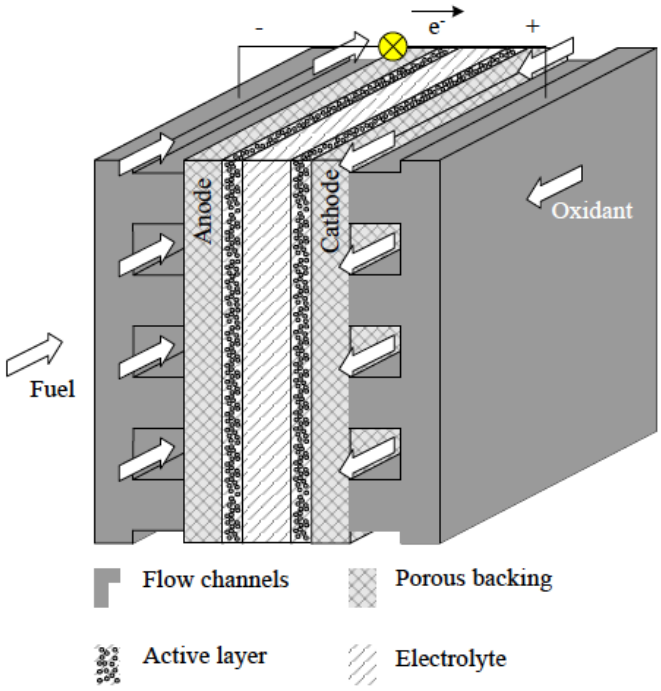

Figure 2-2. Schematic view of a fuel cell [20].

2.2.3 Fuel Cell Classification

Fuel cells can be classified based on their electrolyte type, working temperature and fuel type. However, they are generally classified into six categories: polymer electrolyte membrane fuel cells (PEM fuel cells or PEMFCs), direct methanol fuel cells (DMFCs), alkaline fuel cells (AFCs), phosphoric acid fuel cells (PAFCs), molten carbonate fuel cells (MCFCs), and solid oxide fuel cells (SOFCs). They are all distinguished by the type of their electrolyte, except for DMFCs which use a different fuel (methanol). In all fuel cells, the cathodic reaction is the oxygen reduction reaction. AFCs, PEMFCs, DMFCs, and PAFC operate at low temperatures, while MCFCs and SOFCs are high-temperature fuel cells [15]. A schematic view of different classes of fuel cells is

shown in Figure 2-3. A brief explanation is also given for various fuel cells. It should be noted that different ranges of working temperature are reported in the literature. Here we report the widest range we found for each type:

1- Polymer electrolyte fuel cells (PEFCs): They use a solid polymer proton exchange membrane, and operate at low temperatures (20−90 ºC). High purity hydrogen is the fuel. They are suitable for vehicles, low-power co-generation systems and mobile applications.

2- Direct methanol fuel cells (DMFCs): They work at low temperatures (20−110 ºC), use solid polymer proton exchange membrane, and liquid methanol as the fuel. Since they operate at low power, their potential application is mostly portable devices running for long durations.

3- Alkaline fuel cells (AFCs): These cells operate at temperatures between 60 and 220 ºC. Hydrogen fuel and liquid electrolyte comprising of OH^- (KOH) are used in AFCs, which were used in spacecraft.

4- Phosphoric acid fuel cells (PAFCs): This type of fuel cell operates at slightly higher temperatures (150−220 ºC), with a liquid electrolyte comprising of H^+, and hydrogen as the fuel. Their potential application is in office buildings and schools as medium-power co-generation systems (~200 kW).

5- Solid oxide fuel cells (SOFCs): These are high temperature (500 − 1000 ºC) working fuel cells with an electrolyte comprising a ceramic oxygen conductor. They can be used in all co-generation systems (~2 kW to multi MW). They can use pure H_2 at the anode, but also methanol, gasoline, diesel and some other low-carbon organics as the fuel due to the possibility of internal production of H_2 by reforming these hydrocarbons.

6- Molten carbonate fuel cells (MCFCs): They work at high temperatures (~650 ºC) with an electrolyte consisting of molten carbonate. Carbon dioxide must be included in the air feed. Similar to SOFCs, MCFCs can use pure H_2, methanol, gasoline, diesel and low-carbon organics at the anode. These cells can be used in medium to high-power co-generation systems (up to multi MW) [19, 20].

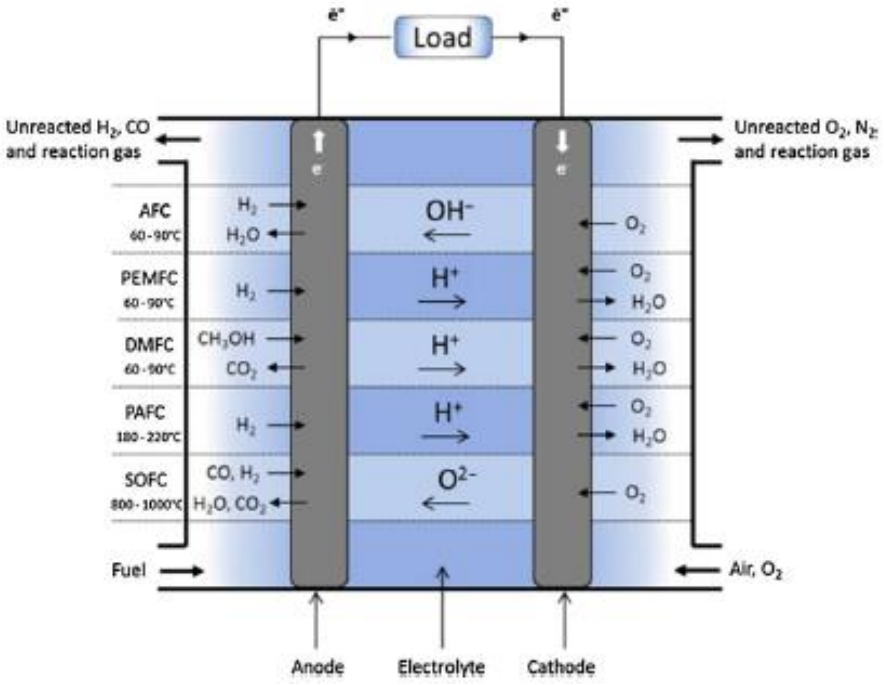

Figure 2-3. Schematic view of working conditions of different fuel cells [21].

2.2.4 Application and Future of Fuel Cells

The new fuel cells also work with the same principles as the original ones. Today, new membranes such as Nafion are being developed, and platinum utilization in PEMFC has decreased significantly from 28 $mg\,cm^{-2}$ in 1967 to less than 2 $mg\,cm^{-2}$ today. Therefore, PEMs are currently one of the most proper electrical energy generating technologies to be adapted in portable and transportation applications (public transport, automobile and battery replacement), utility vehicles (fork-lifts, material handling industrial vehicles, lawn maintenance vehicles, golf carts and airport people movers), and stationary power systems. For instance, Honda introduced the FCX hydrogen fuel cell vehicle in the USA and Japan in 2002, and the FCX Clarity model was launched in California in 2008. Toyota also started the development of a Fuel Cell Hybrid Vehicle (FCHV) in 1992, which was launched in 2002. The Toyota MIRAI that runs on hydrogen PEMFC was sold at approximately 50,000 CAD in 2021. [1, 15, 16, 20, 22, 23].

Government and private funding for fuel cell research have increased noticeably during the last decade. Furthermore, the existence of the International Partnership for Hydrogen and fuel cells in the Economy (IPHE) with 19 state members, including EU, USA, South Africa, Brazil and Japan, and the efforts made regarding the policies and standards for fossil fuels to be replaced by

the fuel cells demonstrate the importance of the economy of hydrogen and fuel cells in the world [24].

The global fuel cells market is estimated to reach USD 848 million by 2025, and the hydrogen infrastructure is rapidly expanding to support the deployment of FC vehicles. It is worth mentioning that researchers are also investigating the potential application of fuel cells in implantable medical devices such as pacemakers, drug pumps, biochips, blood counters, blood glucose meters, and temperature sensors [25, 26].

2.3 Direct Alkaline Methanol Fuel Cells

High expenses of pure green hydrogen gas and difficulties in its storage and transportation made the researchers interested in the direct methanol fuel cells (DMFCs) that are direct alcohol fuel cells. In DMFCs, methanol is oxidized directly at the anode as the fuel. They can operate at relatively low temperatures and are suitable for portable applications. Methanol is a readily available low-cost and easy-to-transport fuel with a high energy density of 702.32 kJ mol^{-1} [15, 27, 28]. In DMFCs, methanol or methanol/water mixture can be fed as liquid or gas at the anode which is usually a Pt-based material with acceptable stability, activity, and ability of methanol adsorption in acidic media. The anodic, cathodic and overall reactions for methanol oxidation in a DMFCs with proton conducting electrolyte can be written respectively in Reaction 2-1 to Reaction 2-3. Moreover, formaldehyde, formic acid or other organic molecules can also be formed during methanol oxidation [15, 20, 24, 29].

$$CH_3OH + H_2O \rightarrow CO_2 + 6H^+ + 6e^- \quad \textbf{Reaction 2-1}$$

$$3/2\ O_2 + 6H^+ + 6e^- \rightarrow 3H_2O \quad \textbf{Reaction 2-2}$$

$$CH_3OH + 3/2\ O_2 \rightarrow CO_2 + 2H_2O \quad \textbf{Reaction 2-3}$$

Muller explored the electro-oxidation of methanol for the first time in 1922. Widespread research on electrocatalysts began in the early 1950s. Investigations showed that the kinetics of methanol electro-oxidation was higher in direct alkaline methanol fuel cells (DAMFCs), with a

common assertion that it is accompanied by alleviated corrosion and higher stability of the electrocatalyst in comparison with the acidic medium. However, the chemical reactions in alkaline electrolytes (like KOH) with the produced CO_2 from methanol oxidation can form carbonate. Moreover, in contrast to the common assertion, the agglomeration, dissolution/redeposition and even accelerated degradation of the electrocatalyst materials in alkaline media compared to acidic have been extensively discussed [20, 29-31]. If the oxidation occurs in alkaline media, the charge carrier is OH^-. Oxygen/air is supplied to the cathode, where it is reduced at the catalyst layer to form hydroxide ions (Reaction 2-4) and then diffuse through the electrolyte to participate in the anodic oxidation reaction, where methanol reacts with the hydroxide ions and produces water (Reaction 2-5) and electrons.

$$3H_2O + 6e^- + 3/2\ O_2 \rightarrow 6OH^-$$ **Reaction 2-4**

$$CH_3OH + 6OH^- \rightarrow CO_2 + 5H_2O + 6e^-$$ **Reaction 2-5**

2.4 Electrocatalyst Material

Methanol oxidation is the main anodic reaction that produces electrons in DMFCs. During the past decades, metallic Pt and PtRu have become important as electrocatalysts for methanol oxidation reaction (MOR) in DMFCs because of their excellent catalytic properties, chemical corrosion resistance, high melting point, high mechanical strength, and good ductility [32]. Even though Pt has the highest activity for methanol oxidation among metals, its electro-oxidation activity is not satisfactory, reducing the overall efficiency, cell output power and increasing the fuel cell costs. Moreover, the slow kinetics of methanol oxidation requires a high Pt loading that hinders their commercialization. In addition, carbon monoxide resulting from methanol oxidation is a very stable intermediate that poisons the platinum surface and reduces the cell efficiency and power output [33]. Considering carbon monoxide poisoning is an important factor in designing an efficient catalyst. The shape, particle size and crystalline structure of Pt can affect the CO adsorption on the surface of Pt and the overall electrocatalytic activity of the anode. This is the main reason that the PtRu electrocatalyst is also favorable for methanol oxidation due to a higher CO tolerance, the mechanism of which is explained in section 2.4.2 [33, 34].

The cathodic reaction, ORR, has complex kinetics because of the multiple electron transfer steps and its sensitivity to the pH value, solvation, and polarity of water. The ORR in an alkaline medium is easier than the acidic. In acidic media, only a few catalysts like Pt have a high enough O_2 adsorption free energy to bind to the surface and allow the ORR to occur at an appreciable rate. It is explained that by increasing the pH value, a thermodynamic shift occurs in the ORR potential vs standard hydrogen electrode (SHE) at standard conditions (0.401 V in alkaline and 1.229 V in acid). This significantly lowers the overpotential of the first electron transfer step ($O_2/O_2^{\bullet-}$) from 1.53 V (pH = 0) to 0.7 V (pH = 14). This decrease in the potential increases the surface energy of the electrocatalyst, resulting in lower free energy of adsorption for oxygen and its intermediates, enables the use of non-noble metals for this reaction [35-37].

On the other hand, the complicated ORR kinetics involves multiple electron transfer steps, which is also affected by the high pH value. The oxygen reduction reaction on the surface of a catalyst can occur under a $4e^-$ (direct or series) or a $2e^-$ pathway. The former involves the transfer of four electrons to the adsorbed oxygen, where during a $2e^-$ pathway, two electrons are transferred to the adsorbed oxygen, forming a peroxide intermediate that diffuses to the bulk electrolyte without any further reduction. The $2e^-$ pathway is undesirable since the reduction reaction is incomplete, and on Pt surface with high O_2 adsorption energy, the $4e^-$ pathway is the dominant route [35-37].

Moreover, oxygen can be reduced at the inner Helmholtz plane (IHP), the region between the electrode surfaces and closely attracted charged species, and at the outer Helmholtz plane (OHP), the region where the charged species are loosely scattered in the aqueous solution (Figure 2-4). Due to the high adsorption of OH^- on the surface of the electrocatalyst in alkaline media and the stabilization of solvated oxygen species in the OHP, the oxygen reduction can occur in both IHP and OHP. Furthermore, the electron transfer in OHP is independent of the surface, enabling the use of a wide range of non-noble metal catalysts in alkaline media. On the other hand, on non-noble catalysts, the outer sphere mechanism dominates the ORR due to the high oxide surface coverage; thus, the undesired $2e^-$ pathway with the formation of peroxide intermediate becomes dominant. Accordingly, Pt-based electrocatalysts remain the catalyst of choice for ORR even in alkaline media [35-37].

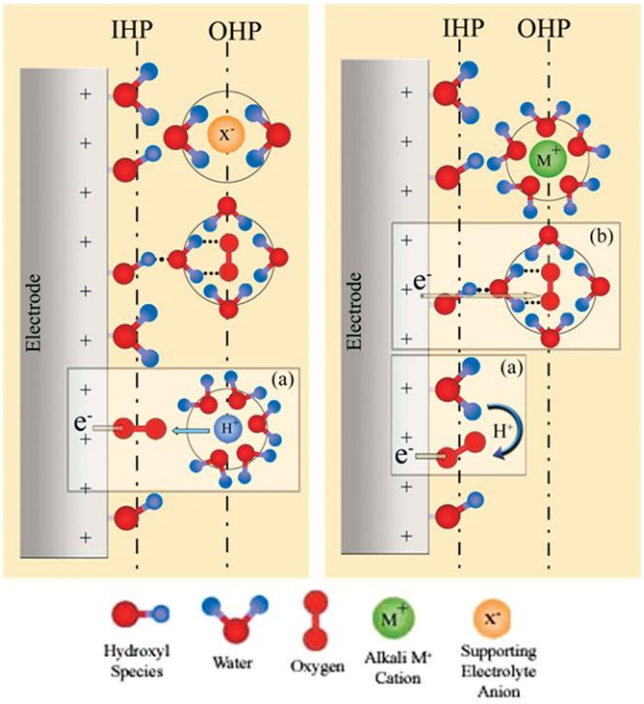

Figure 2-4. Schematic illustration of the double-layer structure during ORR in acidic (left) and alkaline (right) media. (a) inner- and (b) outer-sphere electron transfer processes [36].

As commented earlier, the use of nanostructured electrocatalysts for both anodic and cathodic fuel cell reactions seems essential. For both MOR and ORR in an alkaline fuel cell, platinum remains the benchmark, and all non-platinum group metals are compared to this commercially available electrocatalyst. However, the Pt-based electrode suffers multiple difficulties such as short lifetime, CO poisoning, shortage of resources, high loading and consequently, high costs of Pt-based electrocatalysts. Many researchers have shown that different parameters can affect the activity of an electrocatalyst, including particle shape and size, electronic structure, surface defects, and crystalline structure. Therefore, extensive research is undertaken to develop new electrocatalysts to promote the fuel cell performance by improving the electrocatalytic activity of the anode and cathode at low Pt loading such as using Pt nanoparticles, Pt-based alloys, supported Pt, metal-decorated Pt, deposited Pt thin films on metal, and so forth to reduce the overall Pt loading while enhancing its intrinsic electrocatalytic behavior which directly connects to the cost of FCs [33, 38]. It should be noted that simultaneous enhancement of the activity and durability of an electrocatalyst is a challenging task since electrocatalysts with higher activity are usually less stable.

2.4.1 Surface Engineering

The surface atomic arrangement of the active sites can govern their adsorption behavior and, thus, their electrocatalytic activity. The coordination number (CN) expressing the number of atoms located in the proximities of an atom can be a descriptor of the geometry. Studies have demonstrated the existence of a relationship between CN and adsorption energy, in which high CN corresponds to weak, and low CN corresponds to strong adsorption energies [39].

In a fuel cell, the fuel (methanol or oxygen) needs to interact simultaneously with several atoms of the electrode surface. For example, Pt must first adsorb methanol to be able to break the carbon-hydrogen bonds and form the adsorbed CO. This is why the surface structure of the catalyst, such as the number of surface atoms with a particular geometry, affects the electro-oxidation of methanol [34]. Therefore, fabricating a surface that minimizes the formation of adsorbed CO can be done by studying the structural effects of Pt on the methanol oxidation and determining the smallest number of surface atoms and their geometric arrangement [40, 41].

In two studies by Angel Cuesta [40, 41], the cyclic voltammetry of a cyanide-modified Pt(111) electrode in 0.1 M $HClO_4$ + 0.2 M CH_3OH exhibited an unaffected hydrogen region. At the same time, there was no hysteresis between the positive and the negative-going sweeps, indicating that no poison intermediate (adsorbed CO) was formed on the surface of their electrode, which was further confirmed by the FT-IR spectra. They concluded that the existence of at least three contiguous Pt atoms is necessary for the dehydrogenation reaction of methanol to CO, and the minimum two adjacent platinum atoms suffice the oxidation of methanol to CO_2 through the non-CO pathway (Figure 2-5). However, the reaction of methanol-derived adsorbates with bulk water can form formate [40, 41].

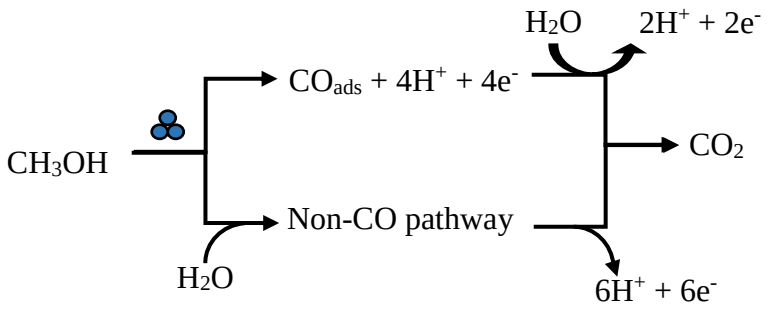

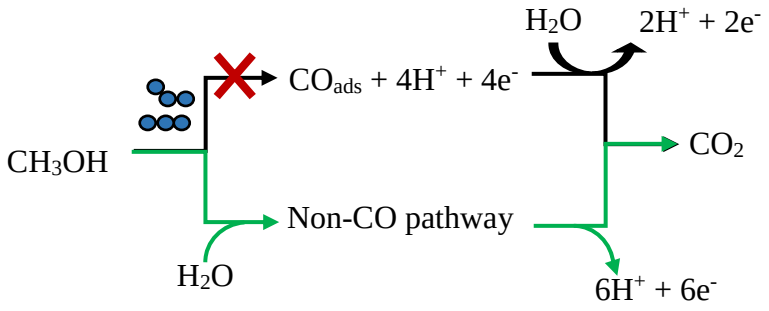

Figure 2-5. Three contiguous atoms for CO formation during methanol electro-oxidation on Pt [40].

Another example is Mo doped PtNi/C electrocatalyst that exhibited excellent ORR performance in acid electrolyte with the mass activity of 6.98 A mg_{Pt}^{-1} at 0.9 V versus RHE compared to the control commercial Pt/C catalyst with the mass activity of 96 mA mg_{Pt}^{-1}. It was stated that Mo improved the ORR kinetics by modifying the coordination environments of Pt atoms on the surface. Moreover, the octahedral shape of the catalyst made the surface enriched with Pt (111) and protected the Ni sublayer from acid dissolution [42, 43].

2.4.2 Shape/Crystallinity and Composition

Tuning the shape and crystalline structure of a Pt-based electrocatalyst represents another effective strategy to tune the performance and durability. This is the main reason that the facet-controlled synthesis of metal nanocrystals has drawn extensive attention by developing more active catalysts with selectively exposed facets. For instance, studies have shown that the ORR kinetics on Pt (*hkl*) surfaces follows an ascending order with Pt(100)<Pt(111)<Pt(110) in 0.1 M $HClO_4$ [43, 44].

Chemical composition is another critical determinant of electrocatalytic activity. Typically, Pt is combined with other metals, especially non-precious metals, to synthesize bi- or multi-metallic catalysts in the form of alloy, multi-layered, core-shells, and heterojunction nanostructures. By a rational selection of metal components, the synthesized catalyst can profit from the contribution of each metal and even synergistic effects while lowering Pt loading. Different metals have been used for alloying Pt, whereas ruthenium (Ru), cobalt (Co) and nickel (Ni) are the most preferred ones. The effective parameters in alloying Pt are the atomic ratios of Pt:metal and the preparation routes. For instance, at a low alloying degree, the catalytic activity of Pt might decrease because

of the dilution effect of Pt that lowers the adsorption of the fuel (methanol or oxygen) [45]. High-energy ball-milling using different powder particles, electrodeposition using different metal-containing salts, and chemical co-precipitation or co-reduction from solutions comprising Pt and the other metal precursors are the most frequently-used routes for Pt alloying [46, 47].

Alloying can affect the electronic structure of the electrocatalyst through the bifunctional and ligand mechanisms. For example, when PtRu is used for MOR, through the bifunctional mechanism, water is activated over Ru atoms at potentials less positive than at Pt and forms active hydroxyl intermediates that can oxidize CO molecules adsorbed on the neighboring Pt sites. Via ligand mechanism, the change in the metal overlayer *d*-band center position, the electron cloud density and lattice structure of the Pt after alloying could reduce the adsorption of CO on Pt active sites [38, 48-51].

2.4.3 Size and Geometry

Physical properties, including particle size, can influence the catalytic activity of nanostructured catalysts. The size of a given nanostructure is highly dependent on the nucleation and growth rates, which are influenced by the synthesis conditions, such as the precursor concentration, temperature, pressure, and solvent. Electrocatalysts in nanoscale possess high electrochemically active surface area and high mass activity. Studies have demonstrated that Pt nanoparticles with particle size above 11 nm exhibit bulk behavior with low binding energy to oxygen intermediates/adsorbates, and those with diameters smaller than 4-5 nm have stronger binding energy to CO, OH, and other adsorbates. It has been observed that Pt nanoparticles with 2-3 nm size possess an optimum surface-to-volume ratio, thus the highest mass activity. However, the smaller particles are more unstable and susceptible to dissolution [39, 52, 53].

2.4.4 Structural Defects

An approach to rationally improve the activity of an electrocatalyst is by generating surface defects, resulting in the introduction of more catalytic active sites, such as surface distortion introduced by alloying or immobilizing the nanoparticles on a support material. Moreover, it has been observed that an ordered catalyst with a maximum number of a specific type of active catalytic sites can rapidly degrade. In contrast, particles with structural surface defects containing

various active surface sites take advantage of both high activity and stability [39]. For example, when a Cu/Pt(111) catalyst for ORR was dealloyed, the formed surface cavities increased the activity of the Pt skin. Alternatively, it has been demonstrated that Pt with more stepped surface atoms is more active for ORR. However, the overall catalytic activity depends on the relative abundance of the defect sites [43, 54].

It should be noted that although defects can increase the catalyst activity, defects on the catalyst support can result in its degradation, primarily when carbon-based material containing a large number of defects is used as support. For instance, during a fuel cell operation, the defective carbon sites can be hydrolyzed and degrade the support material [55].

2.4.5 Supported Platinum

Since the oxidation of methanol and reduction of oxygen occur on the surface of an electrocatalyst, increasing the number of active sites per Pt mass is necessary to maximize the surface exposure of the electrocatalyst. Studies have shown that Pt-based catalysts supported on suitable substrates as the anode and cathode can effectively improve the performance of the FCs. Adopting an appropriate electrocatalyst support with high electrical conductivity, sufficient corrosion resistance, and strong interaction with the metal particles can significantly improve the electrocatalytic activity and stability. Furthermore, when the electrocatalyst is well dispersed, its mass activity is improved by increasing its dispersion. Different polymeric films, such as polypyrrole (PPY), polyaniline (PANI), poly(3 methylethiophene) (PMT), poly(3,4-ethylenedioxythiophene) (PEDOT), and carbon-based materials have been investigated as catalyst supports for methanol oxidation [53, 56]. Moreover, Pt supported on metal oxides/nitrides including TiO_2, ZnO, SnO_2, and WO_3 have shown improved catalytic activity and stability for the methanol oxidation reaction [57, 58].

Different carbonaceous materials, including carbon black, activated carbon, fullerene, carbon nanotubes (CNTs), and graphene, are promising support materials for Pt nanoparticles. However, many of these carbon-based supports can undergo electrochemical corrosion in harsh media, eventually lowering the catalyst activity, durability and fuel cell performance. The electrochemical corrosion reaction of carbon (E^0= 0.207 V_{NHE}) is written in Reaction 2-6, which can be ignored at normal PEM fuel cell operating conditions due to the low electrochemical kinetic rate.

$$C + 2H_2O \rightarrow CO_2 + 4H^+ + 4e^-$$ **Reaction 2-6**

However, in other conditions, such as multiple start-up/shut-down processes or fuel starvation, carbon corrosion occurs at a high rate because of the electrode potential, which frequently goes above the open-circuit voltage. Therefore, carbon materials with high amorphous carbon content and oxygen functional groups are more likely to corrode electrochemically. On the contrary, high graphitization degree and hydrophobicity are the factors preventing the corrosion of carbon. Hence, a carbon-based support with a large surface area, high electrical conductivity and stability in severe environments must be selected [59, 60]. Furthermore, the interactions between Pt and C are partially covalent, which arises from electron delocalization between the carbon p- and the Pt d-orbitals. A strong metal-support interaction can play a significant role in the stability of the electrocatalyst by inhibiting Pt oxidation and dissolution and improving catalyst activity by modifying its electronic structure [61].

Unique structural, electrical and mechanical properties with high specific surface area to accommodate high metal loadings as well as heat conduction efficiency and high stability make CNTs an excellent supporting material for methanol electro-oxidation and oxygen reduction reactions in DAMFCs [59, 62, 63]. Since CNTs are the selected electrocatalyst support material in this thesis, a brief description of carbon nanotube's structure, properties and synthesis routes are presented.

Carbon nanotubes are nano-sized hollow cylinder-like structures that have been extensively investigated over the last two decades. Their discovery was attributed to Iijima in 1991. In general, carbon nanofilaments are divided into hollow-core structures (CNTs) and filled core structures (carbon nanofibers) [63-65].

A single-walled carbon nanotube (SWCNT) is composed of a rolled graphene sheet. There are numerous modes of rolling a graphene sheet into a seamless cylinder; therefore, SWCNT can be classified as the zigzag, armchair, and chiral according to the rolling direction (Figure 2-6) [63-65].

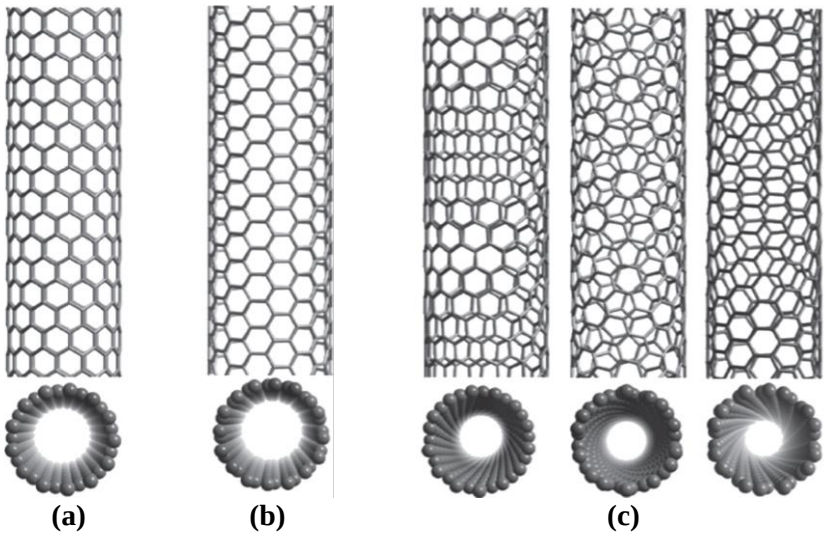

Figure 2-6. SWCNTs with (a) zigzag, (b) armchair, and (c) chiral tubes [65].

Multi-walled carbon nanotubes (MWCNTs) consist of concentric single-walled nanotubes, each being a rolled graphene sheet. In literature, the word "texture" is usually used for different types of MWCNTs shown in Figure 2-7 (MWCNTs of concentric cylinders, truncated graphene cones piled up as cups (cup-stake model), and a single graphene ribbon helically wrapped) [64, 65].

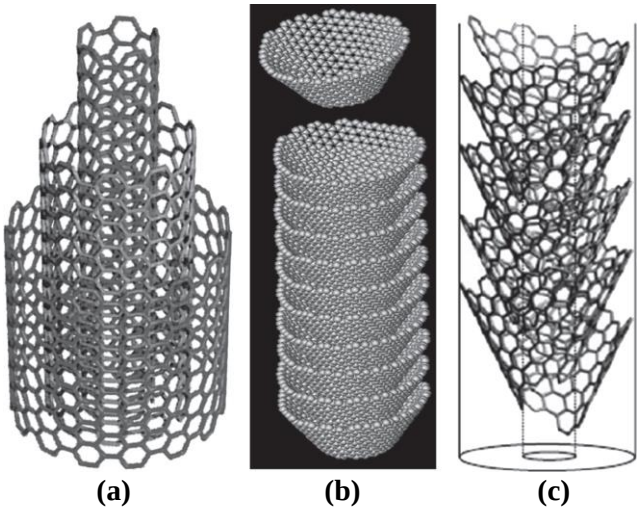

Figure 2-7. MWCNTs of (a) concentric, (b) herringbone-1, and (c) herringbone-2 textures [65].

Several techniques are available for synthesizing CNTs, including electric arc discharge between carbon electrodes, laser vaporization of a carbon target (laser ablation), and thermal

decomposition of hydrocarbon gases (CVD), which are the three most commonly used methods. Given that CVD was the desired method for the current study, it is further described. In this technique, CNTs are directly synthesized on either a solid substrate covered with a metal catalyst or directly on a bulk catalyst. The apparatus typically consists of a quartz tube placed inside a tubular electric furnace. The substrate is inserted in the furnace, the precursor gas flow is provided, and the temperature of the furnace is raised in the range of 650 to 900 °C to pyrolyze the precursor gas [64].

The main advantages of CVD are the production of dense and uniform deposits, reproducibility, good adhesion, adjustable deposition rates, ability to control crystal structure, surface morphology and orientation of the CVD products, reasonable expenses and variety of chemical precursors to synthesize CNTs on different substrates [66]. Different temperatures, duration, precursor gases such as methane, acetylene, alcohol, carbon monoxide, xylene, acetylene (C_2H_2)/benzene mixture and CO/benzene mixtures at different flow rates have been used as the source of carbon [67].

In this project, we directly grew a forest of MWCNTs on the surface of stainless steel meshes using the CVD method. This approach allows fabricating an electrode that can be directly used as the gas diffusion electrode eliminating the carbon backing and current collector. Furthermore, strong bonding between the MWCNTs and substrate enables improved electron/thermal transport properties, positively influencing the fuel cell performance. In a previous study, Baddour et al. had described the synthesis of MWCNTs on a stainless steel mesh [68]. They explained that the mechanical deformation in extruding/pulling the wires upon fabrication generates elongated nano-scale grains. When the mesh is heated, minimizing the surface energy generates curvature on the edges of these grains, and its surface morphology changes from a relatively smooth surface to one covered with nano-sized hills, which act as nanoparticle-like sites for the growth of MWCNTs [68]. In another study, Hordy et al. demonstrated that the size of these sites correlates with the minimum mean MWCNTs diameter directly grown on a SS mesh (Figure 2-8) [69].

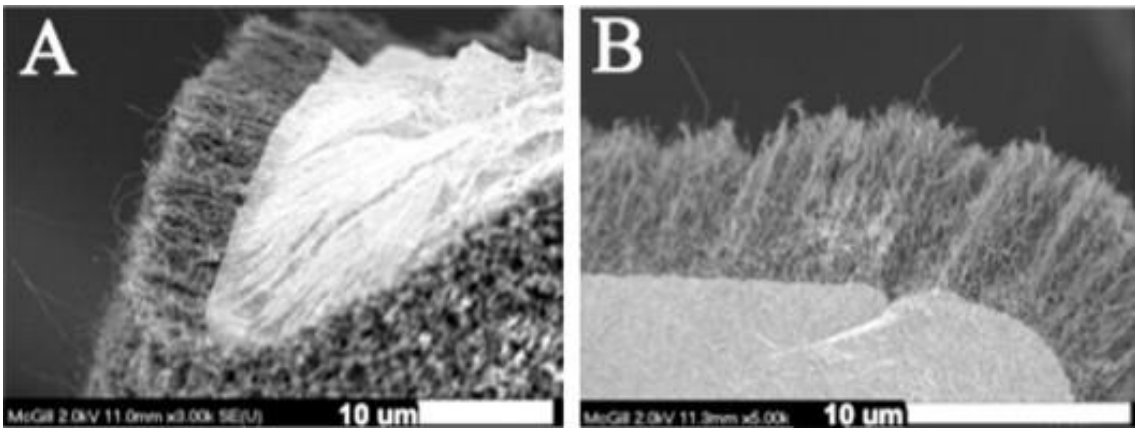

Figure 2-8. Vertically-grown MWCNTs on stainless steel [69].

Moreover, there are many investigations on the use of functionalized CNTs as support for electrocatalysts. Functional groups on the surface of carbon-based supports can play an important role in the properties and behavior of electrocatalysts. Studies have concluded that by functionalizing the CNTs with oxygen-containing groups, the onset potential of the methanol oxidation reaction can shift toward less positive potentials with the higher current density. Also, increasing the hydrophilicity of carbon support can favor the diffusion of the reactants toward the active sites. In addition, these functional groups may participate in MOR by supplying OH groups to the intermediate species (Pt-$(CHO)_{ads}$ or Pt-$(CO)_{ads}$), thus promoting the production of CO_2 at less positive potentials [70].

CNTs can be chemically treated/oxidized in strong acid (nitric acid or a mixture of sulfuric acid and hydrogen peroxide) or alkaline media (ammonium hydroxide/hydrogen peroxide). The main drawback of this method is the alteration of the well-organized structure of CNTs showing relatively low defects content and their physical properties. Exposure to a harsh environment at elevated temperature for a long time can damage the CNT sidewall and surface, such as shortening them and forming graphitic network defects, which alter the physical and electrical properties of CNTs. It can also produce amorphous carbon covering the surface of CNTs, lowering the surface area and related characteristics [59, 62].

The plasma functionalization technique is a practical approach to functionalize CNTs with different functional groups, eliminating the use of solvent, high temperatures, and the aggregation of MWCNTs. This method can be performed directly on the supported nanotubes using a low-pressure capacitively-coupled radio-frequency (RF) glow discharge [71]. In this process, a cold

plasma is produced by applying sufficient voltage between two electrodes placed in a chamber at low pressures. When the gas breaks down, the highly reactive species in the produced plasma (excited and charged species, ions, radicals, photons and electrons) interact with the substrate and modify its surface either by forming a film on the surface or forming new covalent bonds. The duration and power of the treatment, the composition of the purging gases, the position of the sample in the plasma chamber and the post-functionalization conditions (ageing) influence the formation of functional groups on the substrate. For instance, placing the substrate between the electrodes (in the plasma) or outside of plasma in the afterglow region, where the density of charged species differs, will result in different degrees of functionalization. L. Jorge et al. reported amine-functionalization of MWCNTs containing about 19 at% using a low-pressure capacitively-coupled radio frequency (RF, 13.56 MHz) glow discharge with the mixture of ammonia (10 sccm) and ethylene (10 sccm) for 5 min at the pressure of 80 Pa and RF power level of 35 W. The SEM images of MWCNTs in Figure 2-9 showed no morphological alteration after the plasma functionalization [72].

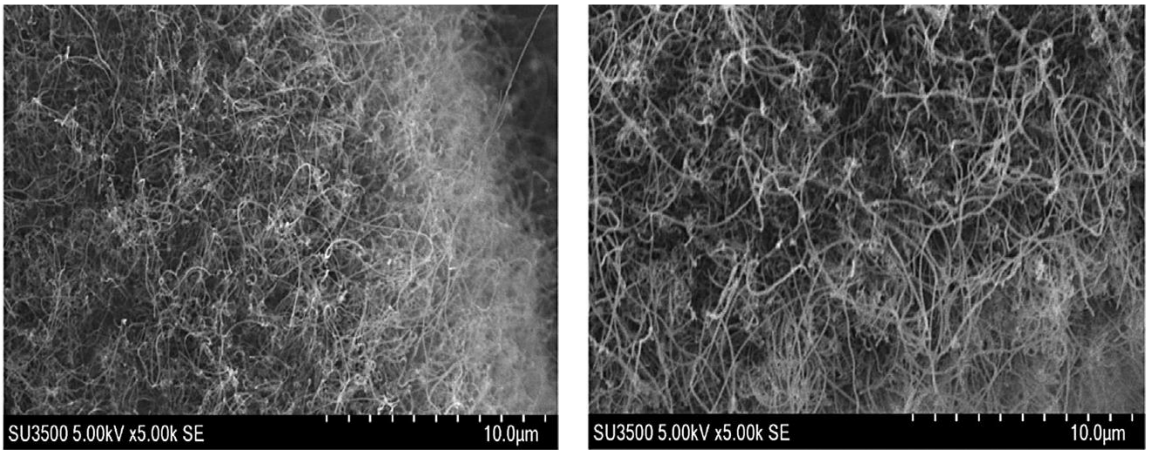

Figure 2-9. MWCNTs (left) before and (right) after amine-functionalization by low-pressure capacitively-coupled RF [72].

2.5 Platinum Nanoparticles Synthesis

Platinum, discovered in the 1780s, is a precious metal widely used for catalytic conversions (35 %–40 %), jewelry (up to 35 %), and the production of petroleum (as a catalyst) and glass (in the structure of dies and molds) (18 %). In order to maintain high catalytic activity at a low material

cost, there are strong efforts worldwide to synthesize small Pt nanoparticles to maximize the surface-to-volume ratio. Pt nanoparticles within the diameter range of 2 to 10 nm are of great interest because of their detectable changes in particle electronic and structural properties and their usage in commercial applications [21, 52, 53].

Various wet and dry chemistry techniques exist to synthesize Pt nanoparticles on support materials. In wet chemical reduction, the impregnated carbon support with Pt salt solution is reduced using a reducing agent, followed by the nucleation and growth of the Pt nanoparticles (1 to 30 nm) [21]. The aggregation of Pt nanoparticles during synthesis due to a 3D nucleation and growth mechanism and high surface energy is one of the main drawbacks of this method [53]. Therefore, stabilizing agents such as ligands or surfactants must be used to prevent aggregation, which will need to be further removed from the synthesized nanoparticles [73]. After synthesizing nanoparticles via chemical or wet processes, the surface of the electrode should be cleaned by various methods such as plasma cleaning, thermal annealing, acetic acid washing, and UV-ozone irradiation, which usually require either high temperature or long treatment time. These cleaning processes may result in the change of particle size and morphology of the catalyst and even detachment of Pt from the substrate surface [74].

On the other hand, dry synthesis methods are alternative techniques to synthesizing controllable metal nanostructures by eliminating some of the drawbacks of wet chemistry, including using solvent/chemicals, applying high temperatures/pressures, and the need for cleaning post-treatments. Among different dry methods available for the synthesis of metal nanoparticles, some plasma-based techniques have proven effective methods to deposit highly stable and dispersed metal nanoparticles with small diameters and narrow diameter distribution on a solid substrate and are thus explained in brief [75].

2.5.1 Cathodic Arc Evaporation

To synthesize Pt nanoparticles by cathodic arc evaporation, a pulsed electric arc is formed between a cathode and anode in a low-pressure inert gas. The cathode is made of the material of the nanoparticles to be synthesized. The cathode erosion occurs at the arc root, where the heat flux can exceed 10^9 W m^{-2}. This leads to the cathode evaporation, forming a plasma plume, followed by cooling, supersaturation, and condensation of the metal vapors, thus forming nanoparticles. As

they remain exposed to the plasma, the formed nanoparticles acquire a negative surface charge, resulting in their repulsion through Coulombic interactions. This peculiarity of in-plasma synthesis processes leads to streams of well-dispersed particles. Furthermore, micron-size particles may also be formed during the formation of nanoparticles, thus contaminating the otherwise narrow-distributed nanoparticle size distributions[76].

2.5.2 Plasma Sputtering

Sputtering refers to a process of bombarding solid surfaces using high-energy plasma to produce nanomaterials, especially thin films. A high voltage is applied to the cathode target in a sputtering chamber where the desired background gas is introduced. The collisions between free electrons and gas molecules result in the formation of energetic gaseous ions. Sputtering can be formed via magnetron, radio-frequency, and DC diode. The high-energy positively-charged gas ions accelerate toward the cathode target and cause the physical ejection of target atoms/clusters [77].

Another approach to synthesize Pt nanoparticles is plasma sputtering in water with the mechanism shown in Figure 2-10. Pt wires as opposite electrodes are immersed in water. By applying a high pulsed DC voltage, the bombardment of electrons and high-energy radical particles, Pt atoms eject in the plasma region and the color of water changes from colorless to dark grey. Diffusion, growth, and condensation are reported to be the formation steps of Pt nanoparticles [57].

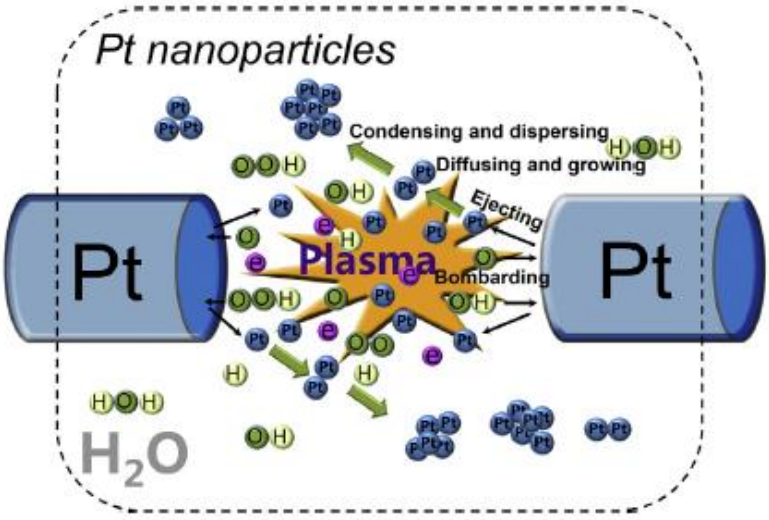

Figure 2-10. Platinum synthesis by plasma sputtering [57].

2.5.3 Pulsed Laser Ablation/Deposition (PLA or PLD)

In a PLD process, a focused laser beam with a fluence above a minimum threshold is aimed at a target mounted in a vacuum chamber. The target material absorbs the laser energy, which is then rapidly converted to electronic excitation, where the temperature can rise to several thousands of Kelvin. The target is rapidly vaporized and the plasma plume, containing ground- and excited-state neutral atoms, ions and electrons, expands away from the target. These species can also absorb the laser beam as the plume reheating. As the plume expands, cooling and supersaturation occur, and nanoparticles are formed. The negative charges that accumulate on the nanoparticles contribute to their dispersion. The nanoparticles are then deposited (collected) on a substrate facing the laser ablation target. Visible or UV nanosecond pulsed Nd:YAG lasers (pulse length 5-10 nm) are typically used for such applications.

The properties of the produced nanoparticles vary widely by changing the ablation conditions, target material and the environment. The distance between the target and the substrate is usually between 2 and 10 cm. The ambient pressure can vary from a few Torrs to ultrahigh vacuum (~10^{-10} Torr). When the gas pressure increases, the ablated species lose kinetic energy due to the more frequent collisions between the plume species and background gas molecules. Thus, the species with lower kinetic energy will form a more porous film, while a dense film is formed at lower gas pressures when the ablated species have higher kinetic energy [78-83]. A PLD device in its simplest form is schematically shown in Figure 2-11.

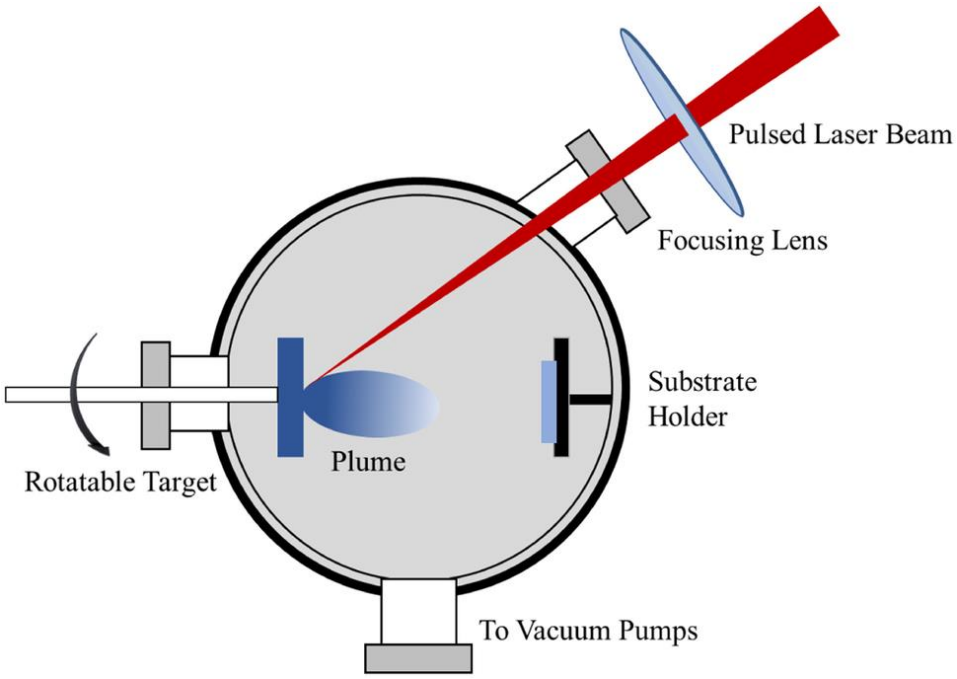

Figure 2-11. Schematic view of pulsed laser deposition [83].

One of the main advantages of this method is the controllable synthesis of nanostructures with a high dispersion onto the substrate. Furthermore, contrarily to arc processes, electrically non-conductive target materials can be used with PLD. Moreover, PLD is an appropriate technique for the synthesis of noble metals at low loadings, given that it also is a binder-free and solvent-free technique without the formation of any byproducts [73].

Pulsed laser ablation can also be performed in the liquid phase (PLAL), where the laser beam is focused on a target immersed in a liquid solution. In this method, the composition of the liquid environment such as solvent type, pH values, temperatures and electrolytes are the effective parameters in the final properties of the synthesized nanoparticles [73].

T. Simao et al. reported the synthesis of core (MnO_x)-shell (Au) structure using PLAL in an aqueous solution at pH= 11. They used $Au_{64}Mn_{36}$ (at. %) target. They described that the phase segregation and the formation of core-shell structures happen in the early stages of the synthesis, and the formation of MnO_x shell as the more hydrophilic species is favored. They illustrated that Au and MnOx nanoparticles are first ablated, and then fragmentation/vaporization and reorganization of the colloids lead to the final core-shell structure [84].

M. McArthur et al. successfully synthesized Ni nanoparticles-decorated MWCNTs using the PLD method. Figure 2-12 displays the SEM images of Ni nanoparticle-decorated MWCNTs with a diameter of (3.2 ± 1.6) nm synthesized by 20 min of PLD using helium background gas at the pressure of 2.5-3.0 mTorr [75].

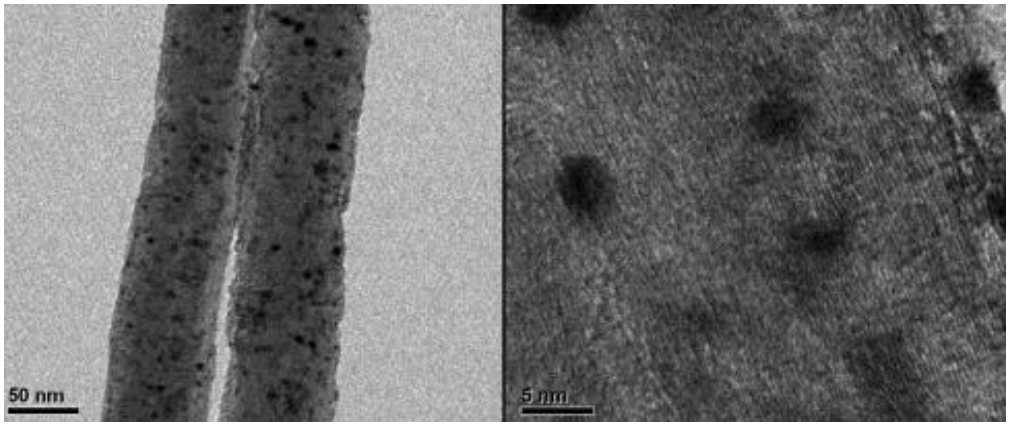

Figure 2-12. SEM images of Ni-MWCNTs [75].

In another study, MWCNTs were first grown by CVD on a carbon paper (CP). Then SnO_2 and Pt (thickness: 17 nm) films covered the surface of CNTs, respectively, producing CP-CNTs-SnO_2-Pt (Figure 2-13 (left)). This electrode was used as anode for ethanol oxidation (1 M) in 0.5 M H_2SO_4, and it yielded 2.1 times increased current density in comparison with the same material using graphite instead of CNTs [85].

In a study by Ting-Wei et al., Pt nanoparticles (diameter ~10 nm) were deposited by PLD on a commercial carbon gas diffusion layer with a microporous layer on top (Figure 2-13 (right)). The prepared sample showed improved methanol oxidation in 0.5 M H_2SO_4 compared to the commercial sample by decreasing the Pt loading from 200 to 17 $\mu g\,cm^2$ [86].

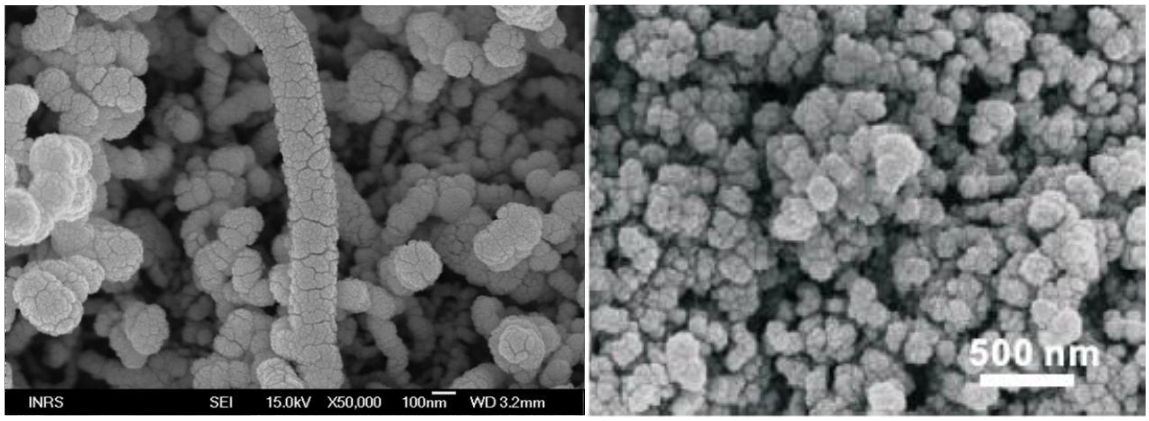

Figure 2-13. SEM images of (left) CNTs-SnO_2-Pt and (right) Pt/carbon [85, 86].

In another study to synthesize bimetal catalyst, crossed-beam pulsed laser deposition (CBPLD) was used to synthesize PtRu alloy thin films. Two laser beams (KrF 248 nm; 17 ns pulse width; repetition rate, 50 Hz) were synchronously focused on Pt and Ru targets at the helium pressure range of 10^{-5} to 11 Torr. As shown in Figure 2-14, when the plasma plumes of Pt and Ru crossed each other, they yielded a plume that contains both Pt and Ru, which resulted in the formation of PtRu alloy on the substrate (carbon disk) [87].

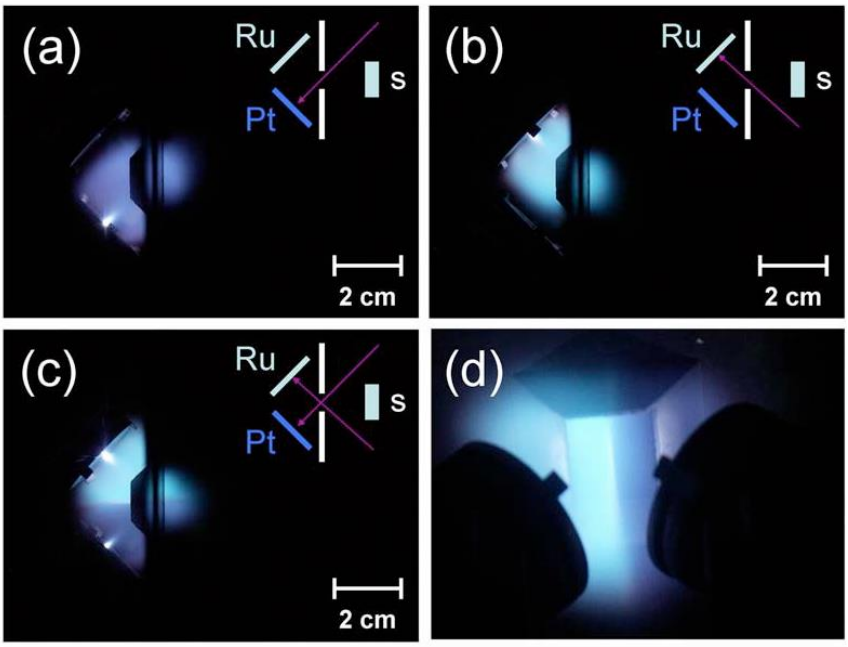

Figure 2-14. Photographs of the plumes at the He background pressure of 1.6 Torr: (a) Pt plume only, (b) Ru plume only, (c and d) both Pt–Ru plume interacting [88].

Chapter 3

3. Methodology

This chapter describes the experimental procedures undertaken to achieve the objectives of this PhD thesis. It summarizes the materials and methods used in synthesizing the electrocatalysts/electrodes, their structural characterization, and their electrochemical assessment.

3.1 Synthesis of MWCNTs on SS

The MWCNTs grown on stainless steel mesh was selected as the electrocatalyst support material due to their high surface area and chemical stability in harsh media, proven ability to support Pt nanoparticles, and high electrical conductivity. Due to their high aspect ratio, MWCNTs provide a large electrode/electrolyte interfacial area, which results in higher electrochemically active surface area for electrochemical reactions and lower loadings of Pt nanoparticles [59, 89-91]. Moreover, since the MWCNTs are already anchored on the SS mesh, the need for both catalyst and binder for the growth and adherence of MWCNTs on a substrate is eliminated. Therefore, the electrical contact resistance is low (as opposed to dispersing them on a carbon paper using a binder, as it is usually done). This porous configuration facilitates mass transport at the gas diffusion electrode resulting in better fuel dispersion and electron transport between the electrocatalyst and support.

In this project, MWCNTs (~30-40 nm in diameter and 13–15 μm in length) were directly grown on the surface of commercial 316L stainless steel (SS) mesh (grid bars: 165 × 800 per 6.45 cm^2; wire diameters: 0.07 and 0.05 mm; grid opening: 15 microns, thickness: 0.150 mm, purchased from TWP Inc.) using a one-step chemical vapor deposition (CVD) technique developed in the Catalytic and Plasma Process Engineering (CPPE) laboratory of McGill University. First, the SS mesh is ultrasonically cleaned in an acetone solution. Next, the dried SS mesh is placed in a tubular CVD furnace and heated to 700°C under ambient air for 2 min. The CVD furnace is then purged with argon (99.999%, all gases were purchased from MEGS Specialty Gases) at 592 ± 5 sccm to

reach an oxygen level below 0.5%. For the MWCNT growth, acetylene, as the carbon source, is co-injected with Ar at 68 ± 5 sccm for 2 min and then stopped while the Ar flow is maintained for another 2 more min. The MWCNT-covered SS mesh coupon (MWCNT/SS) is then taken out from the furnace and allowed to cool down to room temperature. A schematic view of the CVD setup is shown in Figure 3-1.

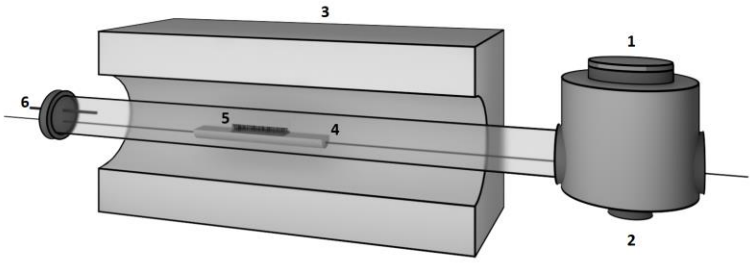

Figure 3-1. Schematic view of the CVD setup: 1) loading chamber, 2) gas exhaust, 3) furnace, 4) quartz boat, 5) MWCNTs on SS, and 6) gas inlet.

3.2 Synthesis/Functionalization Setup

All experiments, including radiofrequency (RF) plasma functionalization, pulsed laser ablation (PLA), and RF plasma-assisted pulsed laser deposition (RF-PAPLD) were performed in a setup schematically shown in Figure 3-2. The setup consists of two main chambers, where the left one is used for loading/unloading the samples. A pulsed nanosecond Nd:YAG laser (Quantel, Brilliant B10, repetition rate: 10 Hz, pulse width: 5 ns, wavelength: 355 nm) is mounted on the backside of the chambers, where the laser beam enters the right chamber and hits the target after passing the mirrors and a lens. The setup is always kept under a high vacuum (10^{-5} Torr) using a primary mechanical pump and a turbomolecular pump. The setup has an inlet for introducing gas into the chamber. The gas flow rates are controlled using mass flow controllers (Brooks SLA5850). Two parallel stainless steel disks with outer diameters (O.D.) of 10 cm (laser target holder) and 6 cm (substrate holder) are mounted inside the chamber at a 3-cm distance. The setup is used under three different modes of operation: RF plasma functionalization (Figure 3-2(a)), PLA (Figure 3-2(b)), and RF-PAPLD (Figure 3-2(c)). The third operation mode of RF-PAPLD (Figure 3-2(c)) was developed during this PhD project, and the entire setup was equipped with the turbomolecular pump.

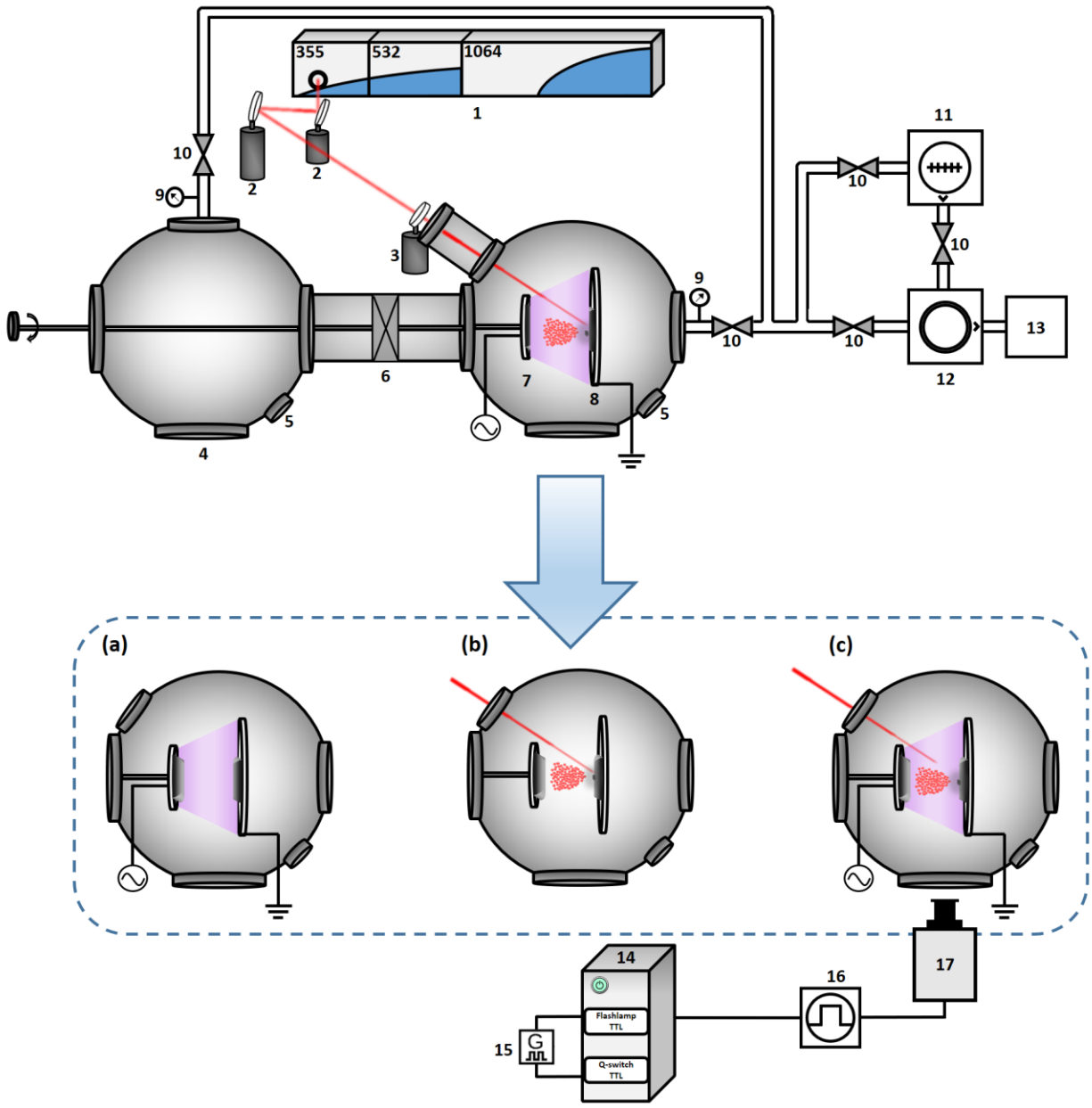

Figure 3-2. Schematic view of the experimental setup: 1) Nd:YAG laser, 2) mirrors, 3) lens, 4) Loading chamber, 5) gas inlet, 6) gate valve, 7) collecting substrate holder/live electrode, 8) target holder/ground electrode, 9) pressure gauge, 10) pneumatic valves, 11) turbomolecular pump, 12) primary mechanical pump, 13) exhaust, 14) laser control, 15) signal generator, 16) TTL trigger, and 17) high-speed camera.

3.2.1 Radiofrequency Plasma Functionalization of MWCNT/SS

The plasma functionalization of MWCNT/SS using a continuous wave low-pressure capacitively-coupled radiofrequency (RF) plasma (13.56 MHz) was performed in the setup shown

schematically in Figure 3-2(a). Prior to functionalization, Ar was injected in the vacuum chamber for 3 min and then pumped down to 10^{-5} Torr to reduce the air/moisture content. During functionalization, the chamber pressure was maintained at 2 Torr by continuously flowing a gas mixture of Ar, C_2H_6, with O_2 or N_2 at the flow rates of 250, 1 and 5 sccm, respectively, to functionalize the MWCNTs with oxygen (O-FMWCNT) or nitrogen (N-FMWCNT) functional groups. The MWCNT/SS sample was placed on the live stainless steel disk electrode. The RF plasma power levels and treatment times were 10, 20 and 30 W and 1, 2.5, 5, 10, 15 and 20 min, respectively. At the end of the experiment, the chamber was pressurized by injecting Ar until atmospheric pressure was reached.

3.2.2 Deposition of Pt Nanostructures on MWCNT/SS

Platinum nanostructures were synthesized and directly deposited on MWCNT/SS by solvent-free laser ablation of a platinum target at different background pressures and laser pulse energies at 21 ± 1 °C using the pulsed laser ablation setup represented in Figure 3-2(b). A Pt target (99.95%, Ted Pella Inc.) was ablated using the nanosecond Nd:YAG laser with the laser beam focused at an incidence angle of 45^o onto the target (a spot size diameter was estimated to be ~1 mm). The MWCNT/SS coupon was affixed to a substrate holder mounted on a manual linear displacement stage and positioned in front of the Pt target. Prior to each PLA experiment, the chamber was flushed with Ar for 3 min and then pumped down to 10^{-5} Torr to reduce the amount of moisture and any other possible gaseous contaminants. The ablation time was in the range of 1 to 10 min (600 to 6000 laser shots). The background gas (Ar) pressure was varied from 10^{-5} to 10 Torr, and the laser energy (measured with a Joule meter, Coherent air-cooled thermopile sensor, PM10 model) was varied from 20 to 66 mJ pulse^{-1}. The energy per pulse of the Nd:YAG laser was varied using the delay time between the flashlamp and the optical Q-switch from 215 to 315 μs, which gave rise to energy per pulse ranging from 66 to 20 mJ pulse^{-1}. The target holder was moved up and down using a motorized stage to enable uniform wear of the target and to mitigate thermal effects. The substrate holder was manually rotated during the 5 min of PLA to achieve uniform coverage of the MWCNTs/SS coupons.

3.2.3 Synthesis of TiO_xN_y on MWCNT/SS

Titanium target (99.995%, Ted Pella Inc.) was ablated using the laser energy of 66 mJ $pulse^{-1}$. The target was mounted on the 10 cm-outer diameter (O.D.) stainless steel disc, while the PLD-produced nanoparticles were deposited on the MWCNT/SS substrate mounted on a 6 cm O.D. stainless steel disc directly facing the target (3 cm target-substrate distance). The PLD-produced metal vapor plume/nanoparticle stream was immersed into a large volume continuous-wave capacitively-coupled radiofrequency (13.56 MHz) plasma sustained using the substrate as the powered electrode and the target as the ground. Prior to each experiment, the chamber was flushed with Ar for 3 min and pumped down to a 10^{-5} Torr base pressure to remove air and minimize the moisture level. The target holder was rocked up and down during ablation to ensure uniform wear and to minimize thermal effects resulting in localized melting and ejection of liquid metal droplets. The substrate holder was manually rotated during PLD to ensure uniform nanoparticle dispersion over the substrate.Titanium oxynitride (TiO_xN_y) films were deposited on MWCNT/SS at N_2 background gas pressures of 0.03 and 1.0 Torr, and RF power levels of 0, 10 and 30 W for 10 min. Pt nanoparticles were deposited by PLD on the MWCNTs and TiO_xN_y-coated MWCNTs at an Ar background gas pressure of 10^{-5} Torr for 2.5 min. The sample coding is based on the chamber pressure and RF power level. For instance, TiO_xN_y-1.0 Torr-0 W refers to an RF plasma of 0 W (no plasma) during PLD at the pressure of 1.0 Torr.

A high-speed camera (Photron FASTCAM SA5, model 1000K-M1, monochromatic) was used to study the expansion dynamics of the laser-induced metal vapor plume. An arbitrary function generator (Tektronix-AFG3102) was used to trigger the laser Q-switch and camera at prescribed delays with respect to the flashlamp output signal. The laser Q-switch was externally triggered with a 215 μs delay, while the camera delay was varied between 214 and 614 μs (20 ns increments) to cover the entire laser plume expansion event. A total of 64 frames (896 × 848 pixels) at 1 μs exposure were captured at any given camera time delay. The frames were then accumulated to produce an average image of the expanding plasma plume, frozen in time, at the corresponding camera delay.

3.3 Commercial Pt/C Catalyst Thin Film Preparation

To compare the performance of the Pt/MWCNT/SS electrocatalysts produced in the current study to the commercial Pt/C electrocatalyst, catalyst ink with specific Pt loadings of Pt/C was prepared. In this regard, 25.6 mg of 20 wt% Pt/C catalyst (Sigma-Aldrich) was mixed with isopropyl (2 mL) and DI water (8 mL) and sonicated for 15 min. The vial containing the ink was fixed at the center of an ice-water ultrasonic bath (Branson 1510, 70 W, 42 kHz). Nafion$^{(R)}$ 117 solution (0.2 mL) purchased from Sigma-Aldrich was added to the mixture while the sonication continued for another 15 min. Different volumes of the prepared ink were dropped on a glassy carbon (GC) rotating disk electrode using a pipette to obtain the desired Pt loadings. To obtain a mirror-like surface, the GC was polished prior to use by a porous neoprene cloth (Black Star, Anamet) with 0.05 μm alumina slurry. Ar gas with an extremely low flow rate was used to dry the ink droplet on the surface of GC.

3.4 Structural Characterization

3.4.1 Scanning Electron Microscopy (SEM)

Ultra-high-resolution field emission scanning electron microscopy (Hitachi, Cold FE SU-8000 SEM) was used for the morphological characterization of the nanostructures deposited on MWCNT/SS before and after the electrochemical evaluation. The energy dispersive X-ray spectroscopy (EDS) (XMax 80 mm^2 Oxford Instruments) coupled with the SEM was used under SEM and STEM modes for elemental mapping of the samples.

3.4.2 Transmission Electron Microscopy (TEM)

The shape, particle size distribution, and crystalline/lattice *d*-spacing of the Pt nanostructures were investigated using transmission electron microscopy (Thermo-Scientific, Talos F200X G2 TEM). For TEM imaging, the metal-coated MWCNT/SS mesh was first sonicated in acetone (Sigma-Aldrich) for 60 s. A TEM grid (Lacey carbon-300 mesh Cu, Ted Pella Inc.) was then immersed in the dispersed solution to collect the individual metal-covered MWCNTs that were broken off the SS mesh. Finally, the TEM grid was left on a holder at room temperature to dry.

3.4.3 X-ray diffraction (XRD)

X-ray diffraction (XRD) analysis (Bruker, D8 Discover) was performed using a Cu X-ray source and monochromatic X-ray optic source at the voltage of 40 kV and current of 40 MA to determine the crystalline structure of the deposited Pt nanostructures. The XRD patterns were recorded from 2Theta of 5 ° to 105 ° with a scan time of 20 min. The sample was rotating during the XRD experiment to help detect the extremely small crystals of the Pt nanoparticles since their particle size was smaller than 5 nm, and the coatings were made of low loading of Pt electrocatalyst.

3.4.4 X-ray Photoelectron Spectroscopy (XPS)

Element identification on the surface and their chemical state were investigated by X-ray photoelectron spectroscopy (Thermo-Scientific, K-Alpha XPS apparatus) with an Al Kα source, micro-focused monochromator and spot size of 200 μm. The flood gun was always ON to avoid charging effect during data acquisition. The obtained spectra were analyzed using the Avantage software. After background subtraction, a mixed Gaussian/Lorentzian peak shape was used for all components for peak fitting.

3.4.5 Raman Spectroscopy

The defect degree of MWCNTs, before and after the RF plasma functionalization, the deposition of Pt nanoparticles, and electrochemical tests, was evaluated employing Raman spectroscopy (Thermo-Scientific, DRX2) using a laser excitation wavelength of 532 nm.

3.5 Electrochemical Setups and Tests

Cyclic voltammetry (CV), linear sweep voltammetry (LSV), chronoamperometry (CA), electrochemical impedance spectroscopy (EIS), and galvanostatic charge-discharge (GCD) were used to evaluate the electrocatalytic activity, stability, capacitance, the electrochemically-active-surface-area (ECSA), reaction kinetics, and reaction mechanism. The electrochemical tests were repeated three times, and the average and standard deviation values were reported. The electrochemical tests in alkaline electrolyte were performed in different setups, which are further explained in the following sections.

3.5.1 Three-Electrode Setup

The electrochemical tests were carried out with an Autolab Potentiostat in a three-electrode cell using a glass beaker, where the three electrodes were placed through a Teflon lid facing each other in the electrolyte. A reference electrode (RE) is an experimental reference point for potential measurements, holding a constant potential during experiments. A counter electrode (CE) completes the current path in the cell, and the working electrode (WE) is the material being tested. The three electrodes used in this project were a Pt coil as CE, A Hg/HgO (1 M KOH) electrode as RE, and the prepared Pt/MWCNT/SS or Pt/C as the WE. The electrolyte with the desired concentration was prepared by dissolving KOH pellets (Sigma-Aldrich, purity 90%) in 18.2 MΩ cm resistive Milli-Q water. Before each experiment, the electrolyte was purged with Ar gas at a pressure below 5 psi and the flow rate of approximately 5 bubbles per second to remove O_2 from the electrolyte.

3.5.2 Rotating Disk Electrode (RDE) Setup

The ORR electrocatalytic activity of the electrocatalyst was evaluated in a rotating disk electrode (RDE) setup. The RDE is vertically placed inside a glass beaker, where the exposed area of the electrode is facing downward. The RDE setup is similar to the three-electrode setup, where the working electrode can rotate around the vertical axis at different speeds during the experiment. The rotation of RDE pulls the electrolyte up toward the center of the electrode and then outwards, creating a flow pattern where only convection occurs. The RDE can be used to calculate several parameters related to mass transport, including the onset potential of the redox reaction and electrocatalyst specific/mass activity. The RDE tip (Pine Instruments, AFE3T050GC, glassy carbon 5 mm disk diameter, 12 mm PTFE shroud diameter) was inserted into the electrode rotator (Pine Instruments, AFMSRCE), where the rotation rate was controlled.

The prepared electrodes without the use of any binder/ionomer were tested at 21 ± 1 °C by fixing the produced Pt/MWCNT/SS samples on a glassy carbon RDE setup by using a Teflon cover (Figure 3-3). The electrode surface diameter exposed to the electrolyte was 5 mm. The evaluation of the prepared 3D porous Pt/MWCNT/SS electrodes for ORR using the RDE setup shown in Figure 3-3 enables their rapid electrochemical characterization in their original configuration without preparing the thin-film RDE (TF-RDE). In order to compare the

electrocatalytic performance of the Pt/MWCNT/SS electrodes with the commercially-available 20 *wt.* % Pt/C electrocatalyst, Pt/C was deposited on a glassy-carbon RDE as a thin-film (TF-RDE) using the method explained in section 3.3.

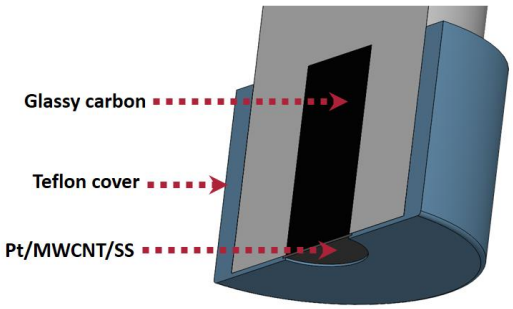

Figure 3-3. Schematic view of RDE setup for ORR evaluation of Pt/MWCNT/SS electrodes. The diameter of the Pt/MWCNT/SS electrode exposed to the electrolyte is 5 mm.

3.5.3 Gas Diffusion Electrode (GDE) Setup

There is a considerable difference between the intrinsic performance of an electrocatalyst assessed by an RDE setup and the practical performance achieved in an MEA setup. Therefore, there is a need for a testing method that mimics a fuel cell operating condition to a feasible extent without the complication of MEA preparation with many operating parameters, its associated high expenses and the use of a large amount of the catalyst material. A gas diffusion electrode (GDE) setup provides a testing condition with high oxygen mass transport properties, allowing electrocatalyst testing at high overpotentials.

To assess the performance of Pt/MWCNT/SS as GDE, the GDE setup presented in Figure 3-4 was used. The setup consists of a cell made of polytetrafluoroethylene (PTFE), Ag/AgCl reference electrode, Pt coil counter electrode, the Pt/MWCNTs/SS or Pt/C GDE as the working electrode, and 6 M KOH as the electrolyte. The growth of MWCNT on both sides of the SS provides the opportunity to employ the developed electrodes directly as the GDEs without using a binder and the GDE backing (carbon paper). The electrochemical tests were performed while purging humidified oxygen gas on the backside of the GDEs.

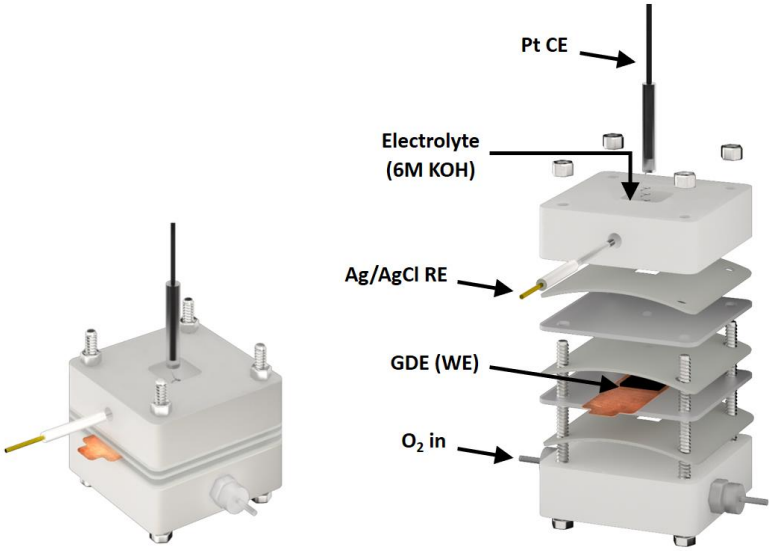

Figure 3-4. Schematic view of GDE setup.

Chapter 4

4. Manuscript 1: Plasma-Functionalized Multi-walled Carbon Nanotubes Directly Grown on Stainless Steel Meshes as Supercapacitor Electrodes

4.1 Preface

This chapter presents a published peer-reviewed article with the following citation:

Elmira Pajootan, Minnan Ye, Muyang Zhang, Sogol Niroumandrad, Sasha Omanovic, Sylvain Coulombe, Plasma-Functionalized Multi-walled Carbon Nanotubes Directly Grown on Stainless Steel Meshes as Supercapacitor Electrodes, *Special Issue on Plasmas for Synthesis of Materials for a Sustainable Energy Future*, Journal of Physics D: Applied Physics, Volume 55, 10, 2022, 194001.

Authors contributions:

Elmira Pajootan (the Ph.D. candidate) was responsible for conceiving the idea, planning of experiments, performing the experimental work including MWCNT growth, electrochemical tests, and material characterization. Minnan Ye, Muyang Zhang and Sogol Niroumandrad assisted in conducting the electrochemical tests. Prof. Sasha Omanovic and Prof. Sylvain Coulombe supervised the work, provided insightful comments on the results, provided funding support for the experiments, and reviewed the manuscript.

This study was the preliminary step in this PhD project. The growth of MWCNTs on stainless steel (SS) mesh using CVD method was optimized to achieve a forest-like structure on the SS, which will be further used as a 3D porous support material for the deposition of Pt nanostructures in later studies. The MWCNTs growth was optimized to minimize the structural defects of MWCNTs and obtain high capacitive behavior. After optimizing the growth condition, a radiofrequency plasma

was used to functionalize the MWCNTs with oxygen- and nitrogen-containing functional groups and increase the capacitance of the electrodes.

Abstract

Multi-walled carbon nanotubes (MWCNTs) directly grown on a stainless steel mesh were functionalized using a fast, solvent-free radiofrequency (RF) plasma technique. Two different gas mixtures of $Ar/C_2H_6/O_2$ and $Ar/C_2H_6/N_2$ were used to add oxygen- and nitrogen-containing functional groups to the surface of MWCNTs. The binder-free forest-like MWCNTs before and after functionalization were tested as supercapacitor electrodes. The structural and electrochemical characteristics of the electrodes were evaluated. The RF power (10-30 W) and functionalization time (1-20 min) were optimized to achieve the highest capacitance. Both nitrogen- and oxygen-functionalized MWCNTs showed improved capacitive behavior due to the presence of the functional groups on the MWCNT surface. The highest capacitance was obtained for the MWCNT electrode functionalized with the RF plasma employing the $Ar/C_2H_6/O_2$ gas mixture at 20 W for 15 min, reaching the specific capacitance of 37.3 ± 1.1 mF cm^{-2} (196.3 ± 5.8 F g^{-1}).

Keywords: Radiofrequency plasma, multi-walled carbon nanotubes, solvent-free functionalization, supercapacitors.

4.2 Introduction

The urgency to transition away from fossil fuels drives new renewable energy production, conversion and storage developments with high efficiency, affordability and sustainability characteristics. Electrochemical capacitors (or supercapacitors, SCs) and batteries are crucial in advancing energy storage devices for many applications, such as hybrid electric vehicles, portable medical electronics and military devices. Because of their high energy density, batteries are widely used in automobile applications. However, the drawbacks of batteries stem from their working principles; low power density, lengthy recharge, progressive degradation and high replacement costs. Compared to batteries, SCs have higher power density, extended cycle stability and faster charge-discharge characteristics and thus, are one of the promising solutions to current energy

storage requirements. Consequently, electrochemical SCs are particularly useful for high power bursts, such as accelerating and breaking of high-speed transportation systems. However, SCs suffer from lower energy density compared to batteries [92-96].

To overcome the low energy density of SCs, carbonaceous materials, especially carbon nanotubes (CNTs) providing a high surface to volume (or mass) ratio, superior electrical conductivity, global abundance, low cost and high stability in severe environments, have become one of the most extensively studied nanomaterials contributing to the growing energy storage applications, more specifically in flexible electrode fabrication. Flexible SCs are in high demand for portable electronic devices, which require a flexible, lightweight, and mechanically robust substrate. However, most carbon materials are in powder or flake form; thus, electrode fabrication requires binders in contact with the current collector. The non-conductive nature of the binders results in a higher resistance, reducing the capacitance by covering (insulating) the active surface of the electrode material [14, 97, 98]. In addition, the relatively poor contact between the active electrode material (carbon powder) and the current collector contributes to an increased equivalent-series-resistance in the SC, lowering the total power and energy density.

A binder-free growth of carbon nanotubes is enabled by using inexpensive stainless steel (SS) mesh material as a flexible support (current collector), allowing the entire surface of the nanotubes to be accessible with low electrical contact resistance [99, 100]. However, CNTs store charge via electrochemical double-layer capacitance (EDLC), and their hydrophobic nature hinders their interaction (contact area) with the aqueous electrolyte, resulting in a low power/energy density. To overcome this issue and increase their surface hydrophilicity, surface modification or functionalization to add hydrophilic functional groups or deposit metal oxides can be performed. Furthermore, functionalizing CNTs allows charge storage through the pseudo-capacitive mechanism via the reversible surface redox reactions, thus increasing the overall capacitance of the electrode [97, 101, 102]. Several techniques have been used to modify the surface of CNTs, including covalent functionalization, e.g. using chemical modification with carboxylic groups by refluxing the CNTs in strong acid solutions [103]. Another method is the non-covalent functionalization using adsorption forces, such as hydrogen bonding and electrostatic, by adsorbing amine-functionalized dendrimer molecules [104]. Functionalization with polymers,

biomolecules, surfactants, decoration with nanoparticles, and plasma functionalization are other techniques used to modify the surface of CNTs [105].

Plasma technologies are gaining more attention for many applications, especially in energy conversion and environmental fields [106, 107]. Since processing plasmas contain various reactive species such as electrons, ions, atoms, and molecules, the plasma can effectively alter the chemical surface properties of carbon materials by forming active species on the surface [108]. The plasma treatment can be dry and solvent-free, thus reducing the environmental footprint. It features fast turn-on and turn-down times, short reaction times, and can be performed at low to moderate temperatures. Extensive tunability of the plasma chemistry and types of functional groups grafted on exposed surfaces can be achieved by changing the plasma conditions (i.e. gas type and pressure, power and duration of treatment) [109-112].

In this work, MWCNTs with a forest-like structure were directly grown on a SS mesh (current collector) via a binder-free and catalyst-free chemical vapor deposition technique. This approach leads to a low contact electrical resistance and no agglomeration of the nanotubes, two important properties for SC electrodes. The MWCNTs were further treated with a radio-frequency (RF) plasma using two gas mixtures of $Ar/C_2H_6/O_2$ and $Ar/C_2H_6/N_2$ to add oxygen- and nitrogen-containing functional groups on their surface. The functionalized and non-functionalized MWCNTs were characterized by transmission electron microscopy (TEM), scanning electron microscopy (SEM), scanning transmission electron microscopy (STEM), energy dispersive X-ray spectroscopy (EDS), X-ray photoelectron spectroscopy (XPS), Raman spectroscopy, and thermal gravimetric analysis (TGA). The capacitance of the MWCNTs before and after plasma functionalization was evaluated using cyclic voltammetry (CV), galvanostatic charge-discharge (GCD), and electrochemical impedance spectroscopy (EIS). Through this study, we aim to demonstrate that the capacitance behavior of porous, agglomeration-free functionalized MWCNT/SS electrodes is improved due to the increased hydrophilicity and additional charge storage through the pseudo-capacitive mechanism.

4.3 Materials and Methods

4.3.1 Growth and Functionalization of MWCNTs

MWCNTs were synthesized by thermal chemical vapor deposition (CVD) in a quartz tube furnace using acetylene gas (MEGS, dissolved) as the carbon source and a stainless steel mesh (SS316L, grid bars: 165x800 per 6.45 cm2; thickness: 0.150 mm; wire diameters: 0.07 and 0.05 mm; grid opening: 15 μm, TWP Inc.) as the support for direct growth. The surface of the mesh was oxidized in the CVD furnace by exposure to air for 2 min; then the furnace was purged with Ar (Praxair, 99.999% purity) for 5 min to remove O_2 from the furnace. The growth of MWCNTs started by feeding C_2H_2 (68 ± 5 sccm) and Ar (592 ± 5 sccm) to the furnace for 2 min. To complete the growth, the C_2H_2 flow was stopped, and Ar was allowed to flow for another 2 min. Finally, the MWCNT-covered mesh was cooled down to room temperature [99, 113]. This synthesis process leads to the growth of a dense forest of intertwined MWCNTs on the SS, thus forming a porous electrode with high specific surface area.

The functionalization step was performed using a continuous wave low-pressure capacitively-coupled radiofrequency (RF) plasma (13.56 MHz). Prior to functionalization, Ar was injected into the vacuum chamber for 3 min and then pumped down to 10^{-5} Torr to reduce the air/moisture content. During functionalization, the chamber pressure was maintained at 2 Torr by continuously flowing a gas mixture of Ar (Praxair, 99.999% purity), C_2H_6 (MEGS, 99.995%), with O_2 (MEGS, 99.993% purity) or N_2 (MEGS, 99.999% purity) at the flow rates of 250, 1 and 5 sccm, respectively, to functionalize the MWCNTs with oxygen (O-FMWCNT) or nitrogen (N-FMWCNT) functional groups. Ar is used as the main plasma forming gas to ensure the stability and treatment uniformity. Ethane (C_2H_6) was added as a source of carbon and hydrogen in the gas mixture, allowing the formation of oxygen- and nitrogen-rich plasma polymers [114]. The sample was placed on a live stainless steel disk electrode (6 cm diameter) and the ground electrode was a stainless steel disk of 10 cm placed 3 cm away. The RF plasma power levels and treatment times were 10, 20 and 30 W and 1, 2.5, 5, 10, 15 and 20 min, respectively. At the end of the experiment, the chamber was pressurized by injecting Ar until atmospheric pressure was reached.

4.3.2 Structural Characterization

The structure of the MWCNT forest on SS was investigated by high-resolution field emission scanning electron microscopy, scanning transmission electron microscopy (Hitachi, Cold FE SU-8000 SEM/STEM), and transmission electron microscopy (Thermo-Scientific, Talos F200X G2 TEM). Energy dispersive X-ray spectroscopy (EDS) (XMax 80 mm^2 Oxford Instruments) was used under STEM mode for elemental mapping of the samples. For TEM imaging, the porous electrode was sonicated for 1 min in acetone (Sigma-Aldrich) to break off individual nanotubes from the SS mesh and collect them on a TEM Cu-grid. X-ray photoelectron spectroscopy (Thermo-Scientific, K-Alpha XPS apparatus, Al Kα source, micro-focused monochromator and spot size of 200 μm) was utilized to study the elemental composition and chemical state of the carbon structure before and after functionalization. The flood gun was used during the measurement to avoid substrate charging, and data analysis was performed by the Avantage software (Thermo Fisher Scientific). Raman spectroscopy (Thermo-Scientific, DRX2, laser excitation wavelength of 532 nm) was carried out to assess the structural integrity of the MWCNTs before and after functionalization. Thermal gravimetric analysis (TGA; TA Q500, TA Instruments, USA) was performed over a temperature range of 20 to 800 °C under air at a constant heating rate of 50 °C min^{-1} to determine the mass of MWCNTs grown on the SS from the mass loss. Optical emission spectroscopy (OES) was used to qualitatively detect the main species present in the plasma. The tip of an optical fibre was placed directly in front of the vacuum chamber glass viewport and the other end connected to a portable spectrometer (Ocean Optics USB2000) to record the spectra in the 200–1000 nm range with the spectral resolution of 1 nm.

4.3.3 Electrochemical Tests

The electrochemical performance of all samples was assessed by cyclic voltammetry (CV), galvanostatic charge-discharge (GCD) and electrochemical impedance spectroscopy (EIS), in a 4M KOH solution (90% assay, Sigma-Aldrich, Germany) using a three-electrode cell with Hg/HgO reference electrode, platinum wire counter electrode, and MWCNTs/SS working electrode. The geometric surface area of the working electrode exposed to the electrolyte was 0.785 cm^2. Prior to all experiments, the electrolyte was purged with Ar for 40 min to remove the oxygen dissolved in the electrolyte. In order to obtain reproducible electrode surface behavior, the working electrode was cycled 70 times in the potential range of -0.7 to 0.3 V at a scan rate of 100 mV/s in

Ar-saturated 4M KOH before each experiment. To determine the capacitance, cyclic voltammetry was performed in the same potential window at different scan rates, and galvanic charge-discharge (GCD) was carried out at different current densities. The specific capacitance from these tests was respectively calculated using Equation 4-1 and Equation 4-2 [115, 116]:

$$C_s = \frac{1}{m \cdot r \cdot (V_f - V_i)} \int_{V_i}^{V_f} I(V)dV = \frac{Q}{2 * m * (V_f - V_i)} \quad \textbf{Equation 4-1}$$

$$C_s = \frac{I \cdot \Delta t}{(V_f - V_i) \cdot m} \quad \textbf{Equation 4-2}$$

where, C_s is the specific capacitance in F g^{-1}, m is the mass of MWCNTs per unit geometric area in g cm^{-2}, r is the scan rate in V s^{-1}, $\int_{V_i}^{V_f} I(V)dV$ is the area under cyclic voltammograms whithin the potential window representing the charge, Q is the total electric charge in Coulombs, Δt is the charge/discharge time in seconds, I is the applied current in Ampers and $V_f - V_i$ is the potential window.

All electrochemical tests were repeated three times, and the average and standard deviation values are reported. Electrochemical impedance spectroscopy (EIS) measurements were conducted by applying a sinusoidal potential of 10 mV (peak) at a *dc* working electrode potential of -0.2 V in a frequency range from 100 kHz to 10 mHz. The NOVA 2.1.5 software was used for modelling the Nyquist plots with an equivalent circuit.

4.4 Results and Discussions

4.4.1 MWCNT Growth

Figure 4-1(a-a″ and b-b″) shows SEM images of the SS mesh before and after the pre-treatment oxidation step. It should be explained that the growth temperature of MWCNTs on SS was first optimized, and the corresponding explanation is provided in the Supporting Information (4.6.1 Optimization of MWCNT Growth Temperature). As shown in Figure 4-1(b-b″), the surface of SS becomes rougher after the oxidation step. According to the SEM and TEM images in Figure 4-1(c-c″ and d-d″), at 700 °C, multi-walled and bamboo-like CNTs predominantly grew on the surface

of the SS (diameter: ~30-40 nm and length: ~13–15 μm). Furthermore, different types of defects such as wall stacking faults, kinks and encapsulated fullerenes were observed in the TEM images. These are high-energy sites suitable for binding functional groups. The d-spacing of 0.35 nm marked in Figure 4-1(c″) is attributed to MWCNTs [99].

The XPS survey scans in Figure 4-1(e) identified Fe, Mn, Cr, C and O on the surface of SS, while after the oxidation step, Ni was also detected during the surface analysis. The surface percentage of Fe increased significantly from 12 to 30 at% during the SS oxidation, providing accessible catalyst on the surface of SS for the direct growth of MWCNTs. After the growth of MWCNTs on SS, the XPS survey scan indicated 98% of C and only 2% of O as the main elements, proving that a forest of metal-free MWCNTs is grown on SS.

Moreover, the Raman spectra displayed in Figure 4-1(f) confirm the existence of oxide species on the surface of the oxidized SS with peaks at 1324, 850, 657, 612, 417, 293, 247 and 224 cm^{-1}, whereas for MWCNTs, the vibrational modes of nanotubes (D, G and 2D bands) are detected, which are further explained in the Supporting Information (section 4.6.1) [117, 118]. Figure 4-1 (g) displays the average mass loss result of MWCNT/SS during TGA. No mass loss related to amorphous carbon is evident at temperatures below 450 °C, while the mass loss of 0.54 wt% at temperatures higher than 540 °C is due to the loss of graphitized carbon (MWCNTs) [71, 99]. Therefore, an area mass density of 0.19 ± 0.02 mg_{MWCNT} $cm^{-2}{}_{SS}$ was used to calculate the specific capacitance of the electrodes.

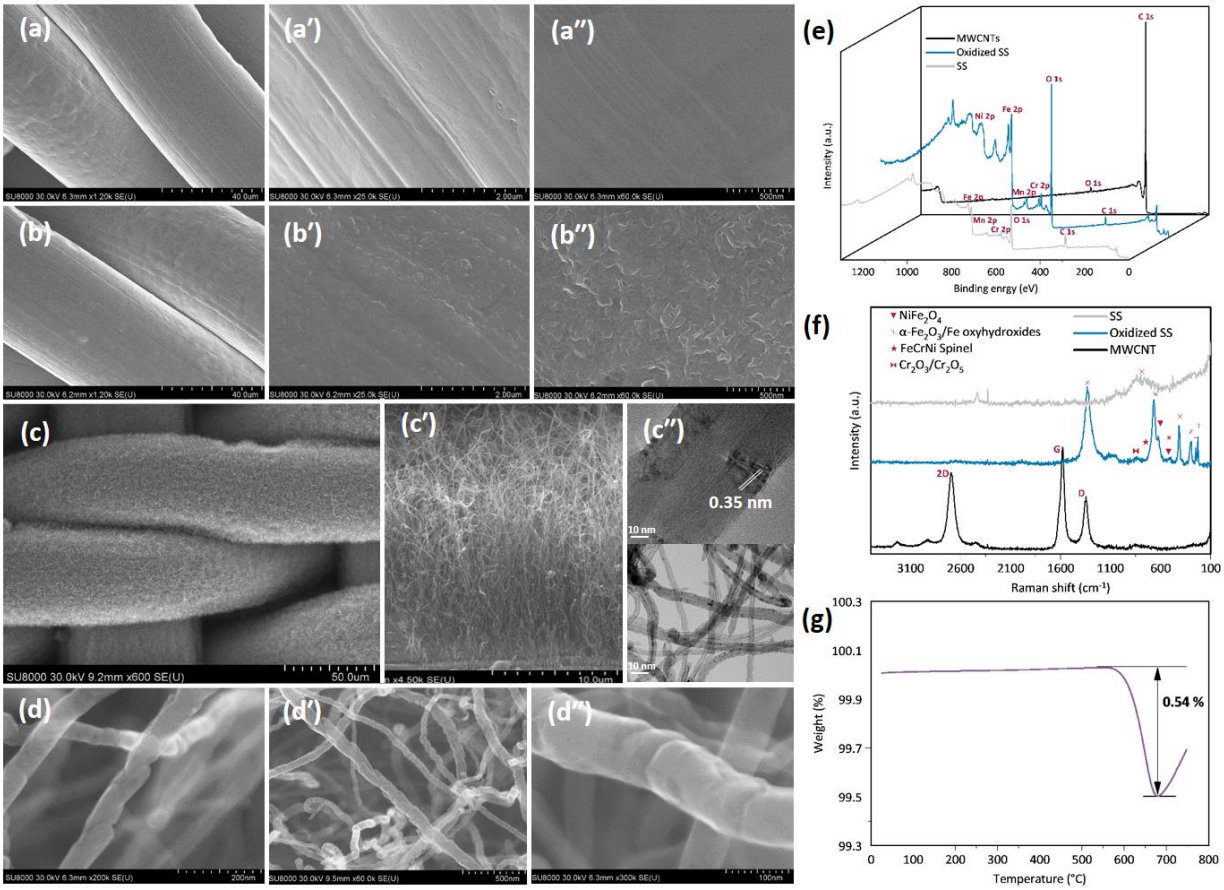

Figure 4-1. SEM images of (a-a″) SS, (b-b″) oxidized SS, and (c-c′) MWCNTs grown at 700°C on SS. (c″) and (d-d″) are TEM images of MWCNTs on SS. (e) XPS survey scans, (f) Raman spectra of SS, oxidized SS and MWCNT/SS, and (g) TGA of MWCNT/SS.

4.4.2 MWCNT Plasma Functionalization

The as-grown MWCNTs were functionalized with nitrogen- and oxygen-containing plasma gas mixtures at RF power levels of 10, 20 and 30 W for 1, 2.5, 5, 10, 15 and 20 min. The optical emission spectra recorded during the RF functionalization step are presented in Figure S4-3(a and b). The hydroxyl radical molecular emission band, argon and oxygen peaks, and the first and second positive band systems of N_2 are recognizable. No significant carbon species emission is observed. The overall forest-like structure of MWCNTs on SS was not affected by the plasma functionalization at moderate power levels, and no observable degradation or damage to individual nanotubes was evident. Figure 4-2(a) shows the selected XPS spectra of C 1s of the as-grown MWCNTs before and after plasma functionalization using the $Ar/C_2H_6/O_2$ gas mixture.

The C 1s peaks were deconvoluted using the Avantage software to investigate the degree of functionalization of MWCNTs. As Figure 4-2(a) shows, the high-energy side of the C 1s peak broadened after functionalization, confirming the presence of oxygen-containing functional groups on the surface of MWCNTs. The C 1s peaks were fitted using six components. The three main carbon components are the asymmetric graphene sp^2 component at 284.45 eV, symmetric sp^3 carbon at 284.9 eV and π-plasmon at 290.5 eV. The functional groups from low (285.5 eV) to high (288.5 eV) binding energies can be C–N, C–O or C–O–N, C=O or C=N, and C=O–O or N=C–O [114, 119, 120]. Furthermore, a thin layer of amorphous carbon was observed by TEM imaging of the surface of a nanotube, shown in Figure 4-2(b). This amorphous structure forms due to the existence of C_2H_6 in the gas mixture, resulting in the formation of a plasma polymer film on the MWCNTs. Additionally, the STEM imaging and EDS mapping of O-FMWCNT functionalized at 20 W for 15 min in Figure 4-2(c) confirm the presence of oxygen in the O-FMWCNT samples.

The mechanism of plasma functionalization is very complex since the RF power, time, gas mixture composition, and pressure have a significant influence. As reported in Table S4-2, increasing the RF power for 1 min of functionalization with $Ar/C_2H_6/O_2$ leads to lower oxygen percentage and sp^3 carbon percentage on the surface of MWCNTs. This can be explained by the formation of oxygen fragments from the C_2H_6 and oxygen mixture, which can etch away some of the coatings or scavenge a portion of the radicals formed in the plasma. At longer treatment times, a higher percentage of oxygen and sp^3 carbon is present in the samples. Furthermore, these percentages continue to increase by increasing the RF plasma power. This can be caused by different interactions between the plasma-produced active species with MWCNTs rather than with plasma polymer formed on the MWCNT surface. Nevertheless, the overall trend indicates that by increasing the treatment time, a higher percentage of oxygen is present on the MWCNT surface. It should be noted that oxygen functionalization at the highest plasma power level of 30 W for 20 min resulted in the chemical etching at the junction point of MWCNTs and SS, thus detaching the nanotubes from the surface of the SS mesh and damaging the electrode structure (data not shown). Therefore, it can be concluded that higher RF plasma power levels and longer treatment times provide more favorable conditions for the active species to react with the nanotubes or even damage them.

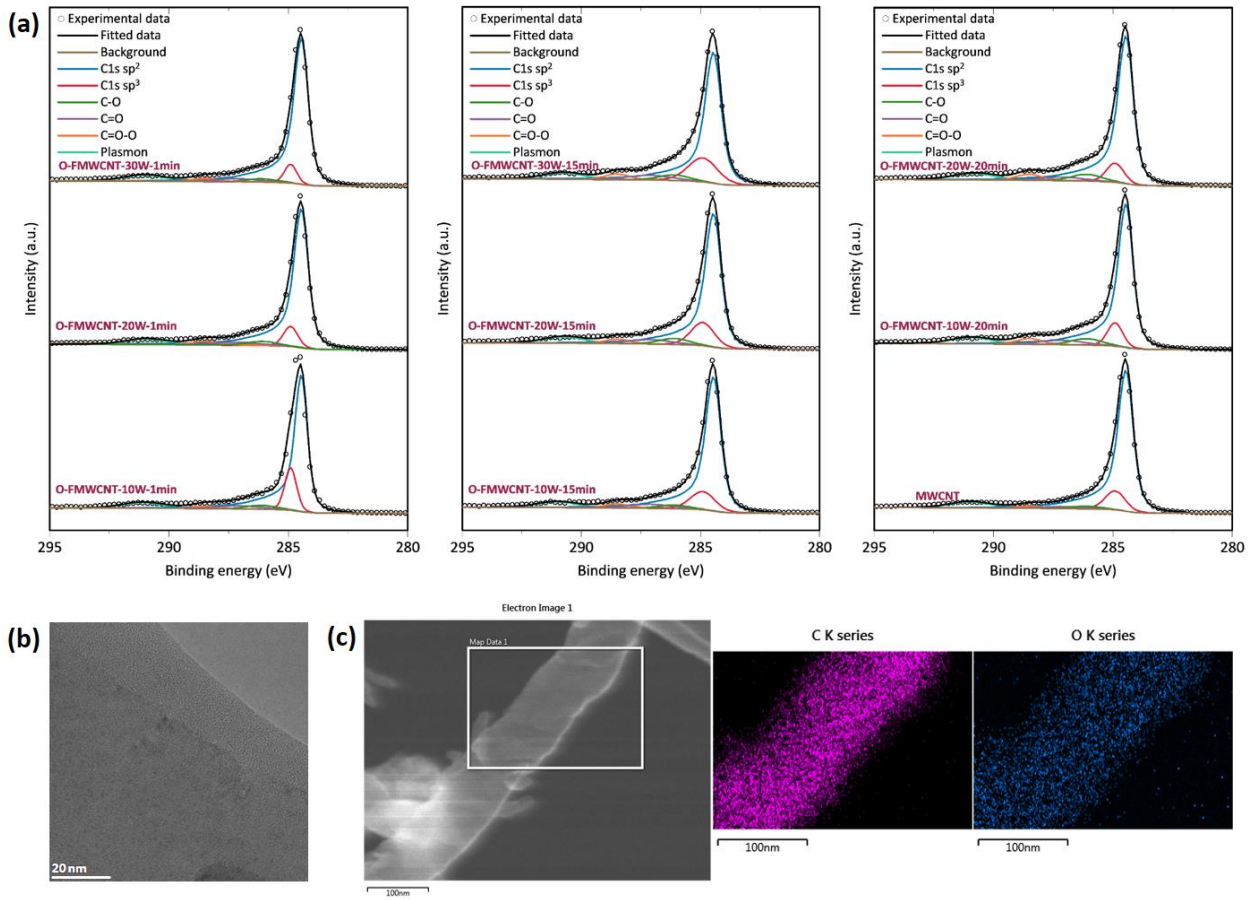

Figure 4-2. (a) Deconvoluded XPS spectra of C 1s for O-FMWCNT samples. (b) TEM image, and (c) STEM image and EDS mapping of O-FMWCNT-20W-15min.

Similar to O-FMWCNT, the C 1s spectra from XPS analysis of N-FMWCNT samples are shown and deconvoluted in Figure 4-3(a). The EDS mapping of the STEM images of N-FMWCNT for 10 W-10 min and 30 W-10 min are also presented in Figure 4-3(b and c), which evidences the presence of both oxygen and nitrogen on the surface of the N-FMWCNT. As listed in Table S4-2, for the functionalization time of 1 min, by increasing the RF power from 10 to 20 W, the sp^3 carbon increased from 9.8 to 21.2%, and then decreased to 1.4% at an RF plasma power of 30 W. This can be caused by the activation of more OH radicals at higher power levels, which can etch away the groups formed on the MWCNTs. However, at the treatment time of 10 min, the sp^3 carbon content is not affected by the increase of RF plasma power. Overall, the results reported in Table S4-2 demonstrate that the total amount of oxygen and nitrogen groups increased significantly by increasing the functionalization time from 1 to 10 min. It should be noted that oxygen functional

groups are added to N-FMWCNTs either by interacting with the plasma-produced OH radicals (detected by OES, Figure S4-3) or through reactions between the fresh sample and atmospheric air, referred to as ageing [114, 119-121].

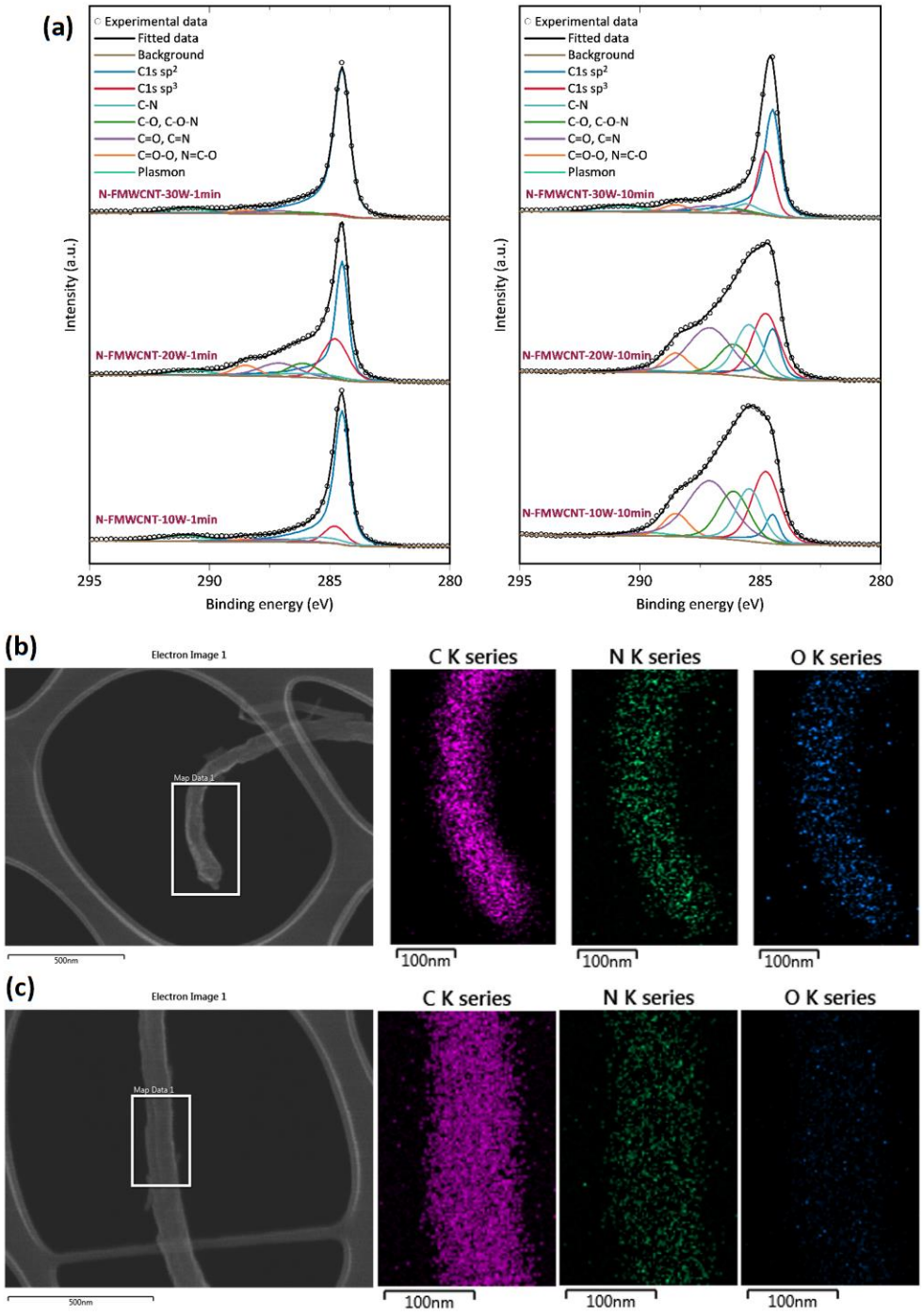

Figure 4-3. (a) Deconvoluted XPS spectra of C 1s for N-FMWCNT. STEM image and EDS mapping of N-FMWCNT (b) 10W-10min and (c) 30W-10min.

4.4.3 Electrochemical Results

Figure 4-4(a) shows cyclic voltammograms of MWCNTs before and after RF plasma functionalization, recorded at a scan rate of 25 mV s^{-1}. The CV recorded with the non-functionalized MWCNT shows a relatively featureless shape (on the scale of the graph presented). However, the CVs recorded with the oxygen- and nitrogen-functionalized electrodes display the shape that indicates the occurrence of redox reactions, i.e. the pseudo-capacitive behavior of the electrodes. This is evident from the presence of broad anodic and cathodic shoulders negative of -0.2 V and positive of -0.1 V. However, these redox shoulders are not well-defined due to a small percentage of functional groups added to the surface and the faster charging kinetics of the electrochemical double layer compared to the slower redox kinetics of surface functional groups [122].

The charge (area) under the O-FMWCNT and N-FMWCNT voltammograms is significantly larger than that of the bare MWCNTs, indicating an increased charge storage/delivery (i.e. capacitance). The corresponding capacitance of the electrodes was calculated using Equation 4-1 at a scan rate of 25 mV s^{-1}, and the values are presented in Figure 4-4(b). The results demonstrate that nitrogen and oxygen functionalities can indeed enhance the charge storage/delivery properties of the nanotubes. The O-FMWCNT electrode functionalized at an RF plasma power of 20 W for 15 min showed the highest capacitance of 37.3 ± 1.1 mF cm^{-2} (196.3 ± 5.8 F g^{-1}), and the N-FMWCNT electrode functionalized at an RF plasma power of 10 W for 2.5 min yielded a capacitance of 32.6 ± 1.6 mF cm^{-2} (171.6 ± 8.4 F g^{-1}). The capacitance of non-functionalized MWCNTs was significantly lower, 14.3 ± 0.7 mF cm^{-2} (75.3 ± 3.7 F g^{-1}). This value is in the range of values reported in the literature for non-functionalized MWCNT electrodes, 15 to 50 F g^{-1} [71, 123-126]. However, higher values were also reported for functionalized CNTs; for instance, Shen et al. prepared a film of single-walled CNTs (SWCNTs) by drying a dispersion of SWCNTs over a filter paper and further dissolving the filter paper to have a thin fil over a membrane. They improved the capacitance from 32.1 F g^{-1} to 146.1 F g^{-1} with 6 hours of reflux treatment with nitric acid to functionalize the CNTs with carboxylic groups [124]. Likewise, Frackowaic et al. made electrodes in a pellet shape by pressing the mixture of MWNTs, acetylene black and polyvinylidene fluoride and using gold current collector. As a result, they enhanced the capacitance of CNTs from 15 to 90 F g^{-1} by chemical KOH activation with a KOH:C ratio of 4:1, at 800 °C

[123]. Although significant improvements were observed in these studies, it should be noted that the electrodes reported in the current work were produced without incorporating a binder into the carbon structure and casting the layer onto a current collector, resulting in a good electrical conductivity and high capacitance of the electrodes. Moreover, using the rapid dry plasma functionalization technique, there is no need to use chemicals or apply high temperatures during the functionalization process.

The effect of scan rate on the capacitance of the electrodes is presented in Figure 4-4(c). As expected, by increasing the scan rate, the capacitance decreases. This decrease can be related to the kinetics of charge-transfer compensation by ion migration. Namely, at higher scan rates, due to the presence of nano-scale pores on the MWCNTs (Figure 4-1), the migration of ions within/inside the pores is limited, rendering the MWCNT surface area accessible for the charge storage smaller. However, it can be noted that the decrease in capacitance on the functionalized MWCNT is much smaller than that on pristine MWCNT. Thus, the capacitance of the O-FMWCNT and N-FMCNT recorded at 1000 $mV\,s^{-1}$ decreased down to ca. 55% of the value recorded at 10 $mV\,s^{-1}$, while on the non-functionalized MWCNT the value decreased much more, down to 26%. This indicates that the functionalized MWCNTs offer a 3D structure that is more favourable for ion migration than that one offered by the pristine MWCNT.

The GCD measurements were performed at 1.0 $mA\,cm^{-2}$, and the charge-discharge curves are provided in Figure 4-4(d). The observed divergence from the general linear triangular form of the curves is due to the existence of redox reactions on the surface of MWCNTs, which contribute to additional charge storage. The curve recorded with the non-functionalized MWCNT also shows a slight deviation from linearity, indicating that there is also the occurrence of redox surface reactions even on this surface, to a certain degree. Figure 4-4(d) shows that the charge-discharge duration of the MWCNT electrode is the shortest, whereas the charge-discharge time of the N-FMWCNT and O-FMWCNT is longer, indicating larger charge storage-delivery of the latter two surfaces, similar to what is observed in voltammograms in Figure 4-4(a) [95]. Employing Equation 4-2, the capacitance values from the GCD curves were calculated to be 10.7 ± 0.5, 24.9 ± 1.3 and 33.8 ± 0.9 $mF\,cm^{-2}$ or 56.3 ± 2.6, 131.1 ± 6.8 and 177.9 ± 4.7 $F\,g^{-1}$ for the MWCNT, N-FMWCNT and O-FMWCNT electrode materials. The enhanced pseudo-capacitive behavior of the F-MWCNTs, through both the occurrence of the redox reaction of the functional groups at the

electrode-electrolyte interface and increased accessibility of the MWCNT surface to the electrolyte, leads to a higher capacitance of the electrodes [127].

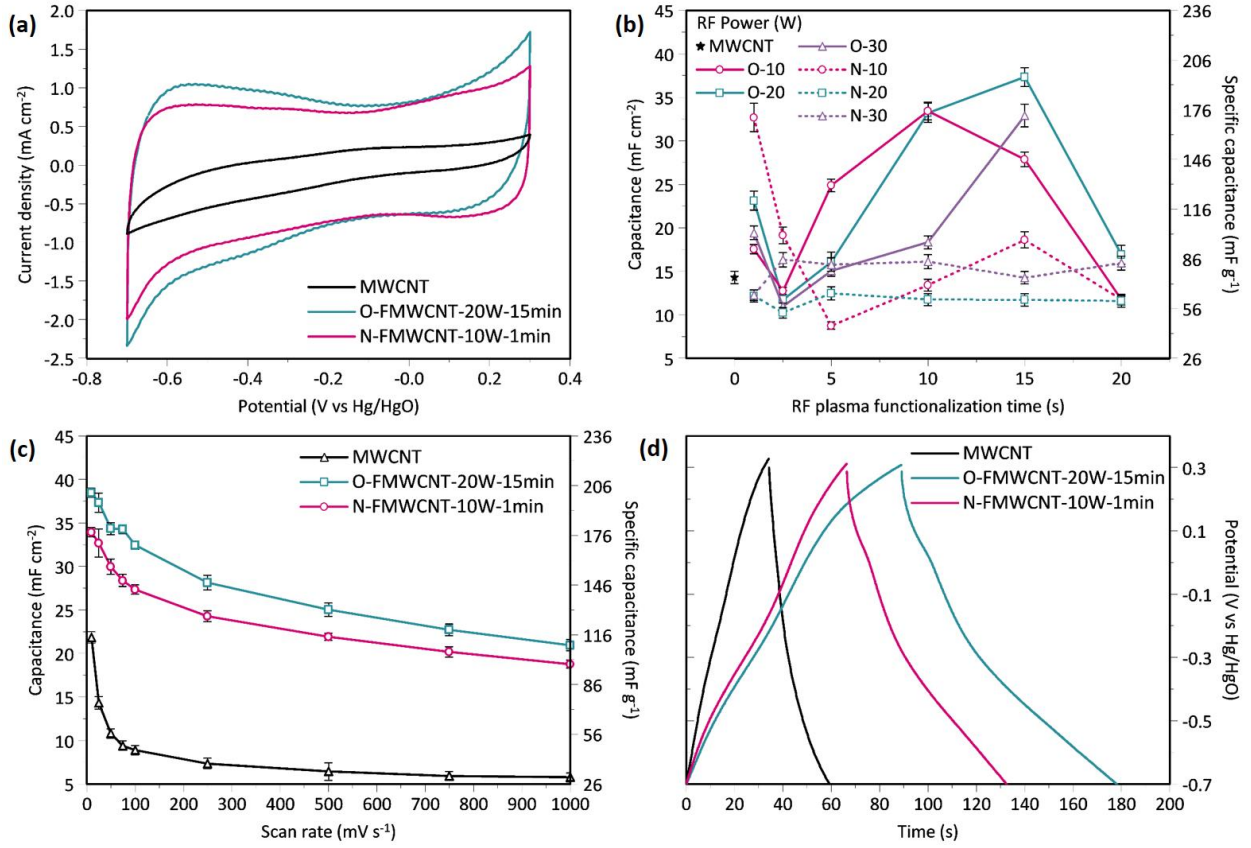

Figure 4-4. (a) Cyclic voltammograms of non-functionalized and functionalized MWCNTs recorded in 4M KOH at a scan rate of 25 mV s^{-1}. (b) Capacitance of all the investigated MWCNT-based electrodes as a function of RF plasma power levels and treatment times, calculated from CVs recorded at 25 mV s^{-1}. (c) Dependence of capacitance on scan rate. (d) GCD of non-functionalized and functionalized MWCNTs recorded in 4M KOH at the current density of 1.0 mA cm^{-2}.

The interpolation matrix of the effect of RF plasma power and time on the percentage of sp^3-to-sp^2 carbon ratio (calculated from the XPS results), functional groups and the corresponding capacitance are reported in the 3D plots in Figure 4-5. Figure 4-5(a-b) illustrate that by increasing the RF plasma time at different RF plasma power level, the percentage of oxygen on the MWCNT surface increases. It seems that more reactions occur on the MWCNT surface at higher treatment time, resulting in adding more oxygen-containing groups to the MWCNT surface. The sp^3-to-sp^2 ratio in the carbon changes over a small range. Figure 4-5(a) shows that an increase in the RF plasma power level results in a decrease of sp^3 carbon at short functionalization times, which can

be due to the removal of amorphous carbon from the MWCNTs by the strong oxygen active species. At longer functionalization times (ca. 10-15 minutes) and higher RF plasma powers, the sp^3-to-sp^2 carbon ratio increases as a consequence of the addition of more oxygen-containing groups to the surface. However, at higher RF powers and times past 15 minutes, the sp^3-to-sp^2 carbon ratio decreases, which can be explained by the structural damage caused by active oxygen species and consequential chemical etching at the junction point of MWCNTs and SS, resulting in detachment of the nanotubes. On the other hand, Figure S4-4 displaying the Raman spectra (normalized to G band) of all functionalized samples under different RF plasma functionalization conditions indicates that the R-value (I_D/I_G ratio) is sensitive to surface modifications upon plasma treatment. As the RF plasma power and time increase, the intensity of the D band and consequently the R-value increase, corresponding to the presence of more structural defects in the nanotubes, which can be originated from the reduced π-conjugated states (Figure S4-4(a-c)) [128]. A similar trend is observed for the capacitance of the electrodes. The capacitance of the O-FMWCNT electrodes (Figure 4-5(c)) increases by applying higher RF plasma power levels and longer functionalization time, which resulted from the addition of more oxygen-containing groups and a higher sp^3-to-sp^2 carbon ratio on the surface of MWCNTs. However, as mentioned earlier, at high RF plasma time and power, the occurrence of chemical etching can reduce the surface area of the electrode by detaching the nanotubes from the SS, resulting in a substantial decrease in capacitance, as evidenced in Figure 4-5(c).

Increasing the RF plasma treatment time with the nitrogen-containing gas mixture leads to a more substantial increase of the number of functional groups and sp^3 carbon on the surface of MWCNTs, compared with oxygen (Figure 4-5). However, with an increase in RF plasma power levels at shorter times, the corresponding values first increase and then drop (Figure 4-5(a,b)). The corresponding Raman spectra Figure S4-4(d-f) demonstrate a decrease in the intensity of the D band, followed by an increase. It has been reported that different competing mechanisms take place during plasma functionalization; etching or removal of surface defects/amorphous carbons by plasma active species, deposition of plasma polymer on the surface and addition of functional groups to the surface [109, 129]. It appears that at low power levels, the excited species produced in the nitrogen-containing plasma can remove the amorphous carbon from the MWCNTs and lower the sp^3-to-sp^2 carbon ratios in their structure. This result is confirmed by the appearance of a less intense D band in the Raman spectra shown in Figure S4-4(d-f), leading to a lower R (I_D/I_G)

value associated with MWCNTs with fewer structural defects. However, at higher plasma power levels, the active species can functionalize or form an amorphous layer over the graphitic layers of MWCNTs. At higher RF plasma power levels, more collision between the plasma-produced active species can reduce their energy level, which will not be sufficient for etching away the incorporated functional groups or the deposited amorphous carbon [109, 129, 130]. However, at higher RF plasma power levels and longer functionalization times, a more significant broadening of the D and G bands is observed as illustrated in Figure 4-5(d-f). This is associated with more structural defects, similarly to the MWCNTs synthesized at low temperature (Figure S4-1(f)). Figure 4-5(f) shows that the capacitance of the N-FMWCNT electrodes seems to be relatively independent of the plasma conditions and surface chemistry. This can be attributed to the existence of a much higher sp^3-to-sp^2 carbon ratio (Figure 4-5(d)) than O-FMWCNT electrodes (Figure 4-5(a)), which damages the structural integrity of MWCNTs, further affecting their electrochemical performance.

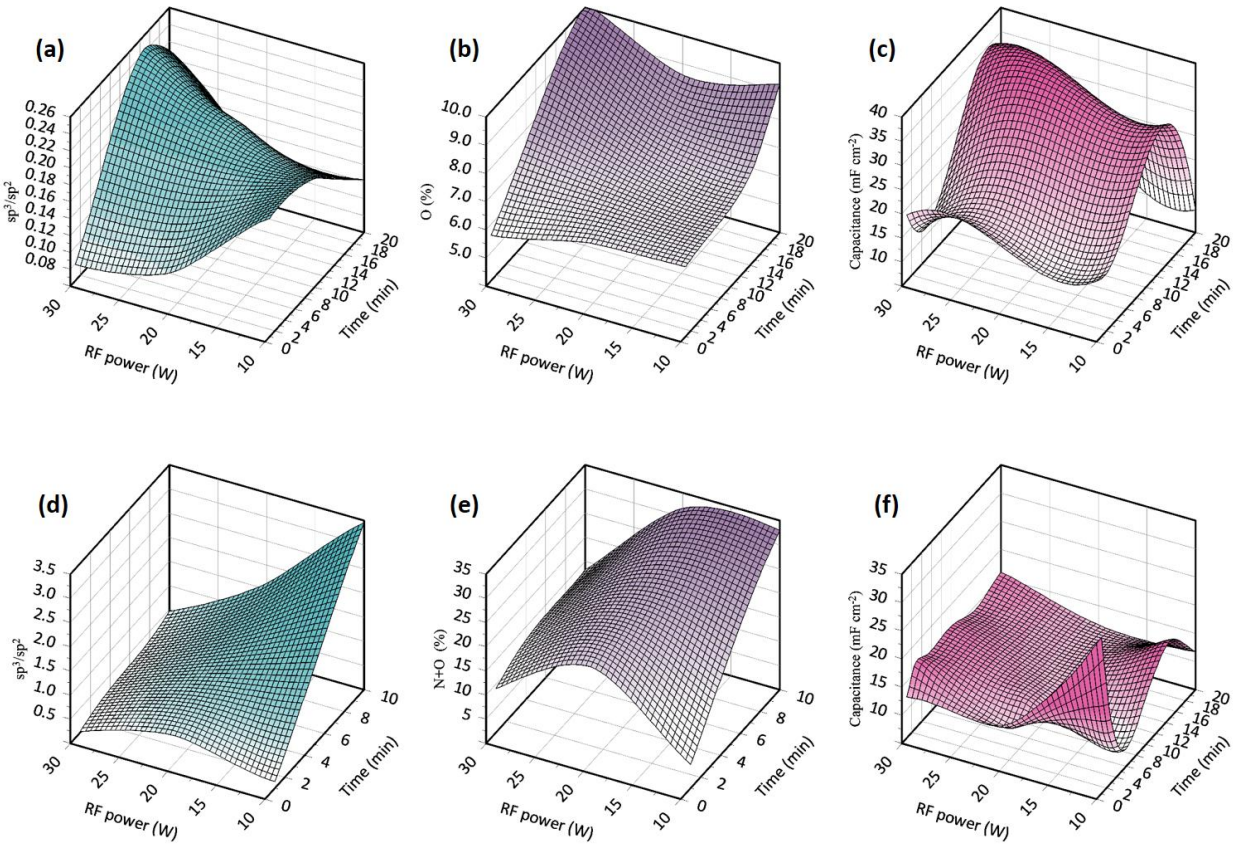

Figure 4-5. The influence of RF plasma power and time on the (a, d) the sp^3 to sp^2 ratio, (b, e) percentage of functional groups, and (c, f) capacitance of O-FMWCNT and N-MWCNT, respectively.

The impedance behavior of the electrodes was assessed using electrochemical impedance spectroscopy (EIS), and the Nyquist plots of MWCNTs before and after functionalization are reported in Figure 4-6(a). It is evident from the quasi-linear/vertical shape of the Nyquist plots that the capacitive contribution dominates the impedance behavior. Unlike pure electrical double-layer capacitors that show a vertical line, the frequency dependence of the real impedance component reveals the pseudo-capacitive properties and/or the existence of impedance resulting from the porosity of all three electrodes. A slightly sloped and curved line in the lower frequency region and a semicircle-like behavior in the higher frequency region (Figure 4-6(b)) originate from the kinetics of the redox reaction and ion movement inside the pores, contributing to the actual impedance component, thus yielding two time constants [131].

The impedance behavior of the electrodes was modelled using the equivalent electrical circuits (EEC) presented in Figure 4-6(c) and (d); the response of the non-functionalize MWCNT electrode was modelled by the EEC in Figure 4-6(c), while the response of the two functionalized electrodes was modelled using the EEC in Figure 4-6(d). In these EECs, R_s, represents the electrolyte resistance, the internal electrode material resistance, and contact resistance between MWCNT and the SS mesh (current collector). The capacitance related to the electrostatic charging of the double-layer (CPE_{dl}) and the resistance for ion migration to compensate the charge (R_{dl}) is described through the CPE_{dl}-R_{dl} time constant, corresponding to the response of the system in the higher-frequency region. The CPE_W element in Figure 4-6(c) represents the impedance related to the migration of ions through the pores of the MWCNT electrode during the charging/discharging process. For the two functionalized electrodes, their pseudo-capacitive behavior can be characterized through the pseudo-capacitance (CPE_p) and its corresponding polarization resistance (R_p), representing the lower-frequency range CPE_p-R_p time constant. Due to the presence of surface roughness, porosity, surface inhomogeneity and non-uniform charge distribution, a constant-phase-element (CPE) was used instead of a pure capacitance [132-135]. Table S4-3 reports the values of the equivalent circuit components. The values of CPE_{dl} power, n_{dl}, deviate from the value for pure capacitance ($n = 1$), which could be due to the heterogeneity (in terms of the surface-chage distribution and morphology) of the MWCNTs. It can be seen that the CPE_{dl} value increases after functionalization of the MWCNT, while the corresponding R_{dl} value decreases, which can be due to the enhancement of surface wettability, offering a more accessible surface area of MWCNT to the electrolyte. Table S4-3 shows that the pseudo-capacitance (CPE_p)

of the O-FMWCNT is higher than that of the N-FMWCNT, which agrees with the CV and GCD results presented earlier in the text. However, it can be noticed that the R_p value for the O-FMWCNT is higher than that recorded for the N-FMWCNT electrode, indicating a slower kinetics of surface redox reactions. This, in turn, indicates that the increased capacitance of the O-FMWCNT surface recorded by CV, GCD, and CPE values in EIS, can also be due to the increased accessibility of the O-FMWCNT surface to the electrolyte, in addition to the contribution of the surface-redox reactions to the total charge storage/delivery capacitance.

The charge-discharge cyclability of the O-FMWCNT-20W-15min electrode was tested by performing GCD for 1000 cycles at a current density of 1 mA cm^{-2}. The results in Figure 4-6(b) show 82% retention of the initial capacitance of the electrodes after 1000 cycles. However, the capacitance increased to its initial value after equilibrating the electrode at the open circuit and repeating the experiment (data not shown). Thus, this drop in capacitance with cycling can be attributed to the drying of the MWCNTs' deep pores, resulting in a lower surface area and thus, a lower capacitance. McArthur et al. [71] and Frackowiak et al. [136] observed a similar phenomenon and explained the reversibility of this reduction after allowing the electrode to equilibrate at an open circuit.

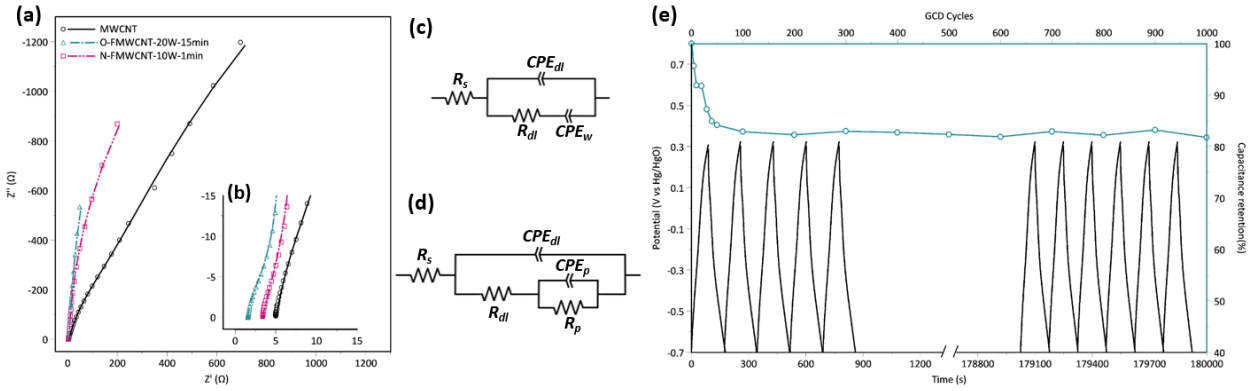

Figure 4-6. (a) Nyquist plots of MWCNT before and after plasma functionalization (inset: (b) low-frequency region), (c and d) the equivalent circuits, and (e) GCD stability of O-FMWCNT for 1000 cycles at a current density of 1 mA cm^{-2}.

4.5 Conclusion

MWCNTs with a forest-like structure were directly grown on stainless steel meshes without the use of any catalyst to produce binder-free electrodes that were tested for application in

supercapacitors. We demonstrated that the radiofrequency capacitively-coupled plasma can be used as a dry MWCNT functionalization method to improve the electrode's charge storage/delivery performance. The porous MWCNT-SS electrode's surface was further modified by using different gas mixtures at different RF plasma power levels and treatment times in order to functionalize the MWCNT surface with oxygen and nitrogen functional groups. It was illustrated that processing parameters, including plasma power and time, indeed governed the surface chemistry of the functionalized nanotubes and thus their capacitive behavior. The capacitance of the MWCNTs electrodes increased from 75.3 ± 3.7 F g^{-1} to 196.3 ± 5.8 F g^{-1} after functionalization by RF plasma using an $Ar/C_2H_6/O_2$ gas mixture at 20 W for 15 min, without any damage to the structure of the MWCNTs. Accordingly, the solvent-free RF plasma method provides convenient and mild operating conditions to ensure the functionalization of carbon-based material used for various applications.

Acknowledgments

The authors acknowledge the financial support of the Faculty of Engineering through the McGill Engineering Doctoral Award (MEDA), the Natural Sciences and Engineering Research Council of Canada (NSERC), the Gerald Hatch Faculty Fellowship, and the Fonds de recherche du Québec – Nature et technologies (FRQNT). The authors thank the technical staff from the Department of Chemical Engineering at McGill University for their assistance. The authors acknowledge Dr. Boris Nijikovsky for the TEM work.

4.6 Supporting Information

4.6.1 Optimization of MWCNT Growth Temperature

As the SEM images in Figure S4-1(a-a″ to e-e″) show, the density of the directly grown MWCNT forest increases when the furnace temperature is increased from 400 to 700 °C. At 700 °C, the nanotubes cover the entire surface of the SS uniformly, providing a high surface area. Moreover, the effect of growth temperature on the structural defects of the grown MWCNTs was investigated by Raman spectroscopy, and the results are reported in Figure S4-2(f). The Raman peaks were associated with the vibrational modes of carbon nanotubes, which are the D, G and 2D bands at ~1355, ~1640 and ~2696 cm^{-1}, respectively. All the spectra were background-corrected and normalized with respect to the G band. The D band is linked to the sp^3 carbon-related defects such as lattice mismatch of the graphitic layer, substitutional hetero-atoms, vacancies and grain boundaries, and the G-band is related to the graphene sp^2 carbon. The 2D band represents the long-range order. Therefore, the G and D bands provide information on the order and disorder levels of the MWCNT structure, and low R (I_D/I_G) and R′ (A_D/A_G) values correspond to a more graphitic MWCNT structure. The variation of the growth temperature results in a significant change in the Raman spectrum. The D band broadening and higher valley lines between D and G bands are observed at the lower growth temperature. The reported R and R′ values in Table S4-1 indicate that the MWCNT structure contains a small number of defects at the highest growth temperature (700 °C), and the low R-value of 0.52 confirms the growth of high-quality MWCNTs on SS [137-142]. The SEM images in Figure S4-2 confirm that at temperatures above 650 °C the nanotubes fully cover the SS. However, the forest-like organization of the MWCNTs seems to be more uniform at 700 °C. Therefore, this temperature has been selected as the optimum synthesis condition to grow MWCNTs for further functionalization.

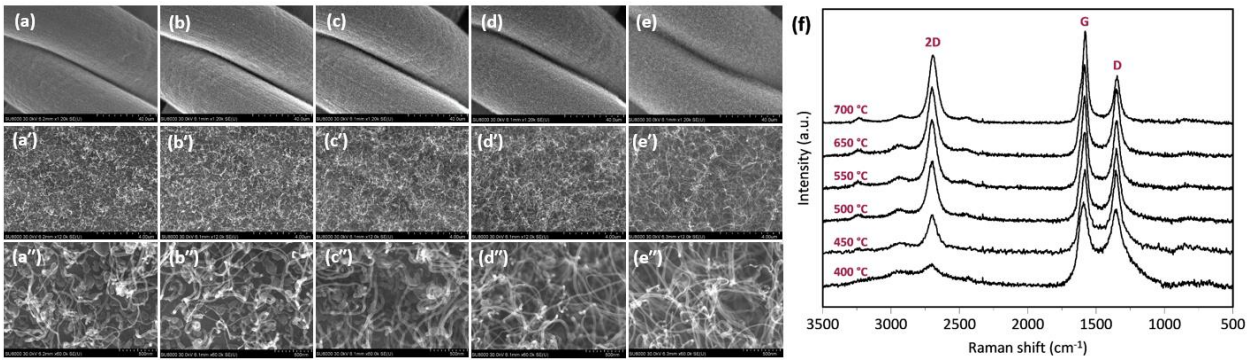

Figure S4-1. SEM images of MWCNTs grown on SS at (a-a″) 400 °C, (b-b″) 450 °C, (c-c″) 500 °C, (d-d″) 550 °C and (e-e″) 700 °C, and (f) normalized Raman spectra (with respect to G band) of MWCNTs grown at different temperatures on SS meshes.

Table S4-1. Ratios of peak intensities and areas in Raman spectra (normalized with respect to G band)

Growth Temperature (°C)	I_D/I_G	A_D/A_G
700	0.40	0.52
650	0.71	0.68
550	0.71	0.67
500	0.77	0.73
450	1.00	0.87
400	0.91	0.77

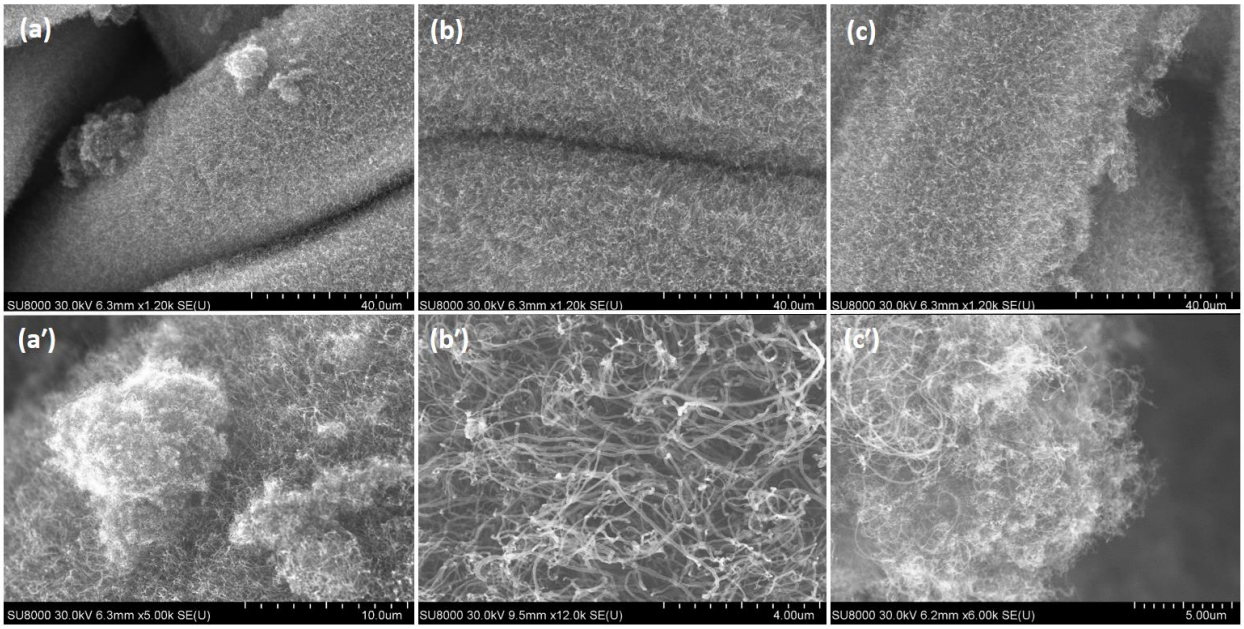

Figure S4-2. SEM images of MWCNTs grown on SS meshes at (a, a′) 650 °C, (b, b′) 700 °C and (c, c′) 750 °C.

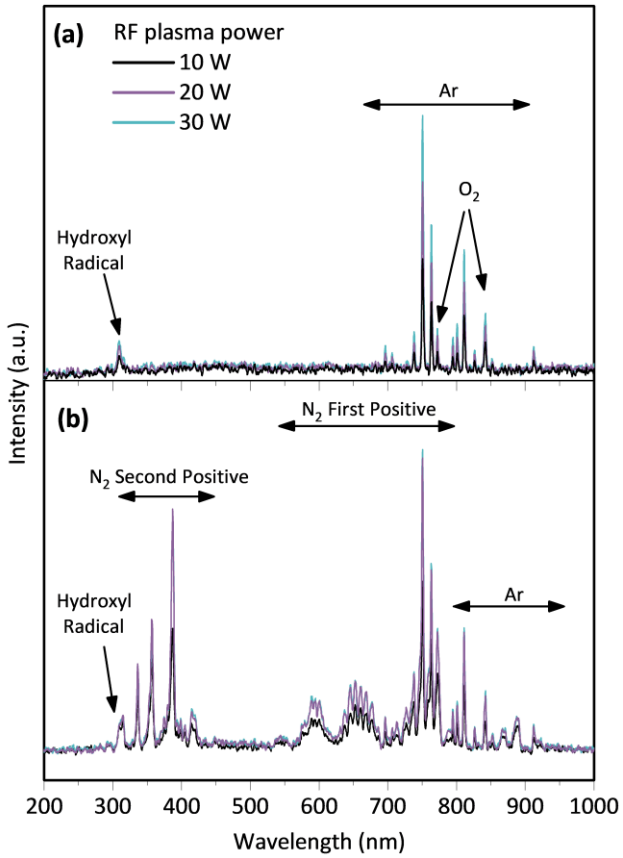

Figure S4-3. Optical emission spectra recorded during RF plasma functionalization with (a) $Ar/C_2H_6/O_2$:250/1/5 and (b) $Ar/C_2H_6/N_2$:250/1/5 at different power levels.

Table S4-2. Elemental composition (average atomic %) of MWCNTs before and after plasma functionalization

Sample	C 1s sp^3	C 1s sp^2	N (%)	O (%)	Sample	C 1s sp^3	C 1s sp^2	O (%)
MWCNT	10.10	77.25	—	2.05	O-FMWCNT-1min-10W	13.96	69.87	6.47
N-FMWCNT-1min-10W	9.81	71.18	1.11	3.8	O-FMWCNT-1min-20W	7.81	75.93	6.33
N-FMWCNT-1min-20W	21.18	43.23	8.76	10.37	O-FMWCNT-1min-30W	6.17	78.06	5.61
N-FMWCNT-1min-30W	1.36	85.10	1.10	7.96	O-FMWCNT-15min-10W	10.51	71.50	7.42
N-FMWCNT-10min-10W	22.26	6.45	17.59	15.39	O-FMWCNT-15min-20W	12.92	68.68	7.71
N-FMWCNT-10min-20W	22.15	13.63	15.91	15.86	O-FMWCNT-15min-30W	15.99	65.59	9.35
N-FMWCNT-10min-30W	23.19	49.20	4.97	8.33	O-FMWCNT-20min-10W	8.73	71.52	9.26
—	—	—	—	—	O-FMWCNT-20min-20W	7.92	73.28	8.60

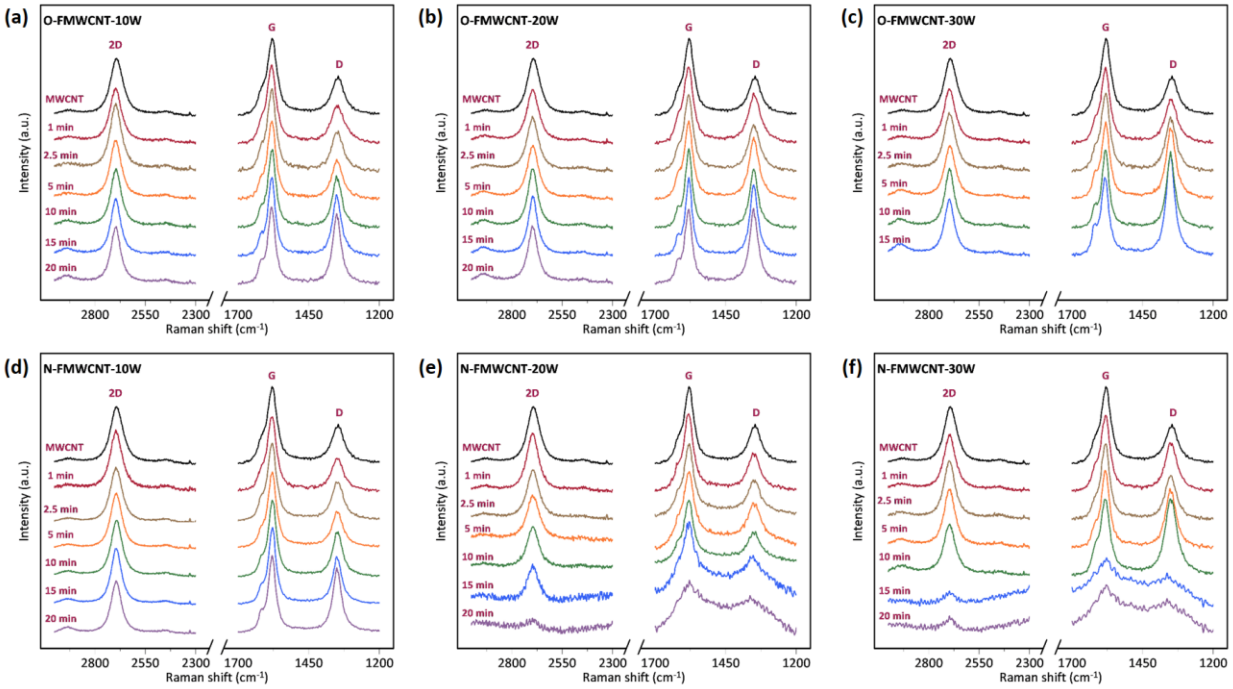

Figure S4-4. Normalized Raman spectra (with respect to G band) of MWCNTs, and O-FMWCNTs and N-FMWCNTs functionalized at different RF power levels and times.

Table S4-3. Equivalent circuit parameters for different electrodes in 4M KOH at -0.2 V

Potential (V)	R_s (Ω cm^2)	$CPE_{dl} \times 10^3$ (Ω^{-n} s^n cm^{-2})	n_{dl}	R_{dl} (Ω cm^2)	$CPE_p \times 10^3$ (Ω^{-n} s^n cm^{-2})	n_{dl}	R_p (kΩ cm^2)
MWCNT	3.89	5.68	0.85	432.54	2.37*	0.54*	—
N-FMWCNT-10W-1min	2.69	23.50	0.96	18.06	6.75	1.00	3.85
O-FMWCNT-20W-15min	1.24	14.19	0.93	18.84	10.90	1.00	23.08

*** CPE_W; n_W**

Chapter 5

5. Manuscript 2: Controllable Dry Synthesis of Binder-Free Nanostructured Platinum Electrocatalysts Supported on Multi-Walled Carbon Nanotubes and their Performance in the Oxygen Reduction Reaction

5.1 Preface

This chapter presents a published peer-reviewed article with the following citation:

Elmira Pajootan, Sasha Omanovic, Sylvain Coulombe, Controllable Dry Synthesis of Binder-Free Nanostructured Platinum Electrocatalysts Supported on Multi-Walled Carbon Nanotubes and Their Performance in The Oxygen Reduction Reaction, Chemical Engineering Journal, Volume 426, 2021, 131706.

Authors contributions:

Elmira Pajootan (the Ph.D. candidate) was responsible for conceiving the idea, planning of experiments, performing the experimental work including electrocatalyst synthesis, electrochemical tests, and material characterization. Prof. Sasha Omanovic and Prof. Sylvain Coulombe supervised the work, provided insightful comments on the results, provided funding support for the experiments, and reviewed the manuscript.

For this study, the PLA setup was upgraded by a turbomolecular pump, providing the opportunity to reach high vacuum conditions to synthesize nanostructures with different characteristics. The Pt nanostructures were directly deposited on the MWCNTs grown on an SS mesh (Manuscript 1). The article provides insight on the effect of background gas pressure and laser pulse energy on the structural properties of the synthesized Pt nanoparticle thin films such as morphology, particle

size, crystalline structure, and chemical state. The samples were evaluated electrochemically for ORR in an alkaline electrolyte using two different setups; a three-electrode cell and a gas diffusion cell. The results showed that the 3D porous structure of the electrodes enhanced the oxygen mass transport, and the synthesized Pt nanoparticle thin films were intrinsically more active than the commercial Pt/C for ORR.

Abstract

Different platinum nanostructures were synthesized by pulsed laser ablation (PLA) of a pure Pt target, a byproduct-free and solvent-free synthesis technique. The Pt nanostructures were directly deposited on multi-walled carbon nanotubes (MWCNT) pre-grown on a stainless steel (SS) mesh by chemical vapor deposition. Performing PLA at different background gas pressures (10^{-5} to 10 Torr, argon) and laser pulse energies (20 to 66 mJ $pulse^{-1}$) led to a range of coating morphologies containing very low Pt loadings (14 to 35 μg cm^{-2}), from the uniform and dense nanoparticle thin coatings at low pressure to highly porous granular coatings at higher pressure. Increasing the background gas pressure led to an increase in primary Pt nanoparticle size from 2.0 ± 0.2 nm to 2.8 ± 0.8 nm. XPS results showed a positive shift in the Pt $4f_{7/2}$ binding energies with lowering the PLA pressure and laser energy, which was linked to the formation of smaller Pt nanoparticles. The presence of Pt (111), (200), (220), and (311) was confirmed by SAED patterns in the Pt nanostructures. The electrocatalytic performance of these binder-free Pt/MWCNT/SS structures was evaluated in the oxygen reduction reaction (ORR) in an alkaline medium, in both the rotating disk electrode (RDE) and gas diffusion electrode (GDE) configurations. In the RDE setup, all Pt/MWCNT/SS electrocatalysts were found to yield a higher specific ORR activity than the commercial Pt/C thin film, while in the GDE setup the Pt/MWCNT/SS electrode with the lowest Pt loading and highest surface area yielded the highest ORR specific activity.

Keywords: Pulsed laser ablation, platinum nanostructures, multi-walled carbon nanotubes, oxygen reduction reaction, alkaline medium, gas diffusion electrode.

5.2 Introduction

The excessive, albeit declining, dependency on fossil fuels as a source of energy in developed countries, and the fast-rising demand and deployment of affordable on-demand energy sources in developing countries still drive CO_2 emissions to unprecedented levels. In parallel, there is a fast-escalating demand for renewable energy sources and in particular, renewable electricity. As a result, low/zero CO_2-emission technologies such as water electrolysis for the production of H_2 for use in fuel cells are gaining importance as possible large-scale replacements in the current energy systems [3, 143, 144]. Although very promising, currently, most novel technologies of the energy transition rely on advanced materials, often utilizing precious metals in high quantities. There is, thus, an urgent need for low-cost sustainable advanced materials, and in particular catalysts for power-to-gas (or liquid) and chemicals-to-electricity systems, in order to make renewable electricity technologies competitive and respectful of sustainable development goals.

The oxygen reduction reaction (ORR) at the cathode of fuel cells is one of the most studied reactions in electrochemistry. The existing attempts to replace platinum with superior electrocatalytic activity and stability in acidic and alkaline media by non-noble electrocatalysts result in high catalyst loadings, and consequently a thick catalyst layer with high mass-transport overpotential and ohmic losses [145-147]. Therefore, noble metals, especially platinum and platinum-based materials remain the ORR electrocatalyst of choice in low-temperature fuel cells, although they contribute to approximately 42% of the total cost of a PEM fuel cell stack, when these systems are produced in series [148-151]. While it is essential to be mindful that on a mass-basis platinum is amongst the catalyst materials with the highest embodied energy and CO_2 emissions, developing synthesis techniques with low environmental footprint could make the production of Pt-based catalyst in line with the sustainable development goals [152]. A. Zadick et al. [30] and L. Xie and D.W. Kirk [153] demonstrated that the instability of Pt/C electrocatalyst in alkaline medium is more severe than acidic one, and the loss of active surface area of Pt electrocalyst is three times higher in alkaline medium after similar accelerated stress test. In attempts to reduce the required usage of Pt-based electrocatalyst, many strategies are employed while enhancing the electrocatalytic activity, stability and utilization of Pt. In this regard, nano-

engineering of supported Pt in a three-dimensional (3D) porous structure is becoming of more interest, where the nanoscale electrocatalyst possesses high surface-to-volume ratio, high mass electrocatalytic activity, and high Pt utilization [154]. The assembly of nanoscale electrocatalysts, often under the form of nanoparticles/nanoparticle thin films, on advanced support materials such as metal or metal oxide foam, mesh and felt, and polymeric or carbonaceous structures can further improve the electrocatalyst performance. The precise tuning of the shape, size and crystallinity-dependent properties of the nanoparticles and dispersion on and interaction with the support enable optimization of the material in a wide variety of applications. Therefore, the ability to design such Pt nanoparticles/nanostructures is an enabler for the low-cost production of electrodes showing high performance and durability [34, 155-157].

Excellent progresses in wet chemistry synthesis such as the use of Pt colloid adsorption onto the substrate, or impregnation of carbon support with Pt solution and its subsequent reduction have been widely reported to synthesize Pt nanostructures with different characteristics [21, 158, 159]. However, wet chemistry methods suffer from the use of hazardous solvents and chemicals, use of moderate to high temperatures (*i.e.* energy intensive), and challenges in shape and size control. The agglomeration of Pt due to 3D nucleation and growth mechanisms is another significant drawback of wet chemistry, which requires further use of stabilizing agents such as ligands or surfactants to prevent aggregation [53, 73]. One promising dry, solvent-free synthesis approach that relies on the physical vapor deposition of controllable Pt nanostructures is nanosecond pulsed laser ablation (PLA) in the gas phase, which was employed in this study. PLA of solid targets has been shown to be an efficient method to deposit high purity metal nanostructures under a wide range of conditions on various substrates. This method features short reaction times, no chemical precursors, no waste or byproduct, no high temperature nor high pressure environment [75, 160-162]. In this technique, the target absorbs the laser energy, which leads to the rapid evaporation of the target and generates a plasma plume containing metal adatoms or clusters, ions, and electrons expanding away from the target [75, 160-167]. The supersaturation, nucleation, and condensation of the gas phase result in the generation of small solid particles (< 100 nm) that can be directly collected on a desired support material [163-166].

In this article, we report on the design and PLA-based synthesis of 3D porous low-Pt-loading electrocatalysts with the intent to use them as a gas diffusion electrode (GDE) for the ORR in alkaline fuel cells. Although there have been several studies on the synthesis of micro- and

nanostructures of different metals, metal oxides/nitrides and alloys by PLA in gas and/or liquid environments [78-82, 168, 169], to our knowledge, there is no report on optimizing the PLA synthesis condition and deposition of various Pt nanostructures on MWCNT directly grown on a stainless steel (SS) mesh using a dry, binder-free synthesis route. The synthesized nanostructures are characterized by field emission scanning electron microscopy (FESEM), transmission electron microscopy (TEM), X-ray diffraction (XRD), Raman spectroscopy and X-ray photoelectron spectroscopy (XPS). Next, results on the electrochemical characterization of the developed electrodes are presented, followed by the evaluation of their electrocatalytic activity for the ORR in comparison to the commercially-available Pt/C, in a rotating-disk-electrode configuration. Lastly, the electrocatalytic behavior of the developed 3D porous Pt/MWCNT/SS electrodes in the ORR are directrly tested employing a gas-diffusion-electrode setup in order to obtain data that is more relevant to their possible application as GDEs in alkaline fuel cells.

5.3 Experimental Section/Methods

5.3.1 Pt/MWCNT Nanostructure Synthesis

Multi-walled carbon nanotubes (MWCNTs) were selected as a Pt support characterized by a large surface area, high electrical conductivity and stability in harsh environments such as that one in fuel cells [59, 89-91]. To eliminate the use of both catalyst and binder for the growth and adherence of MWCNTs on a substrate during the thermal chemical vapor deposition technique, stainless steel (SS) mesh was used as the substrate for MWCNTs to be directly grown on it. This configuration facilitates mass transport at the gas diffusion electrode and electron transport between the electrocatalyst and support. MWCNT (~30-40 nm in diameter and 13–15 μm in length) were directly grown on 316L stainless steel (SS) mesh coupons (grid bars: 165 × 800 per 6.45 cm^2; wire diameters: 0.07 and 0.05 mm; grid opening: 15 microns, thickness: 0.150 mm, purchased from TWP Inc.) using a semi-batch thermal chemical vapor deposition (CVD) method reported previously by Jorge et al. [170]. The SS coupons were placed in a tubular CVD furnace and heated to 700°C under ambient air for 2 min. The CVD furnace was then purged with argon (99.999%, all gases were purchased from MEGS Specialty Gases) at 592 ± 5 sccm to reach an oxygen level below 0.5%. For the MWCNT growth, acetylene was co-injected with Ar at 68 ± 5 sccm for 2 min, and then stopped while the Ar flow was maintained for another 2 more min.

The MWCNT-covered SS mesh coupon (MWCNT/SS) was then removed from the furnace and allowed to cool down in room temperature. A schematic view of CVD setup is shown in Figure S5-1(a).

Different Pt nanostructures were synthesized and directly deposited on MWCNT/SS by solvent-free laser ablation of a platinum target at different background pressures and laser pulse energies at 21 ± 1 °C using the pulsed laser ablation setup represented in Figure S5-1(b). A Pt target (99.95%, Ted Pella Inc.) was ablated using the third harmonic (355 nm) of a nanosecond Nd:YAG laser (Quantel, Brilliant B10) with repetition rate and pulse width of 10 Hz and 5 ns, respectively. A series of lenses and mirrors is used to focus the laser beam at an incidence angle of 45^{o} onto the target (a spot size diameter was estimated to be ~1 mm). The MWCNT/SS coupon was affixed to a substrate holder mounted on a manual linear displacement stage, and positioned in front of the Pt target. Prior to each PLA experiment, the chamber was flushed with Ar for 3 min and then pumped down to 10^{-5} Torr to reduce the amount of moisture and any other possible gaseous contaminants. The ablation time was set to 5 min (3000 laser shots) for a target-to-substrate distance of 3 cm. The background gas (Ar) pressure was varied from 10^{-5} to 10 Torr, and the laser energy (measured with a Joule meter, Coherent air-cooled thermopile sensor, PM10 model) was varied from 20 to 66 mJ pulse^{-1}. Table 5-1 explains the coding of samples based on the experimental conditions. The target holder was moved up and down using a motorised stage to enable a uniform wear of the target and to mitigate thermal effects. The substrate holder was manually rotated during the 5 min of PLA to achieve a uniform coverage of the MWCNTs/SS coupons.

Table 5-1. Sample coding for PLA experiments

Sample Code	Laser Energy (mJ pulse^{-1})	Ar Pressure (Torr)
Pt-high-10^{-5}	66	10^{-5}
Pt-high-10^{-2}	66	10^{-2}
Pt-high-1	66	1
Pt-high-10	66	10
Pt-mid-10^{-5}	50	10^{-5}
Pt-low-10^{-5}	20	10^{-5}

5.3.2 Material Characterization

Ultra-high-resolution field emission scanning electron microscopy (Hitachi, Cold FE SU-8000 SEM) with an accelerating voltage of 30 kV and emission current of 10 μA was used for the morphological characterization of the various Pt nanostructures on MWCNT/SS. X-ray diffraction (XRD) analysis (Bruker, D8 Discover) was carried out using a Cu X-ray source and monochromatic X-ray optic to determine the crystalline structure of the deposited Pt nanostructures. Element identification and their chemical state were investigated by X-ray photoelectron spectroscopy (Thermo-Scientific, K-Alpha XPS apparatus) with an Al Kα source, micro-focused monochromator and spot size of 200 μm. The flood gun was turned on to avoid the charging effect during data acquisition. The obtained spectra were analyzed using the Avantage software after Shirley background subtraction. A mixed Gaussian/Lorentzian peak shape was used for all components for peak fitting. The shape, crystalline/lattice *d*-spacing, and particle size distribution of the Pt nanostructures were investigated using transmission electron microscopy (Thermo-Scientific, Talos F200X G2 TEM). For TEM imaging, the Pt-covered MWCNT/SS mesh coupon was first sonicated in acetone (Sigma-Aldrich) for 60 s. A TEM grid was then immersed in the dispersed solution to collect the individual Pt-covered MWCNTs broken off the SS mesh and left at room temperature to dry. The defect degree of MWCNTs before and after the deposition of Pt nanoparticles was evaluated by Raman spectroscopy (Thermo-Scientific, DRX2) using a laser excitation wavelength of 532 nm.

5.3.3 Electrochemical Analysis

The electrochemical tests were carried out with an Autolab Potentiostat in a three-electrode cell using a Pt wire as counter electrode, Hg/HgO (1 M KOH) as the reference electrode, and the prepared Pt/MWCNT/SS or Pt/C RDE/GDE as the working electrodes. The electrolyte was prepared by dissolving KOH pellets (Sigma-Aldrich, purity 90%) in 18.2 MΩ cm resistive Milli-Q water. All potentials quoted in this manuscript are reported with respect to the reversible hydrogen electrode (RHE). Prior to all electrochemical measurements, the working electrode was preconditioned by cycling (20 cycles) between 0.037 and 1.237 V, at a scan rate of 50 mV s^{-1} in Ar-saturated 1 M KOH, to achieve a stable and reproducible surface.

The electrochemically-active-surface-area (ECSA) ECSA was calculated by measuring the charge of hydrogen adsorption/desorption region (0.15 - 0.5 V), after the correction for the double-

layer charging current, using the theoretical charge of 210 μC cm^{-2} for a monolayer adsorption/desorption of hydrogen on Pt. The ECSA was also calculated from CO-oxidation charge measurements. For electrochemical CO stripping voltammetry, the working electrode was held at 0.317 V in a CO-saturated 1 M KOH for 30 min (to adsorb CO on Pt), and the cell was then purged with Ar for 20 min to expel CO from the electrolyte. Two subsequent cyclic voltammetry (CV) scans were performed. In the first scan, the adsorbed CO was stripped (oxidized) by scanning the potential from 0.037 to 1.237 V at a scan rate of 20 mV s^{-1}, and the second scan provided a baseline for the CO stripping peak.

The electrocatalytic activity of the produced electrodes for the ORR was evaluated in O_2-saturated 0.1 M KOH. The prepared electrodes without the use of any binder/ionomer were tested at 21 ± 1 °C by fixing the produced Pt/MWCNT/SS samples on a glassy carbon rotating-disc-electrode (RDE) setup by using a Teflon cover (Figure S5-2(a)). The electrode surface diameter exposed to the electrolyte was 5 mm. The evaluation of the prepared 3D porous Pt/MWCNT/SS electrodes for ORR using the RDE setup in Figure S5-2(a) enables their rapid electrochemical characterization in their original configuration without preparing the thin-film RDE (TF-RDE). Linear sweep voltammetry (LSV) was performed between 0.45 and 1.1 V at a scan rate of 20 mV s^{-1} and various RDE rotation speeds (400 to 2500 RPM) in O_2-saturated 0.1 M KOH. To assess the stability of the electrocatalyst, the accelerated durability test (ADT) was performed by applying the cyclic potential sweeps between 0.45 and 1.1 V for 2000 cycles at the scan rate of 20 mV s^{-1}. The electrocatalytic performance of the Pt/MWCNT/SS electrodes was compared to the commercially-available 20 *wt.* % Pt/C electrocatalyst. For this purpose, Pt/C was deposited on a glassy-carbon RDE as a thin-film (TF-RDE) with a Pt loading of 35.6 μg cm^{-2}, and the corresponding preparation steps are explained in the Supplementary Information (section 5.6.1). For experiments in which the performance of Pt/MWCNT/SS was evaluated as gas-diffusion-electrodes (GDE), the GDE setup presented in Figure S5-2(b) was used. The setup consists of a cell made of polytetrafluoroethylene (PTFE), Ag/AgCl reference electrode, Pt coil counter electrode, the Pt/MWCNTs/SS or Pt/C GDE, and 6 M KOH as the electrolyte. The growth of MWCNT on both sides of the SS provides the opportunity to employ the developed electrodes directly as the GDEs, without using a binder and the GDE backing (carbon paper). In these experiments, the Pt/MWCNT/SS electrodes were pre-conditioned by potential cycling from 0.4 to 1.1 V (40 cycles) at 21 ± 1 °C while purging humidified oxygen gas, then the LSV was recorded

to evaluate the performance of the GDEs for ORR. Similarly, the results were compared to the GDE made by commercial Pt/C (see section 5.6.1 for Pt/C preparation steps). Electrochemical impedance spectroscopy (EIS) measurements were also conducted employing the GDE setup by applying a sinusoidal potential of ±10 mV at a *dc* working electrode potential of 0.8 V in a frequency range from 100 kHz to 10 mHz.

5.4 Results and Discussion

5.4.1 Structural Characterization of Pt/MWCNT/SS

5.4.1.1 Pt Loading

The amount of Pt collected on the surface of MWCNT/SS mesh coupons depends on the PLA synthesis conditions. The mass of deposited Pt was determined by weighing the coupon before and after PLA by using a high-precision balance. Figure 5-1(a) concisely reports the effects of laser pulse energy and chamber pressure on the Pt loading. By increasing the background gas pressure from 10^{-5} to 10^{-2} Torr, the amount of deposited Pt did not change significantly (blue triangles), which implies minor interaction of the Pt adatoms and clusters with the background gas, resulting in the collection of similar amounts of Pt on the substrate. However, the Pt loading decreased from 35.4 μg cm^{-2} at 10^{-2} Torr to approximately 27 and 15 μg cm^{-2} at 1 and 10 Torr, respectively. Previous studies have shown that at a higher background gas pressure, a higher recoil pressure exists at the surface of the Pt target, leading to a redeposition of the ablated species on the target [171]. As shown in Figure S5-4, no perfect crater is observed after one single laser shot and the spatial array of spikes on the Pt target is more distinct at higher pressure, which means that a higher mass of Pt is redeposited on the target instead of on the substrate. It is noteworthy that the formation of the re-solidified porous layer on the lasered path with disturbed crystalline lattice weakens the Pt target and increases the ablation efficiency during the succeeding overlaying pulses [172].

Reducing the laser energy from 66 to 20 mJ $pulse^{-1}$ led to a decrease of the amount of Pt deposited on MWCNT/SS from 35.6 to 14.2 μg cm^{-2} (Figure 5-1(a), squares), due to the ablation of lesser amounts of Pt at lower laser energies. As illustrated in Figure 5-1(b), the energy per pulse of the Nd:YAG laser was varied using the delay time between the flashlamp and the optical Q-switch from 215 to 400 μs, which gave rise to energy per pulse ranging from 66 to 0.8 mJ $pulse^{-1}$

and laser peak power ranging from 13.2 to 0.16 MW. Based on our estimation of the focused beam size (diameter of 1 mm), the laser fluence at the target ranges from 0.1 to 8.4 mJ cm^{-2}. We found that the ablation threshold for the Pt target is 16 mJ $pulse^{-1}$ (320 μs delay time) [173, 174].

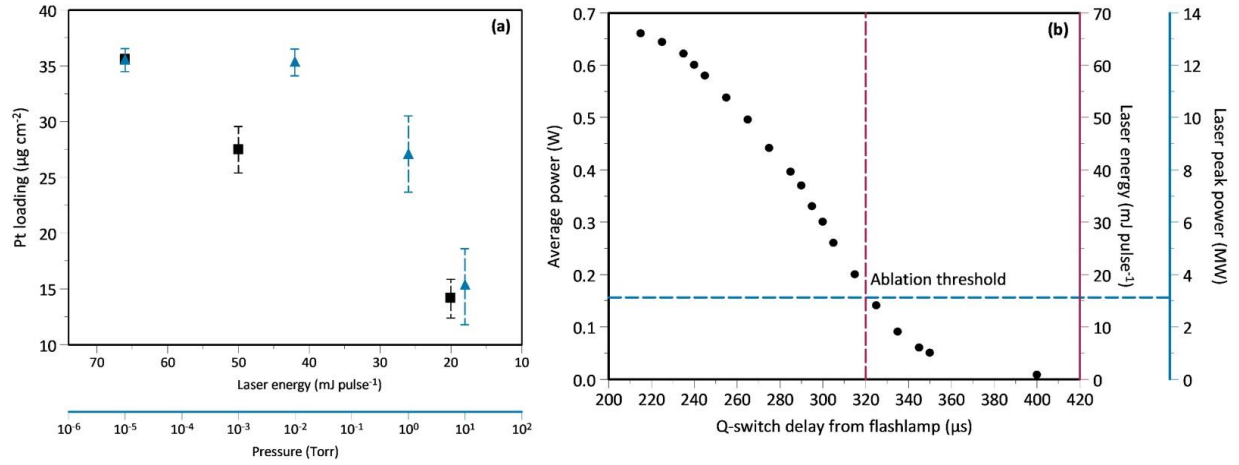

Figure 5-1. (a) Pt loading on MWCNT/SS at different PLA conditions. Blue triangles: effect of gas pressure at laser energy of 66 mJ pulse-1. Black squares: effect of laser energy at a chamber pressure of 10-5 Torr (note the reverse axis direction for the laser energy). Error bars show the standard deviation. (b) Effect of the delay time between the flashlamp and the optical Q-switch on laser energy and power.

5.4.1.2 Morphology and Crystalline Structure of Deposited Pt

Figure S5-5 reveals a complete and uniform MWCNT coverage on the SS surface. The SEM and STEM images in Figure S5-5 also evidence the existence of nanotubes with different structures such as multi-walled, segmented, branched and bamboo-like. MWCNTs grow on both side of the SS mesh. The existence of structural defects in the as-grown MWCNTs is reported to be advantageous for the deposition of Pt nanostructures by enhancing the binding energy between the MWCNTs and Pt nanoparticles [175, 176]. Morphological differences in the Pt deposited on MWCNTs are observed at different PLA background gas pressures and laser energies, as seen in Figure 5-2. A uniform, dense and compact Pt nanoparticle thin film is formed at the lowest chamber pressure (10^{-5} Torr, 66 mJ $pulse^{-1}$) and no apparent pores can be detected across the coating structure (Figure 2(a)). At a pressure of 10^{-2} Torr and energy of 66 mJ $pulse^{-1}$, the deposited Pt structure becomes more porous and the surface of coated MWCNTs appears rougher (Figure 5-2(b)); while at a pressure of 1 Torr and energy of 66 mJ $pulse^{-1}$, the surface of MWCNT shows a globular and very porous Pt structure (Figure 5-2(c)). At the highest PLA pressure (10 Torr) and

laser energy (66 mJ pulse^{-1}), chains of small and large Pt nanoparticles are visible on the surface of MWCNTs (Figure 5-2(d)). The effect of laser energy can be seen in Figure 5-2(e and f); a less dense and cohesive Pt film compared to Figure 5-2(a) can be seen after reducing the laser energy from 66 to 50 and then to 20 mJ pulse^{-1}.

Lowering the laser energy results in the Pt nanoparticles reaching the surface of MWCNTs with a lower kinetic energy, which consequently forms a film not as dense as that one formed by ablation at high laser energies. As the Ar background pressure increases, the kinetic energy of ablated Pt shifts to low values because of the interaction of the expanding plasma plume with the surrounding gas and scattering of ablated ions and atoms by background gas atoms. The lower kinetic energy of the ablated Pt at high pressure reduces the deposition rate, which results in the agglomeration of primary nanoparticles [164]. Riabinina et al. [82] reported a porous Pt structure on a flat silicon substrate, with an ablation pressure of 11 Torr in helium as background gas, which is similar to the structure obtained in this study at the pressure of 1 Torr in Ar (Figure 5-2(c)). The formation of similar porous structures at different chamber pressure is linked to the nature of the background gas used during PLA. The ejected adatoms/clusters have lower velocity and higher scattering index in the argon compared to in the helium atmosphere. The larger mean free path per unit mass of helium causes lower collisional volume resulting in less agglomeration of clusters and particles [82].

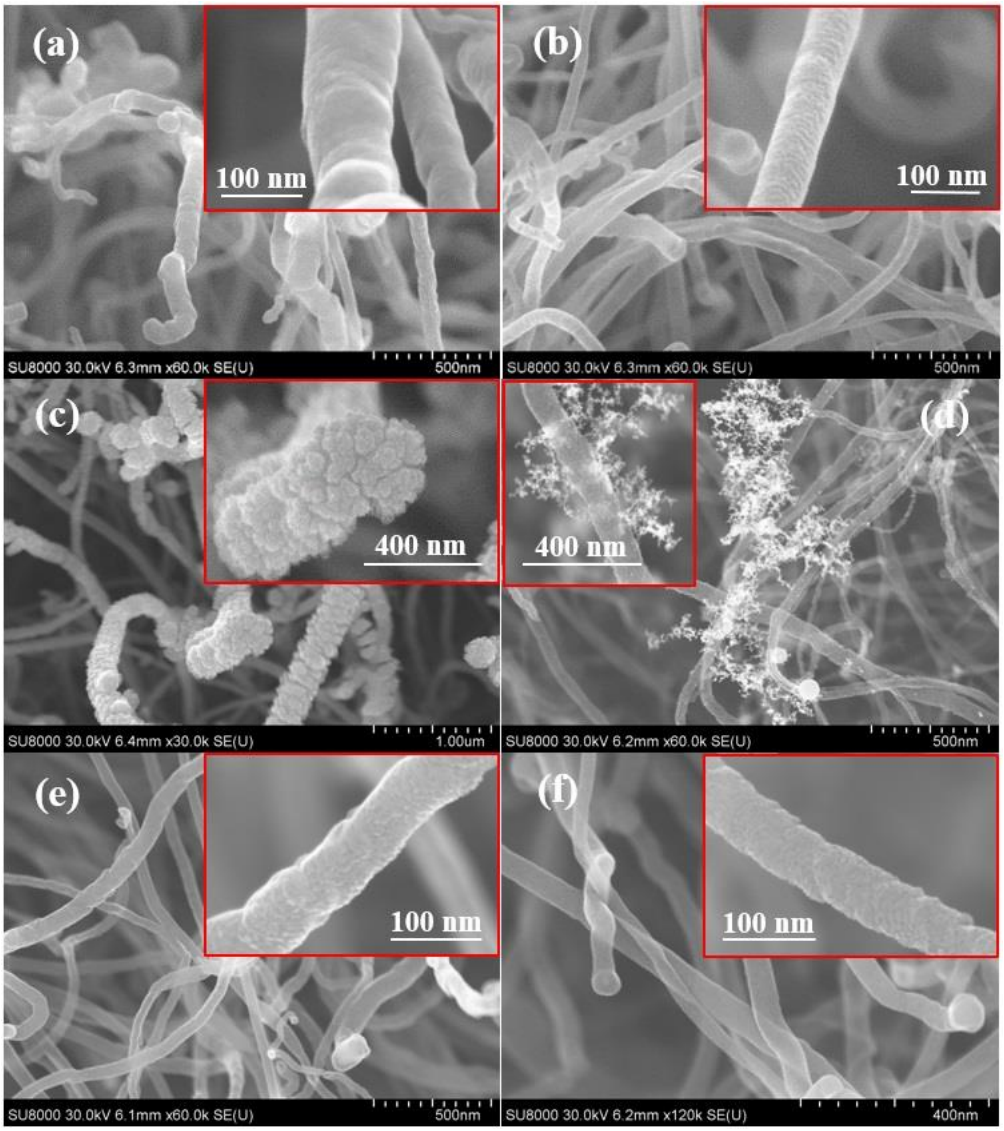

Figure 5-2. SEM images of Pt nanostructures deposited at different background gas pressure and laser energy; (a) Pt-high-10^{-5}, (b) Pt-high-10^{-2}, (c) Pt-high-1, (d) Pt-high-10, (e) Pt-mid-10^{-5}, and (f) Pt-low-10^{-5}.

The penetration depth of ablated Pt into the forest-like structure of MWCNTs was investigated by SEM imaging of the cross-section of the MWCNT bundles grown on SS. A typical SEM image and the corresponding EDS map are presented in Figure 5-3. A dense forest of vertically grown MWCNTs can be seen in Figure 5-3. The EDS line scan indicates that the Pt coverage extends approximately 8 μm-deep. Similar results were obtained at the other PLA conditions, revealing that the penetration depth is strongly linked to the characteristics of the MWCNT forest and not to the PLA conditions. The TEM movie, provided as the Supplementary Information document, reveals the Pt nanoparticle dispersion and coverage on the MWCNTs. It shows a gradual decrease

in the Pt coverage from the tip to the root of each MWCNT. A denser Pt coating is observed at the tip of MWCNTs facing the Pt target, while more dispersed individual nanoparticles are observed farther from the MWCNT tip and away from the target.

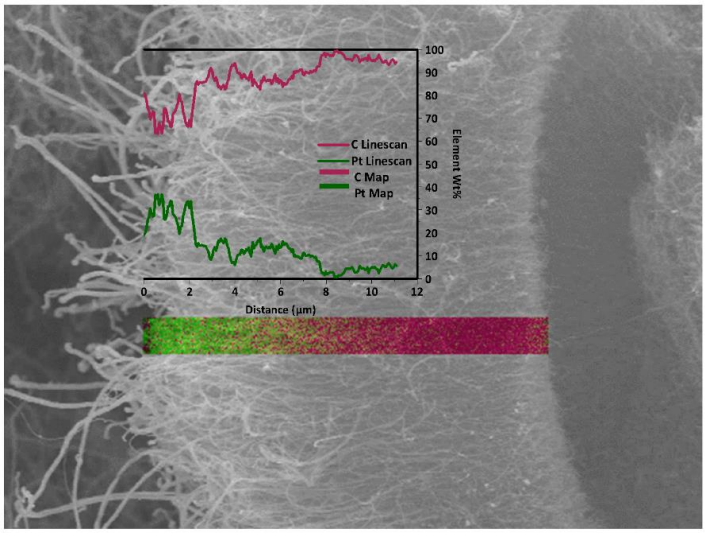

Figure 5-3. SEM image and EDS line scan revealing the spatial distribution of Pt coverage on the MWCNTs obtained with the Pt-high-1.

TEM images of Pt-coated MWCNTs obtained at various PLA conditions are shown in Figure 5-4. One notices that all coatings are formed of nanoparticles; a size distribution and selected area electron diffraction (SAED) patterns are reported for each image. Pt nanoparticles with average size of 2.0 ± 0.2 nm are formed at a chamber pressure of 10^{-5} Torr (Figure 5-4(a)). As the background gas pressure increases to 10^{-2} Torr, the particle size increases to 2.6 ± 0.3 nm (Figure 5-4(b)). Further increase of particle size and aggregation of particles are observed at 1 Torr, which results in the particle size of 2.8 ± 0.8 nm (Figure 5-4(c)). On the other hand, lowering the laser pulse energy from 50 to 20 mJ $pulse^{-1}$ while keeping the chamber pressure at 10^{-5} Torr, decreases the mean particle size from 3.0 ± 1.6 (Figure 5-4(d)) to 2.8 ± 1.6 (Figure 5-4(e)). Figure S5-6(a and b) show the existence of these fine nanoparticles on the surface of MWCNT. Although mean particle size decreases at lower laser energies, bigger Pt nanoparticles with diameters up to 7.7 nm are simultaneously formed during PLA.

The formation of different nanostructures (Figure 5-2) with different size distributions (Figure 5-4) as a function of synthesis conditions can be explained by taking a closer look at different stages of gas/liquid-to-particle conversion during the PLA process. These steps are schematically shown in Figure 5-5 as a function of time. Upon absorption of a high-energy laser pulse by the Pt

target at the spot size of ~ 1 mm, a rapid localized heating takes place leading to material vaporization. The short duration of the laser pulse (5 ns) prevents the development of a large heat-affected zone, thus melting and boiling phenomena are very limited in extent. The high density of micron-sized splashes observed on the target (Figure S5-4) rather supports a phase explosion mechanism caused by homogenous vapor bubble nucleation within the Pt surface. The outer surface relaxes explosively into a mixture of vapor and liquid nanoclusters. Larger solidified Pt particles (> 50 nm) are scarcely observed on the coating (Figure S5-8), thus supporting the fact that the localized heating seldomly leads to significant melting and ejection of macroparticles through hydrodynamic sputtering from Rayleigh–Taylor and Kelvin–Helmholtz instabilities [167, 172, 177-181].

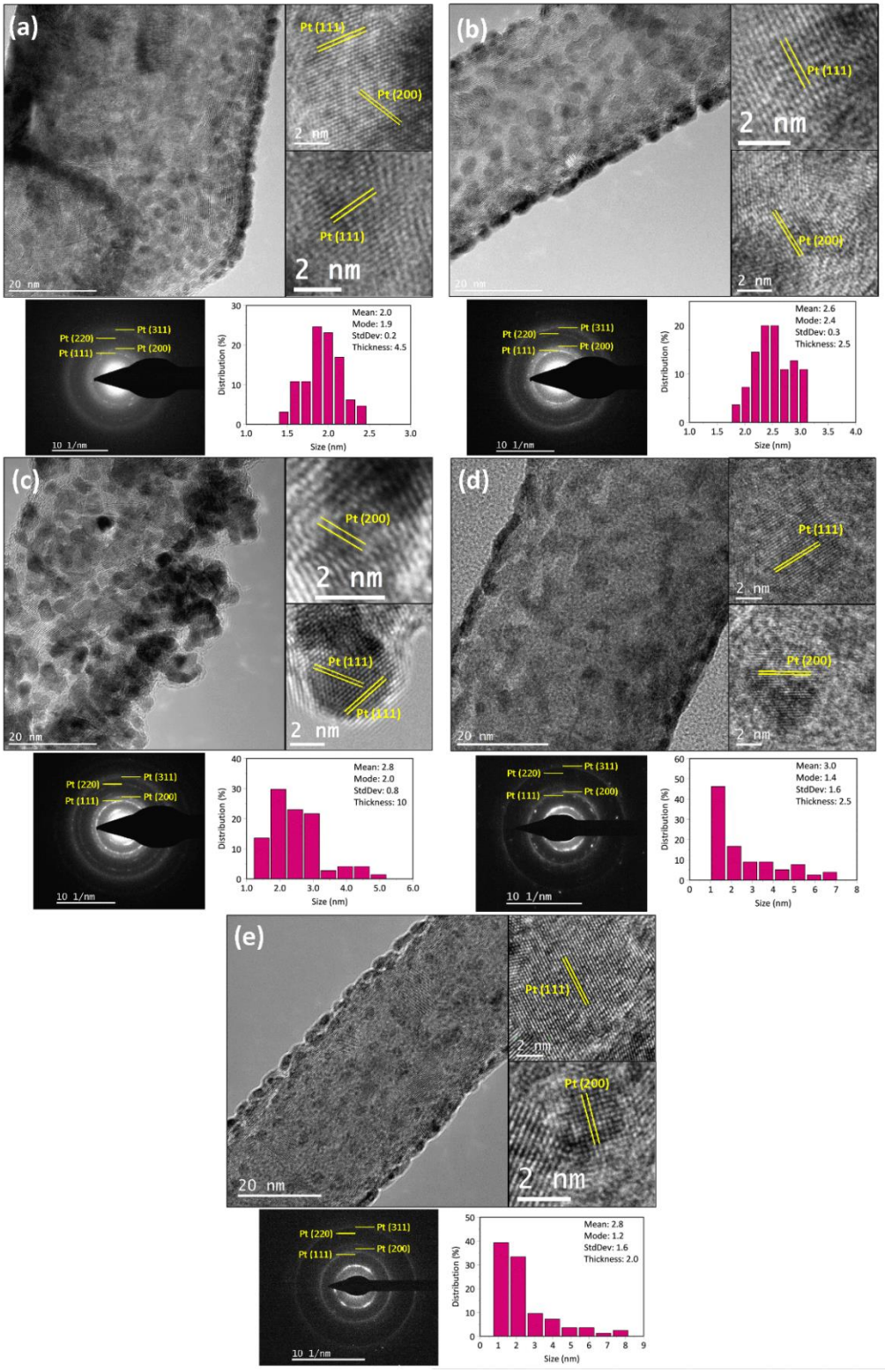

Figure 5-4. High resolution TEM images, size distribution and SAED pattern of (a) Pt-high-10^{-5}, (b) Pt-high-10^{-2}, (c) Pt-high-1, (d) Pt-mid-10^{-5}, and (e) Pt-low-10^{-5}; TEM images of the sample Pt-high-10 is shown in Figure S5-7.

The second step involves the expansion and evolution of the ejected species from the Pt surface and particle generation from the vapor/liquid phase. At first, the ejected Pt adatoms or clusters enter the vacuum expansion or free flight regime (Figure 5-5, region *(I)*), where the pressure of the laser induced plasma is significantly higher than that of the background gas; therefore, Pt adatoms or clusters do not interact. If atomic clusters do not exist in the plasma plume, Pt adatoms must reach the saturation vapour pressure to form clusters by homogeneous condensation until a critical size is reached. When atomic clusters are ablated from the target (e.g. from phase explosion), they behave as nuclei to form larger particles through heterogeneous condensation. The condensation taking place for vapor clusters in this regime is dependent on the cooling rate, vapor expansion rate and the released latent heat of condensation. During the condensation, the number of clusters increases until the cluster density saturates [171, 172, 182]. Later, the shockwave or Sedov regime (Figure 5-5, region *(II)*) influences the particle formation when the effect of the background gas is no longer negligible. In this step, collision and coalescence govern the growth of condensed species at the front layer of the plume [171, 172]. This step ends when the collision probability in the heterogeneous plume becomes negligible or particle solidification occurs for the condensed species (Figure 5-5, region *(III)*). Eventually, agglomeration is the only possible step for the particle growth [171, 172, 182, 183].

Lowering the laser energy reduces the extent of phase explosion and consequently the amount of ablated Pt vapor and liquid, and their initial kinetic energy. At low laser energy, late nucleation shortens the condensation time. This late condensation results in the existence of clusters with small size, their coalescence and ultimately the formation of larger particles prior to solidification. Moreover, smaller particles are more susceptible to coalescence because they require longer time to reach the solidification temperature. The wider particle size distribution at laser energies of 50 and 20 mJ $pulse^{-1}$, in comparison to the highest laser energy (66 mJ $pulse^{-1}$), is a proof of this mechanism, Figure 5-4(d-e) [183].

Increasing the ambient gas pressure leads to an increase of the resisting force for plume propagation, and the early condensation results from the interaction of the primary clusters with the background gas. Therefore, agglomeration of the solidified particles occurs. The deposition of larger agglomerates accompanied by smaller particles attached to the MWCNTs at high pressure (10 Torr) is an indication of collisions between particles after solidification. The largest particles

are formed near the plume front, and the smaller particles are successively formed in the depth of the plasma plume [171, 183].

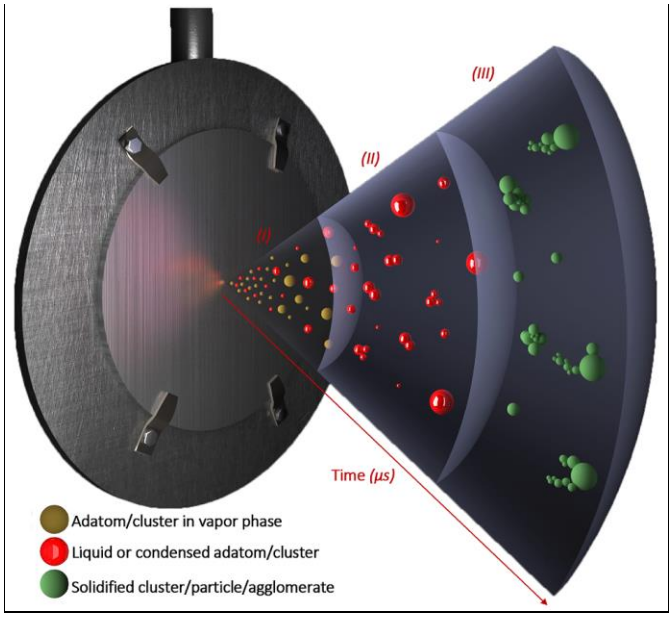

Figure 5-5. Schematic of the proposed mechanism of the formation of Pt nanostructures during PLA, (*I*) free flight region, (*II*) shockwave region, and (*III*) agglomeration region.

The high-resolution TEM images in Figure 5-4 illustrate the presence of Pt nanoparticles containing (111) and (200) crystal phases with a *d*-spacing of ~0.230 and ~0.197 nm, respectively. According to the SAED patterns of all samples, Pt (111), (200), (220), and (311) exist in the Pt coatings covering the MWCNTs. The MWCNTs showed a ring with a corresponding *d*-spacing of ~0.34 nm in all SAED patterns. The XRD patterns of MWCNT/SS before and after the deposition of Pt nanostructures (Figure S5-9) show three diffraction peaks at 2θ of 43°, 51° and 74°, which are assigned to austenite in SS. However, the two peaks of austenite at 43° and 51° coincide with the (100) and (004) crystalline faces of graphite in MWCNTs [184]. The low intensity diffraction peak at 26° (with *d*-spacing of ~0.34 nm observed in all SAED patterns in Figure 5-4) is also attributed to MWCNTs. The XRD pattern of bulk Pt exhibits peaks at ~40°, 46°, 67°, 82°, and 85°, which are respectively ascribed to face-centred cubic Pt (111), (200), (220), (311), and (222). The Pt (111) diffraction peak at ~40° in Pt/MWCNT/SS samples synthesized at highest laser energy and pressures of 10^{-5}, 10^{-2}, and 1 Torr are wider and very smaller compared to those in bulk Pt. The other Pt diffraction peaks are not clearly distinguishable in the XRD patterns of these samples, which can be due to the existence of lower amounts of other crystal facets compared to Pt (111).

On the other hand, no Pt-related peaks are visible in the diffraction patterns of samples synthesized at low laser energies. This is because less Pt mass is accumulated on the MWCNTs (< 28 μg cm^{-2}), and the small grain size of the synthesized nanoparticles is not detected by XRD [82, 166]. The structural integrity of the grown MWCNTs before and after the deposition of Pt nanostructures was fully examined by Raman Analysis and explained in section 5.6.2 (Figure S5-10 and Figure S5-11), which confirmed the high quality of the MWCNTs synthesized in this study.

5.4.1.3 Element Identification of Deposited Pt on MWCNT

Carbon (C 1s), platinum (Pt 4f) and oxygen (O 1s) were the three elements detected by the XPS survey scan. Their high-resolution spectra are shown in Figure 5-6 (note that the intensity scale is different for each plot). All spectra were collected after 20 s of Ar sputtering, which was applied in order to remove surface impurities attributable to exposure to laboratory air. For comparison purposes, the spectra of bulk Pt is also shown in Figure 5-6. The characteristic doublets for Pt $4f_{7/2}$ and Pt $4f_{5/2}$ located at binding energies of ~71 and ~74 eV, which were deconvoluted using two $4f_{7/2}$ and $4f_{5/2}$ peaks, are indicative of the presence of Pt in its metallic state in all samples (Figure 5-6 left panel). The Pt $4p_{3/2}$ (~ 510-529 eV) and O 1s (~ 529-535 eV) spectra are exhibited Figure 5-6 (middle panel). The binding energy of oxygen in metal oxides is in the range of 529 to 530 eV. The appearance of O 1s peak at ~532 eV confirms the existence of organic oxygen in the sample, and indicates that Pt exists only in its metallic state [185, 186].

Peak fitting was also performed on C 1s to confirm the source of oxygen on the surface (Figure 5-6, right panel). To describe the C 1s and prove the existence of oxidized carbon species, several peaks were used for the deconvolution of C 1s. The graphene asymmetric peak (sp^2) is centered at 284.5 eV, and the sp^3 carbon component is centred at 285 eV. The C–O and C=O peaks are respectively positioned at 286.2 and 287.8 eV for all samples. The presence of C–O and C=O peaks in all synthesized samples are related to their existence in the structure of carbon nanotubes used as the support for Pt nanostructures. These oxidized species can be formed during the thermal decomposition of acetylene in the presence of trace amount of oxygen in the CVD furnace.

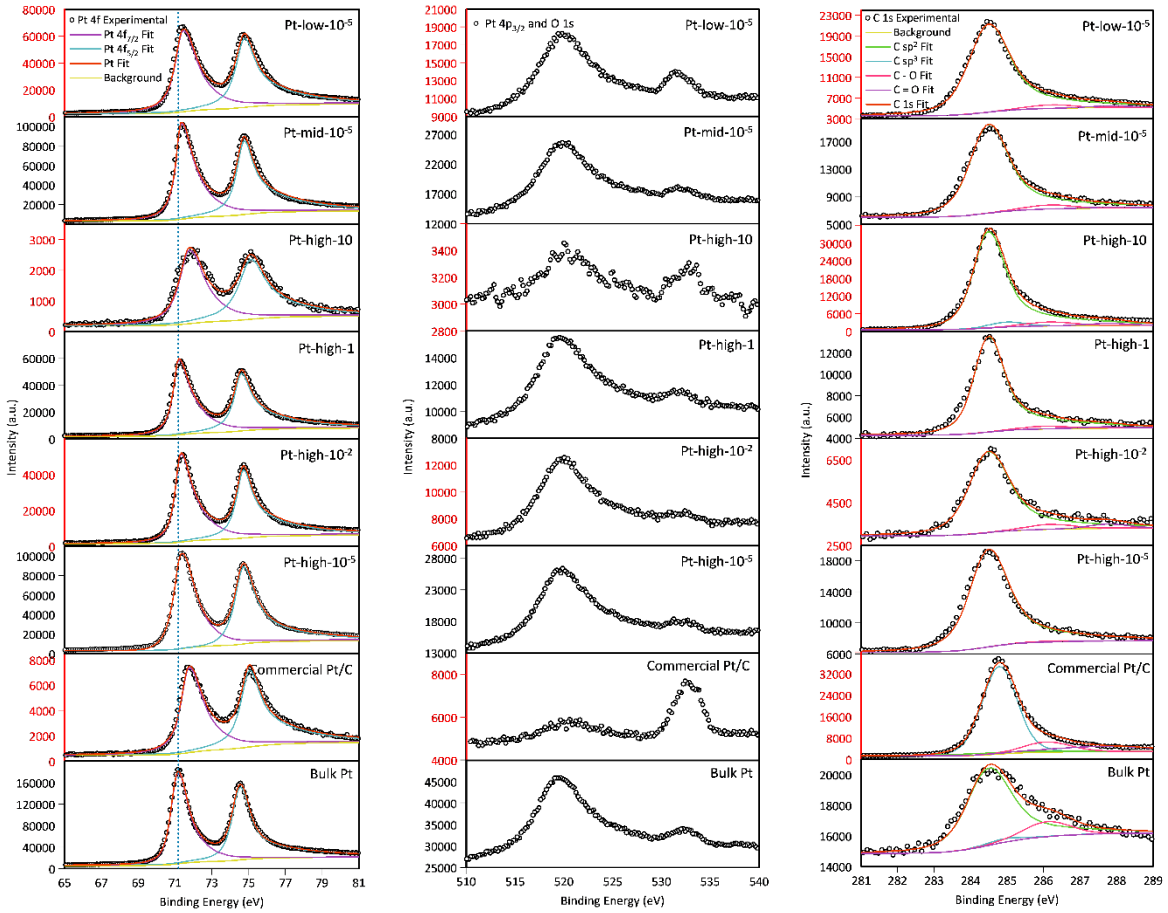

Figure 5-6. XPS analysis of Pt nanostructures deposited on MWCNT/SS at different chamber pressures and laser pulse energies.

As shown in Figure 5-7, a positive shift in the binding energy of the Pt 4f level compared to bulk Pt is observed in all the Pt/MWCNT and commercial Pt/C samples (Figure 5-6). The general trend observed illustrates that the Pt 4f binding energy shifts to more positive values by lowering the background gas pressure and laser pulse energy during PLA, as Pt with smaller particle size is added to the deposited nanostructures (Figure 5-4 and Figure S5-6). However, the Pt-high-10 sample does not follow this trend and shows the highest displacement in the binding energy. We link the origin of this result to the probable existence of small nanoparticles that were attached to larger spherical particles without direct contact with MWCNT. Another reason to obtain this result can be the surface of MWCNT not being fully covered by Pt nanostructures, which is similar to the high binding energy found for the commercial Pt/C (SEM image in Figure S5-3). Generally, the positive shift in binding energy is linked to metal-support interactions and to a change in the electronic structure of the metal valence band due to small particle size that affects the activity of

the catalyst. This effect has been reported to be the result of initial-state effects such as a change in the atomic coordination number or charge-transfer effects. Also, the final-state effect like relaxation effects may be the source of this shift [187-189].

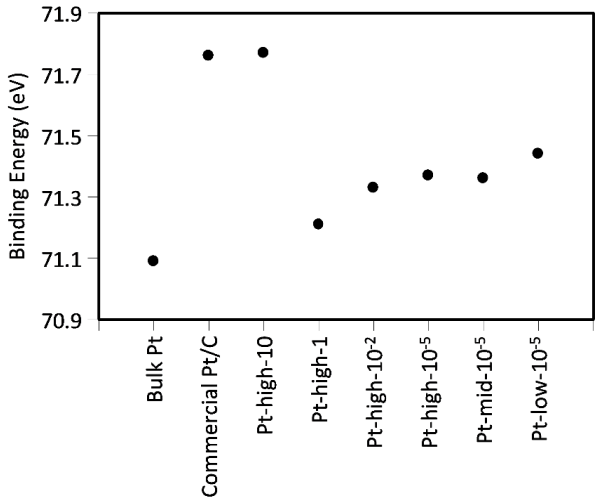

Figure 5-7. Pt 4f $_{7/2}$ binding energies of different samples synthesized at different PLA conditions.

5.4.2 Electrochemical Characterization of Pt/MWCNT/SS

5.4.2.1 Electrochemically Active Surface Area

The total electrocatalytic activity of Pt nanoparticle thin films on MWCNT/SS for the oxygen reduction depends on both its total surface area (extrinsic factor) and intrinsic activity. In order to determine the former, the ECSA of Pt deposited on the surface of MWCNT was determined in 1 M KOH electrolyte employing two approaches: the hydrogen adsorption/desorption and the CO-oxidation charge measurements. The corresponding full cyclic voltammograms recorded in 1 M KOH are presented in Figure S5-12, while the corresponding cathodic voltammetric profiles are shown in left panel of Figure 5-8 for more clarity. As the control sample and for comparison purposes, a bulk Pt and a commercial Pt/C electrode were also investigated. The electrocatalytic activity of Pt-high-10 was not investigated due to the non-uniformity and instability of the deposited Pt nanostructures on MWCNT/SS.

The voltammogram recorded in pure supporting KOH electrolyte for the bulk (control) Pt electrode shows the typical shape of Pt (Figure 5-8 and Figure S5-12). Briefly, the peaks between 0.15 and 0.5 V in the anodic scan are related to the hydrogen desorption charge (Figure S5-12, left

panel), followed by the electrochemical double-layer region between ~ 0.5 and 0.8 V. The region above 0.8 V is related to the formation of a Pt-oxide surface film. In the returning scan, a well-defined Pt-oxide reduction peak is present at ~ 0.82 V, followed by the double-layer region and then the hydrogen adsorption region, at more negative potentials (negative of 0.5 V). The commercial Pt/C electrode shows a similar CV shape; however, it should be noted that a small anodic peak is observed at ~ 0.8 V, and the corresponding cathodic peak/shoulder is at ~ 0.55 V (similar to Pt/MWCNT/SS samples, Figure S5-12). In addition, the main Pt-oxide reduction peak is shifted to more negative potentials. This has been associated with the increase in oxophilicity of Pt nanoparticles compared to bulk Pt, which results in a stronger Pt-O binding energy as the size of the nanoparticles decreases [190, 191]. Additionally, the Pt-oxide reduction peak on the commercial Pt/C voltammogram is less distinct from the one recorded on the bulk Pt, which is expected for Pt nanoparticles.

The voltammograms of the Pt/MWCNT/SS samples do not show well-defined hydrogen adsorption/desorption and Pt-oxide formation/reduction peaks compared to bulk Pt and commercial Pt/C, which is due to the low loading of Pt on MWCNTs and the relatively high Pt/MWCNT electrochemical double-layer-charging contribution (Figure 5-8 and Figure S5-11). Namely, the underlying MWCNTs offer a very large area for capacitive charge storage, and the resulting double-layer charging current (the background current) masks the contribution of the hydrogen adsorption/desorption and Pt-oxide formation/reduction currents. The other reason can be a lower content formation of the Pt-oxygenated species or their weakening on Pt/MWCNT/SS, which could, in turn, promote the ORR kinetics [192-194].

Table S5-2 lists the ECSA (cm^2) values calculated from hydrogen adsorption/desorption and CO-stripping expressed per 1 cm^2 of geometric area of the electrode, and per mass loading of Pt ($m^2\ g^{-1}$) [195, 196]. As expected, the nanostructured Pt electrodes (commercial Pt/C and Pt/MWCNT/SS produced in this study) show a significantly higher ECSA (up to 18.6 cm^2) than the bulk Pt electrode (2.0 ± 0.1 cm^2). The ECSA of Pt-high-10^{-5} electrode (18.6 ± 0.1 cm^2) is comparable to the ECSA recorded on the commercial Pt/C (17.7 ± 0.6 cm^2) in KOH electrolyte. With an increase in pressure, or with a decrease in laser energy during PLA, lower Pt loadings per geometric area of the MWCNT/SS were observed (Figure 5-1), which resulted in lower ECSA of Pt/MWCNT/SS electrodes. On the other hand, Pt-low-10^{-5} electrode with the lowest Pt loading showed the highest mass-based ECSA of 67.5 ± 2.3 m^2 per gram of Pt, which is in the upper range

of values reported in the literature; ~15 to ~62 m^2 g^{-1}_{Pt} is being reported for Pt-containing electrocatalysts supported on MWCNT in alkaline medium [197-199].

In order to confirm the ECSA values determined from the hydrogen adsorption/desorption region, the CO-stripping behavior of the electrodes was investigated in 1 M KOH. The first scan in Figure 5-8 and Figure S5-12 (right panel) represents the response of the Pt-CO_{ads} system, while the 2nd scan represents the response of a clean (CO-free) platinum electrode. The charge of the CO oxidation was determined to calculate the ECSA and compare to those obtained from the hydrogen region [195, 196]. Table S5-2 shows that the corresponding ECSA values are in agreement with those calculated by hydrogen underpotential (the respective ratio of the two ECSA values for all electrodes is 1.06 ± 0.07). Slightly higher values of the ECSA (CO_{ads}) are because the hydrogen charge can be influenced by ligand or strain effects, which can result in an underestimation of ECSA [43].

Figure 5-8 and Figure S5-12 (right panel) show that by sweeping the potential to more anodic values, the current due to the CO oxidation starts increasing at potentials positive of 0.4 V, splitting into two current peaks. Typically, CO oxidation on Pt in alkaline solution is composed of a main oxidation peak and a pre-peak. Marković and Ross assigned the existence of the pre-peak mainly to the oxidation of adsorbed CO on the step sites of nanoparticles and to the oxidation of CO molecules diffused from the terrace to step sites. The main CO oxidation peak is linked to the nucleation of oxygen species on Pt, which rapidly oxidize CO molecules [200-202]. As it can be seen in Figure 5-8 (right panel), the CO oxidation potentials for the pre- and main peaks were, respectively, at 0.60 and 0.65 V for bulk Pt, and at 0.60 and 0.69 V for the commercial Pt/C. All Pt/MWCNT/SS samples showed the main peak at 0.68 V, and the pre-peaks were at 0.56 V for Pt-low-10^{-5}, 0.59 V for Pt-high-1, and 0.6 V for Pt-mid-10^{-5}, Pt-high-10^{-5} and Pt-high-10^{-2}. The lower CO oxidation potential observed for all Pt/MWCNT/SS electrocatalysts compared to commercial Pt/C is attributed to a downshift in *d*-band center, which reduces the oxygen adsorption energy and results in a lower binding energies of Pt-O and Pt-CO [91, 192]. These results are in agreement with XPS results in Figure 5-7 when compared to bulk Pt and commercial Pt/C; namely, there is a direct relation between the binding energy of Pt $4f_{7/2}$ obtained by XPS and the position of the CO stripping peaks. In addition, the ratio of CO oxidation current of the main peak to the pre-peak for Pt electrocatalysts decreases from 2 to 1.4, 1.4, 1.3, 1.2 and 1.03, respectively for commercial Pt/C, Pt-high-1, Pt-mid-10^{-5}, Pt-high-10^{-2}, Pt-high-10^{-5} and Pt-low-10^{-5}. This can be related to the

existence of smaller Pt nanoparticles in the structure of the electrocatalyst, as previously determined by the TEM images (Figure 5-4), which leads to the presence of more step sites on Pt nanostructures.

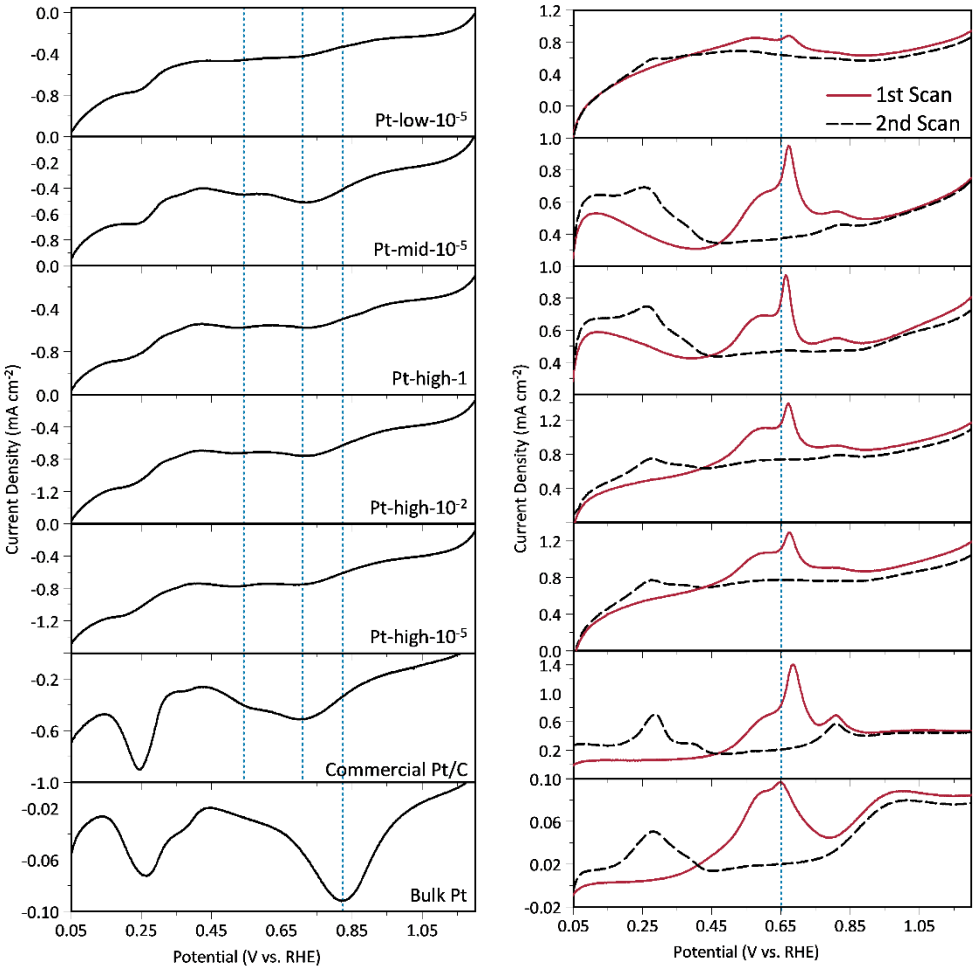

Figure 5-8. (Left panel) Cathodic voltammetric profiles of samples recorded in Ar-saturated 1 M KOH, and (Right panel) first and second cycles of CO stripping voltammograms recorded in 1 M KOH. The voltammograms were recorded at a scan rate of 20 mV s^{-1}.

5.4.2.2 Electrocatalytic Activity for ORR in RDE Setup

The electrocatalytic activity of the Pt/MWCNT/SS electrodes with 3D porous structure and high surface area toward ORR was evaluated in 0.1 M KOH by performing LSV at the scan rate of 20 mV s^{-1} at different rotating-disc-electrode RPMs. Figure S5-13 shows the corresponding LSVs recorded at different RPMs, while the LSVs recorded at 1600 RPM for all electrocatalysts are presented in Figure 5-9(a to c) in terms of current density (per geometric surface area, mA cm-

$^{2}_{geo}$), mass activity (per Pt loading, A mg$^{-1}_{Pt}$), and specific activity (per ECSA of Pt, mA cm$^{-2}_{Pt}$). The ECSA values obtained by CO-stripping were used for the calculation of specific activity to avoid its overestimation [43]. As can be seen in Figure 5-9(a), the ORR on the MWCNT/SS electrode (no Pt) commenced around 0.77 V, followed by a slight gradual increase in the current density, which was to expect since MWCNTs are not electrocatalytically active for ORR. For the commercial Pt/C electrode, the ORR current followed the typical LSV shape, reaching the limiting current density of 5.8 mA cm$^{-2}_{geo}$ at 1600 RPM, which agrees well with values reported in the literature [203-205]. However, all the prepared Pt/MWCNT/SS electrodes exhibited up to three times higher limiting current densities at 1600 RPM, reaching ~21 mA cm$^{-2}_{geo}$ for the Pt-high-1/MWCNT/SS. This is even higher than the theoretical limiting current density of 14 mA cm$^{-2}_{geo}$ calculated from the Levich equation applied to the TF-RDE configuration rotating at a significantly higher RPM (~10,000 RPM) [206]. The limiting currents per Pt loading and per ECSA recorded for Pt/MWCNT/SS electrodes (Figure 5-9(b and c)) are also significantly higher than those for the commercial Pt/C, thus indicating better oxygen mass-transport properties within the structure of the produced electrodes.

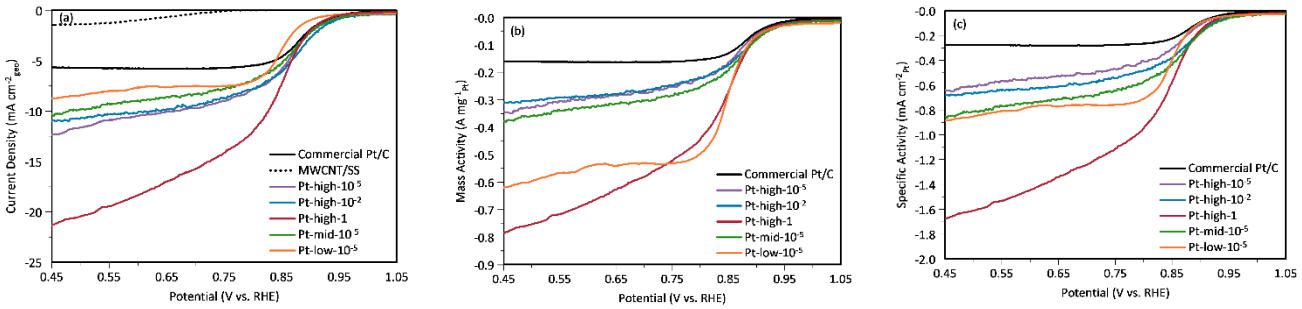

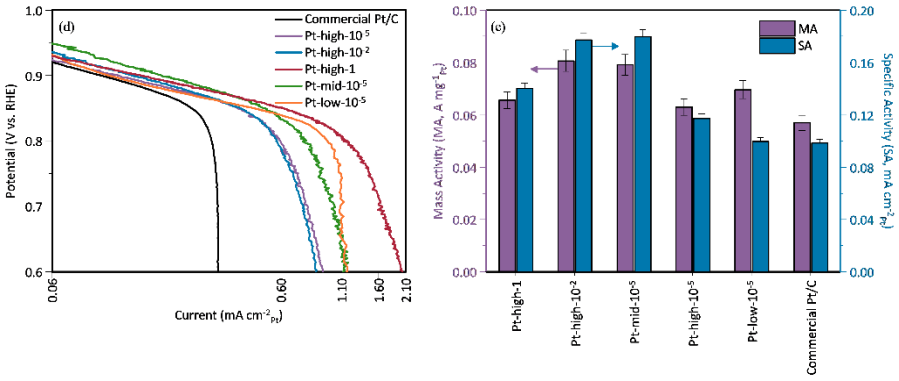

Figure 5-9. Oxygen reduction LSV curves recorded in O^2-saturated 0.1 M KOH at 1600 RPM and scan rate of 20 mV s-1 (a) current density, (b) mass activity, (c) specific activity, (d) comparison of ORR Tafel plots for different electrodes, and (e) mass and specific activity of electrocatalyst at 0.9 V at 2500 RPM.

Figure 5-9(a to c) indicate that the current density region across which the kinetic (electron-transfer) rate is the *rds* is longer on the Pt/MWCNT/SS electrocatalysts than on the commercial Pt/C. To investigate this in more detail, the LSV curves from Figure 5-9(c) are presented in terms of Tafel plots in Figure 5-9(d). Here, the linearity of the curves in the lower current density region evidences that the ORR is under kinetic control. The results clearly illustrate the extension of the kinetic current region for Pt/MWCNTs/SS electrodes in comparison to the commercial Pt/C electrode. The influence of mass transport for the Pt/C commences already at a current density of ~0.4 mA cm^{-2}_{Pt} (point of deviation from the linear region), while for the Pt/MWCNTs/SS electrodes it extends to significantly higher currents, indicating that the Pt/MWCNTs/SS electrodes offer much improved transport of the electroactive species (O_2) to Pt sites versus the commercial Pt/C electrode. A comparison of the electrocatalytic activities of all the electrocatalysts in the kinetic potential region, at the potential of 0.9 V, is presented in Figure 5-9(e). It shows that at 0.9 V, the commercial Pt/C yields mass and specific activity of 57 mA mg^{-1}_{Pt} and 98 μA cm^{-2}_{Pt}, while all Pt/MWCNT/SS yields mass and specific activities above 62 mA mg^{-1}_{Pt} and 100 μA cm^{-2}_{Pt}, reaching the highest ORR currents of 80 mA mg^{-1}_{Pt} and 180 μA cm^{-2}_{Pt} for Pt-high-10^{-2} and Pt-mid-10^{-5}, respectively. The superior mass and specific activity (MA and SA) of the Pt/MWCNT/SS over the commercial Pt/C is evident. Besides the more open (porous) structure of the prepared Pt/MWCNT/SS electrodes, which allows for better utilization of Pt, their superior ORR activity can also be related to the exclusion of Nafion ionomer from their structure, which is not the case with the commercial Pt/C electrode. At lower Pt loadings, the lower active

site density causes higher local O_2 flux, which increases the mass activity of Pt/MWCNT/SS with lower Pt loadings compared to the commercial Pt/C [207]. Kongkanand and Mathias explained that high local O_2 resistance at or near Pt nanoparticles requires higher local O_2 flux to the Pt surface, which results in a poorer voltage performance [208]. This is also in agreement with the observation of Shinozaki et al. who recorded an improvement in the specific activity of Pt/C at 0.9 V when Nafion was excluded from the electrocatalyst layer [204]. However, even by preparing the Nafion-free Pt/C thin-film, the authors still did not reach the ORR limiting current density above ~5.8 mA cm^{-2}_{geo} at 1600 RPM, which is lower than the values recorded on our Pt/MWCNTs/SS electrocatalysts with more open structure at the same RPM (Figure 5-9(a)). The more porous morphology of the Pt-high-1 electrocatalyst, as shown in SEM images (Figure 5-2(c)), can also reduce the local O_2 resistance near Pt nanoparticles, and consequently increase the limiting specific current for this electrocatalyst. It is known that ORR activity of an electrocatalyst (M) is related to the strength of the electrocatalyst-oxygen bond, *i.e.* M-O_{ads}. Thus, a good ORR electrocatalyst should yield an intermediate M-O_{ads} bond strength, to balance the kinetics of the O_2 dissociation/adsorption step and the kinetics of subsequent reaction steps leading to the formation of H_2O (or H_2O_2). As illustrated in Figure 5-7, increasing the background gas pressure and laser energy during PLA result in a negative shift in Pt $4f_{7/2}$ binding energy compared to commercial Pt/C, which can lead to a downshift in the *d*-band center of Pt that weakens the adsorption of oxygen intermediates and make the catalytic active sites accessible to O_2, thus increasing the ORR activity. The ORR activity of the electrocatalysts synthesized in this study seems to follow a volcano-type behavior as illustrated in Figure 5-9(e) (Pt $4f_{7/2}$ binding energy is increasing from left to right on *x* axis). The Pt-low-10^{-5} electrode with the highest positive shift in Pt $4f_{7/2}$ binding energy (Figure 5-7) showed the lowest specific activity (SA) toward ORR at 0.9 V, which can be due to the formation of a strong Pt-O_{ads} bond, resulting in a blockage of Pt active sites. On the other hand, the low ORR activity of Pt-high-1 can originate from the formation of a weak Pt-O_{ads} bond, resulting in a slow kinetics of the surface O_2 molecule dissociation/adsorption [209-211].

To investigate the stability of the produced electrodes, accelerated durability tests (ADT) were undertaken for 2000 cycles and the results are shown in Figure 5-10(a-f). As expected, after the test the onset of ORR of all the samples shifted to higher overpotentials, and the mass transport limiting current shifted to lower values. However, most of the Pt/MWCNT/SS electrodes

demonstrated better electrocatalytic stability compared to the commercial Pt/C. The current density of the commercial Pt/C recorded at 0.9 V decreased by ~ 60%, while Pt/MWCNT/SS electrodes showed current density losses from 1.8% to 58.5%, where Pt-high-1 and Pt-high-10^{-2} showed the smallest and largest change in ORR current density at 0.9 V, respectively. The loss of ECSA after ADT tests are also presented in the insets, which ranges from 7.9% for Pt-low-10^{-5} to 21.8% for Pt/C. The ECSA loss of 4% to 34% and 20% to 31% were reported by J. Schröder et al. and B. Ergul-Yilmaz for Pt/C after long-term stability test, which they linked to all the degradation mechanisms of Pt nanoparticles including migration/coalescence, Pt dissolution/detachment and Ostwald ripening [212, 213]. It is noteworthy to mention that it is difficult to compare the stability results in Figure 5-10 to the literature since there is no common ADT protocol to follow and the potential window, scan rate and the number of cycles differ from one study to another. High-angle annular dark-field (HAADF) and SEM images of the Pt/MWCNT/SS samples (Figure 5-10(g-p)) taken after the ADT depict the stability of Pt nanostructures on MWCNT. No obvious or severe detachment/dissolution of Pt nanoparticles can be seen in the HAADF and SEM images. Because of the strong adhesion of the Pt nanostructures to the MWCNT support, which results from the high deposition kinetic energy of nanoparticles during PLA, only some minor aggregation and/or detachment of Pt nanoparticles from the surface of MWCNTs is evident.

The XPS analysis of the electrocatalysts was carried out after 2000 cycles of ADT to assess the compositional stability of the samples. The C 1s, O 1s and Pt 4f spectra recorded before and after ADT are presented in Figure S5-14. The surface analysis revealed that after ADT, the atomic percentage of Pt on the surface decreased by about 3% for Pt-low-10^{-5} to 12% for Pt-high-1. There seems to be a small negative shift in all Pt 4f peaks compared to as-synthesized samples, which can be attributed to the increase of Pt nanoparticle size due to Ostwald ripening/coalescence [185, 186].

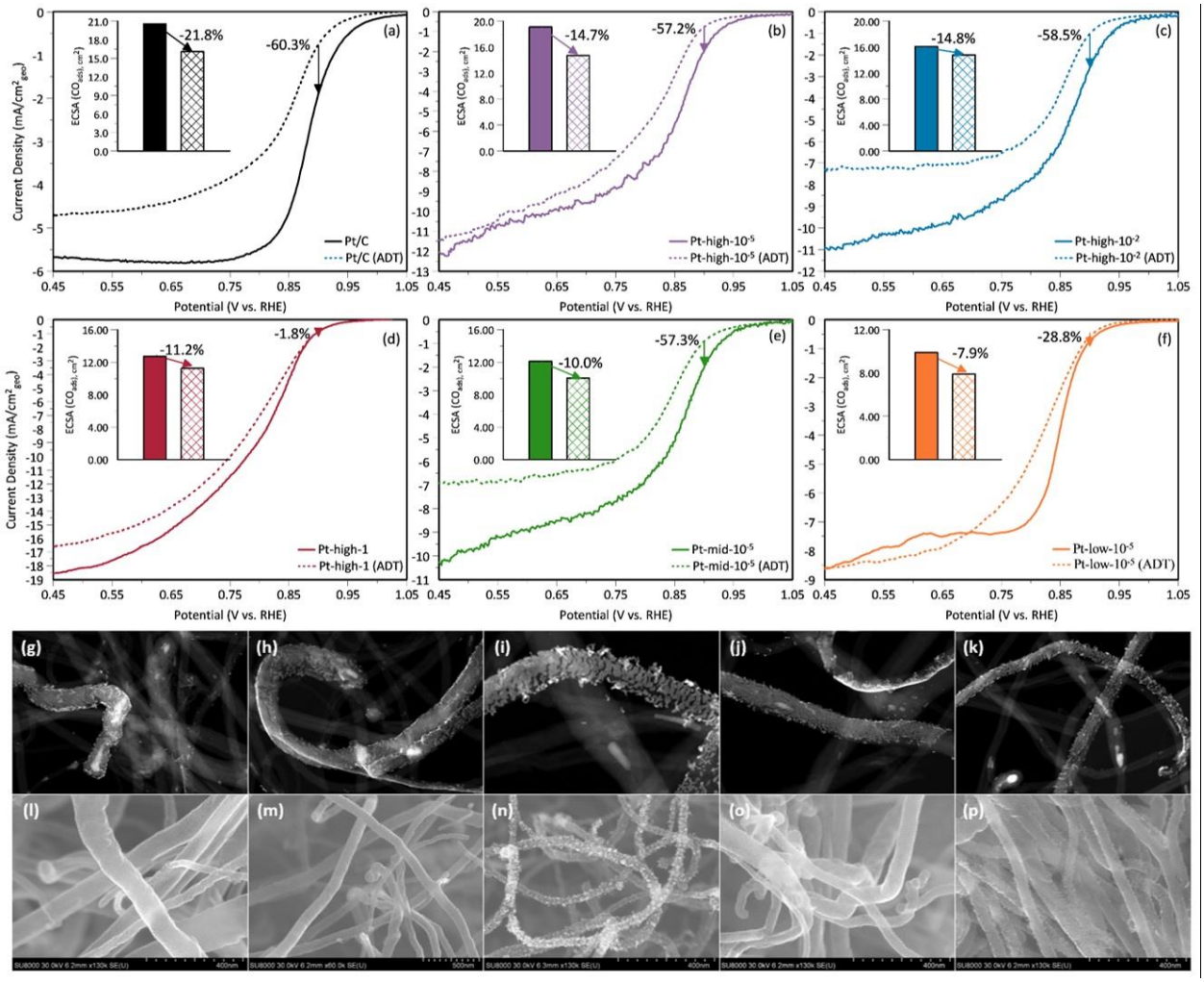

Figure 5-10. LSV of electrodes recorded in O_2-saturated 0.1 M KOH at the rotation speed of 1600 rpm and scan rate of 20 mV s^{-1} before and after 2000 cycles of ADT (a-d). HAADF and SEM images of electrocatalysts after ADT; (e, j) Pt-high-10^{-5}, (f, k) Pt-high-10^{-2}, (g, l) Pt-high-1, (h, m) Pt-mid-10^{-5}, and (I, n) Pt-low-10^{-5}. The insets show the loss of ECSA after ADT.

5.4.2.3 Electrocatalytic Activity for ORR in GDE Setup

Evaluation of the electrocatalytic activity of the 3D porous Pt/MWCNT/SS electrodes for ORR in the RDE setup demonstrated their higher electrocatalytic activity in both the kinetic and mass-transport overpotential regions (Figure 5-9(c)) in comparison with the Pt/C thin-film RDE configuration. However, it is a known fact that the TF-RDE methodology yields poor oxygen mass transport to Pt sites, thus limiting the reliable evaluation of the actual Pt/C performance to the kinetically-controlled region, *i.e.* to low overpotentials and current densities. This could be addressed by evaluating the performance of electrocatalysts in a real fuel-cell configuration that

employs a membrane electrode assembly (MEA), where the ORR activity is measured at much higher overpotentials, (0.6 to 0.7 V vs. RHE) [199]. However, this is a time-consuming process, which requires larger amounts of electrocatalyst and a complex and expensive equipment. In addition, a number of fuel-cell operating conditions affect the performance of the MEA [203, 214-216]. Therefore, the flexible Pt/MWCNT/SS electrodes, with the overall thickness of approximately 180 μm and a Pt coverage on MWCNTs that extends to the depth of ~8 μm (see EDS line scan in Figure 5-3), were successfully tested as GDEs in the custom-made setup presented in Figure 5-11(a), and the results are shown in Figure 5-11(b-d).

Although, the commercial Pt/C GDE yielded the highest current density Figure 5-11(b), it is evident that the current density is influenced by a significant contribution (~40%) of the carbon-paper backing, which is not the case with Pt/MWCNT/SS electrodes since the contribution of MWCNT/SS to the ORR is minor. The results on mass and specific activities illustrate that Pt-low-10^{-5} GDE yielded higher currents than those recorded on the commercial Pt/C GDL, followed by the Pt-mid-10^{-2} GDE.

As explained, the activity of an electrocatalyst in a GDE setup can be assessed at high overpotentials (0.6 - 0.7 V), which represents the performance of a real fuel cell when high power densities are delivered. Many studies have shown that the evaluation of an electrocatalyst under these conditions invalidates findings on electrocatalytic activity enhancement seen in a RDE setup at low overpotentials, and that designing a low-loading electrocatalyst with high electrochemically-active surface area should be prioritized over improving their intrinsic properties, *i.e.* electronic structure [43]. Similar conclusions can be obtained by comparing the GDE performance presented in Figure 5-11(d) to that one of the RDE presented in Figure 5-9(e). Thus, although the Pt-low-10^{-5} electrocatalyst, characterized by the lowest Pt loading of 14.2 μg cm^{-2} and the highest ECSA of 69.9 $m^2\ g^{-1}_{Pt}$, yielded the lowest specific activity in RDE measurements at 0.9 V (Figure 5-9(e)), it outperformed the commercial Pt/C GDE with a higher Pt loading of 35.6 μg cm^{-2} and ECSA of 57.9 $m^2\ g^{-1}_{Pt}$ in the GDE configuration at high overpotentials (Figure 5-11(d)).

To complement the results presented in Figure 5-11, EIS Nyquist plots expressed as impedance per electrochemical active surface area (ESCA) of Pt recorded at a potential of 0.8 V are shown in Figure S5-15. The spectra are characterized by the appearance of a semi-circle and an inductive loop. The inductive loop has been reported to appear due to the relaxation of the adsorbed species

on the surface of Pt such as Pt-OH_{ads}, Pt-OOH_{ads} and PtO_{ads} [217, 218], while the negative-impedance semi-circle can be related to the kinetics of the ORR and double-layer charging. Thus, the diameter of this semicircle can be taken to represent the ORR polarization resistance. It can be seen that the polarization resistance trend is opposite to that of the ORR *dc* current in Figure 5-11(d), and taking into account the Ohm law, the two trend are, thus, similar. The Nyquist plot for the commercial Pt/C on GDL reveals the existence of two capacitive and one inductive loops. The high-frequency semi-circle is attributed to the charge-transfer process through double layer capacitor, and the low-frequency loop is related to the diffusion of oxygen through the carbon backing or diffusion of water in the catalyst layer [217, 218]. This also confirms the existence of better oxygen mass transport in the developed Pt/MWCNT/SS GDEs compared to the commercial Pt/C.

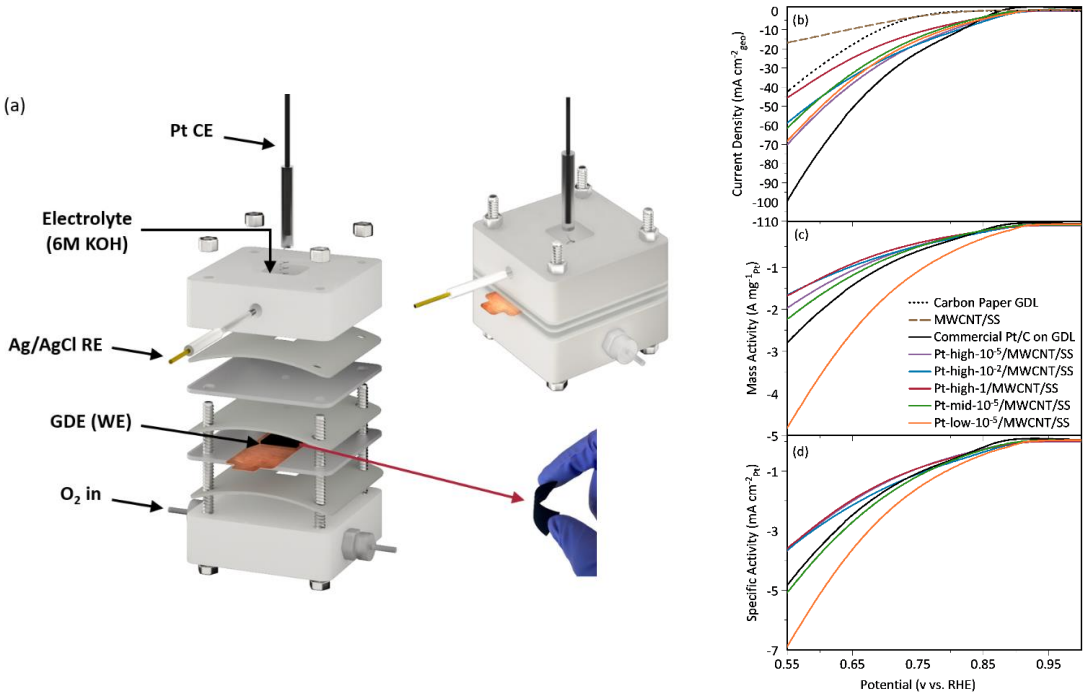

Figure 5-11. (a) Sketch of the in-house GDE cell setup, and oxygen reduction LSV curves recorded in O_2-saturated 6 M KOH at the scan rate of 20 mV s^{-1} in GDE setup (b) per geometric surface area (current density), (c) mass of Pt (mass activity), and (d) ECSA (specific activity).

In Table S5-3, the electrocatalytic activity of our electrocatalysts tested in both RDE and GDE setups are compared to some of the recent studies reporting the use of supported Pt for ORR at a potential of 0.9 V. Considering the experimental conditions, especially the temperature, it can be

concluded that the results obtained in this study are at the high end of the published results for ORR specific activity at 0.9 V.

5.5 Conclusion

In an effort to design a Pt-based electrocatalyst with low loading, high Pt utilization and mass activity for the oxygen reduction reaction in an alkaline environment, various Pt nanoparticle thin films were produced using a pulsed laser ablation technique. Dense MWCNT forests directly grown on stainless steel meshes were used as support material for the deposition of Pt nanostructures. It was demonstrated that the morphology, particle size distribution and mass of Pt nanostructures deposited on the MWCNTs can be controlled by changing the PLA chamber pressure and laser pulse energy. SEM and TEM images illustrated that the Pt nanoclusters/adatoms formed a dense film containing Pt nanoparticles of 2.0 ± 0.2 nm at low pressure, while a porous film containing agglomerates of Pt nanoparticles of 2.8 ± 0.8 nm was formed at high pressure. Lowering the laser pulse energy led to the synthesis and deposition of smaller Pt nanoparticles on the MWCNT surface. All Pt/MWCNT/SS showed a positive shift in the Pt $4f_{7/2}$ binding energies in comparison to bulk Pt, the extent of which was linked to the size of Pt nanoparticles on the MWCNTs; the smaller the nanoparticles, the more positive the shift. This correlation explained the observed electrochemical results of a positive shift in the oxidation potential of a CO monolayer adsorbed on Pt. The electrocatalytic activity of the 3D porous Pt/MWCNT/SS electrodes was directly tested in a rotating disk electrode setup and they all showed an extended kinetic current region and higher ORR current per electrochemically active surface area of Pt at 0.9 V, while being stable after 2000 cycles of ADT. It was found that a balance between the kinetics of O−O bond breaking and the electroreduction of the oxygenated intermediates should exist on the surface of Pt electrocatalyst. When tested in a gas diffusion electrode setup, the Pt-low-10^{-5}/MWCNT/SS GDE with lower Pt loading of 14.2 μg cm^{-2} and the highest ECSA of ~70 $m^2\ g^{-1}_{Pt}$ performed better compared to the commercial Pt/C GDE with Pt loading of 35.6 μg cm^{-2} and the ECSA of ~58 $m^2\ g^{-1}_{Pt}$. The results obtained in the GDE setup demonstrated the true electrocatalytic activity of the synthesized Pt nanostructures for ORR with minimum contribution from the support, unlike many studies reporting the Pt/C electrocatalytic activity without stating the activity of the carbon support used.

Conflicts of interest

There are no conflicts to declare.

Acknowledgments

The authors wish to acknowledge the financial support of the Faculty of Engineering through the McGill Engineering Doctoral Award (MEDA), the Natural Sciences and Engineering Research Council of Canada (NSERC), the Gerald Hatch Faculty Fellowship, and the Fonds de recherche du Québec – Nature et technologies (FRQNT). The authors thank the technical staff from the Department of Chemical Engineering of McGill University for their assistance. The authors acknowledge Dr. Boris Nijikovsky for the operation of TEM. The authors sincerely thank Dr. Larissa Jorge for her collaboration in upgrading the PLA setup.

5.6 Supporting Information

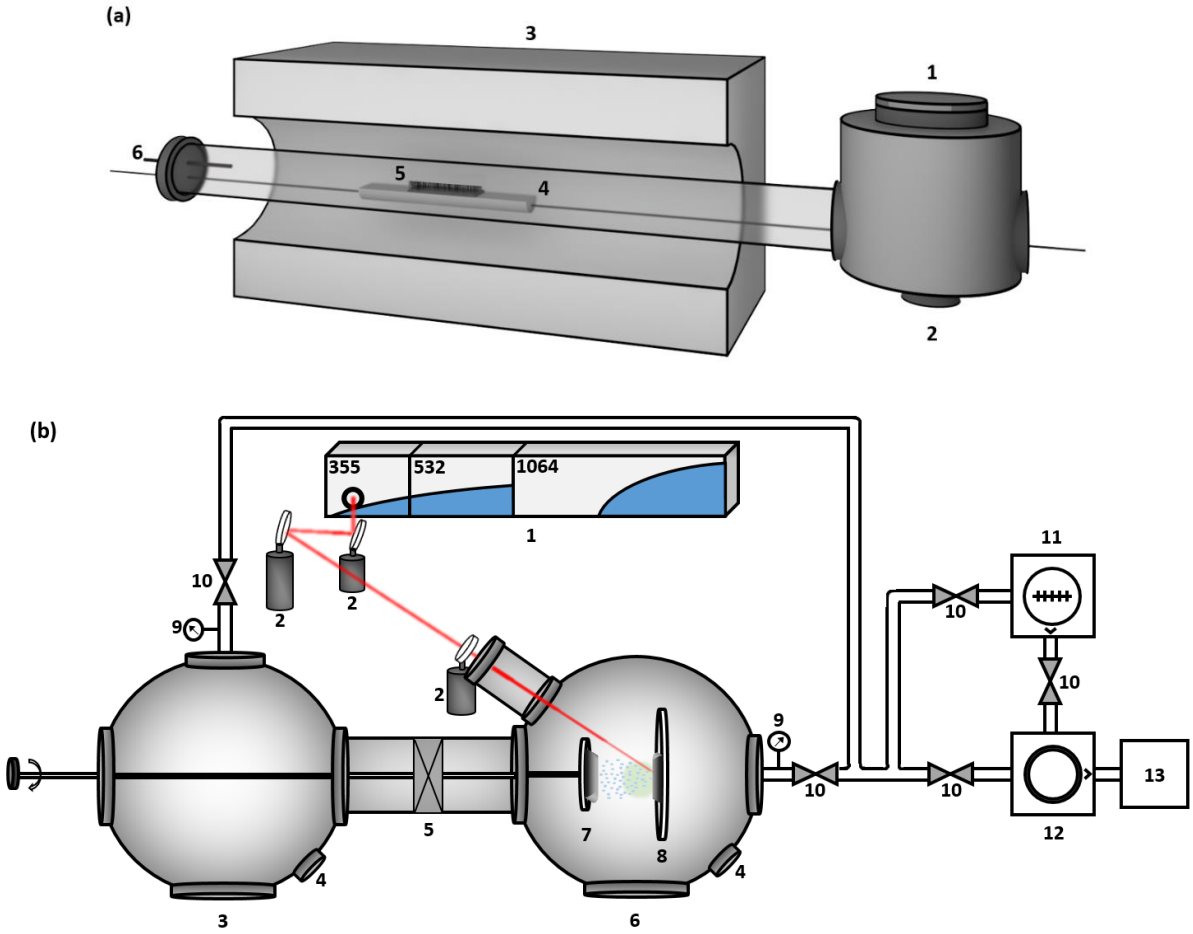

Figure S5-1. Schematic view of the CVD setup: 1) loading chamber, 2) gas exhaust, 3) furnace, 4) quartz boat, 5) MWCNTs on SS, and 6) gas inlet; schematic view of pulsed laser ablation setup: 1) Nd:YAG laser, 2) mirrors and lenses, 3) loading chamber, 4) gas inlets, 5) pneumatic gate valve, 6) ablation chamber, 7) substrate holder, 8) target holder, 9) pressure gauges, 10) pneumatic valves, 11) turbomolecular pump, 12) primary mechanical pump, and 13) exhaust.

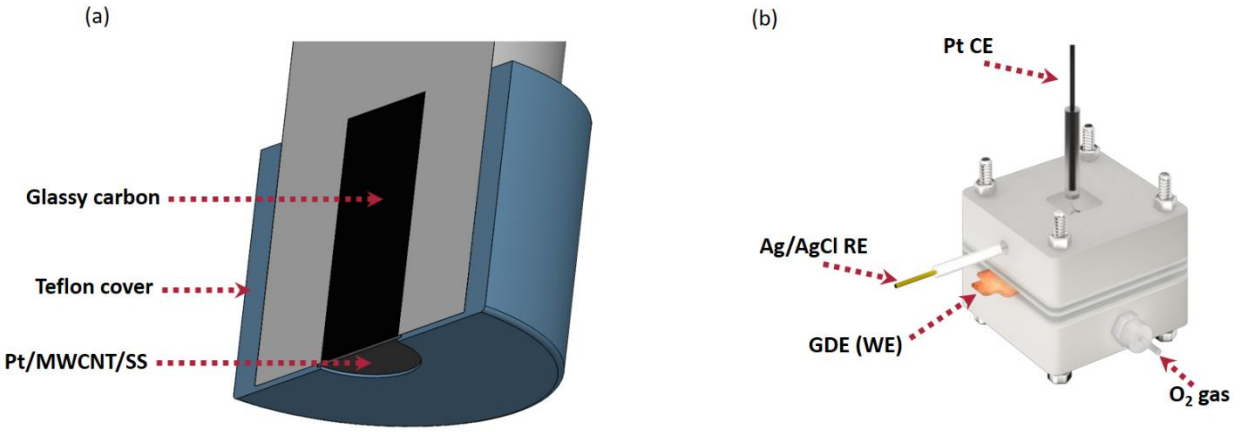

Figure S5-2. (a) Schematic view of RDE setup for ORR evaluation of Pt/MWCNT/SS electrodes. The diameter of the Pt/MWCNT/SS electrode exposed to the electrolyte is 5 mm. (b) GDE setup.

5.6.1 Commercial Pt/C Catalyst Preparation

The commercial Pt/C catalyst was prepared at Pt loading of 35.6 μg cm^{-2}. In this regard, 25.6 mg of 20% *wt* Pt/C catalyst (Sigma-Aldrich, see SEM image in Figure S5-3) was mixed with isopropyl (2 mL) and DI water (8 mL) and sonicated for 15 min. Nafion(R) 117 solution (0.2 mL) purchased from Sigma-Aldrich was added to the mixture while the sonication continued for another 15 min. For the RDE configuration, 13.9 μL of the prepared ink was dropped on a 5-mm diameter glassy carbon (GC) rotating disk electrode. Argon was injected at low flow rate to dry the ink droplet on the surface of GC RDE. For experiments that employed the gas diffusion electrode configuration (Figure 5-11(a)), the working electrode was prepared by dropping 5 μL of the prepared ink onto the gas diffusion layer cabron-paper backing (GDL-Toray carbon paper with 20% wet proofing and a micro-porous layer, TGP 090 20%, MPL, Fuel Cell Store), while the paper was heated on a hot plate (150 °C) and purged with Ar. The carbon paper was covered with a PTFE mask to assure the formation of a circular Pt/C electrocatalyst layer with the diameter of 3 mm.

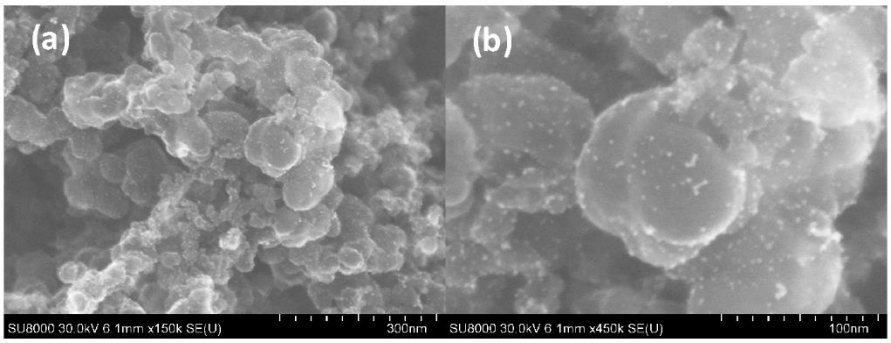

Figure S5-3. SEM images of commercial 20% wt Pt/C catalyst at (a) low and (b) high magnifications.

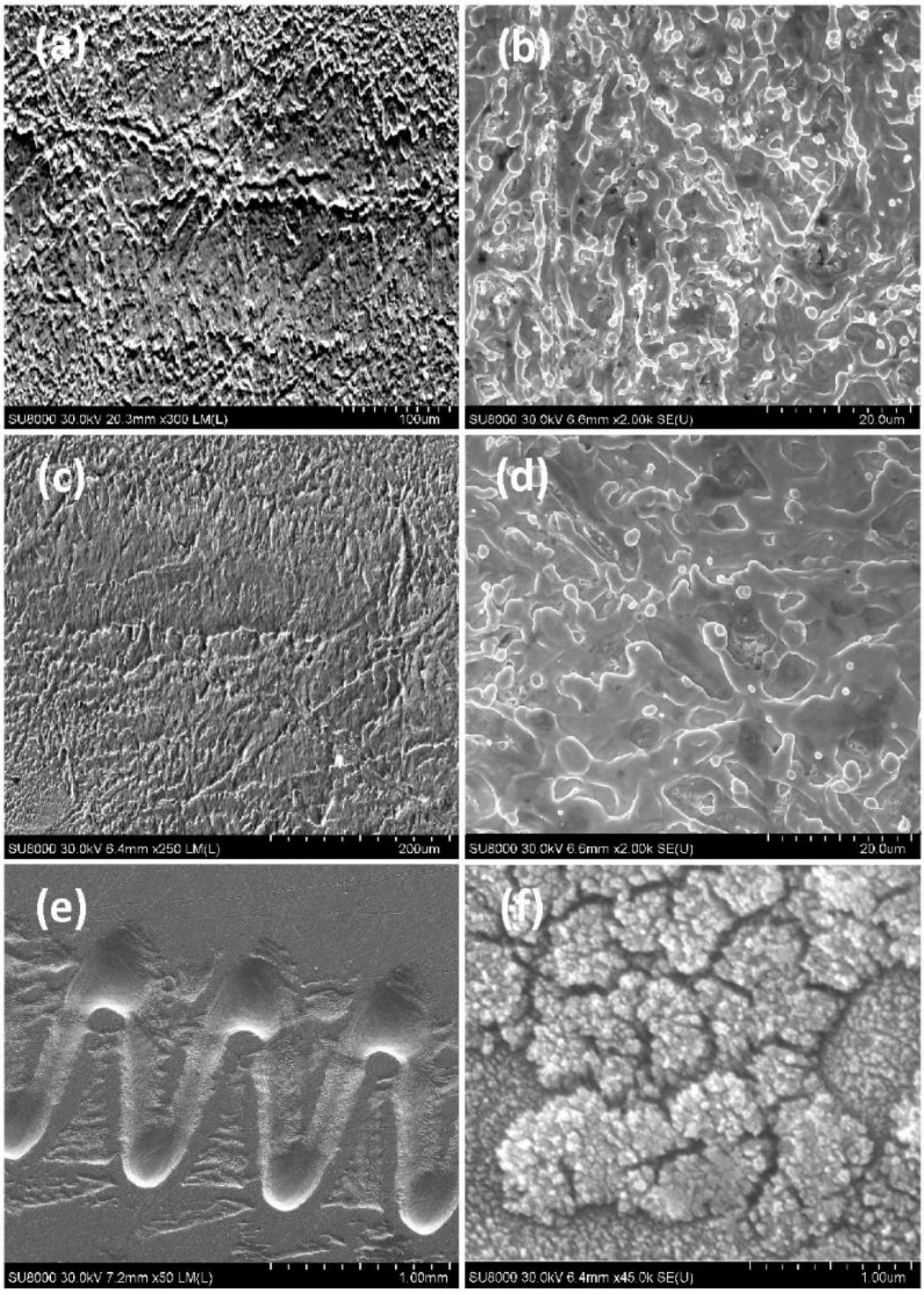

Figure S5-4. SEM images of Pt target at (a, b) 1 Torr, (c, d) 10^{-5} Torr; (e, f) laser pattern on the target and re-solidified Pt on the surface.

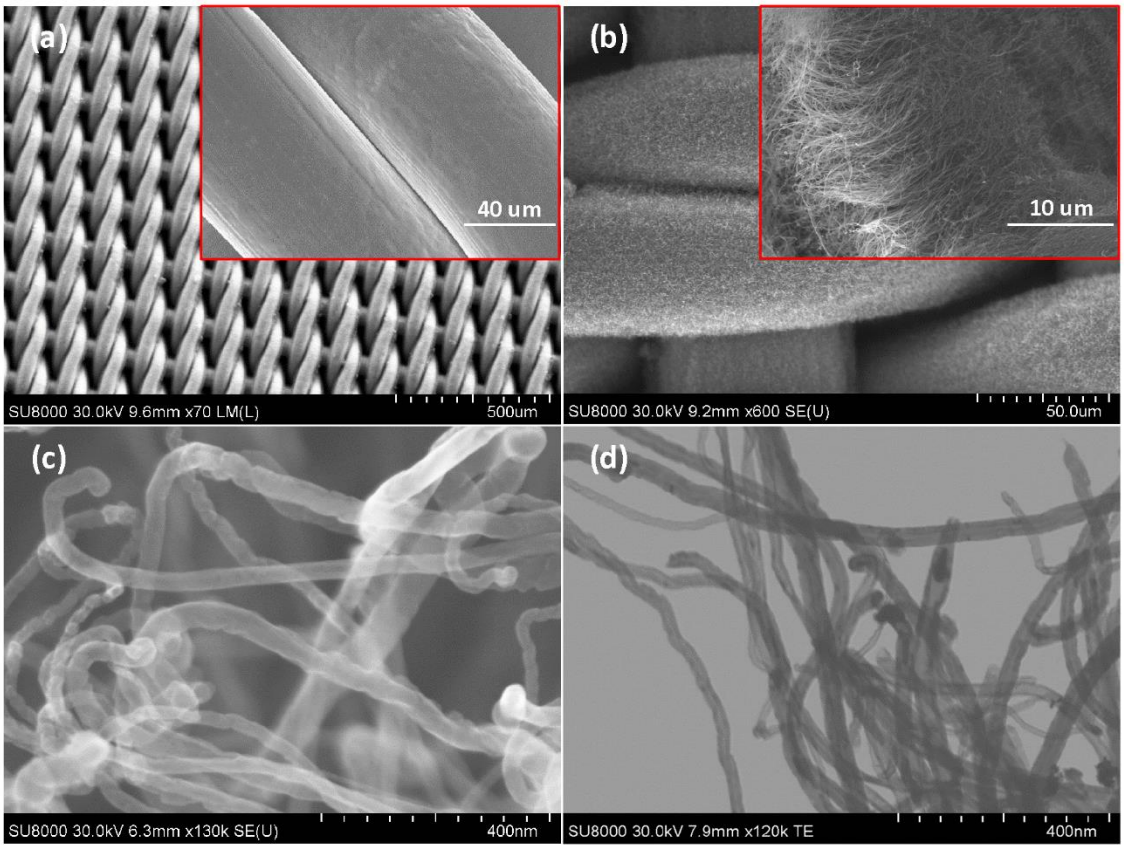

Figure S5-5. SEM images of (a) SS mesh, (b and c) MWCNTs directly grown on SS mesh, and (d) STEM image of MWCNTs.

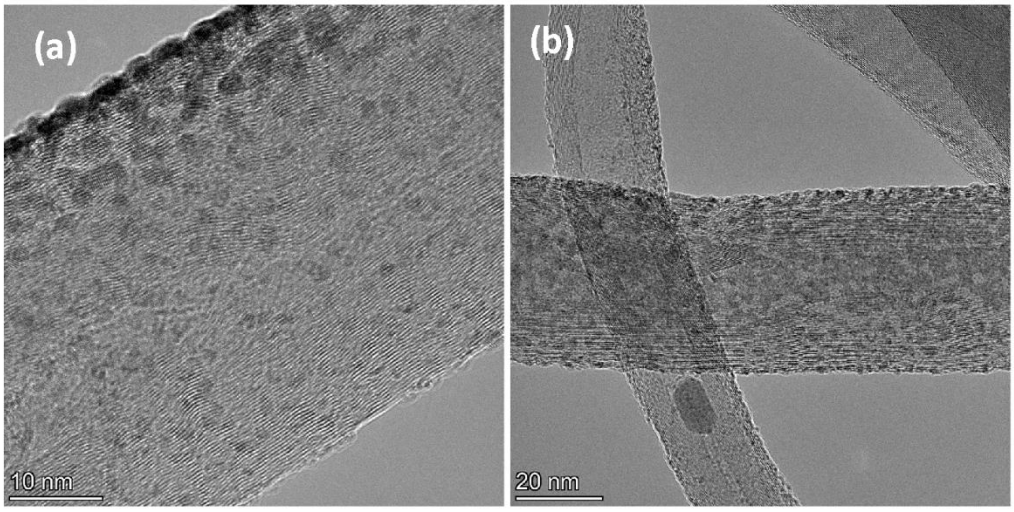

Figure S5-6. High resolution TEM images of (a) Pt-mid-10^{-5}, and (b) Pt-low-10^{-5} showing the deposition of extremely small Pt nanoparticles.

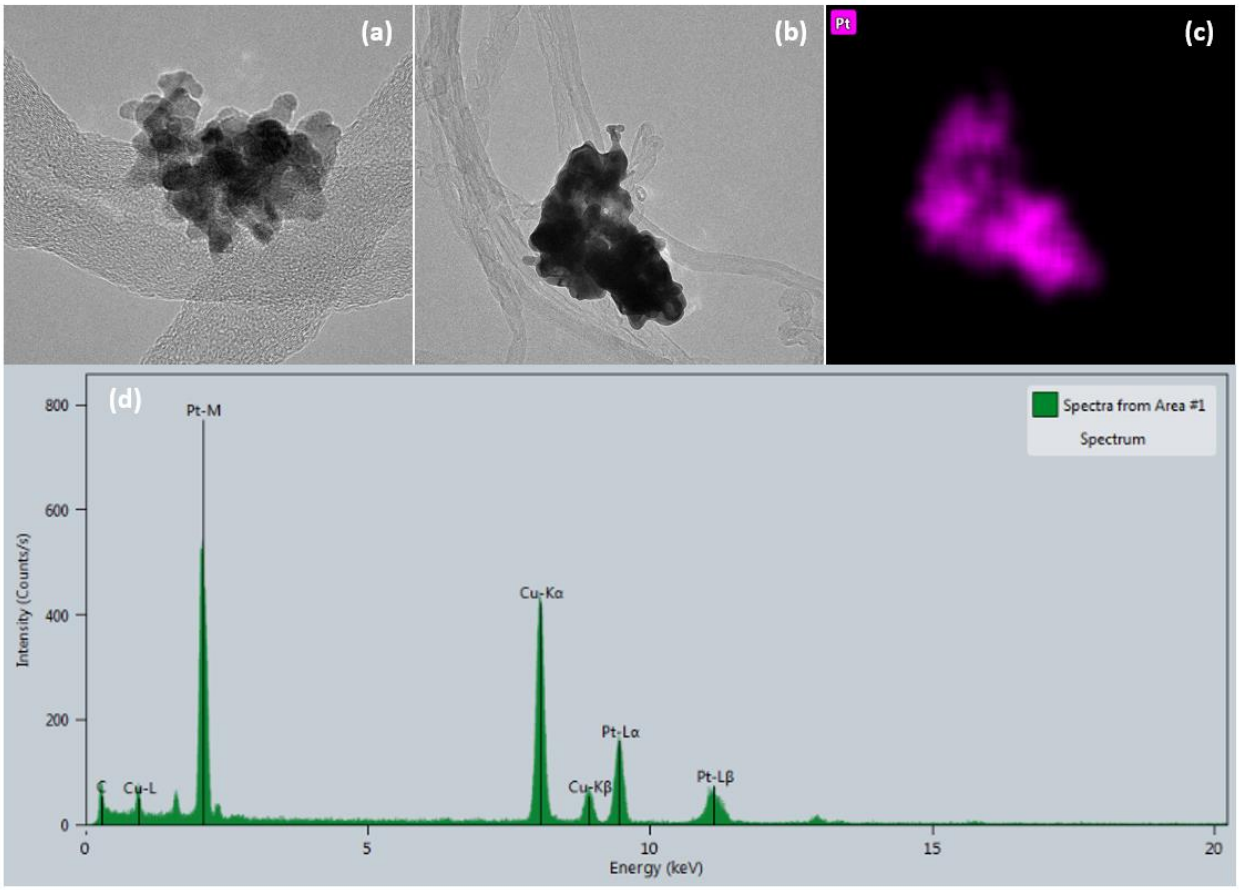

Figure S5-7. High resolution TEM images of (a and b) Pt-high-10, (c) Pt mapping of image (b), and (d) EDS analysis of image (b).

It appears that the sonication step in sample preparation for TEM imaging resulted in the detachment of loosely attached Pt nanoparticles from the MWCNTs and their agglomeration as shown in Figure S5-7.

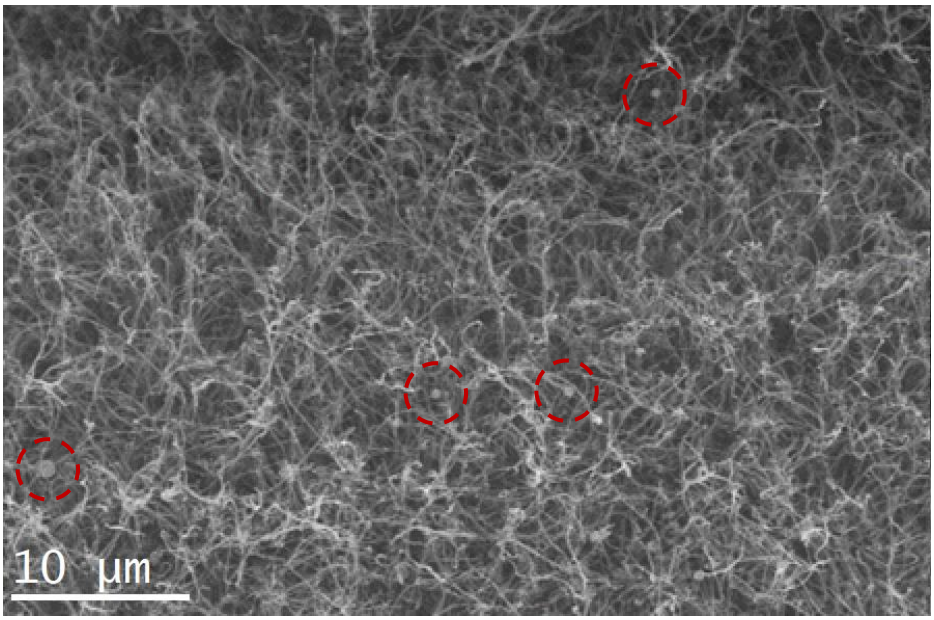

Figure S5-8. SEM image of MWCNT/SS at lo w magnification revealing large Pt particles.

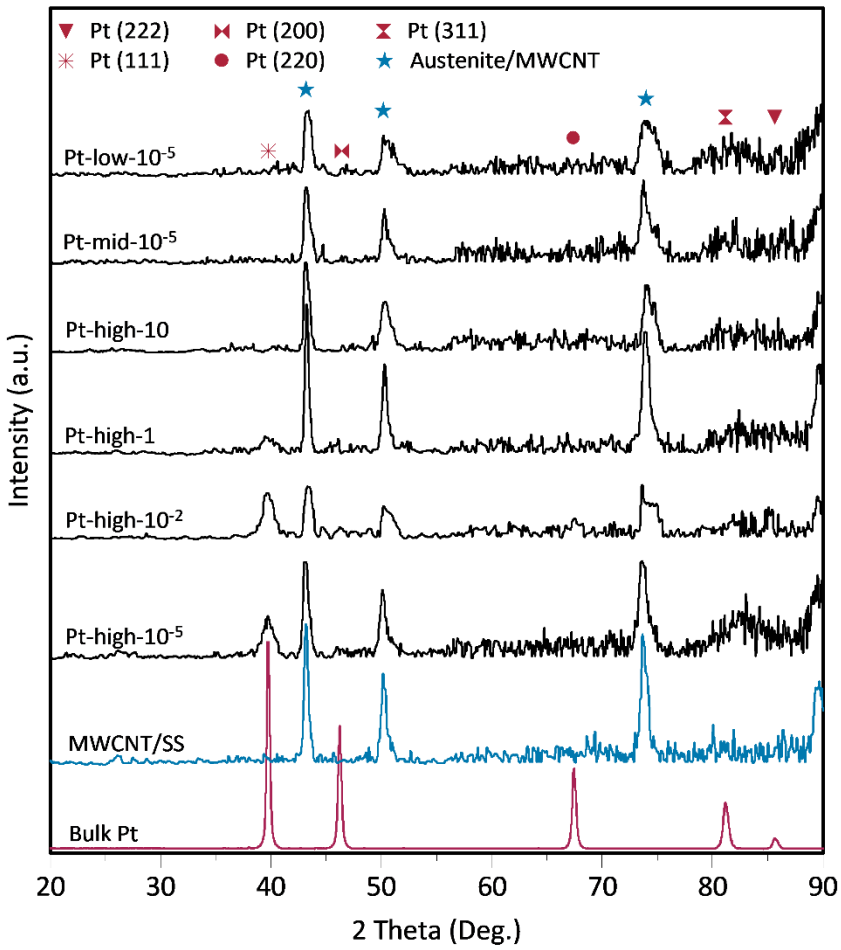

Figure S5-9. XRD patterns of MWCNT/SS before and after Pt nanostructures deposition at different background gas pressures and laser pulse energies.

5.6.2 Defect Level of MWCNTs after Pt loading

Raman spectroscopy was used to investigate the integrity of MWCNTs after Pt deposition by associating the Raman peaks to the vibrational modes of carbon nanotubes. The Raman spectra in Figure S5-10 display the typical D, G and 2D bands at ~1349, ~1640 and ~2696 cm^{-1}, respectively. All the spectra were normalized with respect to the D band and were background-corrected. Lattice mismatch of the graphitic layer, substitutional hetero-atoms, vacancies, and grain boundaries are sp^3 carbon-related defects activating the D-band, while the graphene sp^2 carbon is represented by the G-band. In other words, the G (in-plane vibration) and D (out-of-plane vibration) bands respectively express the "order" and "disorder" in the MWCNT. The 2D band represents the long-range order in a sample. Typically, the decoration of MWCNTs by metal nanoparticles via wet chemistry requires the use of harsh experimental conditions damaging the MWCNT structure, which leads to higher R values (I_D/I_G). In Figure S5-10, the MWCNTs exhibit similar spectral patterns prior to and after the deposition of Pt nanostructures, and there are no significant Raman spectrum changes resulting from various PLA conditions. The low R value (0.52) shows the high quality of the MWCNTs synthesized in this study [137, 138]. Moreover, it can be seen in Figure S5-11 that I_D and I_G both decreased after the deposition of Pt on the MWCNTs, but the ratio I_D/I_G remained almost constant, indicating no damage to the MWCNTs. It is possible that the Pt nanoparticles saturate the defect sites or vacancies of the MWCNTs, which can lower the intensity of the D band, thus indicating a lower level of defects on the MWCNTs. Since a small degree of D band broadening and higher valley lines between D and G bands were present upon the deposition of Pt nanostructures, the area under each peak was also measured and the calculated R′ values (A_D/A_G) are reported in Table S5-1. There is a slight increase in R′ after Pt deposition, which is increasing with Pt particle size. This has been reported previously and has been ascribed to an increased surface roughness, broken hexagonal symmetry of the MWCNT, and lattice vibrational mode of the MWCNT due to the strain resulting from the existence of Pt nanoparticles [139-142, 219-221].

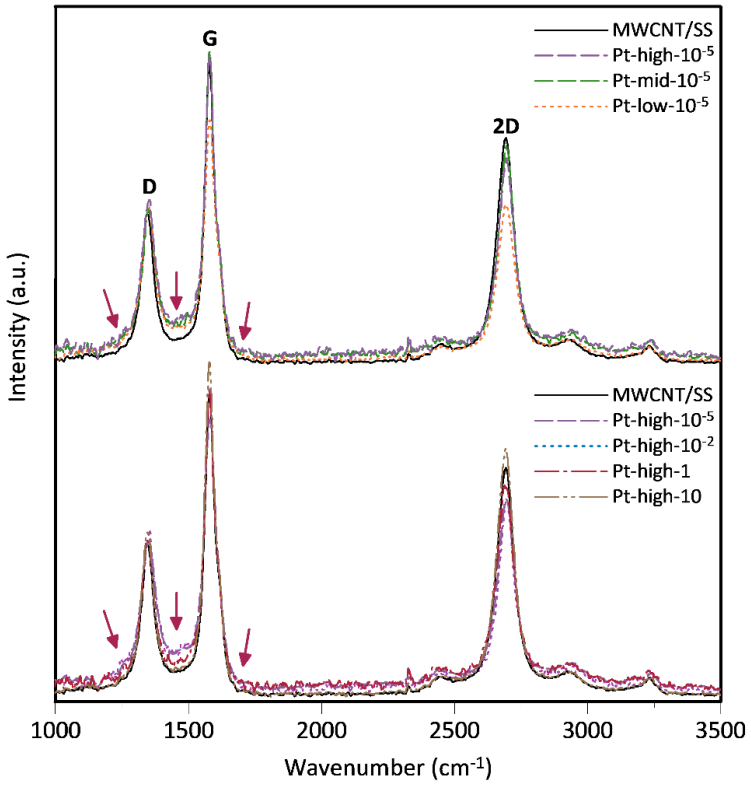

Figure S5-10. Raman spectra of MWCNT/SS before and after the deposition of Pt nanostructures.

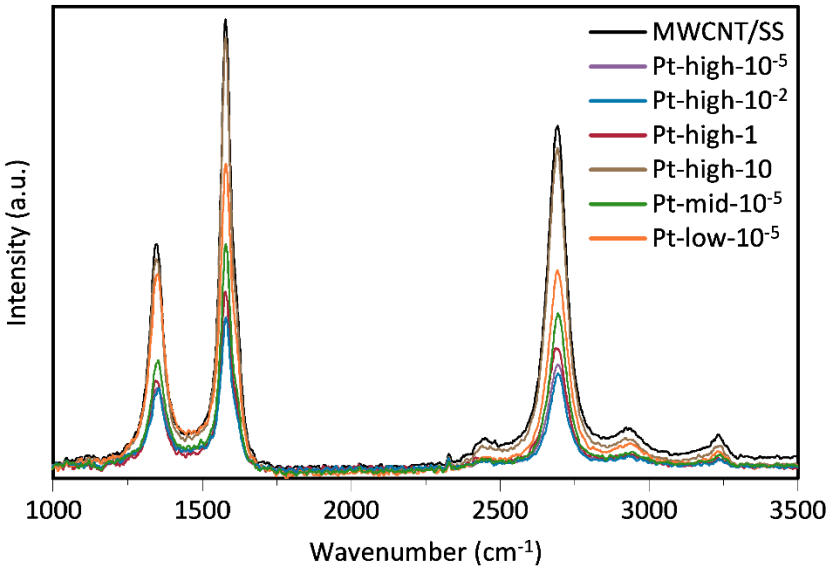

Figure S5-11. Raman spectra (non-normalized) of MWCNT/SS before and after deposition of Pt nanostructures.

Table S5-1. Peak intensities, areas and ratios in Raman spectra (normalized with respect to I_D)

Sample	I_G	I_{2D}	A_D	A_G	A_{2D}	I_D/I_G	A_D/A_G
MWCNT	1.94	1.44	48.94	98.11	111.37	0.52	0.50
Pt-high-10^{-5}	1.99	1.33	51.37	101.35	88.23	0.50	0.51
Pt-high-10^{-2}	2.12	1.31	59.21	105.03	90.19	0.47	0.56
Pt-high-1	1.96	1.32	46.31	89.14	98.28	0.51	0.52
Pt-high-10	2.11	1.55	53.53	108.55	122.95	0.47	0.49
Pt-mid-10^{-5}	2.02	1.38	50.57	95.77	99.80	0.49	0.53
Pt-low-10^{-5}	1.58	1.03	52.44	81.44	78.78	0.63	0.64

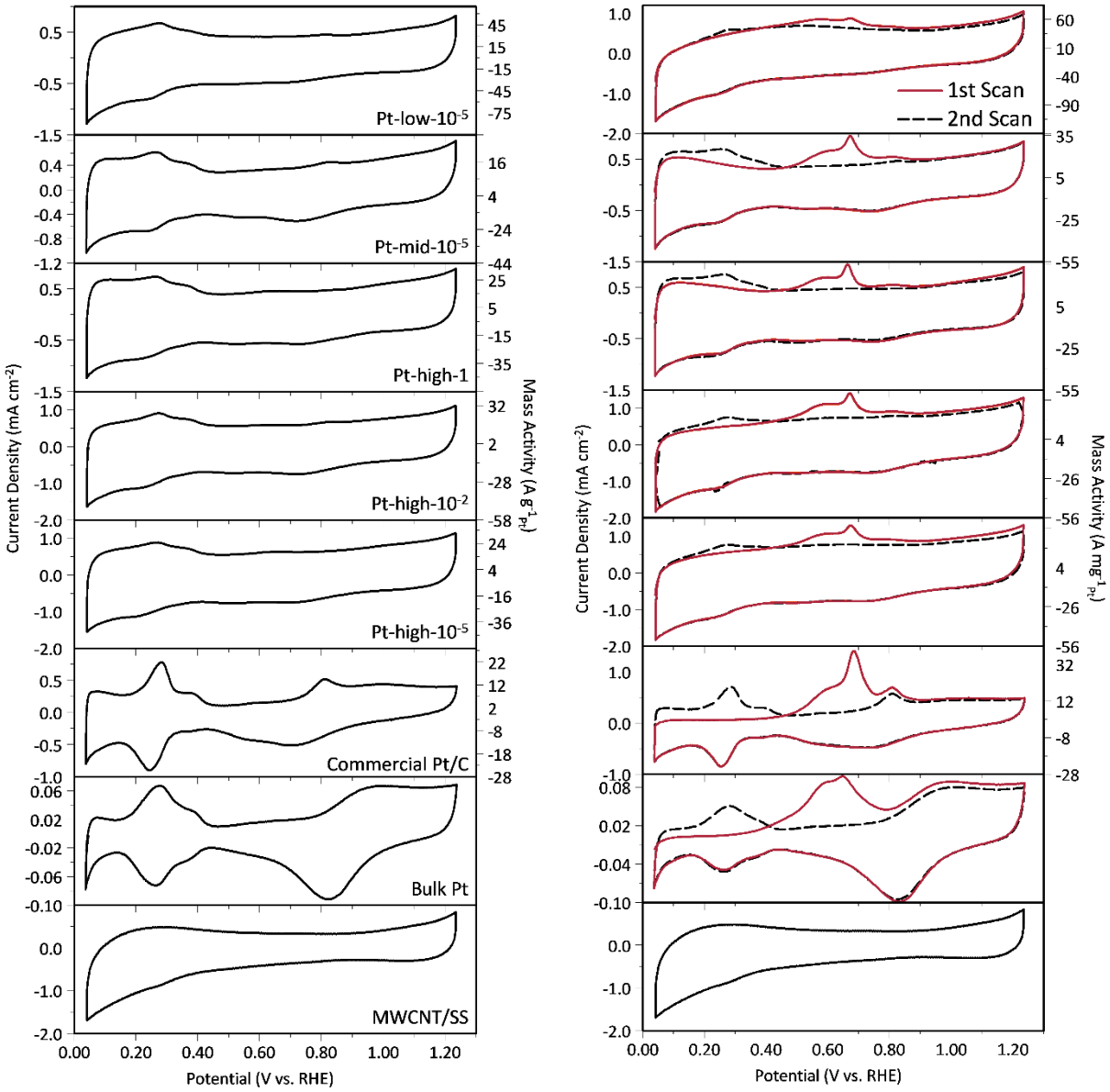

Figure S5-12. (Left panel) Cyclic voltammograms of samples recorded in Ar-saturated 1M KOH, and (Right panel) CO stripping voltammograms recorded in 1M KOH after formation of a CO monolayer on the Pt surface and the removal of dissolved CO from the electrolyte. The voltammograms were recorded at a scan rate of 20 mV s^{-1}.

Table S5-2. ECSA of Pt calculated from H_{ads} and CO_{ads} charges. Values are normalized with respect to 1 cm^2 of geometric surface area of electrodes

Sample	ECSA(H_{ads})		ECSA(CO_{ads})	
	(cm^2)	($m^2\ g^{-1}$)	(cm^2)	($m^2\ g^{-1}$)
Bulk Pt	2.0 ± 0.1	—	2.8 ± 0.2	—
Commercial Pt/C	17.7 ± 0.6	49.9 ± 1.6	20.6 ± 0.1	57.9 ± 0.3
Pt-high-10^{-5}	18.6 ± 0.1	52.4 ± 0.3	19.1 ± 0.1	53.7 ± 0.3
Pt-high-10^{-2}	14.3 ± 0.8	40.5 ± 2.3	16.1 ± 0.3	45.4 ± 0.7
Pt-high-1	12.5 ± 0.4	46.0 ± 1.4	12.7 ± 0.2	46.7 ± 0.5
Pt-mid-10^{-5}	12.5 ± 0.4	45.4 ± 1.5	12.1 ± 0.1	44.0 ± 0.2
Pt-low-10^{-5}	9.6 ± 0.3	67.5 ± 2.3	9.9 ± 0.2	69.9 ± 1.3

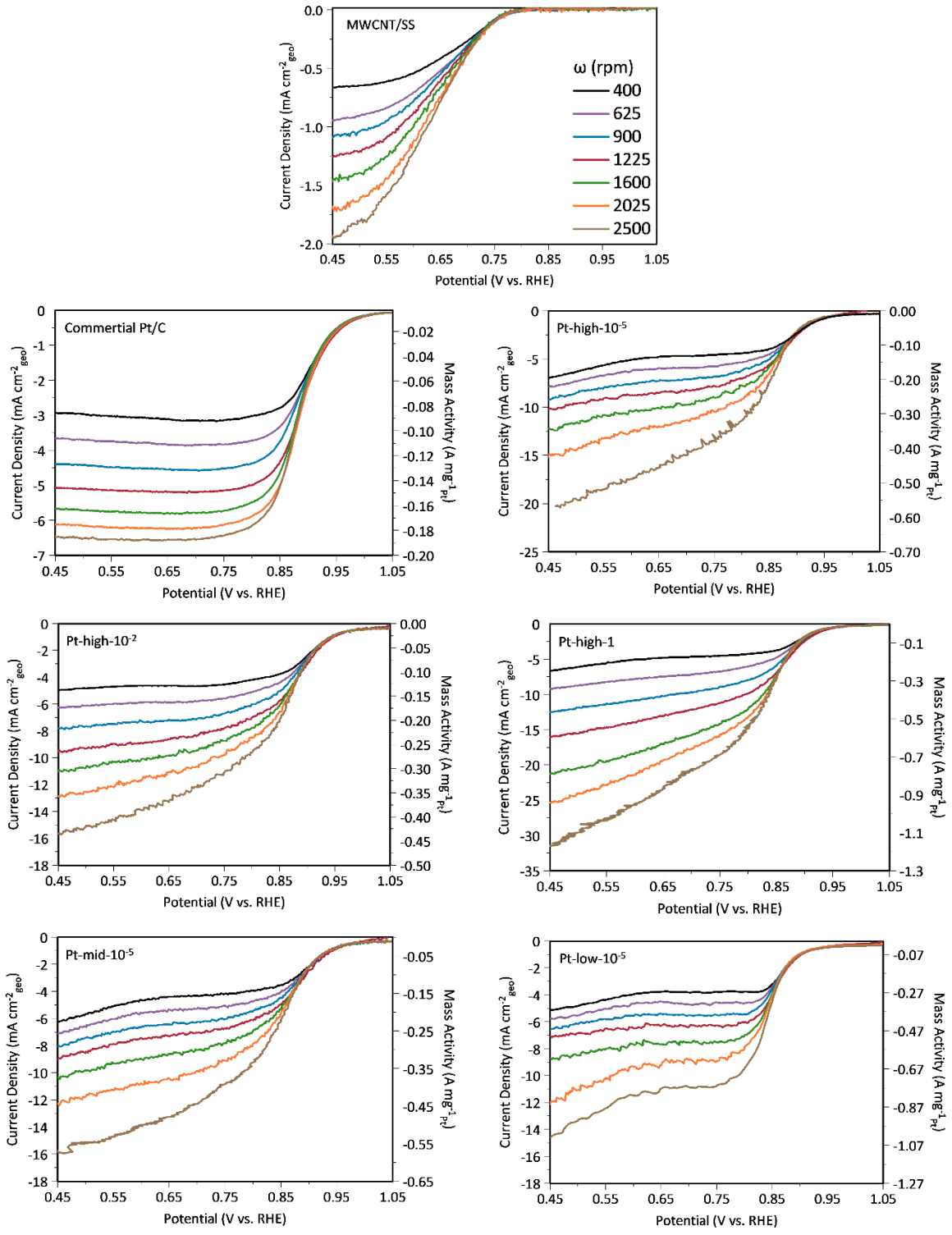

Figure S5-13. LSV curves of electrocatalysts recorded in O_2-saturated 0.1M KOH at a scan rate of 20 mV s^{-1} at different RDE rotation RPMs.

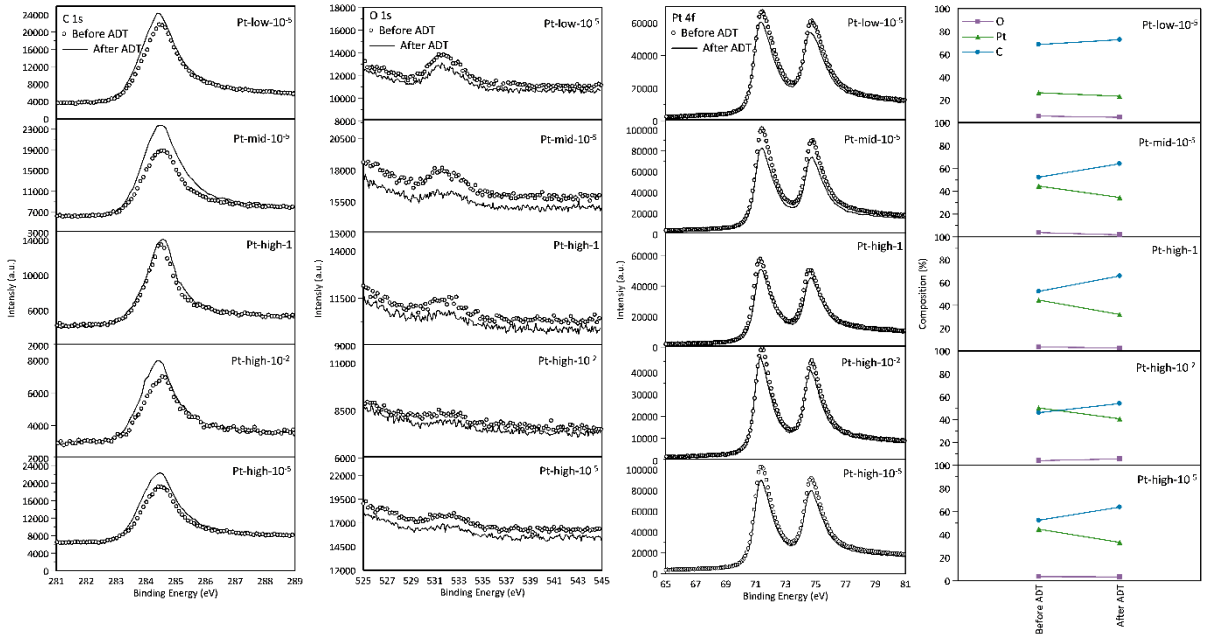

Figure S5-14. XPS analysis and relative surface elemental composition of all Pt/MWCNT/SS before and after 2000 cycles of ADT.

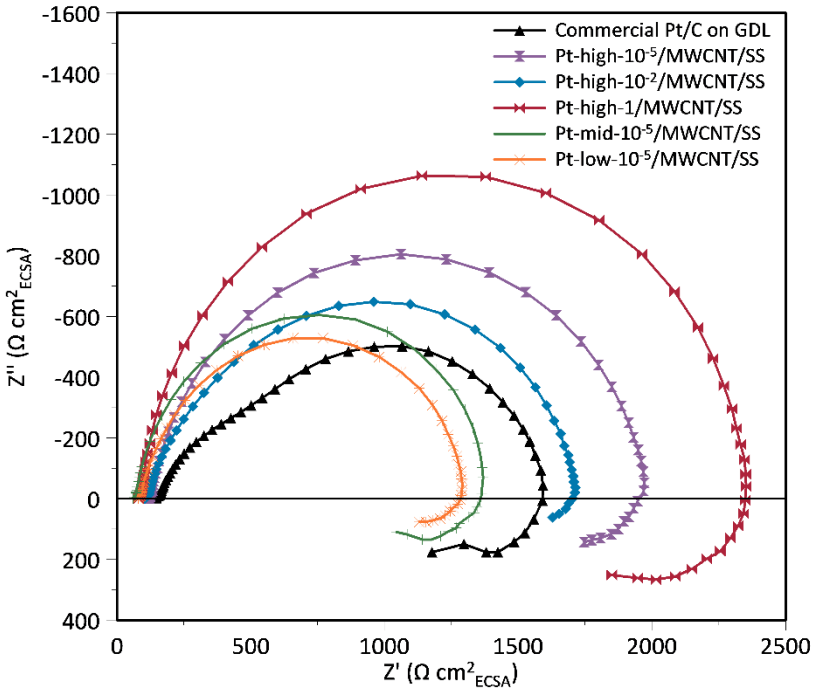

Figure S5-15. Nyquist plots of GDEs recorded in O_2-saturated 6M KOH at a potential of 0.8V.

Table S5-3. Comparison of ORR activity of Pt supported electrocatalysts

Testing Method	Electrocatalyst	Pt Loading (μg_{Pt} cm^{-2}_{geo})	Electrolyte	Temperature (°C)	SA at 0.9 V (mA cm^{-2}_{Pt})	MA At 0.9 V (mA mg^{-1}_{Pt})	Ref.
GDE	50% Pt/C	48.2	4 M $HClO_4$	25	0.100	—	[203]
GDE	Pt Black	10	1 M H_2SO_4	50	0.830	—	[206]
GDE	46.5% Pt/C	5	4 M $HClO_4$	80	0.183	—	[214]
GDE	Pt-low-10^{-5} /MWCNT/SS	27.2	0.1 M KOH	25	0.120	83	This work
RDE	46% Pt single crystals/C	14	0.1 M KOH	25	0.290	225	[222]
RDE	20% Pt/f-MWCNT	50	0.1 M $HClO_4$	25	0.091	74.6	[223]
RDE	20% Pt/MWCNT	50	0.1 M $HClO_4$	25	0.104	58.8	[223]
RDE	7.13% Pt/N-doped C	—	0.1 M $HClO_4$	25	—	108	[224]
RDE	20% Pt/C	35.6	0.1 M KOH	25	0.098	57	This work
RDE	Pt-mid-10^{-5} /MWCNT/SS	27.5	0.1 M KOH	25	0.180	80	This work

Chapter 6

6. Manuscript 3: Two-Step Dry Synthesis of Binderless 3D Low Pt-Loading Electrocatalysts for Direct Alkaline Methanol Fuel Cell Anodes

6.1 Preface

This chapter presents a published peer-reviewed article with the following citation:

Elmira Pajootan, Sylvain Coulombe, Sasha Omanovic, Two-Step Dry Synthesis of Binderless 3D Low Pt-Loading Electrocatalysts for Direct Alkaline Methanol Fuel Cell Anodes, ACS Applied Energy Materials, Volume 4, 10, 2021, 11514.

Authors contributions:

Elmira Pajootan (the Ph.D. candidate) was responsible for conceiving the idea, planning of experiments, performing the experimental work including catalyst synthesis, electrochemical tests, and material characterization. Prof. Sylvain Coulombe and Prof. Sasha Omanovic supervised the work, provided insightful comments on the results, provided funding support for the experiments, and reviewed the manuscript.

In this study, Pt nanoparticle thin films were deposited on MWCNTs grown on SS using the PLA setup at different chamber pressures for different PLA duration. The synthesized electrocatalysts were evaluated for methanol oxidation reaction (MOR) in alkaline electrolyte. The PLA conditions were optimized systematically to reach the highest methanol oxidation current while maintaining the structural integrity of the electrodes. Other parameters, including the temperature and methanol concentration, were also investigated. Electrochemical impedance spectroscopy was used to

compare the MOR kinetics and intermediate oxidation rate on the surface of Pt/MWCNT/SS electrodes with the commercial Pt/C.

Abstract

Three-dimensional (3D) porous electrocatalysts of low platinum loading were synthesized by gas-phase pulsed laser ablation (PLA) and deposited on multi-walled carbon nanotubes (MWCNTs) directly grown on a stainless steel mesh current collector by catalyst-free chemical vapor deposition (Pt/MWCNT/SS). The performance of the developed electrocatalysts was evaluated for the methanol oxidation reaction (MOR). The PLA chamber pressure and ablation time were optimized to achieve the highest methanol oxidation current per Pt loading and electrochemically active surface area while maintaining structural stability. The most robust electrocatalyst, obtained with PLA at 10^{-5} Torr for 5 min, exhibited a 50% higher methanol oxidation current compared to the commercial Pt/C with similar Pt loading. In addition, it showed the lowest loss of active sites after stability tests while maintaining its structural integrity. Increasing the electrolyte temperature from 0 to 80 °C significantly improved the methanol oxidation current on Pt/MWCNT/SS by 13 times compared to 5.8 times for Pt/C. Electrochemical impedance spectroscopy confirmed the faster kinetics of MOR and accelerated oxidation of adsorbed CO on the surface of the Pt/MWCNT/SS relative to the Pt/C.

Keywords: Three-dimensional (3D) porous Pt electrocatalyst, direct alkaline methanol fuel cells (DAMFCs), pulsed laser ablation, multi-walled carbon nanotubes (MWCNTs).

6.2 Introduction

The necessity to build sustainable, clean energy systems on shifting from the carbon emission-intensive traditional fossil fuels is one of the most critical challenges the world faces today and for decades ahead. Direct methanol fuel cells (DMFCs) are devices used to convert the chemical energy stored in methanol into electricity through a clean, safe, and energy-efficient process. Their utilisation displaces fossil fuels and reduces CO_2 emissions [225-227].

Although hydrogen can be efficiently converted into electricity with zero carbon emissions through polymer-electrolyte-membrane (PEM) fuel cells, green hydrogen remains an expensive

energy carrier because the infrastructure for the production, storage, and transport of hydrogen is complex and not developed at scale. Energy-dense, easier to store, and transport energy carriers and technologies are thus also sought. One of the candidates, the low-temperature DMFC technology, relies on the use of readily available, economic, and easy-to-transport methanol, which is a high hydrogen-to-carbon ratio (4:1) energy carrier with a relatively high theoretical energy density (17.28 MJ L^{-1}) and accessibility as a biofuel [228-231]. Moreover, direct alkaline methanol fuel cells (DAMFCs) are known to profit from the faster kinetics of methanol oxidation reaction (MOR), alleviated corrosion, higher stability of the electrocatalyst, and reduced methanol crossover in alkali media when compared to acidic media found in the PEM-based DMFCs [229-232].

Platinum group metal (PGM) electrocatalysts have been identified as the most active anode materials in DAMFC/DMFCs. To replace these expensive metals with cheaper candidates characterized by a low total (apparent) electrocatalytic activity, much higher electrocatalyst loadings are required. This high loading can result in a thicker electrocatalyst layer, which causes challenges in the mass transfer of the fuels/products, protons, and electrons, leading to an increased mass-transport overpotential and ohmic losses [146]. Therefore, PGM, notably Pt, remains the main candidate for the electrooxidation of methanol even in alkaline electrolytes. However, when Pt is used as an anode for the MOR, its deactivation by carbon monoxide, slow kinetics of MOR on its surface, and structural changes including agglomeration, dissolution, and redeposition over time, require substantially higher Pt loadings. In addition, the scarcity and cost of Pt make it the main contributor to the total cost of FCs. It is noteworthy that DAMFCs still suffer from a significantly lower specific power density compared to the PEM hydrogen FC, which currently hinders their use in vehicles and other power-demanding applications/devices. However, DAMFCs are suitable candidates for applications in portable/lower-power devices. Thus, a careful design of the electrocatalyst to lower the Pt loading in the DAMFCs and consequently, their overall cost while maintaining high power output and stability is the main challenge [34, 227].

Several strategies are being widely investigated to address one or all of the problems mentioned above. As the electrocatalytic performances of platinum-free anodes are still far behind those of Pt-based electrocatalysts, nanoscale engineering of supported Pt is a promising solution [158, 159, 226, 233]. In this regard, the development of three-dimensional (3D) porous electrodes is among the most promising approaches used in many electrochemical applications. The porous assembly

provides a large usable electrocatalytic specific area, efficient mass transfer for reactant/product molecules, and improved electron mobility [149, 234-237]. Four main strategies are employed to synthesize porous Pt structures: (*i*) nanoparticle-based, where the electrocatalyst nanoparticles are formed and then integrated into a solid electrode structure; (*ii*) substrate-based, where electrocatalytic sites are created on top of a support structure; (*iii*) self-supporting electrodes or dealloying, which starts from a support material, where the electrocatalytic sites can be formed inside the support structure; and (*iv*) decoration, where an already highly porous structure is decorated by a thin layer of Pt [236]. For instance, the commercially available Pt/C is synthesized via approach *(i)*, where a Pt-containing salt is dispersed in a solvent. Then, carbon black or activated carbon is gradually added and sonicated to achieve a well-dispersed suspension and ensure Pt salt adsorption on the carbon support. Next, in a controlled manner, Pt nucleates on C by adding a reducing agent or thermal reduction [236]. Similarly, Pt is deposited on multi-walled carbon nanotubes (MWCNTs); however, a chemical pre/post-treatment in a harsh acidic/alkaline medium is required for the activation, functionalization, or purification of MWCNTs to guarantee the anchoring of Pt on their surface [238-240]. Using approach *(ii)*, Pt coating on Ti felt was made to be used in PEM fuel cells, where the authors used many steps such as cleaning in nitric and hydrofluoric acids, argon plasma cleaning, and electroplating [241].

As briefly explained, wet chemistry approaches to synthesize 3D porous nanostructured electrocatalysts are entangled with some of the following disadvantages: time-consuming, requirement to use hazardous solvents/chemicals, high temperatures and pressures, additional pre-/post-treatment steps, and difficulties in controlling the purity, shape, and size of the electrocatalyst. Dry synthesis methods are alternative techniques to synthesizing controllable metal nanostructures by eliminating some of the drawbacks of wet chemistry. This manuscript reports a study on using two successive dry procedures to prepare a 3D porous electrode containing diverse single-element Pt nanostructures. In the first step, MWCNTs are directly grown on a woven stainless steel (SS) mesh using a catalyst-free thermal chemical vapor deposition (t-CVD). The woven stainless steel mesh provides a structure to overcome the low power densities resulting from the mass-transport limitations at the DAMFC anode employing conventional gas diffusion electrodes, and it also serves as a current collector without the use of any binder. The MWCNTs firmly attached to the porous SS provide an appropriate structure as a support for Pt deposition, offering a high electrical conductivity for the electrode assembly in the structure of fuel cells and

a high specific surface area that minimizes the aggregation or stacking of Pt nanoparticles [242]. Additionally, the MWCNTs are directly and firmly attached to the SS current collector, thus minimizing electrical contact resistance.

In the second step, pulsed laser ablation (PLA) is used to synthesize various Pt nanostructures through direct synthesis and deposition on the MWCNTs. PLA in the gas phase is an efficient, solvent-free method to deposit highly dispersed metal nanoparticles with small and narrow size distributions on a solid substrate [75]. By varying the chamber pressure and ablation time, different Pt structures and loadings were achieved. By using PLA, due to the high deposition rate of in-gas-formed Pt nanoparticles, any pretreatment of MWCNTs and/or the use of binder/ionomer can be eliminated from the synthesis route. The existence of binder/ionomer has been proven to decrease the local mass transport of the reactant [208]. The morphology of Pt nanostructures on the surface of electrodes was characterized by field-emission scanning electron microscopy (FESEM), transmission electron microscopy (TEM), and X-ray photoelectron spectroscopy (XPS). To optimize the PLA conditions, the electrocatalytic activity of various Pt-decorated 3D porous electrodes was evaluated for MOR in an alkaline electrolyte by conducting cyclic voltammetry (CV) and chronoamperometry (CA) tests to identify the most active and stable electrode. The effect of temperature and methanol concentration on the electrocatalyst efficiency in the MOR was also investigated. Finally, electrochemical impedance spectroscopy (EIS) was used to obtain information on the mechanisms of MOR on the surface of the Pt electrocatalyst at different potentials.

6.3 Materials and Methods

6.3.1 Preparation of 3D Porous Electrode

To synthesize the 3D porous electrodes, a semi-batch thermal chemical vapor deposition (t-CVD) method was used to directly grow MWCNTs (diameter: ~ 30-40 nm and length: ~ 13–15 μm) on stainless steel (SS) 316L mesh coupons (grid bars: 165 × 800 per 6.45 cm^2; wire diameters: 0.07 and 0.05 mm; grid opening: 15 microns, purchased from TWP Inc.) sonicated for 30 min in acetone. The thermal decomposition of acetylene gas (flow rate of 68 ± 5 sccm) co-injected with argon (592 ± 5 sccm) at 700 °C for 2 min in a tubular CVD furnace at oxygen level below 0.5% resulted in the growth of MWCNTs with a forest-like structure on the surface of SS. The prepared

supports (MWCNT/SS) for the deposition of Pt nanoparticles were transferred to the PLA chamber. The Pt target (T99.95%, Ted Pella Inc.) was ablated using the third harmonic (355 nm) of a pulsed nanosecond Nd:YAG laser (Quantel, Brilliant B10, repetition rate: 10 Hz, and pulse width: 5 ns). The PLA chamber was flushed with Ar for 3 min and then pumped down to 10^{-5} Torr to remove air and reduce the moisture level in the chamber. The experimental conditions for the PLA step were: ablation times of 1, 2.5, 5, 7.5 and 10 min; background gas (Ar) pressures of 10^{-5}, 10^{-2} and 1 Torr; a target-to-substrate distance of 3 cm; and laser energy of 66 mJ $pulse^{-1}$. A motorised stage was used to move the target holder vertically during ablation to uniformly wear the target and diminish thermal effects, which may lead to localized melting and ejection of liquid Pt droplets. The substrate holder was manually rotated during the ablation to cover the substrate uniformly.

6.3.2 Structural and Electrochemical Characterization

The morphology of the Pt/MWCNT/SS nanostructures was studied by ultra-high-resolution field-emission scanning electron microscopy (Hitachi, Cold FE SU-8000 SEM) at an accelerating voltage of 30 kV and an emission current of 10 μA. Transmission electron microscopy (Thermo-Scientific, Talos F200X G2 TEM) was used to investigate the coverage of Pt nanostructures on MWCNTs. For TEM imaging, the 3D porous electrode was sonicated in acetone (Sigma-Aldrich) for 60 s to cut off the individual Pt-coated MWCNTs from the SS mesh and collect them on a TEM grid. X-ray photoelectron spectroscopy (Thermo-Scientific, K-Alpha XPS apparatus, Al Kα source, micro-focused monochromator and spot size of 200 μm) was used to determine the chemical state of the deposited Pt nanostructures. To avoid the charging effect during data acquisition, the flood gun was turned on. Avantage software (Thermo Fisher Scientific) was used to analyze the obtained spectra. Raman spectroscopy (Thermo-Scientific, DRX2) using a laser excitation wavelength of 532 nm was carried out to assess the structural integrity of the MWCNTs after methanol oxidation in alkaline electrolyte.

The electrocatalytic evaluation of the electrodes was conducted in Ar-purged 1M KOH (90% assay, Sigma-Aldrich, Germany) and 1M KOH + 1M MetOH (purity of 99.99%, Fisher Scientific, US) using an Autolab Potentiostat with a three-electrode system. The Pt/MWCNT/SS samples were used as a working electrode, Pt wire as a counter electrode, and Hg/HgO (in 1M KOH) as the reference electrode. All potentials are reported with respect to Hg/HgO (in 1M KOH). The

working electrode was cycled 20 times at a scan rate of 50 mV s^{-1} in Ar-saturated 1M KOH prior to each experiment to achieve stable and reproducible voltammograms. To evaluate the electrocatalytic activity of the prepared electrodes toward methanol oxidation, cyclic voltammetry (CV) was recorded in 1M KOH + 1M MetOH from -0.9 V to 0.3 V at a scan rate of 5 mV s^{-1}. The long-term stability, tolerance to poisoning and activity of the electrocatalysts were evaluated by performing chronoamperometric (CA) measurements at a constant potential of -0.2 V in the methanol oxidation region in 1M KOH + 1M MetOH solution. Electrochemical impedance spectroscopy (EIS) measurements were conducted by applying a sinusoidal potential of ±10 mV (peak) over various *dc* working electrode potentials (-0.6, -0.4, -0.2, 0 and 0.2 V) in a frequency range from 100 kHz to 10 mHz. NOVA 2.1.4 software was used to model the obtained Nyquist plots with an equivalent circuit.

To determine the electrochemically active surface area (ECSA) of Pt, CO stripping voltammetry was performed. First, a monolayer of CO was adsorbed on the Pt surface by holding the working electrode potential at -0.62 V in a CO-saturated 1M KOH solution for 30 min. Then, the electrolyte was purged with Ar for 20 min to remove the dissolved CO. The adsorbed monolayer CO was then stripped off the Pt surface by scanning the potential from -0.9 to 0.3 V at a scan rate of 20 mV s^{-1}, and the ECSA was calculated from the CO oxidation charge [74]. The ECSA of Pt electrocatalysts was also determined by measuring the hydrogen desorption charge recorded by CV in 1M KOH. The value of 210 μC cm^{-2} was used in the calculations as the theoretical charge for oxidizing an adsorbed hydrogen monolayer on the Pt surface [243]. The ratio of the ECSA values obtained by CO oxidation to those obtained by hydrogen desorption was 1.1 ± 0.2. However, to avoid overestimating the electrocatalytic activity per true surface area of the electrocatalyst, ECSA obtained from CO oxidation was used in all calculations. In addition, all electrochemical results of the single-element Pt/MWCNT/SS were compared to those recorded on commercial 20 wt% Pt/C electrocatalysts (control). The preparation steps for the electrode made of the Pt/C commercial catalyst layer deposited on a glassy carbon surface are given in detail in the Supporting Information (section 6.6.1). This electrode is referred to as Pt/C in the text.

6.4 Results and Discussions

6.4.1 Effect of PLA Conditions

The effects of background gas pressure (10^{-5} to 1 Torr) and ablation time (1 to 10 min) during PLA on the Pt coating morphology, loading, and chemical state are first discussed. Figure 6-1 shows scanning electron micrographs of the SS mesh (Figure 6-1(a)), MWCNTs grown on the SS grid bars (Figure 6-1(b)), and Pt nanoparticle thin film deposited on MWCNT/SS for various PLA conditions (Figure 6-1(c-j)). In our previous study, we showed that the Pt nanoparticle thin films cover the outer 8 μm of the length of the MWCNTs, where the Pt coating is denser at the tip of MWCNTs, and the coverage gradually decreases to more dispersed Pt nanoparticles farther from the tip, i.e. going deeper into the bulk of the MWCNT layer [99]. A focused, high-energy pulsed laser beam (~1 mm in diameter) is aimed at a Pt target during PLA. The Pt target absorbs the laser energy, and a rapid vaporization-phase explosion (explosive boiling at ~3000-4000 K) occurs. The resulting vapor cloud or liquid adatoms/clusters expands away from the target with high particle velocity (up to 10^4 m s^{-1}). During this expansion, supersaturation, condensation, and solidification occur, and nanoparticles are formed and deposited (collected) on a substrate facing the target. The characteristics of the formed nanoparticles vary widely by changing the operating conditions, target materials, background gas compositions, and pressure [78, 79, 81, 82, 99]. The structure of the Pt nanoparticle thin coating on the MWCNTs evolves from a dense to a porous granular coating by increasing the chamber pressure from 10^{-5} to 1 Torr, as evidenced by the SEM images (Figure 6-1(e-j)). This trend can be schematically presented and explained by referring to the schematic view of the PLA process in Figure 6-2(a)). Namely, depending on the background gas pressure in the chamber, the interaction between the condensing Pt nanoparticles and background gas results in the formation of different nanostructures on the MWCNTs. At low pressures, the collision rate of ejected Pt with the background gas is less significant, resulting in the formation of a dense nanoparticle thin film on the surface of MWCNTs. At higher chamber pressures, the extent of interaction between the ejected Pt and the gas atoms/molecules increases, leading to the agglomeration of Pt clusters/particles and deposition of a more porous structure on the MWCNTs [99, 183].

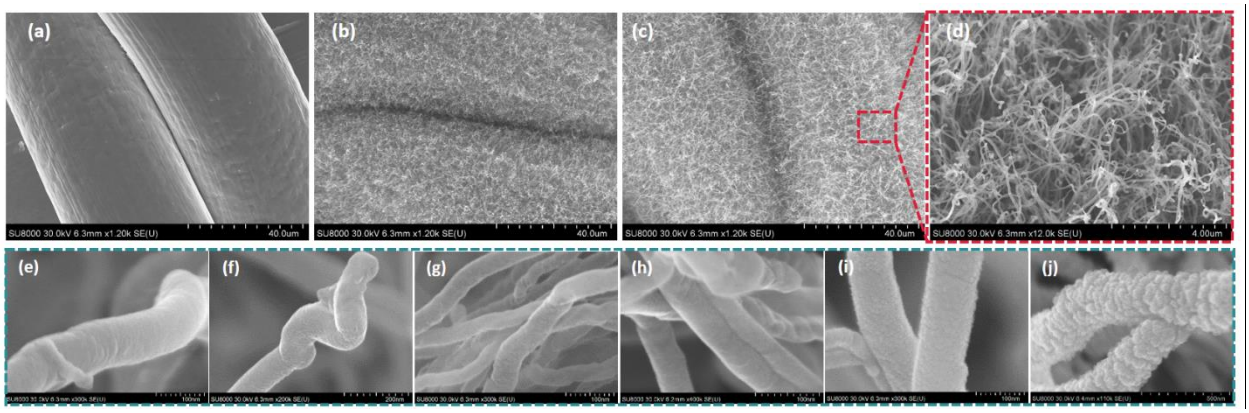

Figure 6-1. SEM images of (a) SS, (b) MWCNT/SS and (c and d) Pt/MWCNT/SS nanostructures. High magnification images of Pt/MWCNT/SS nanostructures obtained by PLA for 10 min and chamber pressures of (e) 10^{-5}, (f) 10^{-4}, (g) 10^{-3}, (h) 10^{-2}, (i) 10^{-1}, and (j) 1 Torr.

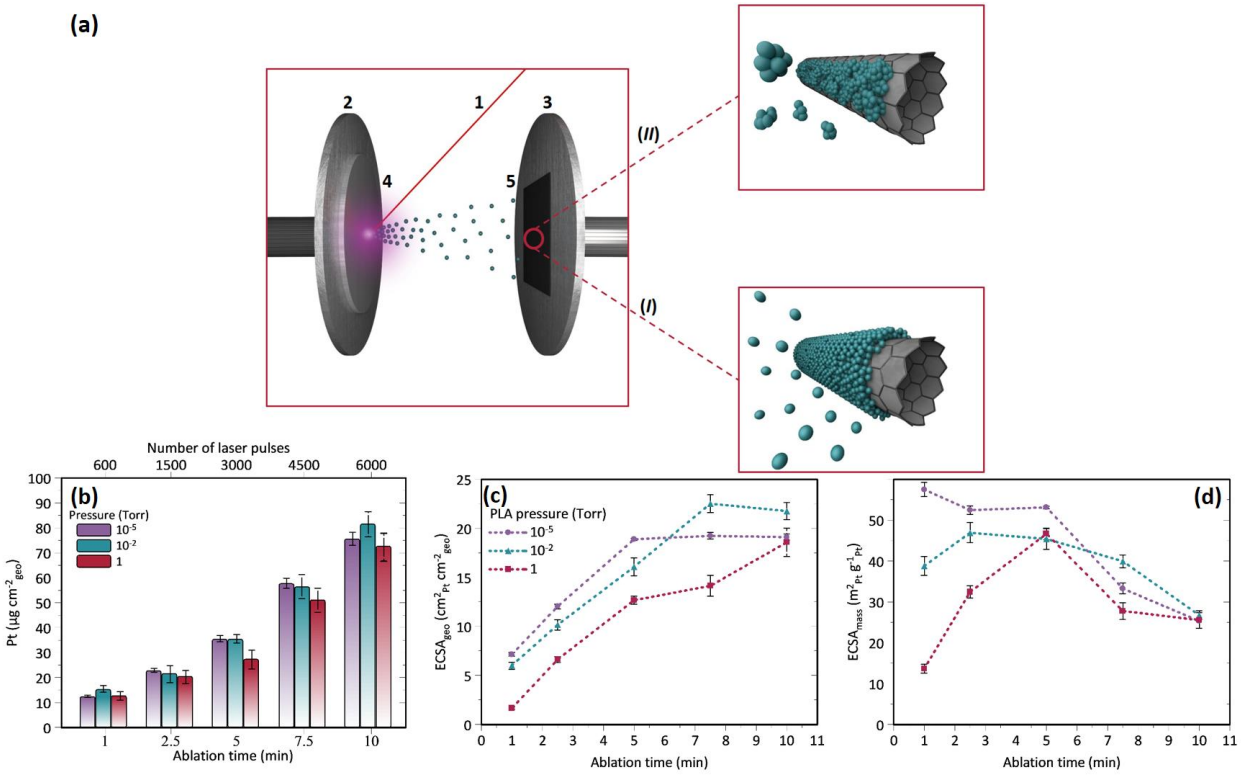

Figure 6-2. (a) Schematic view of the deposited of PLA process and Pt nanostructures on MWCNT/SS at (*I*) low (~10^{-5} Torr) and (*II*) high (~1 Torr) pressure. 1) laser beam, 2) target holder, 3) substrate holder, 4) Pt target, and 5) MWCNT/SS. (b) Pt loading on MWCNT/SS at different PLA background gas pressures and ablation times. (c) Calculated ECSA per geometric surface area and (d) per mass of Pt (error bars show the standard deviation).

The amount of Pt deposited on the MWCNT/SS substrate as a function of PLA synthesis conditions is reported in Figure 6-2(b). This figure shows an increasing trend of Pt loading on the

surface of MWCNT/SS with increasing laser ablation time at all background gas pressures (10^{-5}, 10^{-2} and 1 Torr). The mass of deposited Pt per unit geometric area of MWCNT/SS (*i.e.* Pt loading) varies from an ultralow value of ~12 μg cm^{-2} to ~80 μg cm^{-2} for ablation times of 1 to 10 min, respectively. The elemental composition of the Pt/MWCNT/SS obtained by XPS analysis reported in Table S6-1 shows a gradual increase of the Pt atomic percentage from 19 to 55 % by increasing the ablation time from 1 to 10 min (see XPS analysis in section 6.6.2 and Figure S6-1).

Figure 6-2(c-d) shows the ECSA of different loadings of Pt on MWCNT/SS calculated from the CO-stripping oxidation charge [74, 244]. The ECSA per geometric surface area of the electrodes ($ECSA_{geo}$, Figure 6-2(c)) increases with the ablation time. This increase is continuous for the electrocatalysts synthesized at 1 Torr, indicating the formation of a progressively more nanostructured Pt layer on the surface. However, the $ECSA_{geo}$ levels off after 7.5 and 5 min of deposition for the electrocatalysts synthesized at 10^{-2} and 10^{-5} Torr, respectively. This suggests that the subsequent growth of the Pt layer probably proceeded in a 2D manner, yielding an unchanged surface nanostructure. Although it can be observed in Figure 6-1(j) that a more porous/rougher Pt nanoparticle thin film is formed on the surface of MWCNTs at 1 Torr, the $ECSA_{geo}$ is not higher than those synthesized at 10^{-2} and 10^{-5} Torr. This is because, at low pressures, the uniform Pt nanoparticle thin film with the average nanoparticle size of 2.0 ± 0.2 nm covers a larger surface (radius) of the MWCNTs (Figure S6-2(a,a′,a″ and b,b′,b″)), which is not the case with the porous/agglomerated Pt nanostructure with the average size of 2.8 ± 0.8 synthesized at 1 Torr (Figure S6-2(c, c′, c″)).

The ECSA per Pt mass loading ($ECSA_{mass}$) in Figure 6-2(d) shows a maximum at 5 min for the Pt thin film deposited at a pressure of 1 Torr due to the progressively increased degree of nanostructuring. This maximum shifts to 2.5 min for the electrocatalyst synthesized at the PLA pressure of 10^{-2} Torr, while the $ECSA_{mass}$ of the electrode produced at 10^{-5} Torr remains almost constant during the first 5 min of ablation. This can be explained by the fact that the $ECSA_{geo}$ is counterbalancing the proportional increase in Pt loading. Thus, the sudden drop in $ECSA_{mass}$ after 5 min of PLA for all the samples is solely due to the increase in Pt loading.

6.4.2 Effect of Pt Support on MOR

The 3D porous nanostructured electrodes synthesized in this study are comprised of three components, namely the SS mesh, MWCNTs, and a Pt nanoparticle thin film. In order to

demonstrate the importance of each component on the methanol oxidation current, Pt was deposited at a PLA chamber pressure of 1 Torr for 2.5 min on flat SS disks and SS meshes, with and without MWCNTs grown on them. Since the laser ablation conditions were the same for all samples, the amounts of deposited Pt are expected to be similar. Moreover, the results obtained for these four electrode sets were compared with a bulk (smooth) Pt disk electrode. Figure 6-3(a) displays that when Pt is deposited directly on an SS disk (Pt/SS Disk), the CV profile remains flat at the current density scale of the main graph; however, the inset to the figure shows the presence of a small MetOH oxidation current peak around -0.25 V (the forward-sweep oxidation peak current density is 0.05 μA cm^{-2}_{geo}). With Pt deposited on the SS mesh (Pt/SS Mesh), a typical CV profile characterized by the appearance of two small methanol oxidation peaks in the forward (I_f at ~-0.17 V) and backward (I_b at ~-0.24 V) scans is observed. However, methanol oxidation current densities on the surface of Pt/SS Disk and Pt/SS Mesh are much lower than the maximum value observed with the bulk Pt electrode (Bulk Pt), which is 9 mA cm^{-2}_{geo}. However, the MWCNTs grown on the SS substrate drastically increased the surface area available for the deposition of Pt nanoparticles. By comparing the methanol oxidation current density obtained on the Pt deposited directly on an SS disk (Pt/SS Disk) to one with Pt deposited on the MWCNTs grown on the SS disk (Pt/MWCNT/SS Disk), a significant improvement in the activity of the electrode was achieved, with a forward-scan methanol oxidation peak value at 10 mA cm^{-2}_{geo}. The methanol oxidation current density was further increased to 22 mA cm^{-2}_{geo} when Pt was deposited on MWCNTs grown on the SS mesh (Pt/MWCNT/SS Mesh). The porous structure of SS mesh compared to the flat SS disk provides a higher surface area for the growth of MWCNTs, leading to a better dispersion of the Pt nanoparticles on the MWCNTs and thus higher Pt specific surface area and utilisation [245, 246].

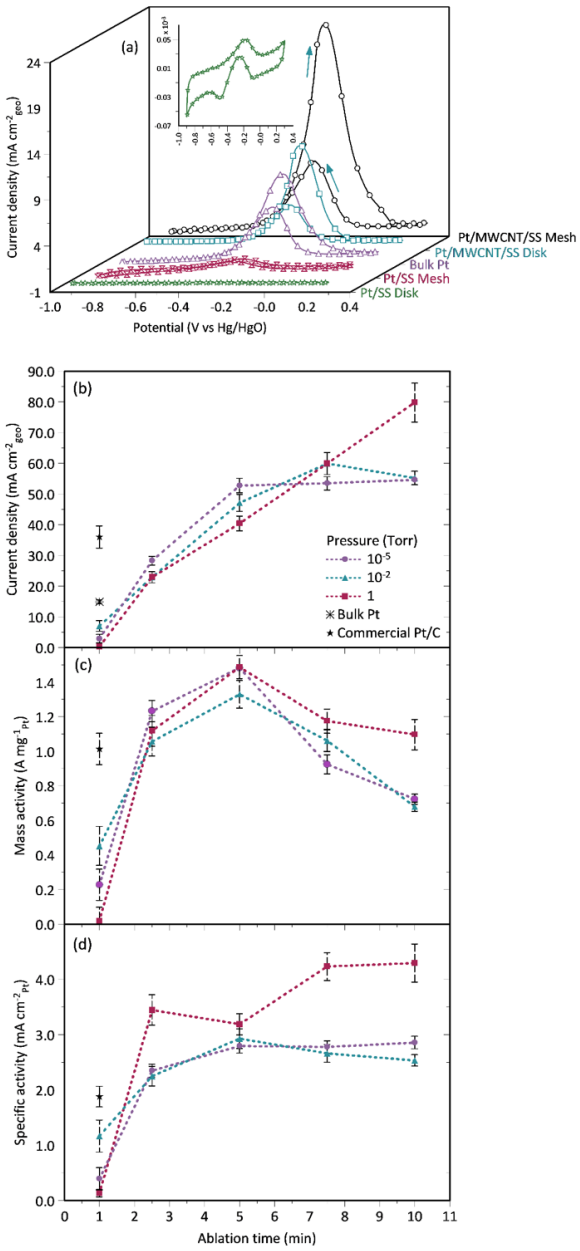

Figure 6-3. (a) Cyclic voltammograms of different electrodes in Ar-saturated 1M KOH + 1M MetOH at the scan rate of 5 mV s^{-1}. Pt was deposited at a PLA chamber pressure of 1 Torr for 2.5 min. (b) Current density, (c) mass activity and (d) specific activity of Pt/MWCNT/SS nanostructures for MOR in 1M KOH + 1M MetOH, extracted from the anodic (forward) peak in CV recorded at the scan rate of 5 mV s^{-1}; error bars show the standard deviation.

6.4.3 Methanol Oxidation Reaction

As the results in Figure 6-2(b-d) demonstrate, performing PLA for different durations (1 to 10 min) leads to the deposition of differrent amounts of Pt, while Figure 6-1 showes that different PLA background gas pressures (10^{-5}, 10^{-2}, and 1 Torr) result in the formation of Pt nanoparticle

thin films with different morphologies on the surface of MWCNTs. In order to investigate the effect of Pt loading and morphology on the methanol oxidation electrocatalytic activity of the prepared 3D porous electrodes, cyclic voltammetry was performed in an alkaline electrolyte (1M KOH containing 1M MetOH) over the -0.9 to 0.3 V potential range at a scan rate of 5 mV s^{-1} (an example of a representative CV is shown in Figure S6-3). The performance of the electrocatalysts is examined through the behavior of the forward (anodic) scan, and the methanol oxidation peak current is represented per geometric surface area (current density, Figure 6-3(b)), per mass of deposited Pt (mass activity, Figure 6-3(c)), and per $ECSA_{geo}$ (specific activity, Figure 6-3(d)). For comparison, the corresponding electrocatalytic activity of the commercial Pt/C (control) electrode is also shown in the same figures (as a starred symbol).

Figure 6-3(b) shows that with an increase in laser ablation time up to 5 min, the methanol oxidation current density also increases at all chamber pressures. However, while the oxidation current density increases with ablation time for a chamber pressure of 1 Torr, it plateaus after 5 and 7.5 min for the pressures of 10^{-5} and 10^{-1} Torr, respectively. These trends agree with those presented in Figure 6-2(c) and are explained based on the Pt surface area available for the methanol oxidation and its accessibility to the molecule. Additionally, the activity of the Pt/MWCNT/SS electrocatalysts produced at all pressures for ablation times longer than 5 minutes was found to be higher than that of the commercial Pt/C and bulk Pt electrodes (Figure 6-3(b)). This could be related to the higher specific area of the Pt/MWCNT/SS electrodes and better accessibility of methanol to active Pt sites on Pt/MWCNT/SS than to those on Pt/C.

Figure 6-3(c) illustrates the activity of the nanostructured 3D electrocatalysts normalized with respect to the mass of the electrocatalytic material. It is observed that the methanol oxidation current density increases by depositing more Pt on MWCNT/SS, reaching the highest methanol oxidation current per mass of catalyst (~1.3 to 1.5 A mg^{-1}_{Pt}) for the samples synthesized with 5 min of ablation (loading of ~35 μg cm^{-2}), which is higher than that recorded on the Pt/C electrocatalyst with the same Pt loading. However, with ablation times longer than 5 min, the mass-based activity of the Pt/MWCNT/SS electrocatalysts decreased, indicating that the number of active methanol oxidation sites on the electrode surface did not increase proportionally (with higher mass loading of Pt). This can be seen in Figure 6-3(d), which shows that the specific activity of Pt initially increased with Pt loading at ablation times up to 5 min, explaining the origin of the trend seen in Figure 6-3(c). However, the specific activity of the electrocatalysts plateaued at

longer ablation times, thus supporting the declining mass-based activity in Figure 6-3(c). It should also be noted that all of the electrocatalysts synthesized at ablation times longer than 2.5 min exhibited higher specific activity than the Pt/C electrocatalyst with a loading of 35 μg cm^{-2}. This indicates better utilization of Pt in Pt/MWCNT/SS, probably due to higher accessibility of methanol to active Pt sites on this surface, compared to commercial Pt/C. Nevertheless, an increase in the intrinsic electrocatalytic activity of Pt in Pt/MWCNT/SS over that one in Pt/C due to high interaction of Pt nanoparticle thin films with MWCNTs can be an additional origin of the differences seen in Figure 6-3(d). The improved intrinsic electrocatalytic activity can be linked to the negative shift of ~ 0.4 eV in the Pt $4f_{7/2}$ binding energy of Pt/MWCNT/SS compared to the commercial Pt/C (Figure S6-1(c)), weakening the adsorption of methanol oxidation intermediates on Pt active sites [192].

Other results from the cyclic voltammograms of MOR for bulk Pt, Pt/C, and different Pt/MWCNT/SS samples, such as MOR onset potential (after correcting for the background current) and MOR anodic peak potential, are reported in Table S6-2 (CV voltammograms not shown). As evidenced, the onset overpotential for methanol oxidation and the methanol oxidation peak potential were significantly lower on all of the Pt/MWCNT/SS electrodes compared to that of bulk Pt, illustrating the superior electrocatalytic activity of Pt/MWCNTSS. The Pt nanostructures with high electrocatalytic activity, and MWCNTs with high electrical conductivity enhance the electron transfer between methanol and electrode, resulting in lower onset and MOR anodic peak potentials compared to bulk Pt and commercial Pt/C [247-249].

A preliminary assessment of the short-time stability of the Pt/MWCNT/SS electrodes was conducted by chronoamperometry at a potential of -0.2 V for 3000 s, and the results are shown in Figure S6-4. A decaying trend recorded for all electrocatalysts can be attributed to the formation of intermediates such as CO and CHO that adsorbs on the Pt and block its surface, which cannot be avoided [53, 250, 251]. The samples prepared with ablation times of 2.5 and 5 min show the highest MOR current per mass of the catalyst. The current decay relative to the initial methanol oxidation current recorded on the clean electrocatalyst (after correcting for the double-layer current) is presented in Figure S6-5 in terms of the percentage of the maintained initial MOR current density. It can be seen that the commercial Pt/C retains 70% of its initial MOR activity, while the Pt/MWCNT/SS electrode synthesized at PLA pressures of 10^{-5} and 10^{-2} Torr for 5 min maintains 75% of their initial activity. This implies that these samples are more stable and tolerant

to the carbonaceous intermediates, which can be explained by the negative shift of Pt $4f_{7/2}$ binding energy observed in Pt/MWCNT/SS electrodes (Figure S6-1(c)), resulting in weaker adsorption of MOR byproducts on Pt active sites [192, 252]. Moreover, the CO stripping voltammograms shown in Figure S6-3(b and c) evidence that Pt/MWCNT/SS has a higher CO poisoning tolerance than Pt/C by showing the CO oxidation pre-peak and main peak at lower potentials.

There are two important aspects concerning the investigation of the structural stability of a 3D porous electrode. One concerns the structural integrity of the 3D skeleton of the electrode, and the other is the adhesion stability of the electrocatalyst nanoparticles. The latter has been extensively studied in the literature, particularly for Pt nanoparticles on a carbon support, while the former has seldom been studied. This is despite the fact that if the electrode does not maintain its 3D structural integrity during an electrocatalytic reaction, it will not be able to fulfill its purposes, which are to provide a high surface of the electrocatalyst to the reactants and to facilitate mass transport. Studies have shown that the alkaline medium can be more aggressive toward Pt nanoparticles at more positive potentials compared to the acidic medium due to the transient corrosion caused by cycling the potential during the cyclic voltammetry [30]. Moreover, the detachment of Pt nanoparticles from the carbon support in the alkaline medium has been mainly attributed to a change of the surface chemistry of the carbon support, which alters the interaction between electrocatalyst nanoparticles and the support at their anchoring sites and causes corrosion [30]. For carbon-supported Pt in alkaline electrolytes, the formation of carbonate crystals at the interface between platinum and carbon in KOH can also break off and detach Pt from carbon. The ionomer typically used in commercial catalyst inks stabilizes the catalyst particles and reduces the catalyst detachment. However, an excessive amount of ionomer decreases the catalyst activity by mass transfer limitation and deactivation of some catalyst sites.

One of the main advantages of the 3D porous Pt/MWCNT/SS electrodes synthesized in this study is that they do not require any binder, ionomer, disperser, or other additives in the electrode preparation. Furthermore, the large surface coverage of MWCNTs by Pt nanoparticles compared to the low coverage of commercial carbon supports results in better interaction between the support and electrocatalyst, making them more resistant to the detachment, dissolution and redeposition of Pt [30, 253, 254].

The structural stability of the 3D Pt/MWCNT/SS electrodes was assessed by SEM imaging and Raman spectroscopy. To evaluate the overall stability of the 3D skeleton, SEM images (Figure

6-4) of the electrodes after the CA tests (Figure S6-4) were analyzed. The low-magnification SEM images in Figure 6-4(a-e, f, k) illustrate that the forest-like structure of MWCNTs on the surface of SS mesh has been transformed to a foam-like structure in most of the electrodes. The strong capillary forces acting during the evaporation of the electrolyte from the interstices of the nanotubes during the sample drying, and the strong van der Waals interactions between nanotubes due to their alignment and narrow spacing induced bending and reassembled them in a cellular or foam-like structure seen in Figure 6-4. This rearrangement of the MWCNTs has been observed in other studies [254, 255]. To test if the MWCNT rearrangement is the result of electrolyte evaporation, the CA-tested samples were immediately freeze-dried after taking them out of the electrolyte to reduce the evaporation time. As it can be seen in Figure S6-6(c), in this case, no foam-like structures were observed, evidencing that the evaporation of the electrolyte indeed caused the rearrangement of the MWCNTs on some of the Pt/MWCNT/SS surfaces [254].

The MWCNT rearrangement was observed for all samples synthesized at the PLA chamber pressure of 1 Torr, and the other samples synthesized for 1 min of ablation time. This can be explained by the fact that by performing PLA at low ablation times and/or high gas pressures, the deposited Pt coatings do not fully cover the MWCNT surface and therefore, the capillary and van der Waals forces between Pt-free sites of the MWCNTs initiate the formation of entanglements between nanotubes. As it can be seen in Figure 6-4(g-j, l-o), the rearrangement of MWCNTs does not occur in other 3D porous electrodes after being used for MOR, which favors the exposure of a high surface area of catalyst to the reactant, improved mass transport, and consequently, high Pt utilization.

After studying the structural stability of the 3D Pt/MWCNT/SS electrodes, Raman spectroscopy was performed before and after CA tests at -0.2 V for 3000 s with Pt/MWCNT/SS electrodes synthesized at different PLA chamber pressures and 5 min of ablation to investigate the possible corrosion of the MWCNT support. Figure S6-7 shows the results of Raman analysis before and after CA tests in 1M KOH + 1M MetOH. The typical D, G and 2D bands at ~1349, ~1640 and ~2696 cm^{-1} normalized with respect to the G band are observed in all spectra. The G, D, and 2D bands express the order, disorder, and long-range order in MWCNTs, respectively, and high R values (I_D/I_G) are associated with structural damages to MWCNTs [139, 219]. According to the results of Figure S6-7, no additional defects or damages are visible for MWCNTs, even for the highly deformed samples synthesized at 1 Torr (Figure 6-4(c and c′)), indicating their stability in

the alkaline electrolyte. However, a dissolution/redeposition of Pt nanoparticles seems to have occurred for all samples synthesized at a PLA chamber pressure of 1 Torr. Namely, Figure 6-4(a′-e′) shows that Pt nanoparticles were dissolved and that the Pt redeposited on neighboring nanoparticles forming long dendritic Pt nanostructures on the surface of the MWCNTs. For samples synthesized at lower PLA chamber pressures and ablation times shorter than 2.5 min (especially for samples synthesized with 1 min of ablation), the detachment of Pt nanoparticles is apparent (Figure 6-4(f′,g′,k′,l′)). In comparison, the samples synthesized at low PLA chamber pressures and ablation times longer than 5 min showed stable Pt-covered MWCNTs in a forest-like structure (Figure 6-4(h′ to j′, and m′ to o′)). Therefore, we infer that the main mechanism for the detachment of Pt nanoparticles can be attributed either to the destruction of their anchoring sites on the MWCNTs or to the formation of carbonate crystals. The formation of dense Pt coatings on the MWCNTs at low PLA chamber pressures renders the MWCNT surface inaccessible to carbonate crystals that contribute to the loosening and detachment of Pt nanoparticles. Moreover, the extended surface area provided by the formation of more uniform and denser Pt coatings on the MWCNTs and associated stronger interaction between the MWCNTs and the deposited Pt makes the electrodes less prone to surface area loss via Pt detachment, agglomeration, and dissolution/redeposition [253].

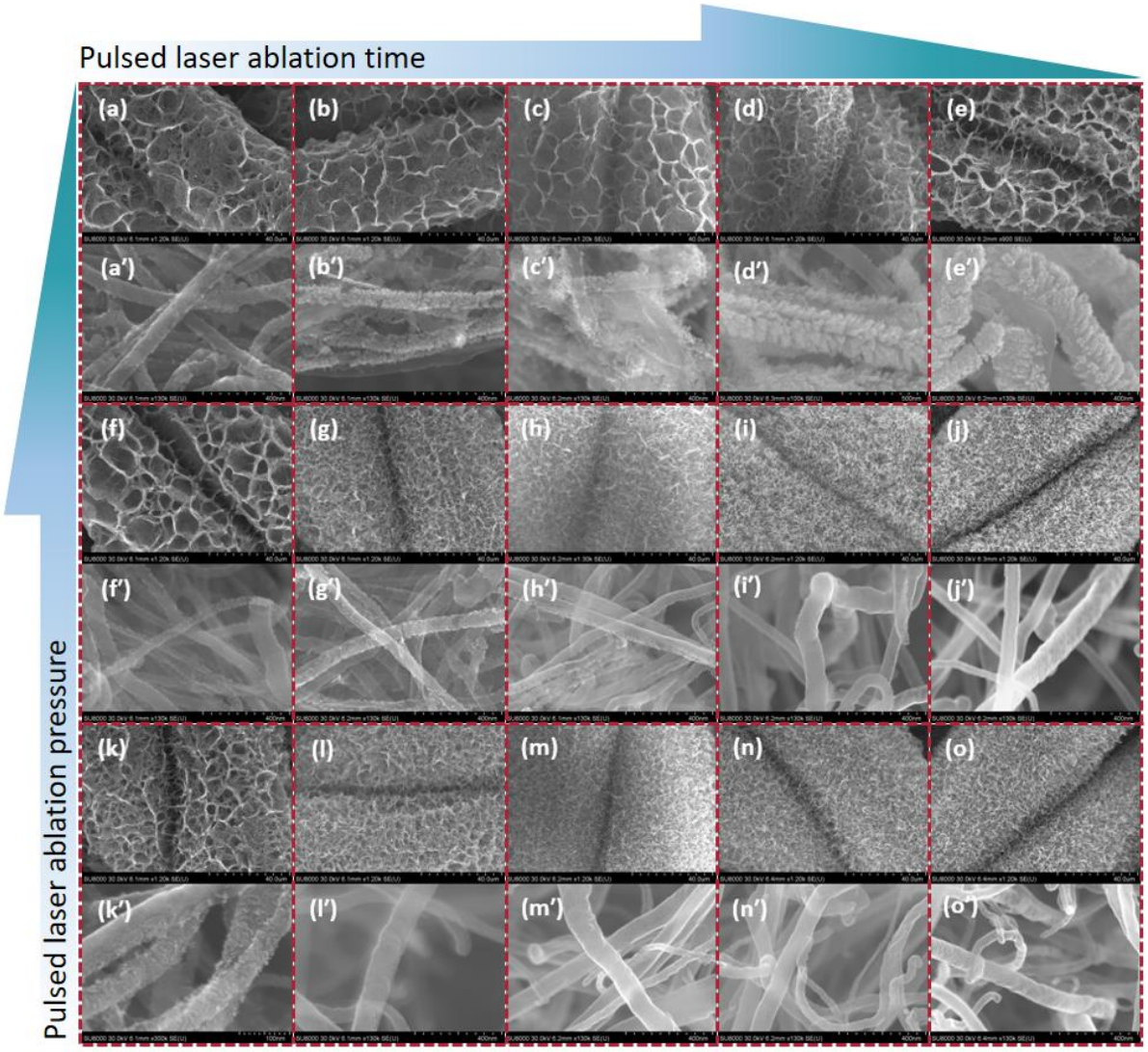

Figure 6-4. SEM images of Pt/MWCNT/SS electrodes after chronoamperometry experiments performed at -0.2 V for 3000 seconds in 1M KOH + 1M MetOH; PLA synthesis condition: (a, a′) to (e, e′) ablation time of 1, 2.5, 5, 7.5, 10 min at 1 Torr, (f, f′) to (j, j′) same ablation time at 10^{-2} Torr, and (k, k′) to (o, o′) same ablation time at 10^{-5} Torr.

The structural stability of the Pt/MWCNT/SS electrodes in the alkaline solution without methanol was also investigated by performing cyclic voltammetry (CV) in Ar-saturated 1M KOH with long-term cycling at a scan rate of 100 mV s^{-1} (Figure 6-5). The Pt/MWCNT/SS electrodes synthesized with ablation times of 2.5 and 5 min at three background gas pressures (10^{-5}, 10^{-2} and 1 Torr) were selected for this test due to their better MOR performance (Figure 6-3). In the absence of methanol in the electrolyte, three characteristic potential regions can be seen on the voltammograms of Pt; the H_{upd} adsorption/desorption (~ -0.8 to -0.5 V), the double-layer region (~ -0.5 to -0.2 V in the anodic scan), and the formation of OH_{ad} layer beyond -0.2 V and its

reduction around -0.2 V. Due to the large specific surface area of MWCNTs, the double-layer region shows high currents that dominate the CVs in Figure 6-5. All electrodes show a similar shape of the cyclic voltammograms. After 2000 cycles, only a slight decrease in the current intensity of the hydrogen peaks (~ -0.8 to -0.5 V) is observed for all samples, indicating a decrease in Pt surface area. To quantify the loss of performance of the Pt electrocatalysts with cycling, the charge of hydrogen *upd* adsorption/desorption (H_{upd}) was determined to yield the normalized electrochemical active surface area ($ECSA_H$), and the trends are shown in Figure 6-5(h) [256]. The two Pt catalysts synthesized at the lowest PLA chamber pressure preserved more than 87% of their initial ECSA, while the ECSA of other electrodes decreased to 82 and 79 %. Comparatively, the Pt/C electrode only preserved 76 % of its initial $ECSA_H$. The chronoamperometry stability tests were also performed on these selected electrodes for 3 h (Figure S6-8) to evaluate the methanol oxidation activity for a more extended time at -0.2 V, during which the Pt/MWCNT/SS electrocatalyst synthesized at 10^{-5} Torr for 2.5 and 5 min outperformed the Pt/C in terms of geometric current density and mass activity, evidencing the superior performance of specific Pt/MWCNT/SS electrodes.

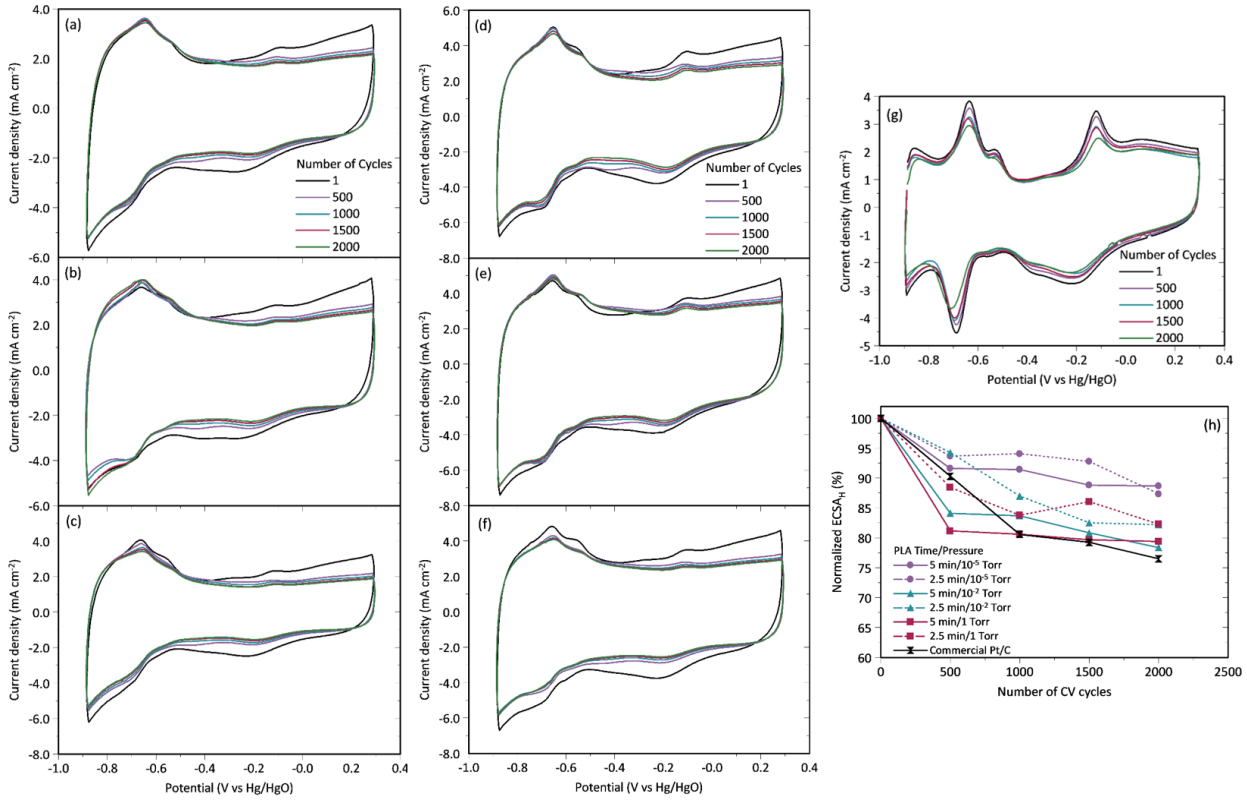

Figure 6-5. Stability test of Pt/MWCNTs/SS electrodes by performing cyclic voltammetry in 1M KOH at scan rate of 100 mV s^{-1} for 2000 cycles. PLA conditions: (a) 2.5 min/10^{-5} Torr, (b) 2.5 min/10^{-2} Torr, (c) 2.5 min/1 Torr, (d) 5 min/10^{-5} Torr, (e) 5 min/10^{-2} Torr, (f) 5 min/1 Torr, and (g) Pt/C. (h) Percentage retention of the initial $ECSA_H$ as a function of CV cycle number.

The three sets of stability tests (Figure 6-5, Figure S6-4 and Figure S6-8) have evidenced the deterioration of the performance of the Pt/MWCNT/SS electrodes during the experiments. Loss of Pt would result in permanent performance degradation, while the deactivation (poisoning) of the Pt surface by methanol oxidation byproducts is temporary and reversible. To investigate which of the two is the source of performance loss, the two most stable electrocatalysts identified in long-term CV tests in 1M KOH (2.5 and 5 min /10^{-5} Torr) were further examined by successive chronoamperometry experiments at a potential of -0.2 V. In these experiments, the samples were first tested for their MOR activity and stability at -0.2V for 1 h. Then the samples were pulled out of the cell, carefully rinsed with 1M KOH and transferred to another electrochemical cell containing only 1M KOH. The surface of the catalyst was then "cleaned" by applying 25 CV cycles in the potential range of -0.9 to 0.3 V, at the scan rate of 100 mV s^{-1} to oxidize/remove any possible MOR byproducts formed on the surface, thus possibly reactivating it. This procedure was

repeated five times. The results of these experiments in terms of mass activity of the Pt electrocatalyst are reported in Figure 6-6. As mentioned earlier, the main reasons for the drop of electrocatalytic activity can be attributed to the dissolution-agglomeration of Pt nanoparticles, the detachment of Pt nanoparticles from the MWCNT substrate by carbonate crystals, and poisoning of the catalyst by methanol oxidation intermediates [143, 257]. All these, but the last, reduce the electrochemically active surface of the electrocatalyst irreversibly. Figure 6-6 shows that the electrocatalyst synthesized with 5 min of ablation time exhibits consistent mass activity for all cycles of chronoamperometry, which implies that the reason for the methanol oxidation current decay is the deactivation/poisoning of the Pt surface by the adsorbed methanol oxidation byproducts. This claim is further inferred with the SEM images of Figure S6-9(a-c), which highlight the better stability and robustness of the 3D porous electrode macrostructure. Moreover, no detachment of Pt is evident from the SEM images. This points toward the existence of a strong interaction between the MWCNTs and the deposited Pt. On the contrary, Figure 6-6 evidences that the mass activity of the electrocatalyst synthesized with an ablation time of 2.5 min deteriorated after each cycle of chronoamperometry and declined to ~0.2 A mg^{-1}_{Pt} at the end of the fifth cycle. SEM images in Figure S6-9(d-f) reveal the reconfiguration of MWCNTs on SS and the detachment of Pt nanoparticles, justifying the diminution of mass activity in this electrode.

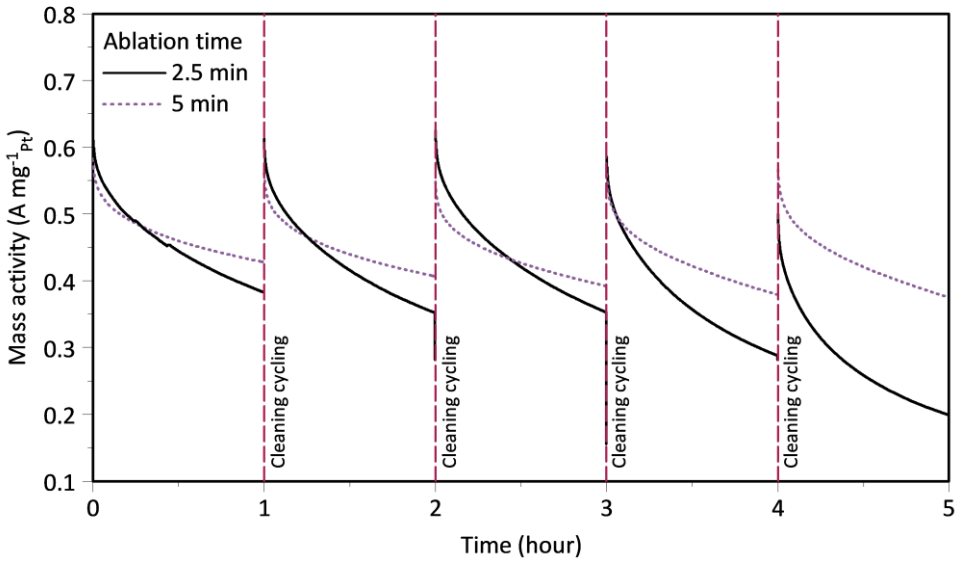

Figure 6-6. Stability test of Pt/MWCNTs/SS electrodes synthesized by PLA at 10^{-5} Torr for 2.5 and 5 min by five successive 60 min cycles of chronoamperometry in 1M KOH + 1M MetOH at the potential of -0.2 V.

6.4.4 Effect of Working Temperature

The performance of the Pt/MWCNT/SS electrocatalyst synthesized by PLA at 10^{-5} Torr for 5 min, as the most active and stable electrocatalyst, was further evaluated under different working temperatures in the range of 0 to 80 °C. The results were compared to the performance of the Pt/C electrocatalyst. The results in Figure 6-7(a) show that lowering the temperature down to 0 °C negatively affects the performance of both electrocatalysts, which is to be expected since the kinetics of MOR follows the Arrhenius law. In addition, the formation of carbonate is favored at lower temperatures since the reaction between KOH and CO_2 is exothermic, and the Pt catalyst layer can be delaminated if any ice crystals are formed. However, the SEM images of the Pt/MWCNT/SS electrocatalyst taken at 0 °C demonstrate its high stability, showing no evident Pt detachment and no 3D structural changes in MWCNTs configuration [258]. It can also be seen that increasing the temperature enhances the methanol oxidation kinetics, as expected. A higher temperature is favorable for the initial methanol dehydrogenation and facilitates the CO desorption [259, 260].

The MOR current of the Pt/C electrocatalyst improves by a factor of 5.8 by increasing the operating temperature from 0 to 80°C, while a significantly larger improvement (by a factor of 13) is observed for the Pt/MWCNT/SS electrode. The apparent activation energy values are 25.2 and 17.0 kJ mol^{-1} for the Pt/MWCNT/SS and Pt/C electrodes, evidencing the largest dependence of the MOR kinetics on temperature for the former electrocatalyst. The superior performance of Pt/MWCNT/SS can be associated with improved mass-transport properties within the 3D structure of the electrode or the elimination of Nafion ionomer from the structure of the Pt/MWCNT/SS [261]. As seen in Figure S6-10, the hydrogen adsorption/desorption current peaks decreased in magnitude at higher temperatures to the extent that the second hydrogen peak at ~0.55 V disappears in both Pt/C and Pt/MWCNT/SS electrodes. This phenomenon has been previously reported to be due to the higher mobility of hydrogen at higher temperatures, resulting in unstable adsorption on Pt sites [262, 263]. Therefore, the calculation of ECSA at elevated temperatures using the charge of H_{upd} was not feasible in this study. Moreover, the CV voltammograms indicate an increase in the formation of Pt oxide at elevated temperatures, which can suppress the electron transport and available active site. The formation of Pt oxide is more evident with the Pt/C electrocatalyst, which can justify the better temperature-dependent performance of Pt/MWCNT/SS compared to Pt/C.

The SEM images of the Pt/MWCNT/SS electrode in Figure 6-7(a) demonstrate the stability of Pt nanoparticles at elevated temperature by showing no significant detachment or agglomeration of Pt nanoparticles nor any significant entanglement of MWCNT forest-like structure. The ability to increase the temperature without deteriorating the structural integrity of the electrode offers new opportunities to promote the performance of a fuel cell [258].

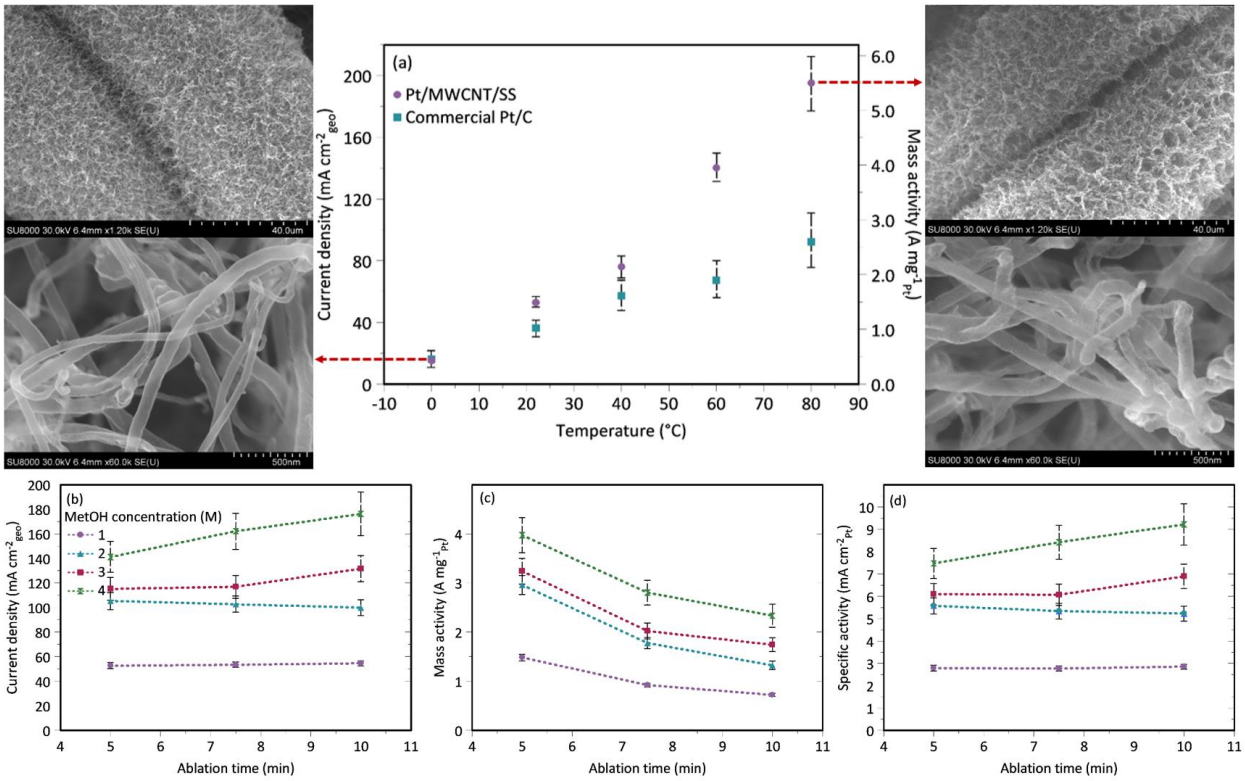

Figure 6-7. (a) Effect of temperature on methanol oxidation forward (anodic) current density and mass activity for Pt/MWCNT/SS synthesized at 10^{-5} Torr for 5 min, and commercial Pt/C. CVs were recorded at a scan rate of 5 mV s^{-1}. SEM images show the morphology after the experiment. (b) Current density, (c) mass activity and (d) specific activity of Pt/MWCNT/SS nanostructures synthesized at a PLA chamber pressure of 10^{-5} Torr for MOR in 1M KOH + different concentrations of MetOH, extracted from CV recorded at a scan rate of 5 mV s^{-1}. Error bars show the standard deviation.

6.4.5 Effect of methanol concentration

In order to further study the kinetics of methanol oxidation and performance of the developed 3D porous Pt electrodes, the MOR was evaluated at higher methanol concentrations on the three Pt/MWCNTs/SS electrodes produced at PLA times of 5, 7.5 and 10 min at 10^{-5} Torr. SEM images (Figure 6-4(m-o and m′-o′)) proved these samples to be stable after the stability test (Figure S6-4).

The dependency of the MOR forward peak current per geometric surface area, per Pt loading, and per $ECSA_{geom}$ on the methanol concentration is shown in Figure 6-7(b-d). Figure 6-7(b) shows that by increasing the ablation time from 5 to 10 min, the methanol oxidation current density does not statistically change, which was expected since the actual Pt surface area ($ECSA_{geo}$) did not change by ablating more Pt by running PLA from 5 to 10 min (Figure 6-2(c)). However, since the Pt loading increases at longer ablation times (Figure 6-2(b)), the corresponding methanol oxidation mass activity decreases (Figure 6-7(d)). On the other hand, since the Pt surface area is constant at the three ablation times, the specific activity remains constant, as shown in Figure 6-7(d). However, all three plots in Figure 6-7 show that with an increase in methanol concentration, the methanol oxidation current also increases, signifying that not all Pt active sites are occupied by initially adsorbed methanol within the methanol concentration range investigated; otherwise, the MOR current density would be independent of methanol concentration.

Knowing that the current density is proportional to the reaction rate, the data in Figure 6-7(d) was further analyzed to determine the order of methanol oxidation reaction with respect to methanol in the given concentration range (Figure S6-11). The corresponding order of the MOR with respect to methanol was found to increase with PLA on the order of 0.69, 0.76, and 0.83 (R^2>0.95) for PLA of 5, 7.5 and 10 min, respectively.

Table S6-3 reports several recent studies employing MWCNT-supported catalysts for methanol oxidation in both alkaline and acidic electrolytes. It is evident from the table that the mass activity of the single-element Pt/MWCNT/SS electrocatalyst developed in this study for the oxidation of 1M MetOH is in the upper range of the reported values. However, at high temperatures (80 °C) or high methanol concentrations (4M), the mass activity of Pt/MWCNT/SS increases to 5.5 and 4.0 A mg^{-1}_{Pt}, respectively, which is noticeably higher than the performance reported in the literature even for state-of-the-art methanol oxidation catalyst, PtRu.

6.4.6 EIS study of Methanol Oxidation

The oxidation of methanol is a complex reaction due to the existence of multiple electron transfer and adsorption/desorption steps that are dependent on the electrocatalyst characteristics. In the most simplified form, three main steps (Reaction 6-1 to Reaction 6-3), following the Langmuir-Hinshelwood kinetics, have been proposed to represent the oxidation of methanol on

the surface of a Pt electrocatalyst. In the first reaction (Reaction 6-1), methanol is first adsorbed and then stepwise oxidized on the surface of Pt, where the adsorbed CO (CO_{ads}) is formed as the main final byproduct, which inactivates (blocks) the Pt active sites. At higher potentials, OH species are adsorbed on the surface of Pt (Reaction 6-2), which then oxidize CO_{ads} to CO_2 (Reaction 6-3). It is worth noting that other hydrocarbon intermediates (HCHO, HCOO, CH_2O, and CH_3O) can also be formed during the oxidation of methanol, which are considered to be further converted to the stable CO_{ads} on the surface of Pt [264-266].

$$CH_3OH + Pt \rightarrow Pt - CO_{ads} + 4H^+ + 4e^- \quad \textbf{Reaction 6-1}$$

$$H_2O + Pt \rightarrow Pt - OH_{ads} + H^+ + e^- \quad \textbf{Reaction 6-2}$$

$$Pt - CO_{ads} + Pt - OH_{ads} \rightarrow CO_2 + 2Pt + H^+ + e^- \quad \textbf{Reaction 6-3}$$

The complexity of MOR and the capability of the EIS technique to detect the electrochemical reactions with different time constants make EIS a valuable tool to study the MOR at different applied potentials on the surface of Pt electrocatalysts. In this study, the MOR was investigated by EIS on the surface of the commercial Pt/C and our best-performing electrode (Pt synthesized by PLA at 10^{-5} Torr for 5 min) at different potentials (CV shown in Figure 6-8(a)), the equivalent circuit model is shown in Figure 6-8(b), and the corresponding Nyquist and Bode plots are shown in Figure 6-8(c and d). A glance at the Nyquist plots obtained from EIS measurements reveals the presence of different features such as semicircles, inductive loops, negative resistance, and multiple time constants, confirming the occurrence of different interfacial processes at different potentials [264, 265].

At a potential of -0.6 V (Figure 6-8(a)), methanol oxidation has already commenced on the surface of both Pt/C and Pt/MWCNT/SS, and therefore, CO_{ads} is produced as the main intermediate (Reaction 6-1). This can be seen by the appearance of a large semicircle in the complex plane at low frequencies in Nyquist plots in Figure 6-8(c and d). The produced CO as an intermediate is adsorbed onto the surface of Pt (Pt-CO_{ads}), which poisons and blocks the Pt active sites and prevents the continuous oxidation of methanol on the surface of the electrocatalyst. The Bode plot also shows this by a phase-angle maximum at low frequencies [264, 265].

At the potentials of -0.4 and -0.2 V, the Nyquist plots in Figure 6-8 show a typical pseudo-inductive behavior that contains a capacitive semicircle at high frequencies and an inductive semicircle at low frequencies. The inductive semicircle appears when a reaction forms intermediate species, and the reaction of those intermediates to products is the rate-determining step. In this potential region, methanol oxidation is fast (Figure 6-8(a)), but the oxidation of CO_{ads} to produce CO_2 is the rate-determining step. The corresponding Bode plots show a peak at low frequencies, which is linked to the kinetics of the reaction between CO_{ads} and OH. As the potential increases from -0.4 to -0.2 V, the phase-angle maximum shifts to higher frequencies (while the semicircles become smaller in the Nyquist plots). This is because, at higher potentials, more OH species cover the surface of Pt (Reaction 6-2), which further accelerates the kinetics of oxidation of CO_{ads} to CO_2 (Reaction 6-3) [264, 265].

As the coverage of OH on the Pt surface continues to increase at higher potentials, the MOR on the surface of pure Pt becomes slower relative to the oxidation kinetics of CO_{ads} to CO_2. Therefore, the methanol oxidation current decreases as the potential reaches 0 V (Figure 6-8(a)), making the methanol oxidation (Reaction 6-1) the rate-limiting step. The impedance at 0 V appears in the second quadrant of the Nyquist plot. At +0.2 V, PtO with lower activity toward methanol oxidation is formed on the surface of Pt. Thus, a large semicircle appears again in the Nyquist plot, and a phase-angle maximum in the low-frequency region is observed in the Bode plots, as an indication of methanol oxidation on the surface of PtO [264, 265, 267].

This impedance behavior of the electrodes at different potentials is further explained and compared in the Supporting Information (section 6.6.3) by proposing an equivalent circuit model shown in Figure 6-8(b). The comparison of Nyquist and Bode plots and the fitted parameters from the equivalent circuit reported in Table S6-4 for Pt/C and Pt/MWCNT/SS, clearly demonstrate the faster kinetics (lower charge-transfer resistance) of MOR at all studied potentials and accelerated oxidation of CO_{ads} to CO_2 on the surface of the developed 3D Pt/MWCNT/SS electrodes.

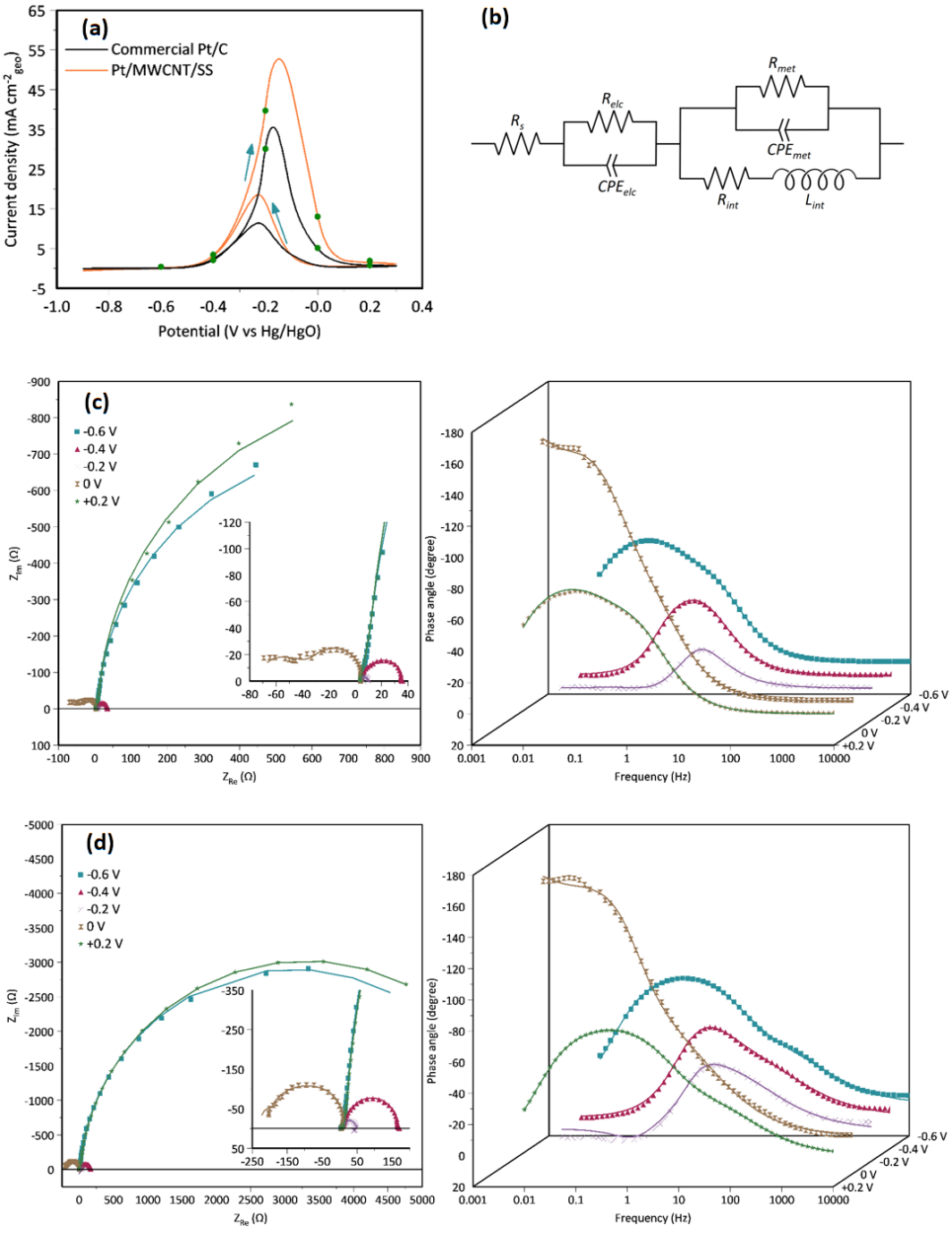

Figure 6-8. (a) cyclic voltammograms of MOR, (b) equivalent circuit used to model the EIS results, Nyquist and Bode EIS plots for (c) Pt-5min-10^{-5} Torr and (d) Pt/C recorded in 1M KOH + 1M MetOH. Symbols: experimental data. Solid line: modeled data.

6.5 Conclusion

This study presented a unique development of 3D porous single-element Pt electrocatalysts at loadings below ~80 μg cm^{-2}. The 3D Pt/MWCNT/SS electrocatalysts were synthesized by first growing dense MWCNT forests on an SS mesh by chemical vapor deposition, followed by the pulsed laser ablation of Pt nanoparticles onto the MWCNTs. Varying amounts of Pt and diverse Pt nanoparticle thin films on the MWCNTs were obtained by changing the laser ablation time and chamber pressure. Optimum synthesis conditions leading to the best performance in terms of activity, poison tolerance and long-term stability of Pt/MWCNT/SS in methanol oxidation reaction were determined. The results showed that for all the chamber pressures investigated (10^{-5}, 10^{-2} and 1 Torr), the highest mass activity is obtained at 5 min of ablation (~35 μg cm^{-2} of Pt loading), while the highest specific activity of the Pt/MWCNT/SS electrocatalysts is achieved after only 2.5 min of laser ablation (~21 μg cm^{-2} of Pt loading). The long-term stability tests indicated that only at Pt loadings of ~35 μg cm^{-2} and higher, the 3D shape of the electrodes and Pt coverage on MWCNTs were well preserved. The methanol oxidation current obtained by all electrocatalysts increased at higher concentrations of methanol in the electrolyte, reaching the highest mass activity of ~4 A mg^{-1}_{Pt}. The rate-determining step in MOR on the surface of the electrocatalyst was identified by recording EIS spectra at different potentials, and the findings ascertained faster oxidation of both methanol and carbon monoxide on the surface of the developed 3D porous Pt electrocatalyst compared to the commercial Pt/C. The increased kinetics of MOR at the surface of the electrocatalyst at elevated temperatures up to 80°C increased the methanol oxidation current for the Pt/MWCNT/SS electrodes more than two times in comparison with the commercial Pt/C, indicating a great potential of Pt/MWCNT/SS for practical use at operating conditions of DAMF. This work creates a paradigm for future studies using the PLA technique to synthesize non-noble and/or multi-component electrocatalysts for a wide range of electrochemical applications.

Acknowledgments

The authors wish to acknowledge the financial support provided by the Faculty of Engineering through the McGill Engineering Doctoral Award (MEDA), the Natural Sciences and Engineering Research Council of Canada (NSERC), the Gerald Hatch Faculty Fellowship, and the Fonds de recherche du Québec – Nature et technologies (FRQNT). The authors thank the technical staff

from the Department of Chemical Engineering at McGill University. The authors acknowledge Dr. Boris Nijikovsky and David Liu for the operation of TEM.

6.6 Supporting Information

6.6.1 Commercial Pt/C Catalyst Preparation

To compare the performance of the Pt/MWCNT/SS electrocatalysts produced in the current study to the commercial Pt/C electrocatalyst, catalyst ink with a Pt loading of 35.5 μg cm^{-2}_{geo} of Pt/C was prepared. In this regard, 25.6 mg of 20 wt.% Pt/C catalyst (Sigma-Aldrich) was mixed with isopropyl (2 mL) and DI water (8 mL) and sonicated for 15 min. The vial containing the ink was fixed at the center of an ice-water ultrasonic bath (Branson 1510, 70 W, 42 kHz). Nafion$^{(R)}$ 117 solution (0.2 mL) purchased from Sigma-Aldrich was added to the mixture while the sonication continued for another 15 min. 20 μL of the prepared ink was dropped on a 6-mm diameter glassy carbon (GC) rotating disk electrode. To obtain a mirror-like surface, the GC was polished prior to use by a porous neoprene cloth (Black Star, Anamet) with 0.05 μm alumina slurry. Ar gas with an extremely low flow rate was used to dry the ink droplet on the surface of GC.

6.6.2 XPS Analysis

The XPS spectra of the commercial Pt/C and the selected Pt/MWCNT/SS electrodes synthesized at 10^{-5} Torr for different pulsed laser ablation times are shown in Figure S6-1. All the spectra were recorded after 20 seconds of Ar ion beam sputtering of the surface at 500 eV to eliminate any surface impurities as the result of exposure of the electrocatalysts to laboratory air. The survey scan (Figure S6-1(a)) identified carbon, platinum and oxygen elements on the surface of the electrocatalysts. Their corresponding high-resolution spectra are shown in Figure S6-1(b-d). The C 1s peak appeared at ~284.8 eV (Figure S6-1(b)). The doublet peaks of Pt $4f_{7/2}$ and Pt $4f_{5/2}$ are located at binding energies of ~71.5 and ~74.5 eV, showing the existence of metallic Pt for all the samples (Figure S6-1(c)). The Pt $4p_{3/2}$ at ~520 eV peak in Figure S6-1(d) is followed by O 1s at ~530 eV, which illustrates the existence of organic oxygen on the surface of the samples. A negative shift of ~0.4 eV in Pt $4f_{7/2}$ binding energy of Pt/MWCNT/SS is observed in Figure S6-1(c) compared to the commercial Pt/C. The Pt $4f_{7/2}$ binding energy is directly linked to the *d*-band center of Pt, which defines the bonding strength between Pt and other elements/compounds. Therefore, lower Pt $4f_{7/2}$ binding energy is attributed to a downshift in the *d*-band center of Pt, which weakens the adsorption of MOR intermediates. Thus, this results in minor blockage of Pt active sites and makes the active catalytic sites of Pt more accessible to methanol molecules and less susceptible to poisoning [192].

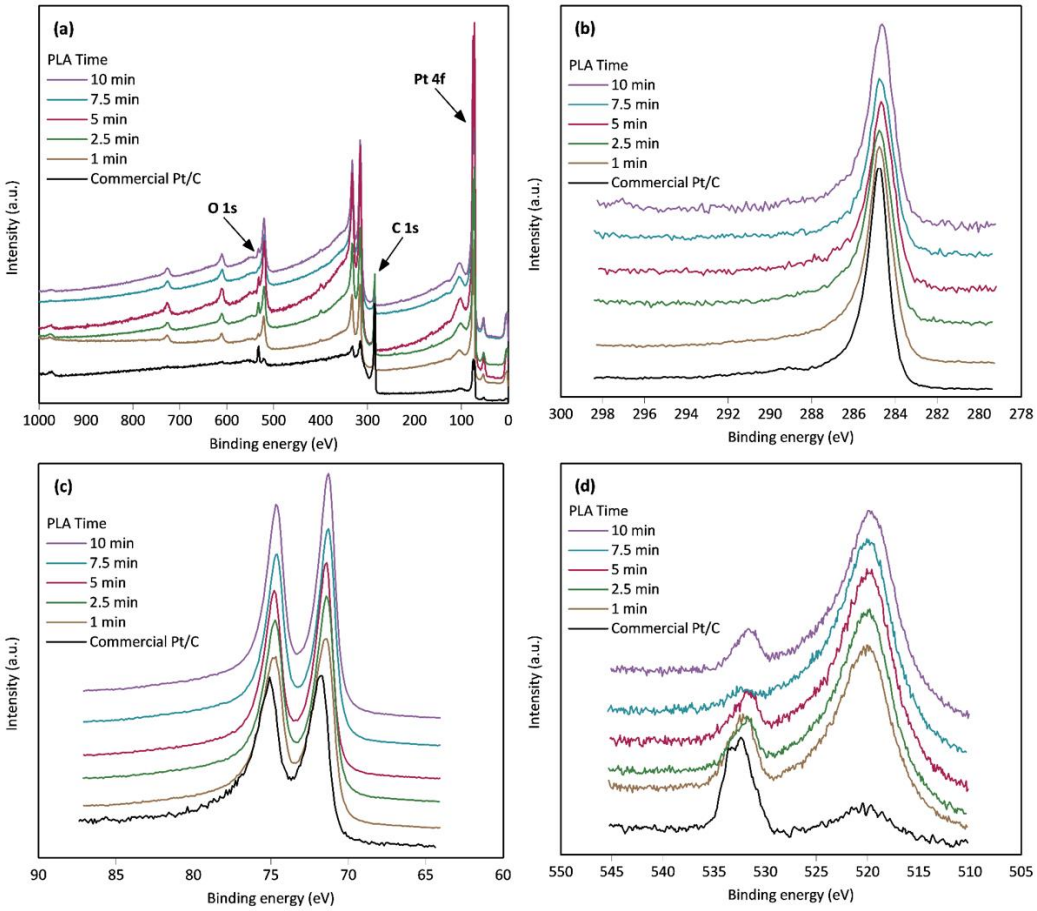

Figure S6-1. XPS analysis of Pt/MWCNT/SS synthesized by PLA at 10^{-5} Torr for different duration, (a) survey, (b) C 1s, (c) Pt 4f, and (d) O 1s and Pt 4p scans.

Table S6-1. Elemental composition (atomic %) of different Pt/MWCNT/SS electrocatalysts synthesized by PLA at 10^{-5} Torr for different durations

Element	Pt-1 min	Pt-2.5 min	Pt-5 min	Pt-7.5 min	Pt-10 min
C 1s	75.21	50.25	48.59	44.16	39.32
Pt 4f	19.02	44.17	46.18	50.51	55.18
O 1s	5.77	5.58	5.24	5.33	5.5

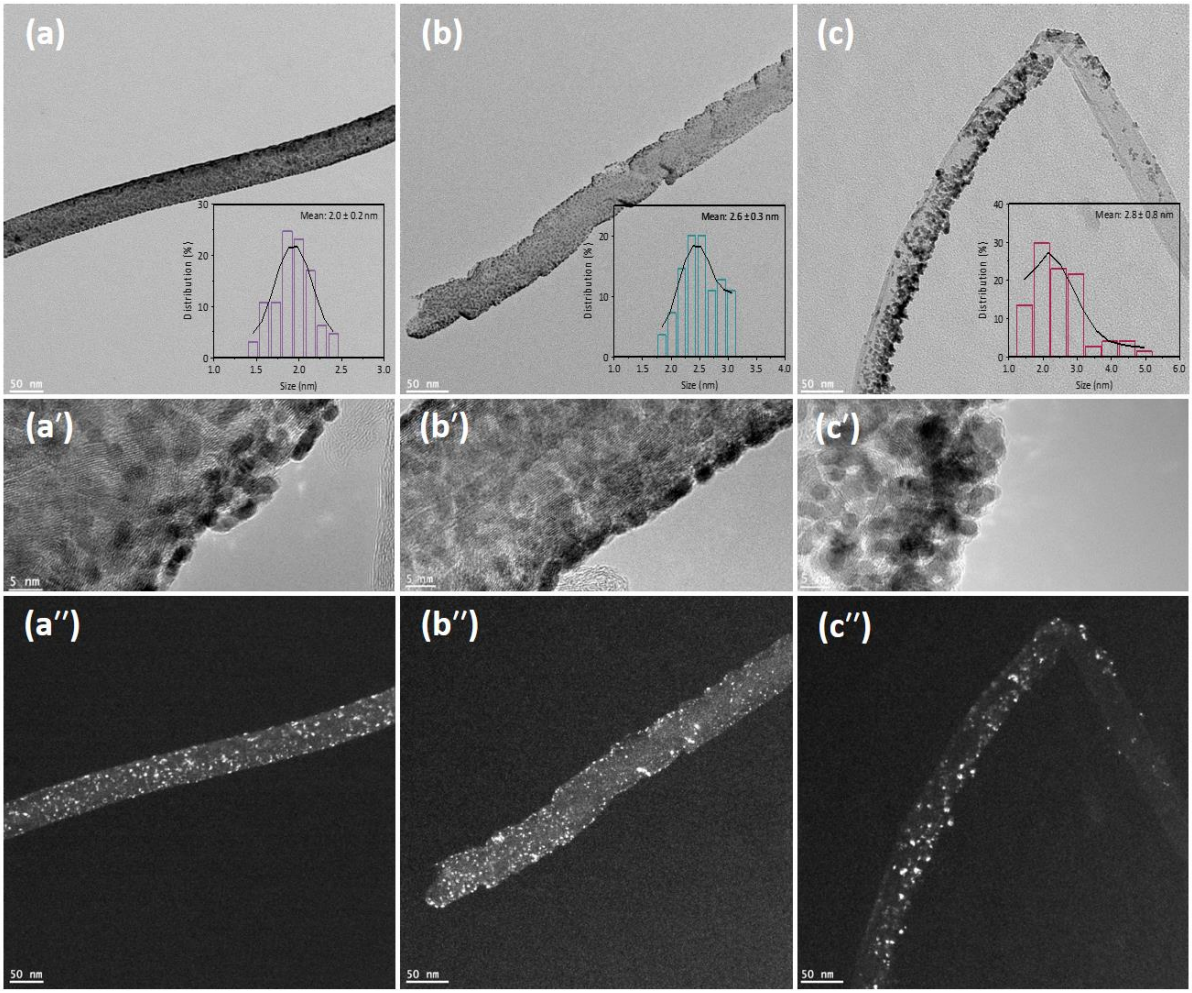

Figure S6-2. Bright field, size distribution, high resolution, and dark field TEM images of Pt/MWCNTs synthesized by PLA for 5 min and background gas pressure of (a, a′, a″) 10^{-5} Torr, (b, b′, b″) 10^{-2} Torr and (c, c′, c″) 1 Torr.

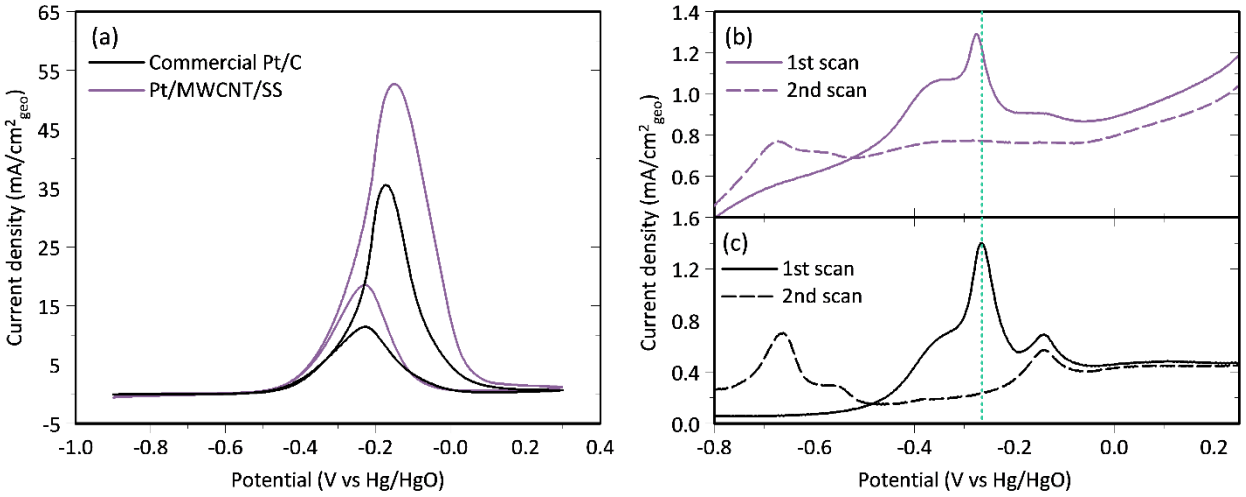

Figure S6-3. (a) Cyclic voltammograms of commercial Pt/C and Pt/MWCNT/SS synthesized by PLA at 10^{-5} Torr for 5 min, recorded in 1M KOH + 1M MetOH at a scan rate of 5 mV s^{-1}. CO stripping voltammograms of (b) Pt/MWCNT/SS synthesized by PLA at 10^{-5} Torr for 5 min, and (c) Pt/C, recorded in 1M KOH at a scan rate of 20 mV s^{-1}.

Table S6-2. Methanol electro-oxidation IR-drop corrected data

Pressure (Torr)	Ablation time (min)	Pt mass (μg cm^{-2})	MOR Onset Potential (V)	MOR Peak Potential (V)
Bulk Pt electrode	—	—	-0.19	-0.05
Commercial Pt/C	—	35.56	-0.60	-0.17
10^{-5}	1	12.4 ± 0.4	-0.56	-0.19
	2.5	22.9 ± 0.6	-0.63	-0.16
	5	35.6 ± 1.0	-0.57	-0.16
	7.5	57.8 ± 1.7	-0.60	-0.17
	10	75.6 ± 2.3	-0.61	-0.17
10^{-2}	1	15.5 ± 1.3	-0.60	-0.18
	2.5	21.6 ± 2.6	-0.66	-0.17
	5	35.4 ± 2.1	-0.64	-0.16
	7.5	56.4 ± 4.2	-0.59	-0.17
	10	81.4 ± 4.4	-0.61	-0.16
1	1	12.3 ± 1.5	-0.71	-0.21
	2.5	20.4 ± 2.5	-0.70	-0.11
	5	27.2 ± 4.2	-0.68	-0.16
	7.5	51.0 ± 4.4	-0.64	-0.18
	10	72.8 ± 5.7	-0.58	-0.15

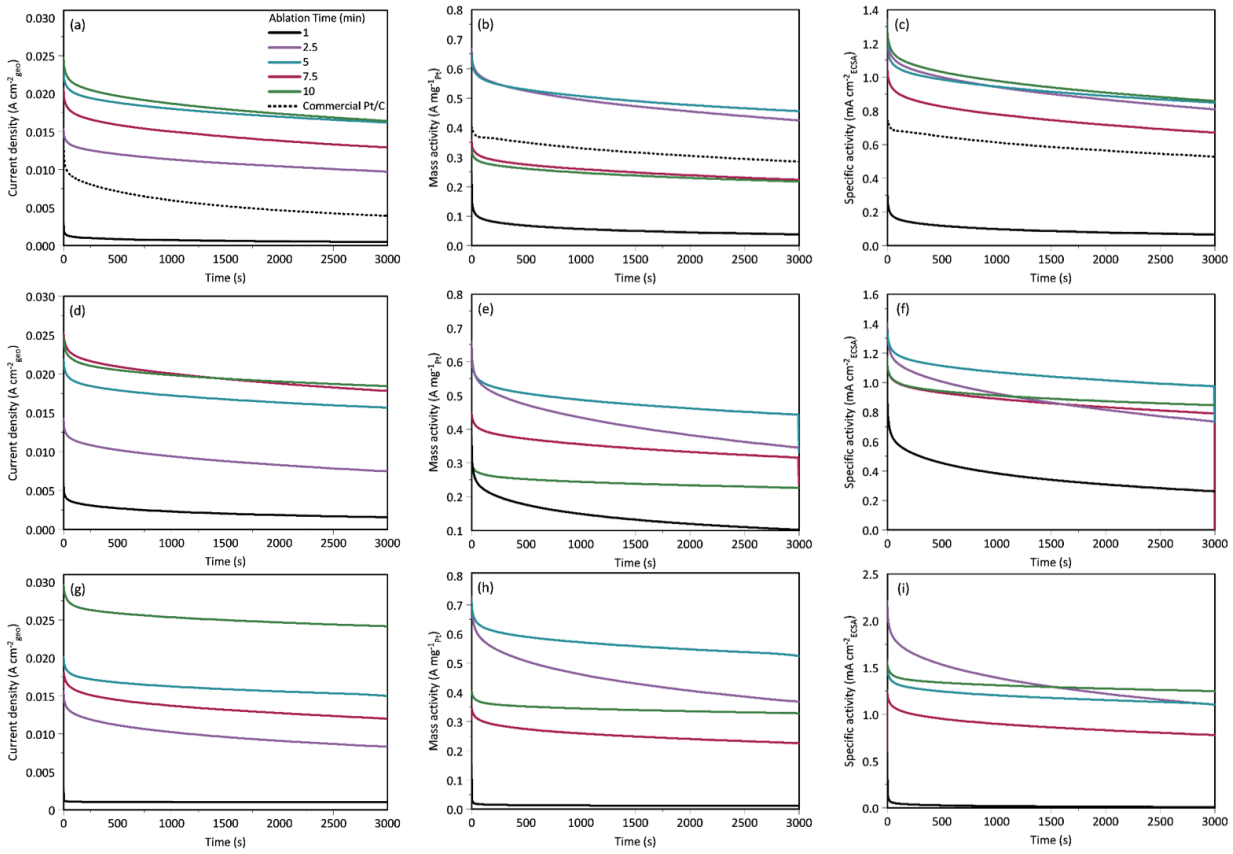

Figure S6-4. Stability of Pt/MWCNTs/SS electrodes measured by chronoamperometry at -0.2 V vs Hg/HgO in 1M KOH + 1M MetOH. Pt deposition for different ablation times at (a, b, c) 10^{-5} Torr and commercial Pt/C, (d, e, f) 10^{-2} Torr and (g, h, i) 1 Torr.

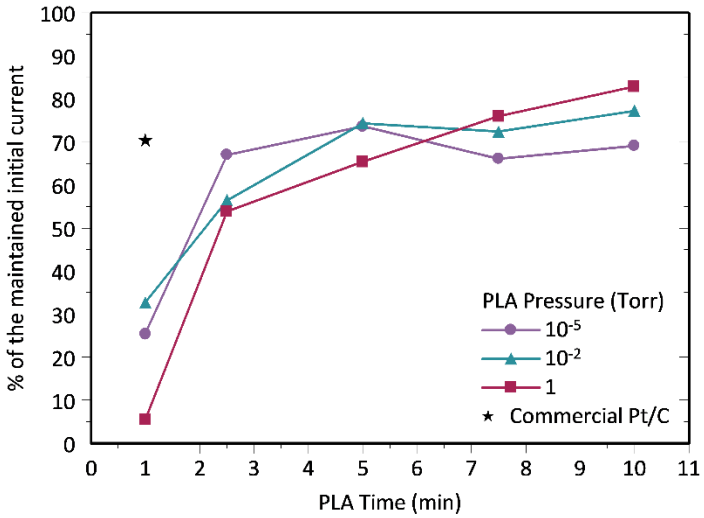

Figure S6-5. Percentage of the maintained initial MOR current after the stability of Pt/MWCNTs/SS electrodes measured by chronoamperometry at -0.2 V vs Hg/HgO in 1M KOH + 1M MetOH for 3000 s.

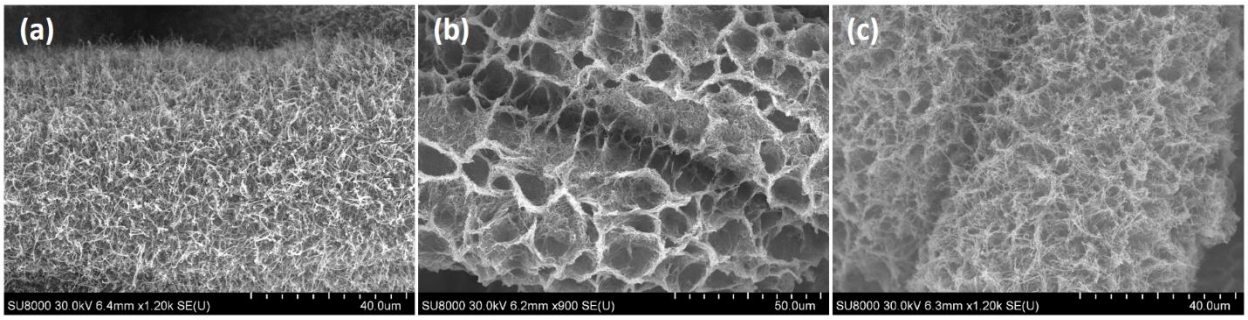

Figure S6-6. SEM images of Pt/MWCNTs/SS synthesized by PLA at 1 Torr for 10 min; (a) before MOR, (b) after performing MOR under the conditions specified in Figure S6-3 and rinsing with water and drying at room temperature and (c) after performing MOR under the conditions specified in Figure S6-3 and immediate freeze-drying.

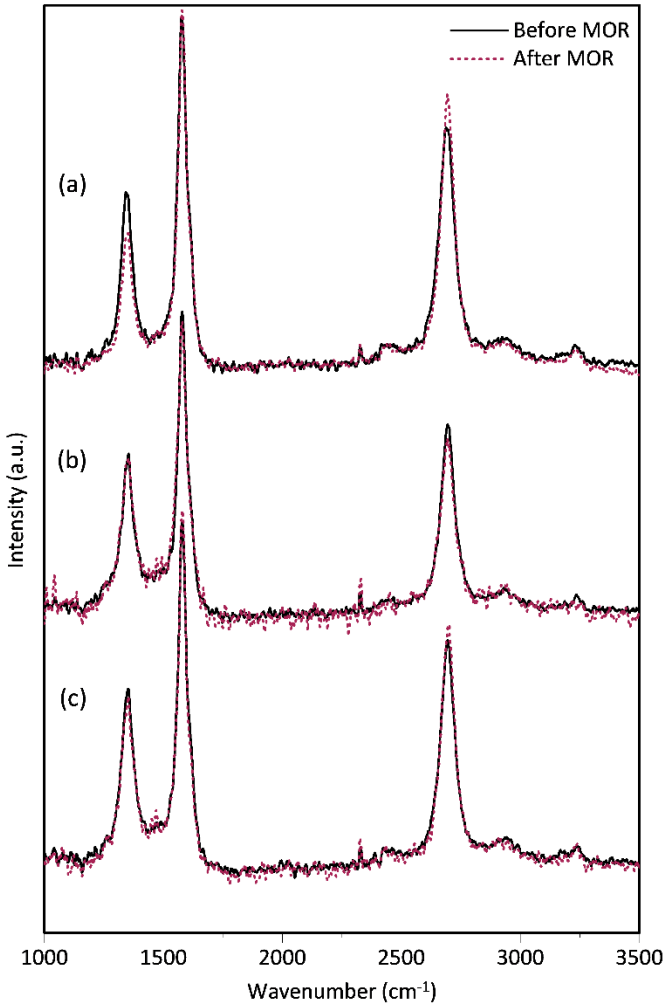

Figure S6-7. Raman spectra of Pt/MWCNTs/SS synthesized by PLA for 5 min at pressures of (a) 10^{-5} Torr, (b) 10^{-2} Torr, and (c) 1 Torr, before and after MOR under the conditions specified in Figure S6-3.

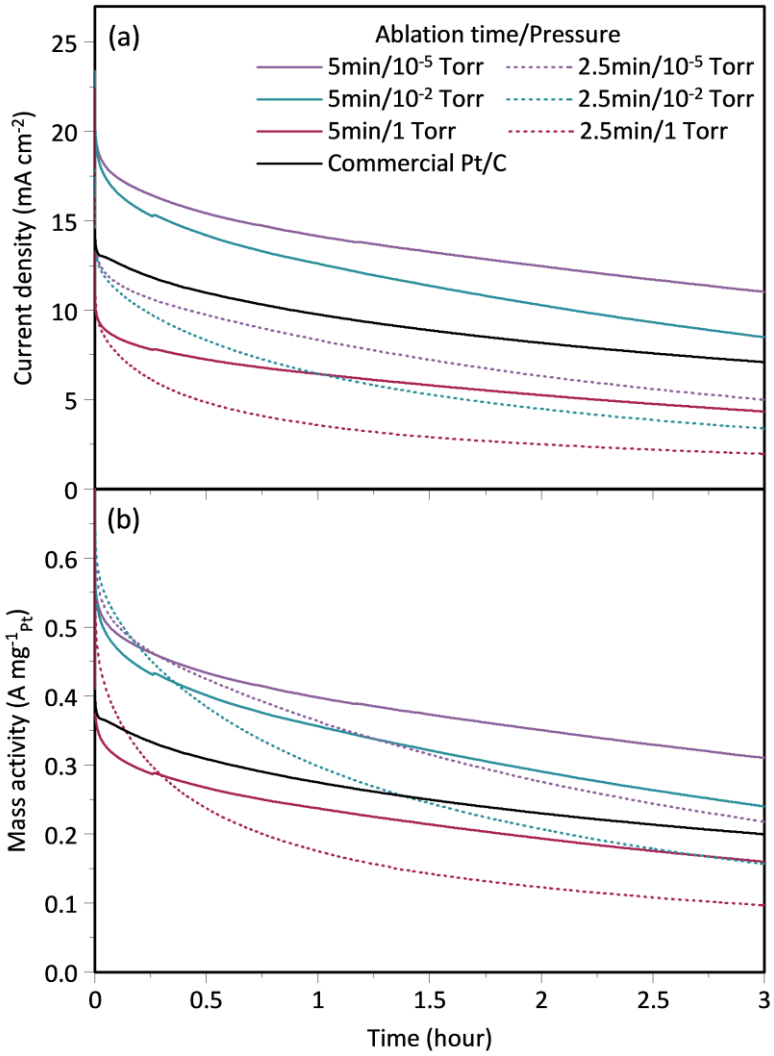

Figure S6-8. Extended stability test of Pt/MWCNT/SS and commercial Pt/C performed by chronoamperometry in 1M KOH + 1M MetOH at -0.2 V vs Hg/HgO for 3 hours, (a) per geometric surface area and (b) per mass of Pt.

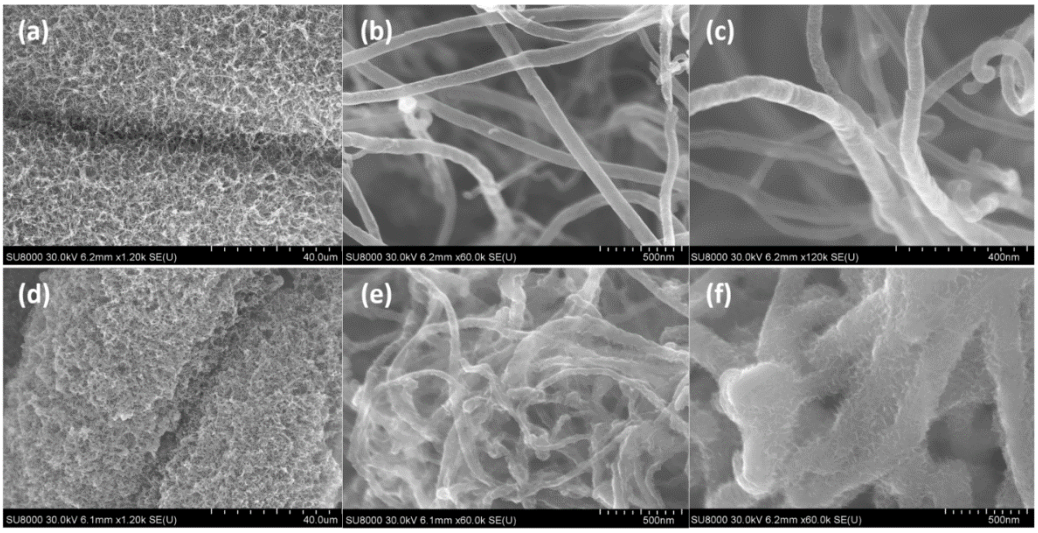

Figure S6-9. SEM images after five 60-min cycles of chronoamperometry in 1M KOH + 1M MetOH at the potential of -0.2 V of (a-c) Pt deposited at 10^{-5} Torr for 5 min, and (d-f) Pt deposited at 10^{-5} Torr for 2.5 min.

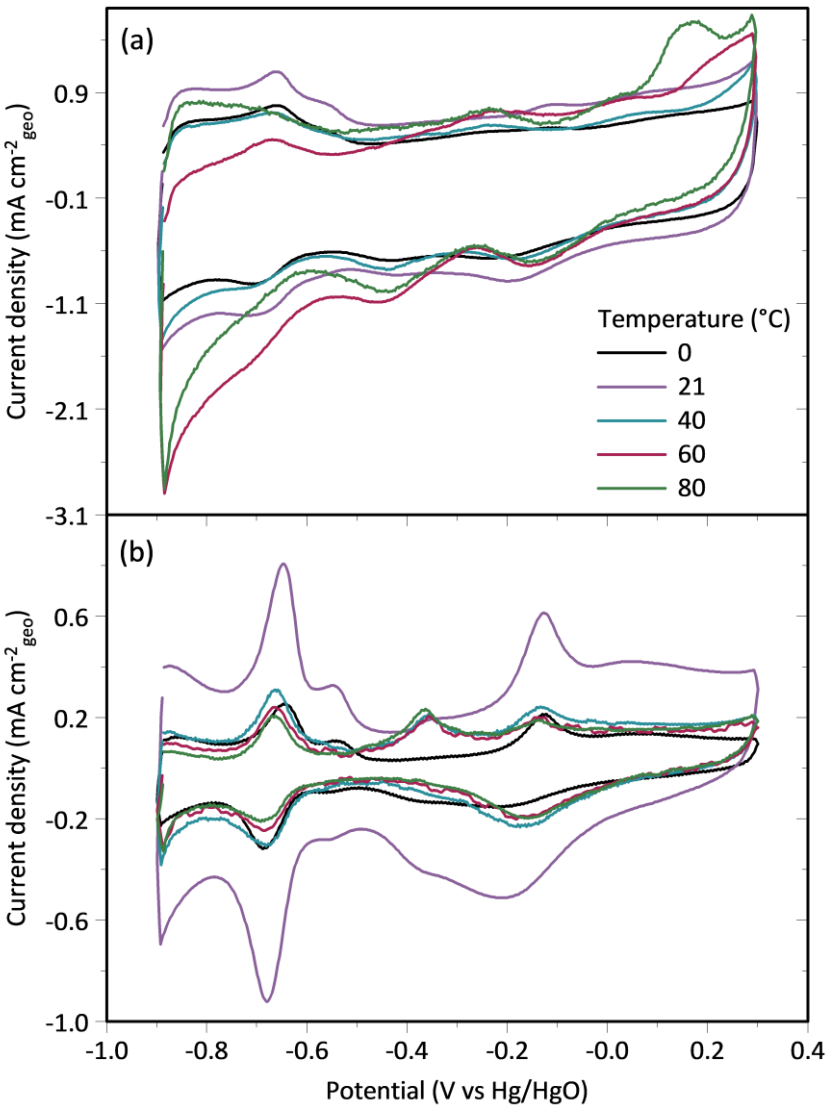

Figure S6-10. Cyclic voltammetry of (a) Pt/MWCNT/SS synthesized by PLA at 10^{-5} Torr for 5 min, and (b) Pt/C recorded in 1M KOH at different temperatures and a scan rate of 20 mV s^{-1}.

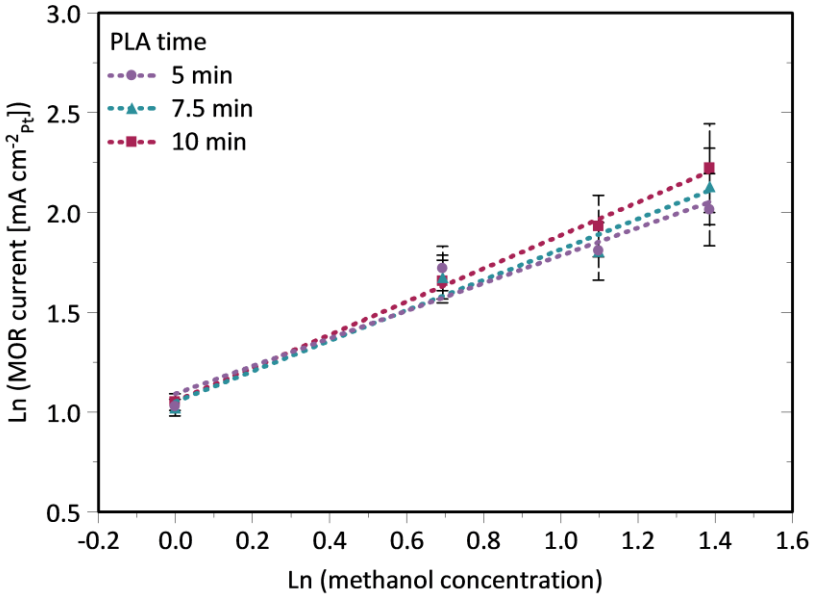

Figure S6-11. Determination of the order of methanol oxidation reaction with respect to methanol.

Table S6-3. Comparative literature and our data on the performance of Pt-based electrocatalysts in the MOR

No.	Catalyst	Electrolyte	A mg^{-1}_{Pt}	Ref.
1	Pt_xIr/MWCNT	0.1 M $HClO_4$ + 0.5 M MetOH	1.1 at 21 °C	[268]
2	urea modified Pt-MWCNTs	0.5 M H_2SO_4 + 1.0 M MetOH	0.52 at 21 °C	[269]
3	Pt–Ru/MWCNTs-OH	0.5 M H_2SO_4 + 1 M MetOH	1.7 at 21 °C	[270]
4	PtRu(1:1)/MWCNT	0.5 M H_2SO_4 + 1 M CH_3OH	0.2 at 21 °C	[271]
5	PtRu/f-MWCNT	0.5 M H_2SO_4 + 1 M CH_3OH	1.4 at 70 °C	[272]
6	Pt/P doped -MWCNTs	1.0 M KOH+ 1.0 M MetOH	0.84 at 21 °C	[273]
7	$Pd_{15}Ag_5$/CNT	1 M KOH + 0.5 M MetOH	0.7 at 21 °C	[244]
8	Commercial 20% Pt/C	1.0 M KOH+ 1.0 M MetOH	1.0 at 21 °C 2.6 at 80 °C	This study
9	Pt/MWCNTs	1.0 M KOH+ 1.0 M MetOH	1.5 at 21 °C 5.5 at 80 °C	This study
10	Pt/MWCNTs	1.0 M KOH+ 4.0 M MetOH	4.0 at 21 °C	This study

6.6.3 EIS Analysis

In order to explain the impedance behavior of the electrodes at different potentials, an equivalent circuit model shown in Figure S6-8(b) was proposed based on the shape of the Nyquist plots, and the fitted parameters are reported in Table S6-4. In the equivalent circuit model, R_s is the resistance of the solution, a parallel RC comprising of R_{elc} and CPE_{elc} reflects the response of the system in the high-frequency region, characterized by the appearance of a small semicircle (Figure S6-8(c,d)). The origin of this semicircle can be related to the porous structure of the electrode, where the R_{elc} represents the resistance to transport of charged/electroactive species through the pores, and CPE_{elc} represents the corresponding non-ideal capacitance in the double-layer at the solid/electrolyte interface, where the non-ideality arises from surface roughness, porosity and complexity of the double-layer structure [274]. R_{met} and CPE_{met} are related to the methanol oxidation reaction, where R_{met} represents the charge-transfer resistance, and CPE_{met} represents the corresponding non-ideal capacitance. R_{int} and L_{int} account for the presence of reaction intermediates on the Pt surface. Due to the non-uniform distribution of surface charge and the presence of irregular porosity and/or surface roughness, a constant-phase-element (CPE) was used instead of pure capacitance for methanol and CO_{ads} oxidation reactions [264, 265, 267].

As the potential increases from -0.6 V to -0.2 V, both R_{met} and R_{int} decreased significantly for both electrocatalysts (Figure S6-8(c,d)). This demonstrates an enhancement in the kinetics of the methanol oxidation and CO_{ads} oxidation on the surface of Pt electrocatalyst at higher potentials. These results are in accordance with CV measurements (Figure S6-8(a)), where the steady-state current increases by increasing the potential. The semicircle in the Nyquist plots becomes noticeably smaller, while the phase-angle maximum peak in the Bode plots shifts toward higher frequencies (Figure S6-8(c,d)). In addition, increasing the potential results in an increase in OH coverage on the surface of the electrocatalysts, facilitating the oxidation of intermediates (CO_{ads}) to CO_2 and thus enhancing the methanol oxidation by exposing new Pt active sites to methanol molecules [264, 265, 267].

It can be seen that for the oxidation of 1M methanol on the surface of Pt/MWCNT/SS and Pt/C electrocatalysts at the potential of 0 V (Figure S6-8(b-d)), the value of R_{met} becomes negative and increases in absolute value. A decrease in faradaic current by increasing the potential can result in the negative value of this resistance ($R = dE/dI$). This can be explained by the lower availability of free electrocatalytic active Pt sites due to the higher coverage of OH on Pt or the formation of PtO,

which decreases the rate of methanol oxidation reaction and subsequently increases R_{met}. The increase in R_{int} at 0 V can also be explained by the slower methanol oxidation that results in the formation of lower amount of CO_{ads} on Pt. Therefore, the kinetics of CO_{ads} oxidation to CO_2 also decreases. Another reason can be the higher formation of PtO over Pt-OH, reducing the rate of CO_{ads} oxidation [264, 265, 267]. By further increase of the potential to +0.2 V, MOR on the surface of Pt/MWCNT/SS and Pt/C electrocatalysts (Figure S6-8(b)) becomes the rate-determining step due to the formation of PtO with low activity toward MOR; thus, R_{met} continues to increase (large semicircle in Nyquist and low-frequency peak in Bode plots).

Table S6-4. Equivalent circuit parameters for different electrodes in 1M KOH + 1M MetOH at different potentials

PLA time	Potential (V)	R_s (Ω cm^2)	CPE_{elc} –T×10^3 (Ω^{-n} s^n cm^{-2})	CPE_{elc} -P	R_{elc} (Ω cm^2)	CPE_{met}-T×10^3 (Ω^{-n} s^n cm^{-2})	CPE_{met} -P	R_{met} (Ω cm^2)	L_{int} (H cm^2)	R_{int} (Ω cm^2)
Pt/C	-0.6	1.23	13.79	0.63	3.53	4.89	0.96	10.1 x10^4	476.01	1758.8
	-0.4	1.21	19.42	0.59	6.02	4.61	1.0	40.47	10716.08	13343.7
	-0.2	1.25	16.22	0.63	10.12	6.45	1.0	4.71	2.74	0.0
	0.0	0.95	20.39	0.18	2.92	8.19	0.84	-36.65	35.23	101.6
	+0.2	1.25	10.92	0.65	3.16	4.50	0.95	11.9 x10^4	472.33	1891.9
5 min	-0.6	3.26	54.39	0.85	5.20	20.75	0.98	4.2x10^4	60.16	1170.4
	-0.4	3.25	18.53	0.9	14.31	35.23	1.0	11.14	103.93	71.1
	-0.2	3.25	34.88	0.81	4.16	17.24	1.0	1.86	0.49	0.0
	0.0	3.22	230.28	0.75	19.49	17.97	0.9	-28.25	327.58	108.5
	+0.2	3.24	57.20	0.81	7.85	17.32	0.98	7026.54	1490.72	1738.8

Chapter 7

7. Manuscript 4: Radiofrequency Plasma-Assisted Pulsed Laser Deposited Pt/TiO_xN_y Coatings on Multi-walled Carbon Nanotubes as Gas Diffusion Electrodes for the Oxygen Reduction Reaction

7.1 Preface

This chapter presents an article submitted to a peer-reviewed journal with the following citation:

Elmira Pajootan, Sammie Amin Alolabi, Sasha Omanovic, Sylvain Coulombe, Radiofrequency Plasma-Assisted Pulsed Laser Deposited Pt/TiO_xN_y Coatings on Multi-walled Carbon Nanotubes as Gas Diffusion Electrodes for the Oxygen Reduction Reaction, Paper under review by Advanced Materials Technologies.

Authors contributions:

E. Pajootan (the Ph.D. candidate) was responsible for conceiving the idea, planning of experiments, performing the experimental work including catalyst synthesis, electrochemical tests, and material characterization. Sammie Amin Alolabi assisted in synthesizing the samples, performing XPS analysis, and analyzing the corresponding results. Prof. Sasha Omanovic and Prof. Sylvain Coulombe supervised the work, provided insightful comments on the results, provided funding support for the experiments, and reviewed the manuscript.

The potential use of Pt/MWCNT/SS as anode and cathode electrodes for methanol oxidation and oxygen reduction reactions, respectively was discussed in the preceding chapters. In this chapter,

the PLA setup was coupled with radiofrequency plasma to deposit titanium oxynitride (TiO_xN_y) thin films with different morphologies and chemical compositions on MWCNTs. The electrodes were tested for oxygen reduction reaction in a gas diffusion setup in an alkaline medium. Finally, Pt nanoparticles were deposited on the TiO_xN_y thin films to further enhance the ORR electrocatalytic activity.

Abstract

This study reports on the fabrication and characterization of novel multilayered electrocatalyst nanostructures for the oxygen reduction reaction (ORR). Thin titanium oxynitride (TiO_xN_y) coatings were deposited on a forest of multi-walled carbon nanotubes (MWCNTs), directly grown on a stainless steel mesh, by capacitively-coupled radiofrequency plasma-assisted pulsed laser deposition (RF-PAPLD) in N_2 environment. The resulting high-surface-area binder-free electrode was further coated with a low quantity of well-dispersed Pt nanoparticles (NPs) by PLD in an inert atmosphere. High-speed imaging of the laser-induced plasma expansion provided evidence of a higher kinetics of the expanding plume at higher RF plasma powers, changing the morphology of the TiO_xN_y coatings. X-ray photoelectron spectroscopy demonstrated that the coatings are homogeneous throughout their thickness, where the Ti-N, Ti-O-N and Ti-O bonds exist in all samples. The oxygen content in the coating increases with the RF plasma power. Both TiO_xN_y/MWCNT and Pt/TiO_xN_y/MWCNT nanostructures were tested in a gas diffusion electrode setup to evaluate their activity in the ORR. The results showed the superior activity of the Pt/TiO_xN_y-0.03 Torr-30 W/MWCNT, reaching the highest current density of 180 mA cm^{-2}, while the commercial Pt/C electrode with the same Pt loading yielded 105 mA cm^{-2} at the overpotential of 0.5 V.

Keywords: RF plasma-assisted pulsed laser ablation; titanium oxynitride; high-speed imaging; gas diffusion electrode.

7.2 Introduction

The fuel cell technology is one of the green alternatives pursued for the decarbonization of the energy and transportation sectors. However, the development of low-temperature fuel cells is

hampered by the slow kinetics of the oxygen reduction reaction (ORR) at the cathode, even when the most effective electrocatalyst, platinum, is used. Moreover, the cost, scarcity and high environmental footprint of Pt have directed research toward minimizing its loading, while improving its intrinsic electrocatalytic activity and stability, as a feasible strategy to balance electrocatalytic activity and fuel cell costs [207, 275]. Downsizing Pt to nanoparticles (NPs) is one of the practical approaches to lower its loading, while significantly enhancing its activity. However, the parallel problems are the complexity of the Pt NPs synthesis process and their aggregation during the ORR, limiting their range of practical applications. Introducing a support material for Pt can enhance the activity and stability of Pt NPs by enabling strong metal-support interactions [276, 277].

Owing to their wealth of properties, transition metal nitrides, especially titanium nitride (TiN) and titanium oxynitride (TiO_xN_y), have become essential technological materials, offering highly desirable properties such as hardness, excellent wear resistance, high melting point, thermodynamic stability, electrical conductivity, and corrosion resistance. Thin films of these materials have drawn considerable attention for use as coating materials for various applications such as cutting and drilling tools, diffusion barriers in integrated circuits, contact materials in semiconductors, and as catalyst supports for various heterogeneous reactions [278-282]. In addition, the thermodynamically-favorable formation of the native layer containing a mixture of oxide and oxynitride film on the surface of TiN makes it resistant to further oxidation [283, 284].

TiN NPs are mainly produced by magnetron sputtering, nitridation of titanium oxide by nitrogen sources such as ammonia or nitrogen at high temperature, and chemical vapor deposition utilizing volatile precursors such as $TiCl_4$ [281, 285, 286]. The latter, however, faces problems such as chlorine impurity incorporation and high-temperature requirements (higher than 600 °C). On the other hand, gas-phase techniques are solvent-free routes toward synthesizing TiN at low temperatures [287]. With advances in continuous, high-quality large-area film growth by pulsed laser deposition (PLD), more attention is directed toward using this method for thin film deposition [288]. PLD is an efficient gas-phase technique in which a focused short-pulse high-fluence laser beam is aimed at a target. The target absorbs the laser energy, and a rapid temperature increase occurs in the external layers of the target. This leads to the rapid evaporation of the target, which generates a laser-induced plasma plume containing metal adatoms or clusters, ions, and electrons. The produced plume with high gas temperature (~ 3000-4000 K) and high particle velocity (up to

10^6 cm s^{-1}) expands away from the target [75, 160-167, 289]. The supersaturation of the metal vapor cloud is followed by the nucleation, condensation as nanoparticles and possible aggregation upon interaction with the background gas. The energy loss of the formed clusters/nanoparticles and associated fast cooling rate (> 10^4 to 10^{10} K s^{-1}) in less than 50 μs result in the generation of small solid particles (< 100 nm). The ablated metal and formed nanoparticles can be directly collected on the desired support material [163-166]. PLD is competitive compared with other techniques like vacuum evaporation and sputtering in terms of deposition rate, strong nanoparticle-support interactions, chemical purity, and homogenity of the deposited film [290, 291].

In this study, a combination of a nanosecond pulsed laser deposition (PLD) and a low-pressure capacitively-coupled radiofrequency plasma, called radiofrequency plasma-assisted pulsed laser ablation (RF-PAPLD), was used to synthesize TiN and TiO_xN_y coatings on multi-walled carbon nanotubes (MWCNTs) grown directly on stainless steel (SS), followed by the deposition of Pt NPs by PLD. The interaction of the radiofrequency plasma with the laser-induced plasma containing ground- and excited-state atoms, ions and electrons is known to affect the morphology, roughness and composition of the deposited layers [292]. Therefore, high-speed imaging of the laser-induced plasma formed during the ablation process was performed to investigate the evolution of the laser-induced plasma and its expansion dynamics to explain the different morphologies obtained when comparing the PLD and RF-PAPLD processes. X-ray photoelectron spectroscopy (XPS) and scanning electron microscopy (SEM) imaging were used as the main characterization techniques to investigate the composition and morphology of the coatings. The synthesized TiO_xN_y/MWCNT/SS nanostructures with and without Pt NPs as the top electrocatalyst layer were evaluated for the oxygen reduction reaction in an alkaline medium using a gas-diffusion-electrode setup.

7.3 Materials and Methods

7.3.1 Synthesis of Pt/TiO_xN_y/MWCNT/SS Nanostructured Electrodes

The process developed to directly grow MWCNTs on stainless steel (SS) 316L mesh coupons (grid bars: 165 × 800 per 6.45 cm^2; wire diameters: 0.07 and 0.05 mm; grid opening: 15 microns, purchased from TWP Inc.) is explained in greater details in our previous manuscripts [99, 100]. In brief, a semi-batch chemical vapor deposition (CVD) method was used to directly grow MWCNTs

(diameter: ~ 30-40 nm and length: ~ 13–15 μm) on SS. The SS mesh was used for the growth of MWCNTs owing to its high iron content; the iron islands on the SS surface act as growth sites for the MWCNTs. This binder-free synthesis approach leads to strongly-anchored MWCNTs, decreasing the electrical contact resistance between the MWCNTs and the current collector (SS mesh). The SS mesh was first cleaned in acetone for 30 min using an ultrasonic bath and loaded in a CVD furnace (oxygen level below 0.5%). Acetylene (flow rate of 68 ± 5 sccm) was co-injected with argon (592 ± 5 sccm) and thermally decomposed at 700 °C for 2 min during the MWCNT growth phase. The as-produced MWCNTs are intertwined, forming a dense forest-like nanostructure on the SS surface. The MWCNT/SS coupons were then transferred to the RF-PAPLD chamber to be used as the support material for the deposition of TiO_xN_y and Pt/TiO_xN_y.

Figure 7-1(a) shows a schematic of the RF-PAPLD setup. Pt and Ti targets (99.995%, Ted Pella Inc.) were ablated using the third harmonic (355 nm) of a pulsed nanosecond Nd:YAG laser (Quantel, Brilliant B10, repetition rate: 10 Hz, and pulse width: 5 ns) with the laser energy of 66 mJ $pulse^{-1}$. The (Ti or Pt) target was mounted on a 10 cm-outer diameter (O.D.) stainless steel disc, while the PLD-produced nanoparticles were deposited on the MWCNT/SS substrate mounted on a 6 cm O.D. stainless steel disc directly facing the target (3 cm target-substrate distance). The PLD-produced metal vapor plume/nanoparticle stream was immersed into a large volume continuous-wave capacitively-coupled radiofrequency (13.56 MHz) plasma sustained using the substrate as the powered electrode and the target as the ground. Prior to each experiment, the chamber was flushed with Ar for 3 min and pumped down to a base pressure of 10^{-5} Torr to remove air and minimize the moisture level. The target holder was rocked up and down during ablation to ensure uniform wear and to minimize thermal effects resulting in localized melting and ejection of liquid metal droplets. The substrate holder was manually rotated during PLD to ensure uniform nanoparticle dispersion over the substrate. Titanium oxynitride (TiO_xN_y) films were deposited on MWCNT/SS at N_2 background gas pressures of 0.03 and 1.0 Torr, and RF power levels of 0, 10 and 30 W for 10 min. Pt NPs were deposited by PLD on the MWCNTs and TiO_xN_y-coated MWCNTs at an Ar background gas pressure of 10^{-5} Torr for 2.5 min. The sample coding presented in Table S7-1 is based on the chamber pressure and RF power level. For instance, TiO_xN_y-1.0 Torr-0 W refers to a RF plasma of 0 W (no plasma) during PLD at the pressure of 1.0 Torr.

A high-speed camera (Photron FASTCAM SA5, model 1000K-M1, monochromatic) was used to study the expansion dynamics of the laser-induced metal vapor plume. An arbitrary function

generator (Tektronix-AFG3102) was used to trigger the laser Q-switch and camera at prescribed delays with respect to the flashlamp output signal. The laser Q-switch was externally triggered with a 215 μs delay, while the camera delay was varied between 214 and 614 μs (20 ns increments) to cover the entire laser plume expansion event. A total of 64 frames (896 × 848 pixels) at 1 μs exposure were captured at any given camera time delay. The frames were then accumulated to produce an average image of the expanding plasma plume, frozen in time, at the corresponding camera delay.

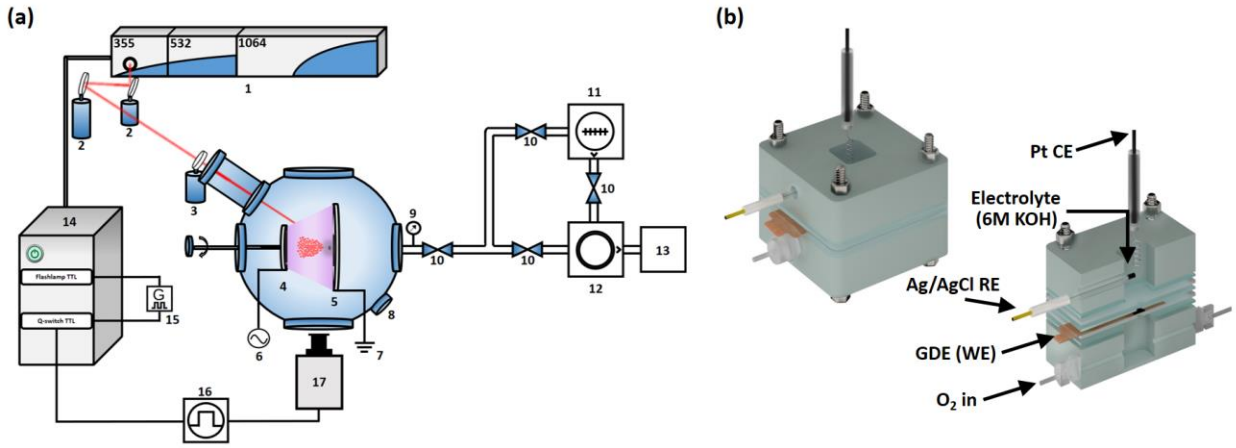

Figure 7-1. (a) RF-PAPLD setup; 1) Nd:YAG laser, 2) mirrors, 3) lens, 4) substrate, 5) target, 6) RF powered (live) electrode, 7) ground electrode, 8) gas inlet, 9) pressure gauge, 10) pneumatic valves, 11) turbomolecular pump, 12) primary mechanical pump, 13) exhaust, 14) laser control, 15) signal generator, 16) TTL trigger, 17) high-speed camera; (b) gas diffusion electrochemical cell setup.

7.3.2 Structural and Electrochemical Characterization

The morphology of the TiO_xN_y nanostructures before and after deposition of Pt NPs was studied by ultra-high-resolution field-emission scanning electron microscopy (Hitachi, Cold FE SU-8000 SEM). Transmission electron microscopy (Thermo-Scientific, Talos F200X G2 TEM) was used to investigate the morphology of the TiO_xN_y coatings, Pt NP size distribution and crystalline/lattice d-spacing, and elemental mapping of the synthesized Pt/TiO_xN_y. X-ray photoelectron spectroscopy (Thermo-Scientific, K-alpha XPS apparatus, Al Kα source, micro-focused monochromator and spot size of 200 μm) was used to investigate the chemical state of the TiO_xN_y before and after the deposition of Pt NPs. The flood gun was turned ON during the XPS data acquisition to avoid the charging effect. The Avantage software (Thermo Fisher Scientific)

was used to analyze the obtained spectra. A mixed Gaussian/Lorentzian peak shape was used for all components for peak fitting.

The electrocatalytic activity of the binder-free nanostructured electrodes in the oxygen reduction reaction (ORR) was evaluated employing them as a gas-diffusion-electrode (GDE) assembly in an alkaline (6M KOH) electrolyte. The GDE assembly depicted in Figure 7-1(b) consists of a polytetrafluoroethylene (PTFE) cell, Ag/AgCl reference electrode, Pt coil counter electrode and the GDE, which is in contact with the electrolyte on one side and oxygen on the other. The presence of MWCNTs on both sides of the SS mesh allows to employ the developed electrodes directly as the GDEs, without using a binder and GDE backing (carbon paper). In these experiments, the GDEs were first pre-conditioned by potential cycling from 0.4 to 1.1 V (40 cycles) at 21 ± 1 °C at a scan rate of 20 mV s^{-1}, while feeding humidified oxygen (purity 99.5%), then the linear-scan-voltammogram (LSV) was recorded in the same potential range and scan rate to evaluate the performance of the GDEs for ORR. To assess the stability of the electrocatalyst, an accelerated durability test (ADT) was performed by applying cyclic potential sweeps between 0.4 and 1.1 V for 500 cycles at a scan rate of 20 mV s^{-1}. Similarly, the results were compared to the GDE made with commercial Pt/C as control (see section 7.6.1 for Pt/C preparation steps).

7.4 Results and Discussion

7.4.1 TiO_xN_y/MWCNT

The SEM images in Figure 7-2 reveal the morphology of the TiO_xN_y coatings deposited on MWCNTs by RF-PAPLD at different N_2 background gas pressures and RF power levels. Figure S7-1 also shows the surface of MWCNTs before and after the deposition of TiO_xN_y films at high magnification, which clearly demonstrates the coverage of the MWCNT surface by TiO_xN_y with different morphologies. At lower magnification, Figure 7-2(a-c) shows that the MWCNTs are uniformly coated by a thin TiO_xN_y film of 10-20 nm in thickness (measured using HRTEM images) when deposited at a chamber pressure of 0.03 Torr. It is evident from the SEM images that the interaction of the RF plasma with the laser-induced plasma plume altered the morphology of the thin film. By increasing the RF plasma power, it appears that the smooth TiO_xN_y coating converts to a prominently step-like or layer-by-layer thin coating on the MWCNTs. On the other hand, it can be seen in Figure 7-2(d-f) that at a chamber pressure of 1.0 Torr, small aerosol-like

nanoparticles are attached to the MWCNT surface without forming a film on the surface. By increasing the RF plasma power, the extent of these aerosol-like nanostructures significantly decreases and a rough TiO_xN_y film covers the surface of MWCNTs [100, 293]. The formation and growth of Ti nanoparticles are governed by the saturation, condensation, collision/coalescence and agglomeration of the ejected Ti adatoms/clusters. Increasing the chamber pressure leads to more interaction of Ti adatoms/clusters with N_2 gas molecules. Therefore, early condensation and agglomeration of the solidified particles occurs, resulting in the formation of aerosol-like nanostructures [99, 100].

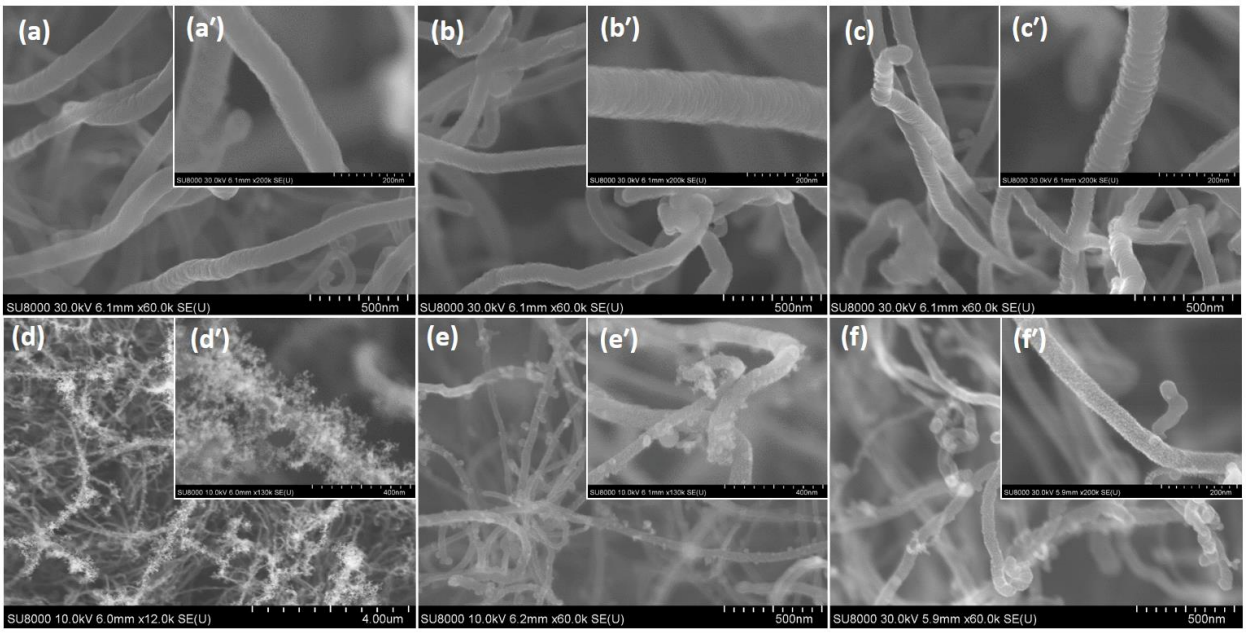

Figure 7-2. SEM images of TiO_xN_y thin film-coated MWCNTs (a, a′) 0.03 Torr-0 W, (b, b′) 0.03 Torr-10 W, (c, c′) 0.03 Torr-30 W, (d, d′) 1.0 Torr-0 W, (e, e′) 1.0 Torr-10 W and (f, f′) 1.0 Torr-30 W.

To study the effect of RF plasma power on the morphology of the deposited films, the evolution of the laser-induced plasma plume expansion for RF-PAPLD at the chamber pressure of 0.03 Torr was investigated and the results are presented in Figure 7-3(a). The laser-solid interaction results in the sublimation of the surface layer of the titanium target, and subsequent formation of a metallic vapor cloud energetic enough to be significantly ionized, expanding in the low-pressure environment. This enhances the collisions on the expansion front and inter-plume regions, which increases the fluorescence from all species, as observed in Figure 7-3(a). The right-most column in Figure 7-3(a) corresponds to the time delay of 30 μs after the end of the laser ablation pulse. It

can be seen that at this point in time, speckles are captured by the camera. The authors attribute these speckles to droplet ejection from the localized erosion of the titanium target by the laser pulse. These droplets are ejected at temperatures between the melting and boiling point of titanium (1941 K to 3560 K) and emit blackbody-like radiation visible to the camera. Before and after applying the RF plasma, the main difference is observed at longer time delays after the laser pulse, when the droplet ejection happens. Lower emission intensities were recorded when the RF plasma was applied. By investigating the Position-Time plots of the luminous plume front depicted in Figure 7-3(b), a faster expansion of the plume front is observed with the existence of RF plasma. As shown in Figure 7-3(b) and reported in other studies, adding the RF-plasma to PLD results in a higher flux and kinetics of the expanding plume [294, 295]. Therefore, applying RF plasma reduces the interaction time of Ti adatoms/clusters with the N_2 background gas and consequently, the condensed nanoparticles cover the surface of MWCNT without the formation of aerosol-like structures. As seen in Figure 7-3(e,f), aerosol-like structure are less present due to the lower extent of nanoparticle agglomeration, and a rough film is formed on the surface of MWCNTs at 1.0 Torr after applying RF plasma at 30W.

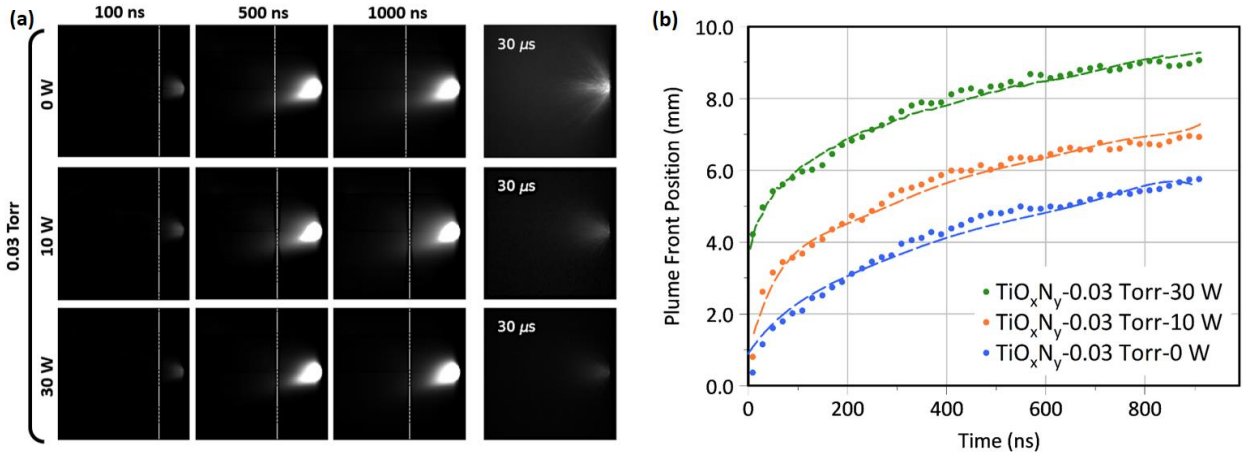

Figure 7-3. (a) laser-induced plasma plume evolution at 0.03 Torr at different RF plasma power levels, and (b) laser-induced plasma plume front propagation.

The elemental composition and chemical state of the elements in the thin TiO_xN_y films were studied by XPS. The chemical composition and homogenity of the thin film synthesized at a chamber pressure of 0.03 Torr were characterized at multiple depths through the coating with in-situ successive Ar^+ ion sputtering steps for a total time of 13 min. Further characterization of the

samples synthesized at 1.0 Torr was not performed due to their non-uniformity. Ti2p, O1s and N1s were identified as the main elements from the survey scans. Figure 7-4(a) displays the atomic percentages of Ti2p, N1s and O1s as a function of Ar^+ ion sputtering time for the TiO_xN_y thin film synthesized by RF-PAPLD at 10 W and 0.03 Torr. The film showed a homogeneous composition over its depth after approximately 360 s of sputtering, with relatively constant atomic percentages of Ti, O and N. The surface of the thin film was mainly composed of TiO_2, which was the expected native oxide layer that forms on the surface from the atmospheric oxidation of TiN. This reaction is thermodynamically favorable (its Gibbs free energy at 20 °C is -611.8 kJ mol^{-1}). Therefore, Ar^+ ion sputtering with 500 eV was carried out for 360 s over the surface of all samples to remove oxygen and other adventitious surface contamination before XPS analysis.

The deconvoluted Ti2p, N1s, and O1s core-level spectra obtained for all the thin films studied are shown in Figure 7-4(b-d). The assignment of peaks was performed based on the presence of the components in all Ti2p, N1s, and O1s spectra. The existence of TiN, TiO_2, TiON is evident in all samples, and the variation of their corresponding percentage is reported in Table S7-2. As a reference, the Ti target was ablated in an argon background gas, which resulted in the formation of a nitrogen-free thin film. Similar to previous studies, the Ti2p scan shows two different titanium oxide states in the film: TiO (455.7 and 461.3 eV) and TiO_2 (458.3 and 464.0 eV) [286, 296]. The oxide state of TiO was detected only in the thin film deposited with the argon background gas. The Ti2p spectra of TiO_xN_y samples show the Ti2p spin-orbit split $2p_{3/2}$ and $2p_{1/2}$ components at 454.7 and 460.7 eV, respectively, with a pair of satellites shifted from the primary peaks by approximately 2.8 eV toward higher binding energies (BEs) [286, 296]. The existence of TiON and TiO_2 in the film composition is also evident. The deconvolution of Ti2p spectra for the sample synthesized by RF-PAPLD at the power levels of 10 and 30 W shows an increase in the percentage of oxygen-containing species (TiO_2 and TiON). The compositional analysis for the TiO_xN_y deposited on MWCNTs revealed that this thin film is composed of approximately 87.6% TiN when the RF plasma was off during the PLD, and it dropped to 63.6% and 56.3% when the RF power levels of 10 and 30 W were used, respectively.

Referring to Figure 7-4(c and d), the N1s and O1s spectra are composed of three distinct peaks. The N1s spectra for all nitrogen-containing samples are dominated by the main peak centered at around 397.3 eV, assigned to TiN. The low-intensity feature at the high BE side of the main peak, at 399.4 eV, is assigned to the TiN satellite, and the peak at lower BE of 396.6 eV is linked to the

oxynitride (TiON). O1s is also deconvoluted to three peaks of Ti-O, Ti-OH or Ti-ON, and adsorbed moisture on Ti (Ti-H_2O) [286, 296].

Optical emission spectroscopy (OES) was used to qualitatively assess the presence of active species, including nitrogen and oxygen, generated by the RF plasma. Figure S7-2 shows an emission spectrum collected during an RF-PAPLD experiment performed at a background gas pressure of 0.03 Torr and RF plasma power of 30 W. The first and second positive systems of N_2 are clearly identified, as well as the molecular emission band around 309 nm, corresponding to the hydroxyl radical, which indicates the presence of water in the chamber. Excited molecular and atomic nitrogen species can react with Ti to form TiN. On the other hand, applying RF plasma and shorter reaction time of Ti with N_2 background gas (Figure 7-3), and the presence of hydroxyl radicals in the chamber can result in the formation of more oxygen-containing species such as TiO_2 and TiON in the deposited thin films. Similar observations and effects have been previously reported [297-299].

The electrocatalytic activity of the TiO_xN_y/MWCNT/SS electrodes in the oxygen reduction reaction (ORR) was evaluated in 6M KOH, and the samples were directly tested as gas-diffusion electrodes in our customized GDE setup with a structure mimicking the actual fuel cell application. In this setup, oxygen was provided on one side of the electrode and the electrolyte was in contact with its other side. Thus, evaluating the electrocatalysts in a gas-diffusion setup enabled testing their activity at high overpotentials due to the promoted oxygen mass transport at the electrocatalyst/electrolyte interface. In addition, it allowed a rapid electrochemical characterization without the complication and expense of a full membrane electrode assembly (MEA) screening [99, 203, 214-216].

The results in Figure 7-4(e) reveal that the ORR onset potential for the commercial Pt/C is around 0.93 V and that the ORR current reaches 105 mA cm^{-2} at the potential of 0.5 V. However, the carbon paper backing of the commercial Pt/C GDE contributes to more than 50% of the performance of the electrode at 0.5 V, with the current density of 59 mA cm^{-2}; consequently, the Pt/C ORR current at 0.5 V can be estimated to be 46 mA cm^{-2}, assuming the full access of the electrolyte to the carbon paper surface.

For the TiO_xN_y-0.03 Torr-0 W with the lowest oxygen content in its structure, the ORR commences at 0.91 V, most proximate to the commercial Pt/C onset potential, whereas an ORR onset potential of around 0.8 V is observed for TiO_xN_y-coated electrocatalysts with higher oxygen

content in their structures (TiO_xN_y-0.03 Torr-10 W and TiO_xN_y-0.03 Torr-30 W). However, the TiO_xN_y coating synthesized at an RF plasma power level of 30 W showed the highest current of 95 mA cm^{-2} at 0.5 V, and after correcting it for the background MWCNT current of 20 mA cm^{-2}, it is still higher than that on the commercial Pt/C. This result can be attributed to a more layered structure of the thin film on the MWCNT, as shown in SEM images (Figure 7-2) and high-angle annular dark-field (HAADF) images in Figure 7-5, providing higher surface area and consequently more active sites for the reduction of oxygen.

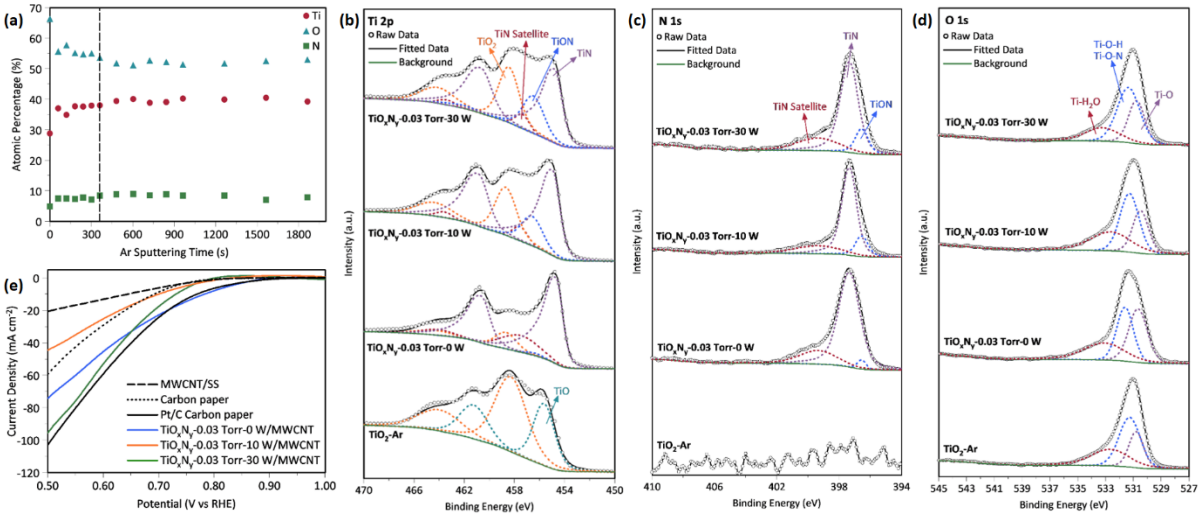

Figure 7-4. (a) Percentage of Ti, O and N elements after Ar^+ ion sputtering for different duration; deconvoluted (b) Ti2p, (c) N1s and (d) O1s spectra; (e) ORR performance of the electrodes as GDEs in 6M KOH recorded at a scan rate of 20 mV s^{-1}.

7.4.2 Pt/TiO_xN_y/MWCNT

After the successful deposition of TiO_xN_y thin films on the surface of MWCNTs, Pt NPs at low loading (22 μg cm^{-2}) were deposited on the TiO_xN_y-0.03 Torr-0W/MWCNT, TiO_xN_y-0.03 Torr-10W/MWCNT and TiO_xN_y-0.03 Torr-30W/MWCNT nanostructures using PLD at 10^{-5} Torr for 2.5 min. The morphology, crystalline structure and size distribution of Pt NPs deposited on the TiO_xN_y thin films were investigated by TEM and the images are reported in Figure 7-5(a-c). The SEM images of these samples are also shown in Figure S7-3, and the HRTEM images illustrating the coverage of the MWCNT with Pt/TiO_xN_y are depicted in Figure S7-4. The TEM images depict the dispersion of Pt NPs with an average diameter of 2.2 ± 0.4 nm over the TiO_xN_y thin films covering the MWCNTs. The elemental mapping confirms the presence of Ti, Pt, O, and N on the

surface of MWCNTs, and the selected area electron diffraction (SAED) patterns show the existence of Pt (111), (200), (220), and (311) on the surface of TiO_xN_y. However, the d-spacing of TiO_xN_y cannot be detected, which might be an indicator of an amorphous structure. Moreover, no peaks related to TiO_xN_y were detected by using the X-Ray Diffraction characterization method (results not shown). Furthermore, it is noticed that the Pt (111) d-spacing increased from 0.215 to 0.230 nm as the oxygen content in the TiO_xN_y support layer increased, which is indicative of tensile strain on Pt NPs [300, 301].

Moreover, the XPS analysis of the Pt NPs-coated samples (Figure 7-5(d)) exhibited a negative shift of 0.45 eV in the Pt4f binding energy when Pt NPs are deposited on the TiO_xN_y thin films, rather than directly on the MWCNT. This decrease in Pt4f binding is associated with a negative shift in the *d*-band center of Pt NPs. The strong metal-support interaction between Pt and TiO_xN_y can result in a redistribution of charges or drift of electrons from Pt to TiO_xN_y that modifies the electronic structure of the Pt NPs. Therefore, the adsorption of oxygen reduction intermediates is weakened on the surface of Pt NPs, and more active Pt sites are available for the reduction of oxygen molecules rather than the intermediates [276, 302, 303].

Figure 7-5(e) presents the ORR polarization curves of the Pt/TiO_xN_y/MWCNT GDEs in 6M KOH, while the corresponding activity of the GDEs is compared at 0.5 V in Figure S7-5. The results clearly indicate a significant enhancement in the ORR current density after the deposition of around 22 μg cm^{-2} of Pt on the TiO_xN_y/MWCNT. For instance, after the deposition of Pt NPs, the ORR current density of the TiO_xN_y-0.03 Torr-30 W/MWCNT increased from 95 mA cm^{-2} to 180 mA cm^{-2} for the Pt/TiO_xN_y-0.03 Torr-30 W/MWCNT. It can also be seen that the ORR current density is higher on Pt/TiO_xN_y/MWCNT than when Pt was deposited directly on MWCNTs, which can be the result of electrocatalyst-support interactions [276]. Figure 7-5(e) shows that the ORR onset potentials of all electrocatalysts are very close to each other. However, at an overpotential of 0.5 V, as the oxygen content in the TiO_xN_y increases, the ORR current density also increases from 120 mA cm^{-2} for the Pt/TiO_xN_y-0.03 Torr-0 W/MWCNT to 180 mA cm^{-2} for the Pt/TiO_xN_y-0.03 Torr-30 W/MWCNT. After removing the contribution of the support materials (carbon paper backing and MWCNT/SS) to ORR, the performance of Pt/TiO_xN_y-0.03 Torr-30 W/MWCNT (153 mA cm^{-2}) is 3 times higher than that of Pt/C (50 mA cm^{-2}). It is reported that during ORR, O and OH bind preferably to the surface Ti site and not to the Pt atom. Thus, the binding preference of an adsorbed oxygen-containing intermediate to Ti site, and the downshift of Pt *d*-band center lower

the surface poisoning of Pt electrocatalysts, and provide more Pt active site for ORR [276, 302, 303].

The stability of the electrocatalysts was assessed by accelerated durability test (ADT) for 500 cycles, and the results are shown in Figure S7-6. All the Pt/TiO_xN_y/MWCNT GDE electrodes demonstrated better electrocatalytic stability compared to the Pt/MWCNT. The structural stability of the Pt/TiO_xN_y-0.03 Torr-30 W/MWCNT and Pt/MWCNT assessed by SEM imaging and EDS mapping is shown in Figure S7-6 and Figure S7-7, respectively. The low magnification SEM images reveal that the strong capillary forces and van der Waals interactions between the not fully coated MWCNTs with a forest-like structure (Figure S7-7(a and b) during the evaporation of the electrolyte forced them to bend and reassemble in a foam-like structure in Figure S7-7(c). This results in the loss of surface area of the electrode. However, this configuration change was not observed for TiO_xN_y-supported Pt due to a larger coverage of the MWCNTs by the TiO_xN_y thin film (Figure S7-7(d)). Unlike the coating visible in Figure S7-7(d′), the detachment of Pt NPs from MWCNTs is evident in Figure S7-7(c′), which reduces the amount of electrocatalytic active sites. The EDS mapping of the Pt/TiO_xN_y-0.03 Torr-30 W/MWCNT after ADT (Figure S7-8) confirmed the existence of Pt NPs on the TiO_xN_y-coated MWCNT.

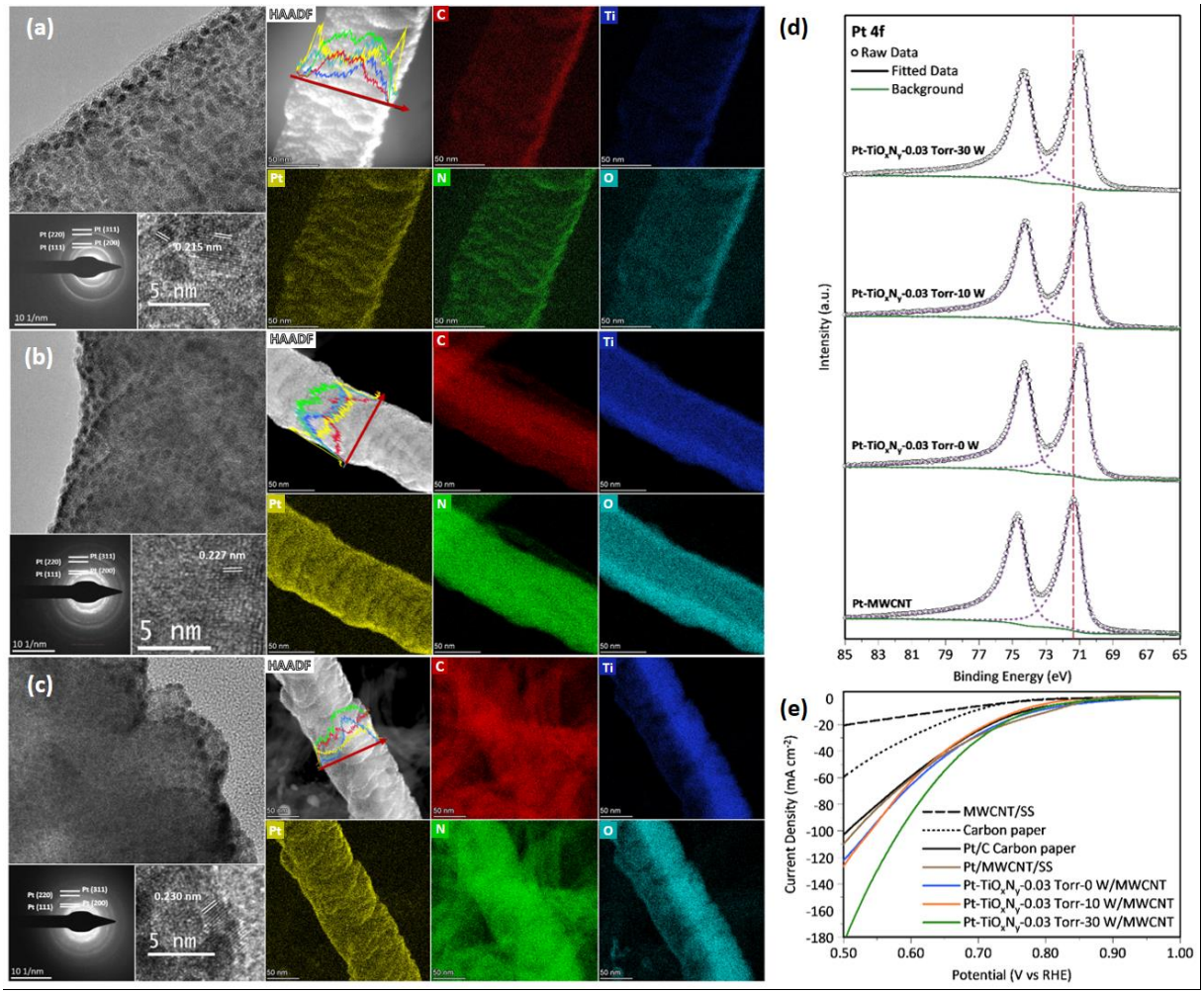

Figure 7-5. High resolution TEM images, elemental mapping, SAED pattern and d-spacing of (a) Pt/TiO$_x$N$_y$-0.03 Torr-0 W (b) Pt/TiO$_x$N$_y$-0.03 Torr-10 W, (c) Pt/TiO$_x$N$_y$-0.03 Torr-30 W; (d) deconvoluted Pt4f XPS spectra; (e) ORR performance of the electrodes as GDEs in 6M KOH recorded at a scan rate of 20 mV s^{-1}.

7.5 Conclusion

A capacitively-coupled radiofrequency plasma-assisted pulsed laser deposition approach was employed to synthesize thin films of titanium oxynitride with different morphologies and oxygen and nitrogen contents on a multi-walled carbon nanotube forest grown on a stainless steel mesh. Uniform films with similar compositions through their thickness were synthesized. The RF-PAPLD technique allowed film morphology and composition alterations due to the different laser-induced plume-background gas interaction at different chamber pressures with/without the presence of the RF plasma. The chamber pressure and RF plasma power level led to different percentages of TiN, TiON and TiO_2 in the thin films, as well as different film morphologies such

as smooth, step-like or layer-by-layer, and aerosol-like. Pt NPs were also deposited on the TiO_xN_y/MWCNT to compare their electrocatalytic activity in the oxygen evolution reaction to that of the commercially-available Pt/C catalyst. The evaluation of TiO_xN_y/MWCNT and Pt/TiO_xN_y/MWCNT samples as gas diffusion electrodes for ORR after removing the contribution of support materials (carbon paper backing and MWCNT/SS) demonstrated that the Pt/TiO_xN_y-0.03 Torr-30 W/MWCNT outperformed the commercial Pt/C by yielding approximately 3 times higher current density at 0.5 V. This outcome was attributed to the interaction of Pt NPs with the TiO_xN_y support, lowering the poisoning extent of Pt active site by the oxygen-containing intermediates.

Acknowledgments

The authors acknowledge the financial support of the Faculty of Engineering through the McGill Engineering Doctoral Award (MEDA), the Natural Sciences and Engineering Research Council of Canada (NSERC), the Gerald Hatch Faculty Fellowship, and the Fonds de recherche du Québec – Nature et technologies (FRQNT). The authors thank Dr. Felipe Artistizabal for his assistance with high-speed imaging, Prof. Ali Seifitokaldani, the technical staff at the Department of Chemical Engineering of McGill University, and Dr. David Liu for the TEM work.

7.6 Supporting Information

7.6.1 Commercial Pt/C Catalyst Preparation

The commercial Pt/C catalyst was prepared at Pt loading of 22 μg cm^{-2}. In this regard, 25.6 mg of 20% *wt* Pt/C catalyst (Sigma-Aldrich) was mixed with isopropyl (2 mL) and DI water (8 mL) and sonicated for 15 min. Then, 0.2 mL of Nafion(R) 117 solution (Sigma-Aldrich) was added to the mixture, and the sonication continued for 15 min. To prepare the gas diffusion electrode using Pt/C, the working electrode was prepared by dropping 2.5 μL of the prepared ink onto the gas diffusion layer carbon-paper backing (GDL-Toray carbon paper with 20% wet proofing and a micro-porous layer, TGP 090 20%, MPL, Fuel Cell Store), while the paper was heated on a hot plate (150 °C) and purged with Ar at an extremely low flow rate. The carbon paper was covered with a PTFE mask to assure the formation of a circular Pt/C electrocatalyst layer with a diameter of 3 mm.

Table S7-1. Sample coding based on the N_2 background gas pressure and RF plasma power during RF-PAPLD

Sample Coding	Pressure (Torr)	RF Plasma Power (W)
TiO_xN_y-0.03 Torr-0 W	0.03	0
TiO_xN_y-0.03 Torr-10 W	0.03	10
TiO_xN_y-0.03 Torr-30 W	0.03	30
TiO_xN_y-1.0 Torr-0 W	1.0	0
TiO_xN_y-1.0 Torr-10 W	1.0	10
TiO_xN_y-1.0 Torr-30 W	1.0	30

Table S7-2. Ratios of different compounds in the TiO_xN_y coatings

Compound	Ti oxide in Ar	TiO_xN_y-0 W	TiO_xN_y-10 W	TiO_xN_y-30 W
TiO (%)	40.9	0.0	0.0	0.0
TiN (%)	0.0	87.6	63.6	56.3
TiO_2 (%)	59.1	11.5	25.7	28.4
TiON (%)	0.0	0.9	10.7	15.2

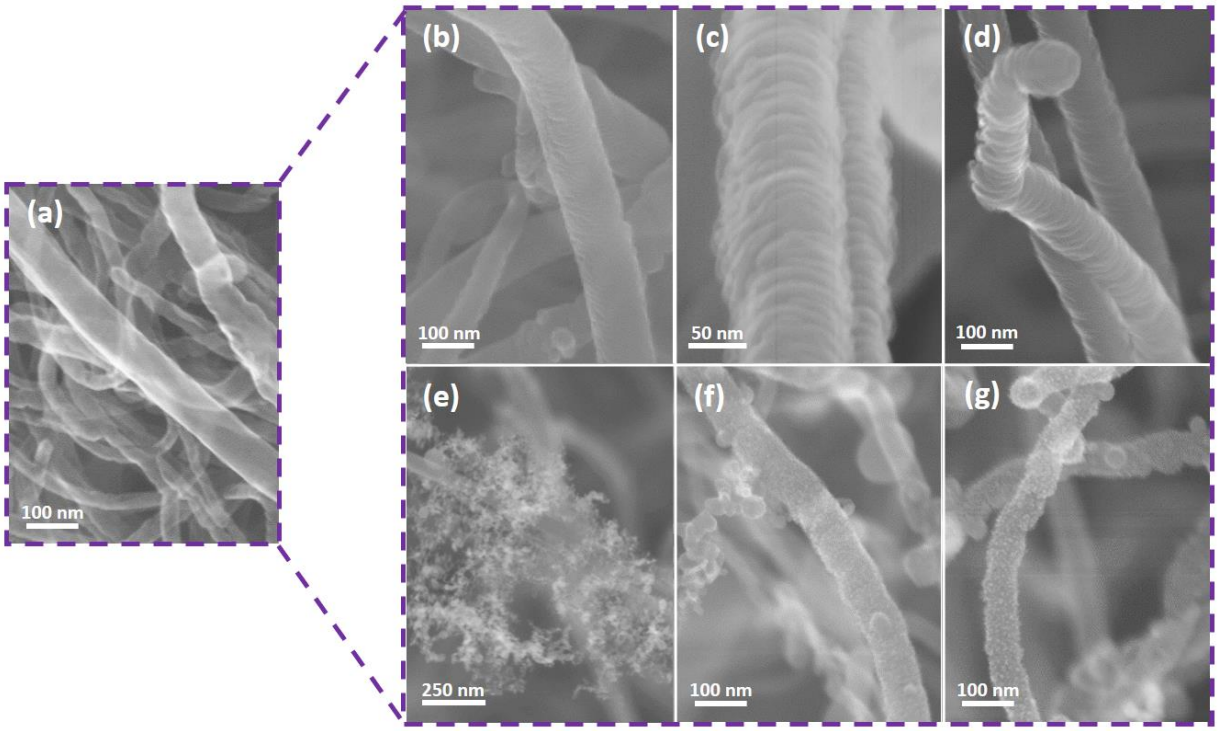

Figure S7-1. SEM images of (a) MWCNTs before coating, and TiO_xN_y thin film-coated MWCNTs (b) 0.03 Torr-0 W, (c) 0.03 Torr-10 W, (d) 0.03 Torr-30 W, (e) 1.0 Torr-0 W, (f) 1.0 Torr-10 W and (g) 1.0 Torr-30 W.

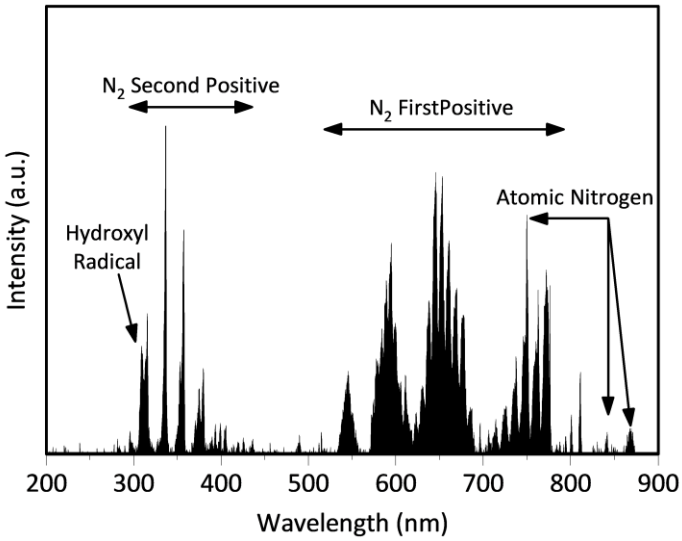

Figure S7-2. Optical emission spectrum obtained during an RF-PAPLA experiment with N_2 background gas pressure of 0.03 Torr and RF power of 30 W.

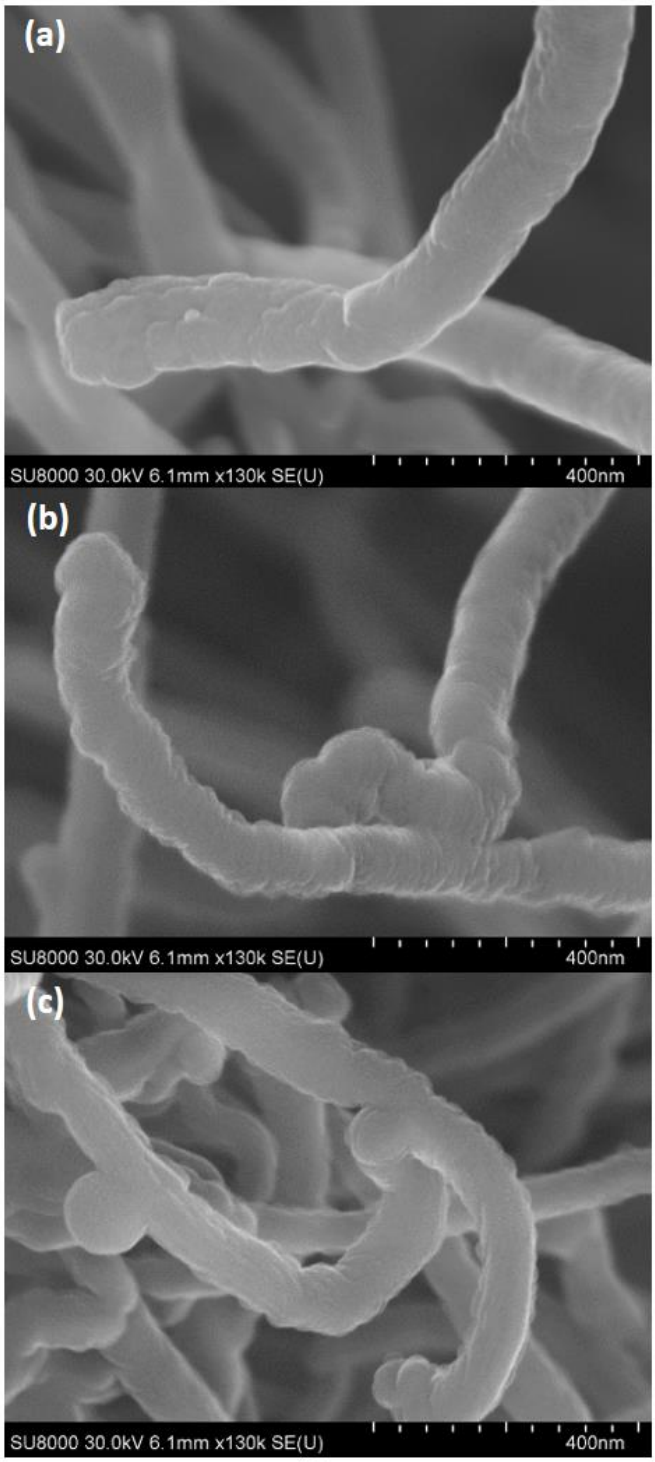

Figure S7-3. SEM images of as synthesized (a) Pt/TiO_xN_y-0.03 Torr-0 W/MWCNT, (b) Pt/TiO_xN_y-0.03 Torr-10 W/MWCNT, and (c) Pt/TiO_xN_y-0.03 Torr-30 W/MWCNT.

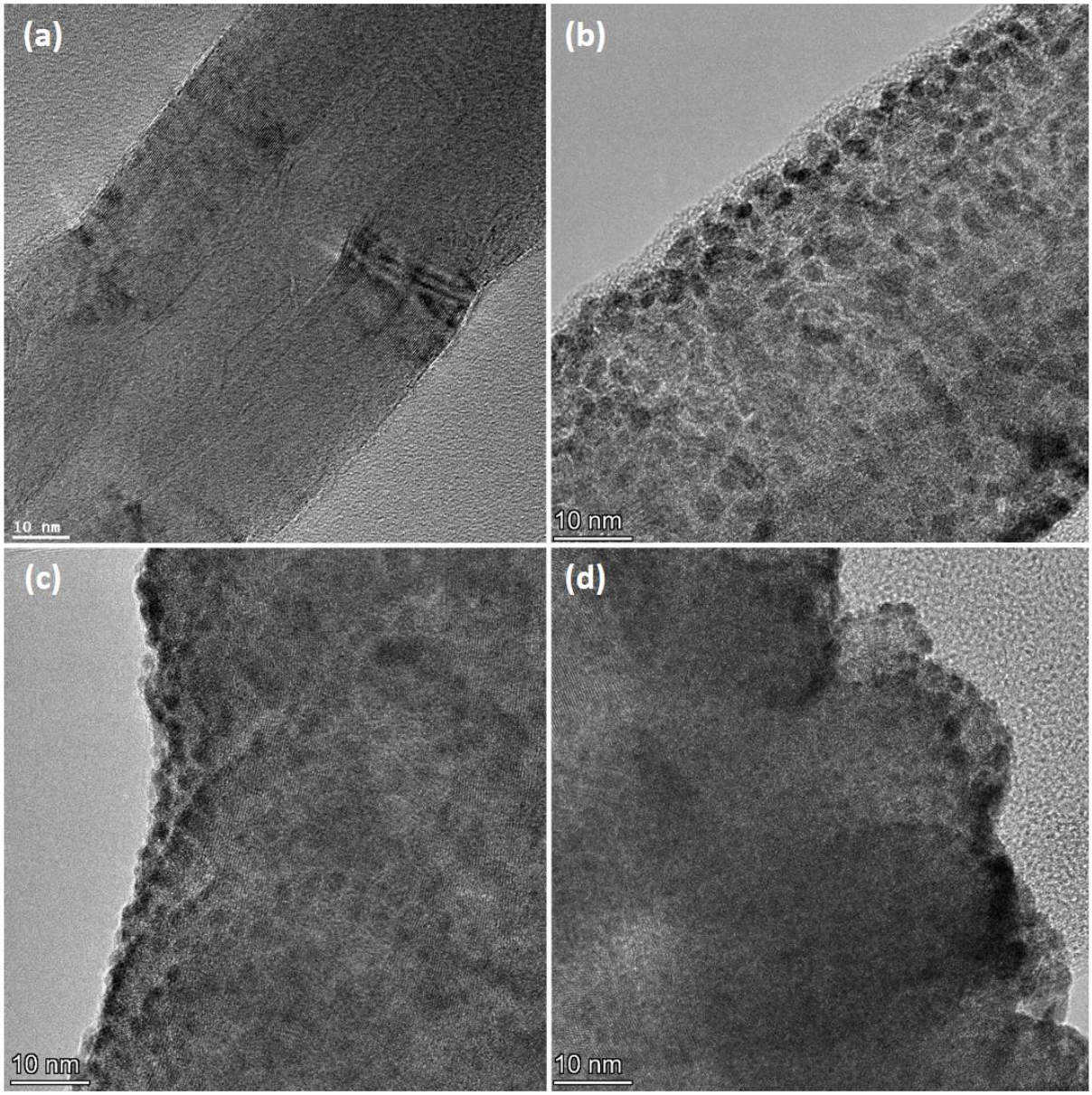

Figure S7-4. HRTEM images of (a) MWCNT, (b) Pt/TiO_xN_y-0.03 Torr-0 W/MWCNT, (c) Pt/TiO_xN_y-0.03 Torr-10 W/MWCNT, and (d) Pt/TiO_xN_y-0.03 Torr-30 W/MWCNT.

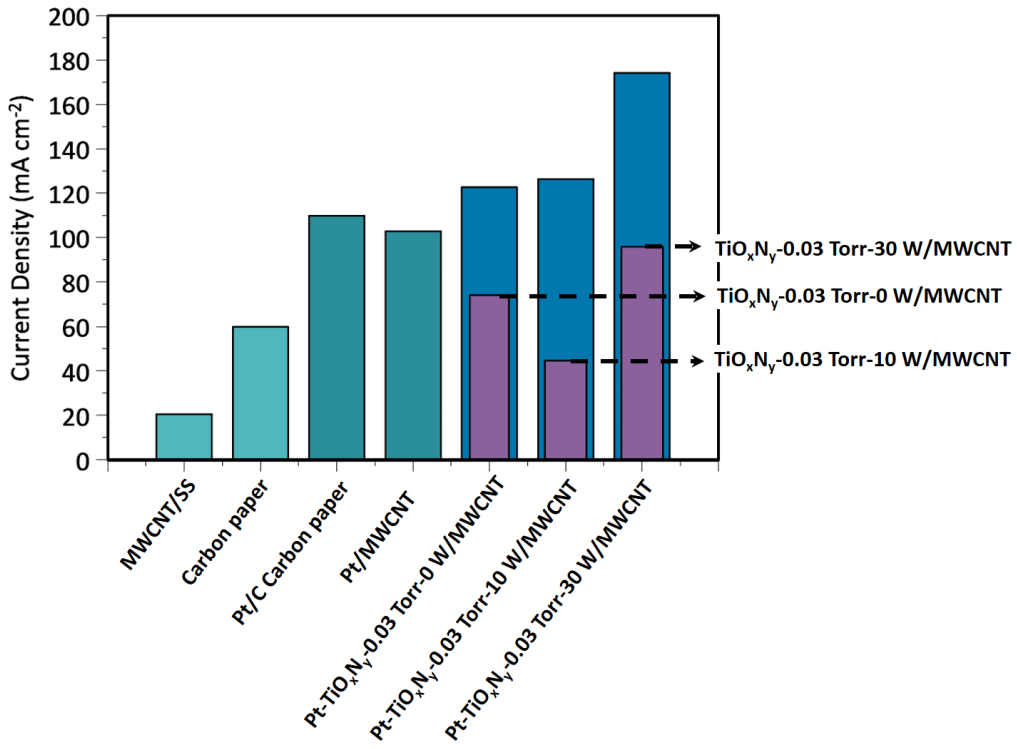

Figure S7-5. ORR current density of electrocatalysts at the potential of -0.5 V.

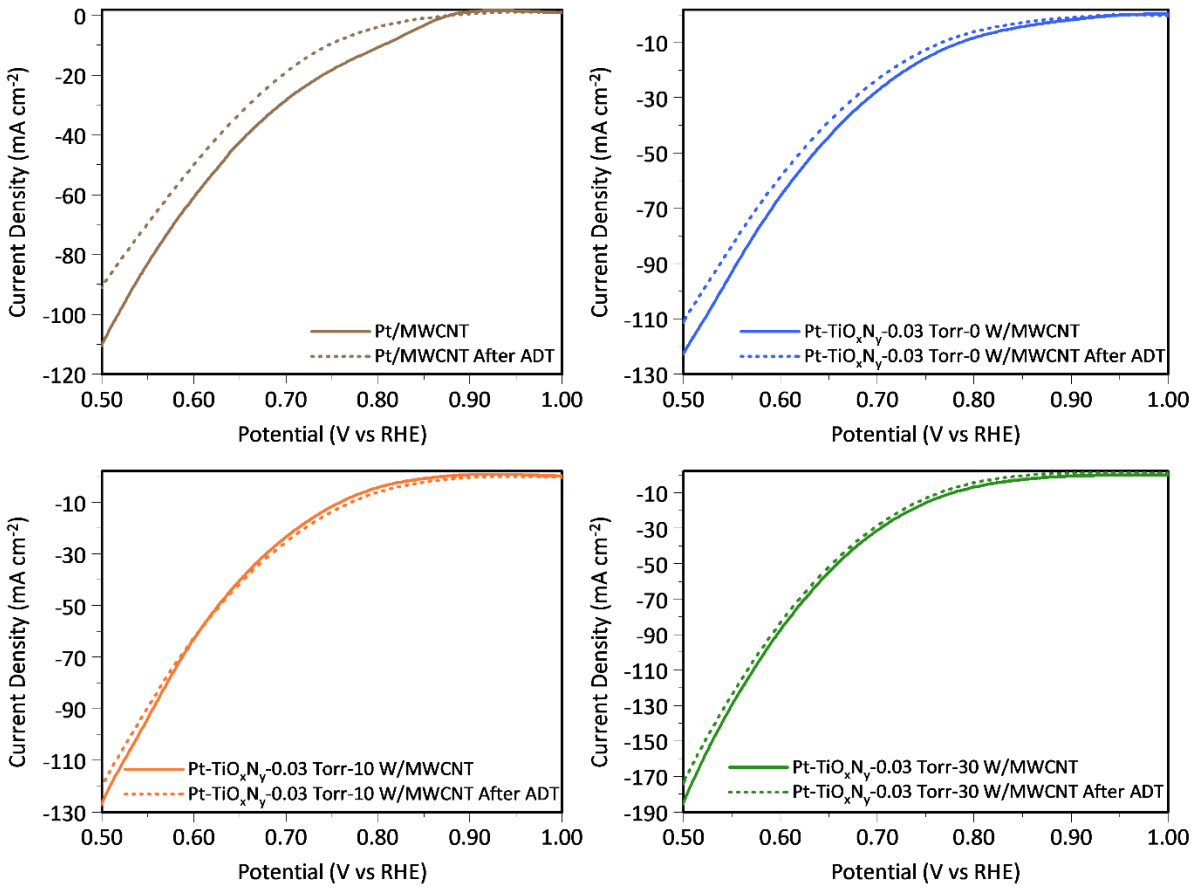

Figure S7-6. ORR current density of electrocatalysts before and after stability test (ADT) for 500 cycles.

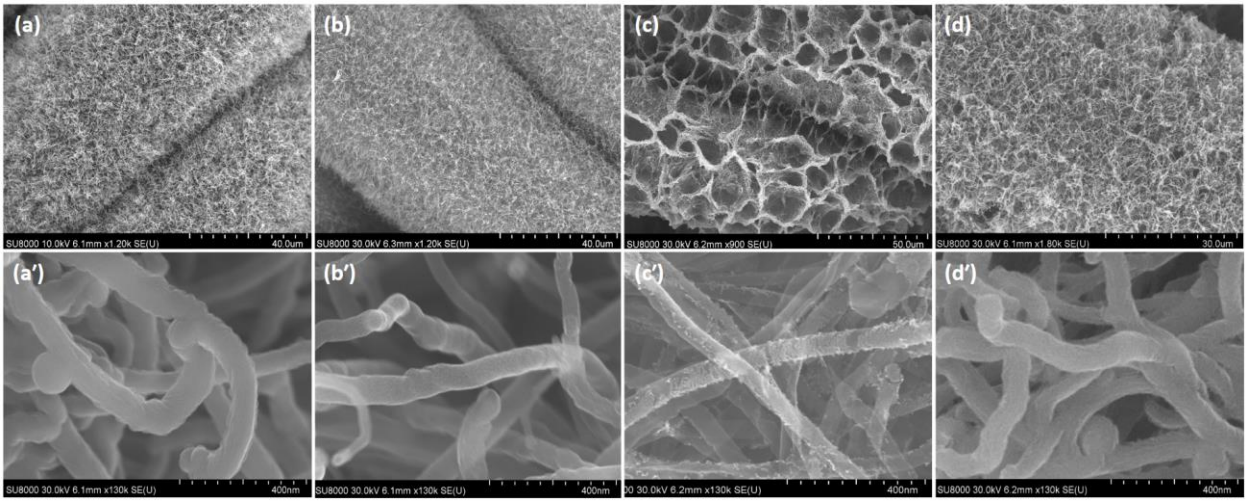

Figure S7-7. SEM images of as synthesized (a, b) Pt/TiO_xN_y-0.03 Torr-30 W/MWCNT and (a′, b′) Pt/MWCNT, and (c, d) Pt/TiO_xN_y-0.03 Torr-30 W/MWCNT and (c′, d′) Pt/MWCNT after ADT stability test for 500 cycles.

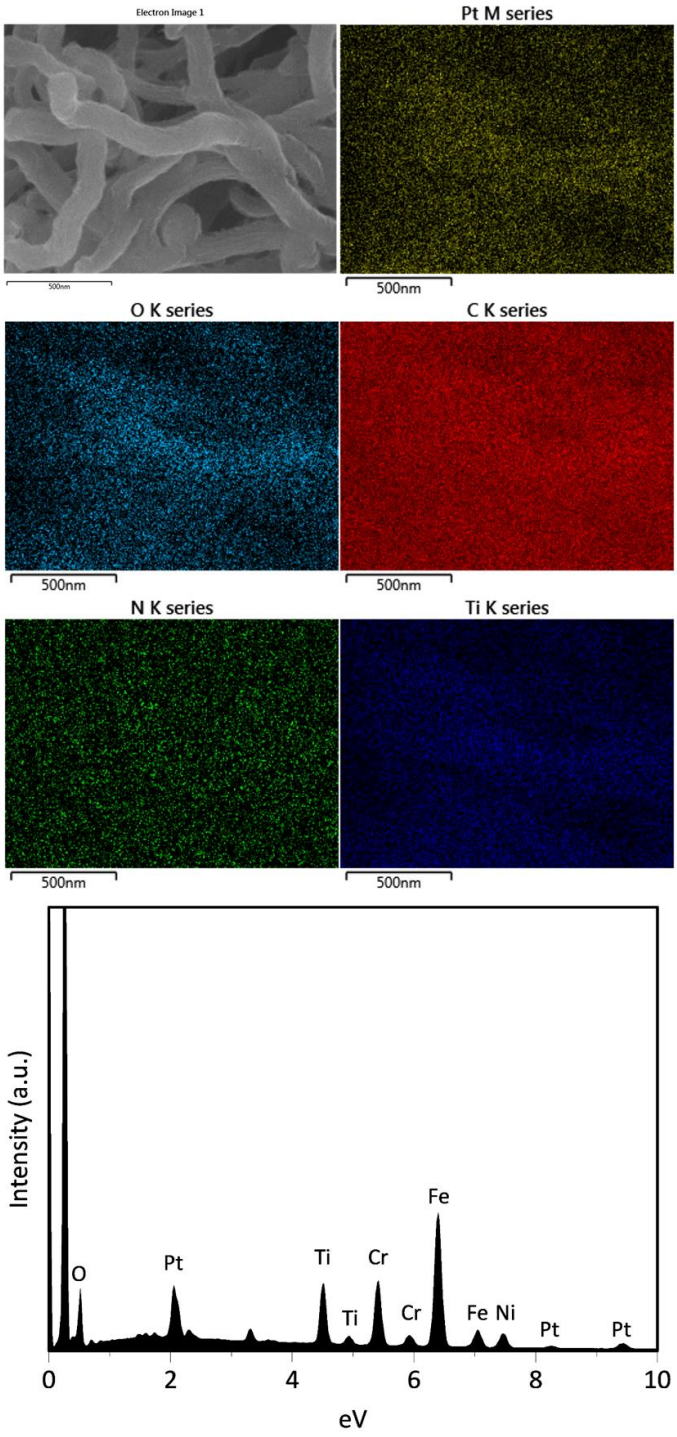

Figure S7-8. EDS mapping of Pt/TiO_xN_y-0.03 Torr-30 W/MWCNT electrocatalysts after ADT stability test for 500 cycles.

Chapter 8

8. Conclusions, Contribution to Knowledge, and Future Work

8.1 Conclusions

As the world requires a shift from fossil fuels to greener and renewable energy sources, a fuel cell is considered a clean, low environmental impact, and efficient technology to supply energy continuously as long as the fuel is fed to the system. Moreover, supercapacitors are energy storage devices to store the energy of the intermittent renewable energy sources and deliver it at high power density. Today, environmentally friendly FCs and SCs are the subjects of growing interest in both academic and industrial studies.

MWCNT-based electrodes are promising candidates for SCs due to their superior electrical conductivity, large specific surface area and chemical inertness. However, the low energy density of MWCNT originating from the double-layer charging mechanism, their hydrophobic nature, high agglomeration tendency after wet processes, and the blockage of the surface of MWCNT by the use of binders during electrode manufacturing limit their performance as SC electrodes.

In DAMFCs, although very promising, the commercially-available electrocatalyst for both anode and cathode electrodes is made of precious metal, Pt, in high loadings, thus being the main contributor to the low-temperature FCs' high cost and environmental footprint. Previous attempts to replace the highly active platinum by non-noble electrocatalysts have required the utilization of high electrocatalyst loadings, leading to thicker catalyst layers with the consequent high mass-transport overpotential and ohmic losses.

Therefore, this dissertation proposes using the chemical vapor deposition method to directly grow MWCNTs on a stainless steel mesh to develop a 3D agglomeration-free structure of MWCNTs, eliminating the use of binders for electrode assembly. Then a dry radiofrequency plasma technique was used to functionalize the 3D MWCNT electrode, avoiding the agglomeration of MWCNTs. Moreover, to develop anode and cathode electrodes for DAMFCs, a

dry, binder-free, and byproduct-free pulsed laser ablation technique was used to synthesize highly dispersed Pt-based nanostructures at low loadings to reduce the environmental impacts while advancing the performance of FCs. It is well-known that the results obtained at the laboratory scale differ from the actual fuel cell conditions, but they can surely help predict the performance of fuel cells in practical applications. This section summarizes the main conclusions drawn from this research.

1- A consistent and uniform growth of MWCNTs with a forest-like structure was achieved on SS mesh using CVD at 700 °C. A radiofrequency plasma with two different gas mixtures was further applied to graft nitrogen and oxygen-containing functional groups on the surface of the MWCNTs. A range of RF power levels and functionalization time was investigated to reach a high capacitance from the developed MWCNT/SS electrodes with minimum structural defects. By applying the RF plasma employing the $Ar/C_2H_6/O_2$ gas mixture at 20 W for 15 min, the specific capacitance of MWCNTs increased from 75.3 ± 3.7 F g^{-1}, for the as-produced (non-functionalized MWCNTs) to 196.3 ± 5.8 F g^{-1} for the oxygen functionalized MWCNTs.

2- A comprehensive study on the synthesis of Pt nanoparticles using the PLA technique was performed. A complete structural characterization was carried out, and the effect of laser pulse energy, background gas pressure, and ablation time on the deposited Pt nanoparticle thin films on MWCNTs was investigated. The results demonstrated a close relationship between the particle size and film morphology with the synthesis conditions. Therefore, a mechanism for the formation of Pt nanoparticles was proposed relating the synthesis conditions to the structural characteristics of the formed nanoparticles.

3- The developed 3D porous Pt-based electrocatalysts were electrochemically evaluated by measuring the electrochemically active surface area and studying the CO oxidation and hydrogen adsorption/desorption. The electrodes were tested for ORR in alkaline electrolyte using a rotating disk electrode setup, and the results illustrated that all the Pt/MWCNT/SS electrocatalysts yielded higher mass and specific ORR activity, outperforming the commercially available Pt/C electrocatalyst. Moreover, the Pt/MWCNT/SS electrodes offered improved oxygen mass transport to Pt sites compared to the commercial Pt/C electrode.

4- The developed Pt/MWCNT/SS structure allowed testing them directly as gas diffusion electrodes without using carbon backing paper. The GDEs provided high oxygen mass transport, and the electrocatalyst with the lowest Pt loading of 14.2 μg cm^{-2} and the highest electrochemically active surface area of ~70 m^2 g_{Pt} yielded the highest ORR current, outperforming the commercial Pt/C GDE.

5- The developed Pt/MWCNT/SS with high Pt utilization in a 3D porous structure were evaluated for the anodic MOR. The PLA time and background pressure were systematically optimized to gain the highest methanol oxidation current with superior structural stability in a wide range of working temperatures. The electrocatalyst synthesized by PLA at 10^{-5} Torr for 5 min, exhibited a 50% higher methanol oxidation current and better stability compared to the commercial Pt/C with a similar Pt loading.

6- Capacitively-coupled radiofrequency plasma-assisted pulsed laser deposition (RF-PAPLD) in an N_2 environment was used to synthesize titanium oxynitride (TiO_xN_y). Structural characterization and high-speed imaging evidenced an increased deposition rate and oxygen content at higher applied RF plasma power levels.

7- The TiO_xN_y/MWCNT electrodes before and after the deposition of Pt nanoparticles were evaluated for ORR in the GDE setup. The Pt/TiO_xN_y-30 W/MWCNT showed superior electrocatalytic activity by yielding 3 times higher ORR current density than the commercial Pt/C.

8.2 Contribution to Knowledge

In this PhD thesis, 3D porous low Pt loading electrodes were successfully developed using a dry synthesis approach. The Pt-based electrocatalysts synthesized at different pulsed laser ablation conditions fulfilled the activity and stability requirements to be used as anode and cathode electrodes in direct alkaline methanol fuel cells. The original contributions to knowledge are as follow:

1- Implementation of an entirely dry binder-free approach to synthesize 3D porous supported Pt nanostructures with different morphologies, and extrinsic and intrinsic characteristics.

2- Understanding the mechanism of in-gas nanoparticle formation during pulsed laser ablation technique, driven from the performed structural characterization techniques. This can

provide a paradigm to determine the synthesis conditions for future works mindfully and anticipate the results.

3- Demonstration that the PLA synthesis conditions affect the intrinsic and extrinsic properties of the deposited nanostructures.
4- Successful demonstration of using 3D porous Pt/MWCNT/SS electrodes directly as gas diffusion electrodes with higher electrocatalytic activity, mass transport properties, and stability compared to the commercially available Pt/C electrode. The use of electrodes in gas diffusion setup provides more realistic data for fuel cell testing.
5- Demonstration that achieving a highly active and stable electrocatalyst for ORR and MOR requires Pt electrocatalyst with different intrinsic and extrinsic characteristics, which can be obtained by using different PLA synthesis conditions.
6- Successful synthesis of titanium nitride/oxynitride using the combination of radiofrequency plasma and pulsed laser deposition technique (RF-PAPLD) in a reactive environment containing N_2 background gas.
7- Understanding the interaction between radiofrequency and laser-induced plasmas during the plasma-assisted pulsed laser deposition. High-speed imaging and structural characterization of titanium oxynitride films demonstrated a higher deposition rate of the ablated material and higher oxygen content of the deposited films by increasing RF power levels during PAPLD.
8- Demonstration that a successful synthesis of a bi-layer electrocatalyst containing Pt deposited on the surface of MWCNT-supported TiO_xN_y and their application as gas diffusion electrodes for ORR.

8.3 Future Work

Based on the results and conclusions obtained from this PhD thesis, the following recommendations can be implemented in future works to complement and further enhance the current research.

1- Conducting a two-electrode study of the functionalized MWCNTs supercapacitor electrodes, which allows a more realistic capacitance measurements.

2- Evaluating the capacitive behavior of the functionalized MWCNTs supercapacitor electrodes under strains to assess their applicability as flexible electrode materials.
3- Testing the developed gas diffusion electrodes in actual fuel cell setups. This could also involve the potential elimination of the current collector. However, flow modelling will be required to evaluate its viability fully.
4- Utilizing carbon backing paper with lower weight to replace the SS mesh support/current collector. Using a carbon support is closer to the traditional electrode assembly in commercial cells.
5- Synthesis of non-platinum group metals using the PLA technique and investigate the effect of ablation conditions on the structural and electrochemical characterization of the films.
6- Using other techniques, including atomic layer deposition (ALD), to enable full coverage of the surface of MWCNTs. As explained, PLA covers almost 50% of the length of the nanotubes. Therefore, the full surface coverage of MWCNTs will offer higher surface area at even lower loadings reported in this study.
7- Extend the application of the Pt-based electrodes for energy storage, water electrolysis and fuel cells to electrochemical sensors. Based on the use of noble Pt at low loading and high surface area, the developed electrodes are expected to be highly sensitive, for instance, to detect contaminants in the water/wastewater.
8- The PLA setup has been upgraded, enabling the ablation of two different targets in a single experimental run. Therefore, it is highly recommended to synthesize bi-metal electrocatalysts for electrolysis/fuel cell applications.

Appendix A – Collaborative Work

This appendix lists the collaborative projects underway or accomplished using the PLA or PAPLD technique to synthesize different metal catalysts on MWCNTs or other support materials for applications exterior to those presented in this thesis.

Projects

The collaborative graduate and undergraduate projects are listed as follow:

1. Synthesis of Ru_xN_y with different nitrogen content and their deposition on MWCNT for flexible supercapacitors, Summer 2021 to Winter 2022, McGill University, Collaboration with a Ph.D. student, Research directors: Prof. Sylvain Coulombe and Prof. Pascal Hubert. The result of this collaborative project is a published paper:

   Hanie Kazari, Elmira Pajootan, Pascal Hubert, and Sylvain Coulombe, Dry synthesis of binder-free ruthenium nitride coated carbon nanotube as flexible supercapacitor electrode, ACS Applied Materials & Interfaces, Volume 14, 2022, 13, 15112.

2. Deposition of MoN, Ni_3N and NiMoN nanoparticle thin films on the mixed boron nitride nanotubes/MWCNT for hydrogen evolution reaction, Summer/Fall 2021, McGill University, Undergraduate project, Research director: Prof. Sylvain Coulombe, in collaboration with NRC.

3. Synthesis of Ru_xFe_{1-x} bimetallic nanoparticle thin films on boron nitride nanotubes and MWCNT for hydrogen evolution reaction and plasma-catalytic ammonia synthesis, 2020-22, McGill University, Graduate project, Research director: Prof. Sylvain Coulombe, in collaboration with NRC.

4. Dry synthesis of Ni and Pt nanoparticle thin films on boron nitride nanotubes for plasma-catalytic ammonia synthesis, 2019-21, McGill University, Graduate project, Research director: Prof. Sylvain Coulombe, in collaboration with NRC.

5. Ultra-low loading of Pt on nickel nitride nanoparticle thin films on MWCNT for hydrogen evolution reaction, Summer 2021, McGill University, Undergraduate project, Research directors: Prof. Sasha Omanovic and Prof. Sylvain Coulombe.

6. Synthesis of Ni and Mo nanoparticle thin films on carbon nanotubes for hydrogen evolution reaction, Winter 2021, McGill University, Undergraduate project, Research directors: Prof. Sasha Omanovic and Prof. Sylvain Coulombe.
7. Synthesis of TiO_xN_y using plasma-assisted pulsed laser ablation technique, Summer-Fall 2019, McGill University, Visiting student from the Netherlands, Research directors: Prof. Sasha Omanovic and Prof. Sylvain Coulombe.
8. Functionalization of carbon nanotubes for supercapacitors application, Summer 2019, McGill University, Undergraduate project, Research directors: Prof. Sasha Omanovic and Prof. Sylvain Coulombe.
9. Plasma-assisted pulsed laser deposition of titanium oxynitride, Fall 2018, McGill University, Graduate project, Research directors: Sasha Omanovic and Prof. Sylvain Coulombe.
10. Optimization of carbon nanotubes growth on stainless steel for supercapacitors application, Summer and Fall 2018, McGill University, Undergraduate project, Research directors: Prof. Sasha Omanovic and Prof. Sylvain Coulombe.

Conferences

The oral and poster contributions in national and international conferences are summarized below:

1. Kazari H., **Pajootan E.**, Deguns E., Sowa M., Kao E., Coulombe S., Application of Ruthenium Nitride Deposited on Multi-walled Carbon Nanotube Forest as Electrode Material for Supercapacitors, Oral presentation in IEEE 16th Nanotechnology Materials and Devices Conference (NMDC) 2021, December 12-15.
2. Walker S., Price G., **Pajootan E.**, Coulombe S., Viability of Boron Nitride Nanotubes as a Support Structure for Metal Nanoparticle Catalysts for the Plasma-Catalytic Synthesis of Ammonia, Oral presentation in IEEE 16th Nanotechnology Materials and Devices Conference (NMDC) 2021, December 12-15.

3. Spada J., **Pajootan E.**, Coulombe S., Omanovic S., ECS Canada Section Spring Meeting 2021, Young Investigator Forum, Nickel and Molybdenum Based Thin Films Deposited on Multi-Walled Carbon Nanotubes as Electrocatalysts for Hydrogen Evolution Reaction.
4. **Pajootan E. (Oral Presenter and Award Winner)**, Omanovic S., Coulombe S., Controlled deposition of platinum film and nanoparticles on multi-walled carbon nanotubes as electrocatalysts for methanol oxidation in alkaline direct methanol fuel cells, 6th Nano Today Conference, June 2019, Lisbon, Portugal.
5. **Pajootan E. (Oral Presenter and Award Winner)**, Alolabi S.A., Coulombe S., Omanovic S., Radio-Frequency Plasma-Assisted Pulsed Laser Deposition of TiO_xN_y on Multi-walled Carbon Nanotubes: A Structural and Compositional Study, 24th International Symposium of Plasma Chemistry (ISPC24), June 2019, Naples, Italy.
6. **Pajootan E. (Poster Presenter)**, Aristizabal F., Coulombe S., Omanovic S., Evolution of Laser-Induced Plasma during Radio-Frequency Plasma-Assisted Pulsed Laser Ablation of Titanium**,** 24th International Symposium of Plasma Chemistry (ISPC24), June 2019, Naples, Italy.

References

[1] Santos, E. and W. Schmickler, *Impact of Electrochemical Science on Energy Problems*, in *Catalysis in Electrochemistry*. 2011, John Wiley & Sons, Inc. p. 487-498.

[2] Dai, L., *Chapter 1 - From conventional technology to carbon nanotechnology: The fourth industrial revolution and the discoveries of C60, carbon nanotube and nanodiamond*, in *Carbon Nanotechnology*. 2006, Elsevier: Amsterdam. p. 3-11.

[3] Barkakaty, B., B.G. Sumpter, I.N. Ivanov, M.E. Potter, C.W. Jones, and B.S. Lokitz, *Emerging materials for lowering atmospheric carbon.* Environmental Technology & Innovation, 2017. **7**: p. 30-43.

[4] NASA, G.C.C.V.S.o.t.P., https://climate.nasa.gov/vital-signs/carbon-dioxide/, Accessed 28 December 2021.

[5] Nguyen, T.V., *Reversible (H_2-Br_2 & H_2V) Fuel Cells as Energy Storage Systems for the Electrical Grids and Renewable Energy Sources, McGill University, Chemical Engineering Department, Research Day, October 31, 2016.*

[6] Hassan, N., *Catalytic performance of nanostructured materials recently used for developing fuel cells' electrodes.* International Journal of Hydrogen Energy, 2021. **46**(79): p. 39315-39368.

[7] Lamba, P., P. Singh, P. Singh, P. Singh, Bharti, A. Kumar, M. Gupta, and Y. Kumar, *Recent advancements in supercapacitors based on different electrode materials: Classifications, synthesis methods and comparative performance.* Journal of Energy Storage, 2022. **48**: p. 103871.

[8] Da Silva, L.M., R. Cesar, C.M.R. Moreira, J.H.M. Santos, L.G. De Souza, B.M. Pires, R. Vicentini, W. Nunes, and H. Zanin, *Reviewing the fundamentals of supercapacitors and the difficulties involving the analysis of the electrochemical findings obtained for porous electrode materials.* Energy Storage Materials, 2020. **27**: p. 555-590.

[9] Liu, N., R. Chen, and Q. Wan, *Recent Advances in Electric-Double-Layer Transistors for Bio-Chemical Sensing Applications.* 2019. **19**(15): p. 3425.

[10] Eftekhari, A., *Surface Diffusion and Adsorption in Supercapacitors.* ACS Sustainable Chemistry & Engineering, 2019. **7**(4): p. 3692-3701.

[11] Shukla, A.K., S. Sampath, and K. Vijayamohanan, *Electrochemical supercapacitors: Energy storage beyond batteries.* Current Science, 2000. **79**(12): p. 1656-1661.

[12] Zhang, L.L. and X.S. Zhao, *Carbon-based materials as supercapacitor electrodes.* Chemical Society Reviews, 2009. **38**(9): p. 2520-2531.

[13] Yaseen, M., M.A.K. Khattak, M. Humayun, M. Usman, S.S. Shah, S. Bibi, B.S.U. Hasnain, S.M. Ahmad, A. Khan, N. Shah, A.A. Tahir, and H. Ullah, *A Review of Supercapacitors: Materials Design, Modification, and Applications.* 2021. **14**(22): p. 7779.

[14] Wang, Y., X. Wu, Y. Han, and T. Li, *Flexible supercapacitor: Overview and outlooks.* Journal of Energy Storage, 2021. **42**: p. 103053.

[15] Carrette, L., K.A. Friedrich, and U. Stimming, *Fuel Cells – Fundamentals and Applications.* Fuel Cells, 2001. **1**(1): p. 5-39.

[16] Sharaf, O.Z. and M.F. Orhan, *An overview of fuel cell technology: Fundamentals and applications.* Renewable and Sustainable Energy Reviews, 2014. **32**: p. 810-853.

[17] Galich, A. and L. Marz, *Alternative energy technologies as a cultural endeavor: a case study of hydrogen and fuel cell development in Germany.* Energy, Sustainability and Society, 2012. **2**(1): p. 2.

[18] Yuan, X.-Z. and H. Wang, *PEM Fuel Cell Fundamentals*, in *PEM Fuel Cell Electrocatalysts and Catalyst Layers: Fundamentals and Applications*, J. Zhang, Editor. 2008, Springer London: London. p. 1-87.

[19] Larminie, J., A. Dicks, J. Larminie, and A. Dicks, *Introduction*, in *Fuel Cell Systems Explained*. 2013, John Wiley & Sons, Ltd,. p. 1-24.

[20] Birgersson, E., *Mathematical Modeling of Transport Phenomena in Polymer Electrolyte and Direct Methanol Fuel Cells, Ph.D., Royal Institute of Technology, Completed in 2004.*

[21] Seselj, N., C. Engelbrekt, and J. Zhang, *Graphene-supported platinum catalysts for fuel cells.* Science Bulletin, 2015. **60**(9): p. 864-876.

[22] Mstsunaga, M., T. Fukushima , and K. Ojima *Powertrain System of Honda FCX Clarity Fuel Cell Vehicle.* World Electric Vehicle Journal, 2009. **3**: p. 0820-0829.

[23] Yoshida, T. and K. Kojima, *Toyota MIRAI Fuel Cell Vehicle and Progress Toward a Future Hydrogen Society.* The Electrochemical Society Interface, 2015: p. 45-49.

[24] Duclos, L., L. Svecova, V. Laforest, G. Mandil, and P.X. Thivel, *Process development and optimization for platinum recovery from PEM fuel cell catalyst.* Hydrometallurgy, 2016. **160**: p. 79-89.

[25] Xu, Q., F. Zhang, L. Xu, P. Leung, C. Yang, and H. Li, *The applications and prospect of fuel cells in medical field: A review.* Renewable and Sustainable Energy Reviews, 2017. **67**: p. 574-580.

[26] *Markets and Markets, Fuel Cell Market, https://www.marketsandmarkets.com/Market-Reports/fuel-cell-market-348.html?gclid=CjwKCAiA55mPBhBOEiwANmzoQuAD6t9yMrVlVQfQ6i072_lx5vy7jeGTyDZrWA1LEMwmPFu3nv21NRoCIrMQAvD_BwE, (accessed 18 January 2022).*

[27] Charoen, K., C. Prapainainar, P. Sureeyatanapas, T. Suwannaphisit, K. Wongamornpitak, P. Kongkachuichay, S.M. Holmes, and P. Prapainainar, *Application of response surface methodology to optimize direct alcohol fuel cell power density for greener energy production.* Journal of Cleaner Production, 2017. **142, Part 3**: p. 1309-1320.

[28] Santos, M.C.L., C.A. Ottoni, R.F.B. de Souza, S.G. da Silva, M.H.M.T. Assumpção, E.V. Spinacé, and A.O. Neto, *Methanol Oxidation in Alkaline Medium Using PtIn/C Electrocatalysts.* Electrocatalysis, 2016. **7**(6): p. 445-450.

[29] Aricò, A.S., V. Baglio, and V. Antonucci, *Direct Methanol Fuel Cells: History, Status and Perspectives*, in *Electrocatalysis of Direct Methanol Fuel Cells*. 2009, Wiley-VCH Verlag GmbH & Co. KGaA. p. 1-78.

[30] Zadick, A., L. Dubau, N. Sergent, G. Berthomé, and M. Chatenet, *Huge Instability of Pt/C Catalysts in Alkaline Medium.* ACS Catalysis, 2015. **5**(8): p. 4819-4824.

[31] Hersbach, T.J.P., A.C. Garcia, T. Kroll, D. Sokaras, M.T.M. Koper, and A.T. Garcia-Esparza, *Base-Accelerated Degradation of Nanosized Platinum Electrocatalysts.* ACS Catalysis, 2021. **11**(15): p. 9904-9915.

[32] Bencs, L., K. Ravindra, and R. Van Grieken, *Platinum: Environmental Pollution and Health Effects A2 - Nriagu, J.O*, in *Encyclopedia of Environmental Health*. 2011, Elsevier: Burlington. p. 580-595.

[33] Ferrin, P. and M. Mavrikakis, *Structure Sensitivity of Methanol Electrooxidation on Transition Metals.* Journal of the American Chemical Society, 2009. **131**(40): p. 14381-14389.

[34] Cuesta, Á. and C. Gutiérrez, *CO Adsorption on Platinum Electrodes*, in *Catalysis in Electrochemistry*. 2011, John Wiley & Sons, Inc. p. 339-373.

[35] Firouzjaie, H.A. and W.E. Mustain, *Catalytic Advantages, Challenges, and Priorities in Alkaline Membrane Fuel Cells.* ACS Catalysis, 2020. **10**(1): p. 225-234.

[36] Ramaswamy, N. and S. Mukerjee, *Influence of Inner- and Outer-Sphere Electron Transfer Mechanisms during Electrocatalysis of Oxygen Reduction in Alkaline Media.* The Journal of Physical Chemistry C, 2011. **115**(36): p. 18015-18026.

[37] Ge, X., A. Sumboja, D. Wuu, T. An, B. Li, F.W.T. Goh, T.S.A. Hor, Y. Zong, and Z. Liu, *Oxygen Reduction in Alkaline Media: From Mechanisms to Recent Advances of Catalysts.* ACS Catalysis, 2015. **5**(8): p. 4643-4667.

[38] Kumar, S. and S. Zou, *Electrooxidation of Carbon Monoxide and Methanol on Platinum-Overlayer-Coated Gold Nanoparticles: Effects of Film Thickness.* Langmuir, 2007. **23**(13): p. 7365-7371.

[39] Garlyyev, B., J. Fichtner, O. Piqué, O. Schneider, A.S. Bandarenka, and F. Calle-Vallejo, *Revealing the nature of active sites in electrocatalysis.* Chemical Science, 2019. **10**(35): p. 8060-8075.

[40] Cuesta, A., *At Least Three Contiguous Atoms Are Necessary for CO Formation during Methanol Electrooxidation on Platinum.* Journal of the American Chemical Society, 2006. **128**(41): p. 13332-13333.

[41] Cuesta, A., M. Escudero, B. Lanova, and H. Baltruschat, *Cyclic Voltammetry, FTIRS, and DEMS Study of the Electrooxidation of Carbon Monoxide, Formic Acid, and Methanol on Cyanide-Modified Pt(111) Electrodes.* Langmuir, 2009. **25**(11): p. 6500-6507.

[42] Huang, X., Z. Zhao, L. Cao, Y. Chen, E. Zhu, Z. Lin, M. Li, A. Yan, A. Zettl, Y.M. Wang, X. Duan, T. Mueller, and Y. Huang, *High-performance transition metal-doped Pt_3Ni octahedra for oxygen reduction reaction.* 2015. **348**(6240): p. 1230-1234.

[43] Liu, M., Z. Zhao, X. Duan, and Y. Huang, *Nanoscale Structure Design for High-Performance Pt-Based ORR Catalysts.* 2019. **31**(6): p. 1802234.

[44] Marković, N.M., R.R. Adžić, B.D. Cahan, and E.B. Yeager, *Structural effects in electrocatalysis: oxygen reduction on platinum low index single-crystal surfaces in perchloric acid solutions.* Journal of Electroanalytical Chemistry, 1994. **377**(1): p. 249-259.

[45] Albers, P.W., W. Weber, K. Kunzmann, M. Lopez, and S.F. Parker, *Characterisation of carbon supported platinum-ruthenium fuel cell catalysts of different degree of alloying.* Surface Science, 2008. **602**(23): p. 3611-3616.

[46] Denis, M.C., M. Lefèvre, D. Guay, and J.P. Dodelet, *Pt-Ru catalysts prepared by high energy ball-milling for PEMFC and DMFC: Influence of the synthesis conditions.* Electrochimica Acta, 2008. **53**(16): p. 5142-5154.

[47] Tolmachev, Y.V. and O.A. Petrii, *Pt–Ru electrocatalysts for fuel cells: developments in the last decade.* Journal of Solid State Electrochemistry, 2017. **21**(3): p. 613-639.

[48] Neurock, M., M. Janik, and A. Wieckowski, *A first principles comparison of the mechanism and site requirements for the electrocatalytic oxidation of methanol and formic acid over Pt.* Faraday Discussions, 2009. **140**(0): p. 363-378.

[49] Antolini, E., J.R.C. Salgado, and E.R. Gonzalez, *The methanol oxidation reaction on platinum alloys with the first row transition metals: The case of Pt–Co and –Ni alloy electrocatalysts for DMFCs: A short review.* Applied Catalysis B: Environmental, 2006. **63**(1–2): p. 137-149.

[50] Chen, J., Q. Niu, G. Chen, J. Nie, and G. Ma, *Electrooxidation of Methanol on Pt @Ni Bimetallic Catalyst Supported on Porous Carbon Nanofibers.* The Journal of Physical Chemistry C, 2017.

[51] Zhu, X., X. Tan, K.-H. Wu, S.-C. Haw, C.-W. Pao, B.-J. Su, J. Jiang, S.C. Smith, J.-M. Chen, R. Amal, and X. Lu, *Intrinsic ORR Activity Enhancement of Pt Atomic Sites by Engineering the d-Band Center via Local Coordination Tuning.* 2021. **60**(40): p. 21911-21917.

[52] Park, S., Y. Xie, and M.J. Weaver, *Electrocatalytic Pathways on Carbon-Supported Platinum Nanoparticles: Comparison of Particle-Size-Dependent Rates of Methanol, Formic Acid, and Formaldehyde Electrooxidation.* Langmuir, 2002. **18**(15): p. 5792-5798.

[53] Patra, S. and N. Munichandraiah, *Electrooxidation of Methanol on Pt-Modified Conductive Polymer PEDOT.* Langmuir, 2009. **25**(3): p. 1732-1738.

[54] Calle-Vallejo, F., M.D. Pohl, D. Reinisch, D. Loffreda, P. Sautet, and A.S. Bandarenka, *Why conclusions from platinum model surfaces do not necessarily lead to enhanced nanoparticle catalysts for the oxygen reduction reaction.* Chemical Science, 2017. **8**(3): p. 2283-2289.

[55] Wendt, H., *K. Kinoshita: Carbon, Electrochemical and Physical Properties, John Wiley + Sons, Chichester, New York, Brisbane, Toronto 1988. 533 Seiten, Preis: £ 65.–*. 1988. **92**(9): p. 1060-1060.

[56] You, P.Y. and S.K. Kamarudin, *Recent progress of carbonaceous materials in fuel cell applications: An overview.* Chemical Engineering Journal, 2017. **309**: p. 489-502.

[57] Su, N., X. Hu, J. Zhang, H. Huang, J. Cheng, J. Yu, and C. Ge, *Plasma-induced synthesis of Pt nanoparticles supported on TiO2 nanotubes for enhanced methanol electro-oxidation.* Applied Surface Science, 2017. **399**: p. 403-410.

[58] Zhao, Z., C. Chen, Z. Liu, J. Huang, M. Wu, H. Liu, Y. Li, and Y. Huang, *Pt-Based Nanocrystal for Electrocatalytic Oxygen Reduction.* 2019. **31**(31): p. 1808115.

[59] Liu, J., C. Liu, F. Wang, Y. Song, Z. Li, and J. Ji, *Preparation of Pt Nanocrystals on Ultrasonic Cavitation Functionalized Pristine Carbon Nanotubes as Electrocatalysts for Electrooxidation of Methanol.* Industrial & Engineering Chemistry Research, 2014. **53**(52): p. 20099-20106.

[60] Lee, W.H., J. Seo, T. Lee, and H. Kim, *Preparation of a self-assembled organosilane coating on carbon black as a catalyst support in polymer electrolyte membrane fuel cells.* Journal of Power Sources, 2015. **274**: p. 1140-1146.

[61] Nie, Y., L. Li, and Z. Wei, *Recent advancements in Pt and Pt-free catalysts for oxygen reduction reaction.* Chemical Society Reviews, 2015. **44**(8): p. 2168-2201.

[62] Punetha, V.D., S. Rana, H.J. Yoo, A. Chaurasia, J.T. McLeskey Jr, M.S. Ramasamy, N.G. Sahoo, and J.W. Cho, *Functionalization of carbon nanomaterials for advanced polymer nanocomposites: A comparison study between CNT and graphene.* Progress in Polymer Science.

[63] Rümmeli, M.H., P. Ayala, and T. Pichler, *Carbon Nanotubes and Related Structures: Production and Formation*, in *Carbon Nanotubes and Related Structures*. 2010, Wiley-VCH Verlag GmbH & Co. KGaA. p. 1-21.

[64] Saito, Y., *Structures and Synthesis of Carbon Nanotubes*, in *Carbon Nanotube and Related Field Emitters*. 2010, Wiley-VCH Verlag GmbH & Co. KGaA. p. 1-14.

[65] Monthioux, M., *Introduction to Carbon Nanotubes*, in *Carbon Meta-Nanotubes*. 2011, John Wiley & Sons, Ltd. p. 7-39.

[66] Golshadi, M., J. Maita, D. Lanza, M. Zeiger, V. Presser, and M.G. Schrlau, *Effects of synthesis parameters on carbon nanotubes manufactured by template-based chemical vapor deposition.* Carbon, 2014. **80**: p. 28-39.

[67] Hashempour, M., A. Vicenzo, F. Zhao, and M. Bestetti, *Direct growth of MWCNTs on 316 stainless steel by chemical vapor deposition: Effect of surface nano-features on CNT growth and structure.* Carbon, 2013. **63**: p. 330-347.

[68] Baddour, C.E., F. Fadlallah, D. Nasuhoglu, R. Mitra, L. Vandsburger, and J.-L. Meunier, *A simple thermal CVD method for carbon nanotube synthesis on stainless steel 304 without the addition of an external catalyst.* Carbon, 2009. **47**(1): p. 313-318.

[69] Hordy, N., N.-Y. Mendoza-Gonzalez, S. Coulombe, and J.-L. Meunier, *The effect of carbon input on the morphology and attachment of carbon nanotubes grown directly from stainless steel.* Carbon, 2013. **63**: p. 348-357.

[70] Hernández-Fernández, P., S. Baranton, S. Rojas, P. Ocón, J.-M. Léger, and J.L.G. Fierro, *Insights into the Effects of Functional Groups on Carbon Nanotubes for the Electrooxidation of Methanol.* Langmuir, 2011. **27**(15): p. 9621-9629.

[71] McArthur, M.A., N. Hordy, S. Coulombe, and S. Omanovic, *A binder-free multi-walled carbon nanotube electrode containing oxygen functionalities for electrochemical capacitors.* Electrochimica Acta, 2015. **162**: p. 245-253.

[72] Jorge, L., S. Coulombe, and P.-L. Girard-Lauriault, *Nanofluids Containing MWCNTs Coated with Nitrogen-Rich Plasma Polymer Films for CO_2 Absorption in Aqueous Medium.* Plasma Processes and Polymers, 2015. **12**(11): p. 1311-1321.

[73] Zhang, J., M. Chaker, and D. Ma, *Pulsed laser ablation based synthesis of colloidal metal nanoparticles for catalytic applications.* Journal of Colloid and Interface Science, 2017. **489**: p. 138-149.

[74] Lu, Y., Y. Jiang, H. Wu, and W. Chen, *Nano-PtPd Cubes on Graphene Exhibit Enhanced Activity and Durability in Methanol Electrooxidation after CO Stripping–Cleaning.* The Journal of Physical Chemistry C, 2013. **117**(6): p. 2926-2938.

[75] McArthur, M.A., L. Jorge, S. Coulombe, and S. Omanovic, *Synthesis and characterization of 3D Ni nanoparticle/carbon nanotube cathodes for hydrogen evolution in alkaline electrolyte.* Journal of Power Sources, 2014. **266**: p. 365-373.

[76] McArthur, M.A., *Multi-Walled Carbon Nanotube-Based Electrodes for Alternative Electrochemical Energy Storage, Ph.D., McGill University, completed in 2015.*

[77] Baig, N., I. Kammakakam, and W. Falath, *Nanomaterials: a review of synthesis methods, properties, recent progress, and challenges.* Materials Advances, 2021. **2**(6): p. 1821-1871.

[78] Ashrafi, M.A., M. Ranjbar, H. Kalhori, and H. Salamati, *Pulsed laser deposition of Mo-V-O thin films for chromogenic applications.* Thin Solid Films, 2017. **621**: p. 220-228.

[79] Russo, R.E., X. Mao, J.J. Gonzalez, V. Zorba, and J. Yoo, *Laser Ablation in Analytical Chemistry.* Analytical Chemistry, 2013. **85**(13): p. 6162-6177.

[80] Fujioka, H., *8 - Pulsed Laser Deposition (PLD) A2 - Kuech, Thomas F*, in *Handbook of Crystal Growth (Second Edition)*. 2015, North-Holland: Boston. p. 365-397.

[81] De Mesa, J.A., A.M. Amo, J.J.C. Miranda, H.O. Salazar, R.V. Sarmago, and W.O. Garcia, *Effects of Deposition Pressure and Target-Substrate Distance on Growth of ZnO by Femtosecond Pulsed Laser Deposition.* JLMN-Journal of Laser Micro/Nanoengineering, 2016. **11**(1): p. 21-24.

[82] Riabinina, D., E. Irissou, B.L. Drogoff, M. Chaker, and D. Guay, *Influence of pressure on the Pt nanoparticle growth modes during pulsed laser ablation.* Journal of Applied Physics, 2010. **108**(3): p. 034322.

[83] Jing, Y., R. Wang, Q. Wang, Z. Xiang, Z. Li, H. Gu, and X. Wang, *An overview of surface-enhanced Raman scattering substrates by pulsed laser deposition technique: fundamentals and applications.* Advanced Composites and Hybrid Materials, 2021. **4**(4): p. 885-905.

[84] Simao, T., D.M. Chevrier, J. Jakobi, A. Korinek, G. Goupil, M. Lau, S. Garbarino, P. Zhang, S. Barcikowski, M.-A. Fortin, and D. Guay, *Gold–Manganese Oxide Core–Shell Nanoparticles Produced by Pulsed Laser Ablation in Water.* The Journal of Physical Chemistry C, 2016. **120**(39): p. 22635-22645.

[85] Tabet-Aoul, A., F. Saidani, D. Rochefort, and M. Mohamedi, *Pulsed Laser Synthesis of SnO-Pt Nano-Thin Films onto Carbon Nanotubes and their Electrocatalytic Activity Towards Ethanol Oxidation.* International Journal of Electrochemical Science, 2011. **6**: p. 6385-6397.

[86] Ting-Wei, H., Q. Hamza, L. Guan-Ren, C. Szu-yuan, and T. Chung-Jen, *Production of high-performance and improved-durability Pt-catalyst /support for proton-exchange-membrane fuel cells with pulsed laser deposition.* Journal of Physics D: Applied Physics, 2016. **49**(25): p. 255601.

[87] Hamel, C., S. Garbarino, É. Irissou, M.-P. Bichat, and D. Guay, *Structural and Electrochemical Properties of Nanocrystalline PtRu Alloys Prepared by Crossed-Beam Pulsed Laser Deposition.* The Journal of Physical Chemistry C, 2010. **114**(44): p. 18931-18939.

[88] Irissou, E., F. Vidal, T. Johnston, M. Chaker, D. Guay, and A.N. Ryabinin, *Influence of an inert background gas on bimetallic cross-beam pulsed laser deposition.* Journal of Applied Physics, 2006. **99**(3): p. 034904.

[89] Li, L., L. Hu, J. Li, and Z. Wei, *Enhanced stability of Pt nanoparticle electrocatalysts for fuel cells.* Nano Research, 2015. **8**(2): p. 418-440.

[90] Liu, S., I.S. Amiinu, X. Liu, J. Zhang, M. Bao, T. Meng, and S. Mu, *Carbon nanotubes intercalated Co/N-doped porous carbon nanosheets as efficient electrocatalyst for oxygen reduction reaction and zinc–air batteries.* Chemical Engineering Journal, 2018. **342**: p. 163-170.

[91] Chen, W., J. Xue, Y. Bao, and L. Feng, *Surface engineering of nano-ceria facet dependent coupling effect on Pt nanocrystals for electro-catalysis of methanol oxidation reaction.* Chemical Engineering Journal, 2020. **381**: p. 122752.

[92] Davies, A. and A. Yu, *Material advancements in supercapacitors: From activated carbon to carbon nanotube and graphene.* 2011. **89**(6): p. 1342-1357.

[93] Dou, S., L. Tao, R. Wang, S. El Hankari, R. Chen, and S. Wang, *Plasma-Assisted Synthesis and Surface Modification of Electrode Materials for Renewable Energy.* 2018. **30**(21): p. 1705850.

[94] Goodenough, J.B., *Electrochemical energy storage in a sustainable modern society.* Energy & Environmental Science, 2014. **7**(1): p. 14-18.

[95] Wu, X., H. Yang, M. Yu, J. Liu, and S. Li, *Design principles of high-voltage aqueous supercapacitors.* Materials Today Energy, 2021. **21**: p. 100739.

[96] Movassagh-Alanagh, F., A. Bordbar-Khiabani, and A. Ahangari-Asl, *Fabrication of a ternary PANI@Fe_3O_4@CFs nanocomposite as a high performance electrode for solid-state supercapacitors.* International Journal of Hydrogen Energy, 2019. **44**(49): p. 26794-26806.

[97] Sridhar, D., H. Yu, J.-L. Meunier, and S. Omanovic, *Carbon nano-fiber forest foundation for ruthenium oxide pseudo-electrochemical capacitors.* Materials Advances, 2020. **1**(2): p. 215-227.

[98] Xie, P., W. Yuan, X. Liu, Y. Peng, Y. Yin, Y. Li, and Z. Wu, *Advanced carbon nanomaterials for state-of-the-art flexible supercapacitors.* Energy Storage Materials, 2021. **36**: p. 56-76.

[99] Pajootan, E., S. Omanovic, and S. Coulombe, *Controllable dry synthesis of binder-free nanostructured platinum electrocatalysts supported on multi-walled carbon nanotubes and their performance in the oxygen reduction reaction.* Chemical Engineering Journal, 2021. **426**: p. 131706.

[100] Pajootan, E., S. Coulombe, and S. Omanovic, *Two-Step Dry Synthesis of Binderless 3D Low Pt-Loading Electrocatalysts for Direct Alkaline Methanol Fuel Cell Anodes.* ACS Applied Energy Materials, 2021. **4**(10): p. 11514-11527.

[101] Sridhar, D., J.-L. Meunier, and S. Omanovic, *Directly grown carbon nano-fibers on nickel foam as binder-free long-lasting supercapacitor electrodes.* Materials Chemistry and Physics, 2019. **223**: p. 434-440.

[102] Ilnicka, A., M. Skorupska, M. Szkoda, Z. Zarach, P. Kamedulski, W. Zielinski, and J.P. Lukaszewicz, *Combined effect of nitrogen-doped functional groups and porosity of porous carbons on electrochemical performance of supercapacitors.* Scientific Reports, 2021. **11**(1): p. 18387.

[103] Meng, L., C. Fu, and Q. Lu, *Advanced technology for functionalization of carbon nanotubes.* Progress in Natural Science, 2009. **19**(7): p. 801-810.

[104] Eskandarian, L., M. Arami, and E. Pajootan, *Evaluation of Adsorption Characteristics of Multiwalled Carbon Nanotubes Modified by a Poly(propylene imine) Dendrimer in Single and Multiple Dye Solutions: Isotherms, Kinetics, and Thermodynamics.* Journal of Chemical & Engineering Data, 2014. **59**(2): p. 444-454.

[105] Mallakpour, S. and S. Soltanian, *Surface functionalization of carbon nanotubes: fabrication and applications.* RSC Advances, 2016. **6**(111): p. 109916-109935.

[106] Corella Puertas, E., M.-L. Peyot, M. Pineda, K. Volk, S. Coulombe, and V. Yargeau, *Degradation of diatrizoate in a pin-to-liquid plasma reactor, its transformation products and their residual toxicity.* Science of The Total Environment, 2021. **782**: p. 146895.

[107] Martin-del-Campo, J., M. Uceda, S. Coulombe, and J. Kopyscinski, *Plasma-catalytic dry reforming of methane over Ni-supported catalysts in a rotating gliding arc – Spouted bed reactor.* Journal of CO_2 Utilization, 2021. **46**: p. 101474.

[108] Saka, C., *Overview on the Surface Functionalization Mechanism and Determination of Surface Functional Groups of Plasma Treated Carbon Nanotubes.* Critical Reviews in Analytical Chemistry, 2018. **48**(1): p. 1-14.

[109] Nair, L.G., A.S. Mahapatra, N. Gomathi, K. Joseph, S. Neogi, and C.P.R. Nair, *Radio frequency plasma mediated dry functionalization of multiwall carbon nanotube.* Applied Surface Science, 2015. **340**: p. 64-71.

[110] Xu, T., J. Yang, J. Liu, and Q. Fu, *Surface modification of multi-walled carbon nanotubes by O_2 plasma.* Applied Surface Science, 2007. **253**(22): p. 8945-8951.

[111] Vesel, A. and M. Mozetic, *New developments in surface functionalization of polymers using controlled plasma treatments.* Journal of Physics D: Applied Physics, 2017. **50**(29): p. 293001.

[112] Meyyappan, M., *Plasma nanotechnology: past, present and future.* Journal of Physics D: Applied Physics, 2011. **44**(17): p. 174002.

[113] Pajootan, E., S. Coulombe, and S. Omanovic, *Two-Step Dry Synthesis of Binderless 3D Low Pt-Loading Electrocatalysts for Direct Alkaline Methanol Fuel Cell Anodes.* ACS Applied Energy Materials, 2021.

[114] Jorge, L., S. Coulombe, and P.-L. Girard-Lauriault, *Nanofluids Containing MWCNTs Coated with Nitrogen-Rich Plasma Polymer Films for CO_2 Absorption in Aqueous Medium.* 2015. **12**(11): p. 1311-1321.

[115] Hussain, S., R. Amade, E. Jover, and E. Bertran, *Nitrogen plasma functionalization of carbon nanotubes for supercapacitor applications.* Journal of Materials Science, 2013. **48**(21): p. 7620-7628.

[116] Roy, A., A. Ray, S. Saha, M. Ghosh, T. Das, B. Satpati, M. Nandi, and S. Das, *NiO-CNT composite for high performance supercapacitor electrode and oxygen evolution reaction.* Electrochimica Acta, 2018. **283**: p. 327-337.

[117] Ramya, S., T. Anita, H. Shaikh, and R.K. Dayal, *Laser Raman microscopic studies of passive films formed on type 316LN stainless steels during pitting in chloride solution.* Corrosion Science, 2010. **52**(6): p. 2114-2121.

[118] Chen, J., Q. Xiao, Z. Lu, X. Ru, H. Peng, Q. Xiong, and H. Li, *Characterization of interfacial reactions and oxide films on 316L stainless steel in various simulated PWR primary water environments.* Journal of Nuclear Materials, 2017. **489**: p. 137-149.

[119] Jorge, L., P.-L. Girard-Lauriault, and S. Coulombe, *pH-reversible destabilization-dispersion of MWCNTs coated with functional plasma polymer films in water.* 2017. **14**(11): p. 1700026.

[120] Hordy, N., S. Coulombe, and J.-L. Meunier, *Plasma Functionalization of Carbon Nanotubes for the Synthesis of Stable Aqueous Nanofluids and Poly(vinyl alcohol) Nanocomposites.* 2013. **10**(2): p. 110-118.

[121] Stancu, E.C., A.-M. Stanciuc, S. Vizireanu, C. Luculescu, L. Moldovan, A. Achour, and G. Dinescu, *Plasma functionalization of carbon nanowalls and its effect on attachment of fibroblast-like cells.* Journal of Physics D: Applied Physics, 2014. **47**(26): p. 265203.

[122] Choi, C., K.M. Kim, K.J. Kim, X. Lepró, G.M. Spinks, R.H. Baughman, and S.J. Kim, *Improvement of system capacitance via weavable superelastic biscrolled yarn supercapacitors.* Nature Communications, 2016. **7**(1): p. 13811.

[123] Frackowiak, E., K. Jurewicz, K. Szostak, S. Delpeux, and F. Béguin, *Nanotubular materials as electrodes for supercapacitors.* Fuel Processing Technology, 2002. **77-78**: p. 213-219.

[124] Shen, J., A. Liu, Y. Tu, G. Foo, C. Yeo, M.B. Chan-Park, R. Jiang, and Y. Chen, *How carboxylic groups improve the performance of single-walled carbon nanotube electrochemical capacitors?* Energy & Environmental Science, 2011. **4**(10): p. 4220-4229.

[125] Li, X., T. Gu, and B. Wei, *Dynamic and Galvanic Stability of Stretchable Supercapacitors.* Nano Letters, 2012. **12**(12): p. 6366-6371.

[126] Pan, H., J. Li, and Y. Feng, *Carbon Nanotubes for Supercapacitor*. Nanoscale Research Letters, 2010. **5**(3): p. 654.

[127] Chauhan, N.P.S., M. Mozafari, N.S. Chundawat, K. Meghwal, R. Ameta, and S.C. Ameta, *High-performance supercapacitors based on polyaniline–graphene nanocomposites: Some approaches, challenges and opportunities.* Journal of Industrial and Engineering Chemistry, 2016. **36**: p. 13-29.

[128] Abdel-Fattah, E., D. Ogawa, and K. Nakamura, *Oxygen functionalization of MWCNTs in RF-dielectric barrier discharge Ar/O_2 plasma.* Journal of Physics D: Applied Physics, 2017. **50**(26): p. 265301.

[129] Daletou, M.K. and C.A. Aggelopoulos, *Highly-energy efficient oxidation of MWCNT with nanosecond pulsed dielectric barrier discharge plasma.* Applied Surface Science, 2021. **563**: p. 150139.

[130] Saikia, N.J., C. Ewels, J.-F. Colomer, B. Aleman, M. Amati, L. Gregoratti, A. Hemberg, D. Thiry, R. Snyders, and C. Bittencourt, *Plasma Fluorination of Vertically Aligned Carbon Nanotubes.* The Journal of Physical Chemistry C, 2013. **117**(28): p. 14635-14641.

[131] Yu, H., D. Sridhar, and S. Omanovic, *Ru_xBi_{1-x}-oxide as an electrode material for pseudocapacitors.* The Canadian Journal of Chemical Engineering, 2021. **https://doi.org/10.1002/cjce.24306**.

[132] Pajootan, E. and M. Arami, *Structural and electrochemical characterization of carbon electrode modified by multi-walled carbon nanotubes and surfactant.* Electrochimica Acta, 2013. **112**: p. 505-514.

[133] Mei, B.-A., O. Munteshari, J. Lau, B. Dunn, and L. Pilon, *Physical Interpretations of Nyquist Plots for EDLC Electrodes and Devices.* The Journal of Physical Chemistry C, 2018. **122**(1): p. 194-206.

[134] Simon, P. and Y. Gogotsi, *Materials for electrochemical capacitors.* Nature Materials, 2008. **7**(11): p. 845-854.

[135] Bathula, C., I. Rabani, A. Kadam, H. Opoku, S.A. Patil, N.K. Shreshta, J.-H. Hwang, Y.-S. Seo, and H.-S. Kim, *Sonochemically exfoliated polymer-carbon nanotube interface for high performance supercapacitors.* Journal of Colloid and Interface Science, 2022. **606**: p. 1792-1799.

[136] Frackowiak, E., K. Jurewicz, S. Delpeux, and F. Béguin, *Nanotubular materials for supercapacitors.* Journal of Power Sources, 2001. **97-98**: p. 822-825.

[137] Mohan, R., A. Modak, and A. Schechter, *A Comparative Study of Plasma-Treated Oxygen-Doped Single-Walled and Multiwalled Carbon Nanotubes as Electrocatalyst for Efficient Oxygen Reduction Reaction.* ACS Sustainable Chemistry & Engineering, 2019. **7**(13): p. 11396-11406.

[138] Roumeli, E., M. Diamantopoulou, M. Serra-Garcia, P. Johanns, G. Parcianello, and C. Daraio, *Characterization of Vertically Aligned Carbon Nanotube Forests Grown on Stainless Steel Surfaces.* Nanomaterials (Basel, Switzerland), 2019. **9**(3): p. 444.

[139] Rebelo, S.L.H., A. Guedes, M.E. Szefczyk, A.M. Pereira, J.P. Araújo, and C. Freire, *Progress in the Raman spectra analysis of covalently functionalized multiwalled carbon nanotubes: unraveling disorder in graphitic materials.* Physical Chemistry Chemical Physics, 2016. **18**(18): p. 12784-12796.

[140] Li, Y., H.-i. Kim, B. Wei, J. Kang, J.-b. Choi, J.-D. Nam, and J. Suhr, *Understanding the nanoscale local buckling behavior of vertically aligned MWCNT arrays with van der Waals interactions.* Nanoscale, 2015. **7**(34): p. 14299-14304.

[141] DiLeo, R.A., B.J. Landi, and R.P. Raffaelle, *Purity assessment of multiwalled carbon nanotubes by Raman spectroscopy.* 2007. **101**(6): p. 064307.

[142] Sun, Y., K. Liu, Y. Han, Q. Li, S. Fan, and K. Jiang, *Excitation of Surface Plasmon Resonance in Composite Structures Based on Single-Layer Superaligned Carbon Nanotube Films.* The Journal of Physical Chemistry C, 2013. **117**(44): p. 23190-23197.

[143] Akbar, S., A. Anwar, M.Z. Noon, J.M. Elliott, and A.M. Squires, *Platinum as an electrocatalyst: effect of morphological aspects of Pt/Pt-based materials.* Materials Science and Technology, 2019. **35**(1): p. 1-11.

[144] Raj, C.R., A. Samanta, S.H. Noh, S. Mondal, T. Okajima, and T. Ohsaka, *Emerging new generation electrocatalysts for the oxygen reduction reaction.* Journal of Materials Chemistry A, 2016. **4**(29): p. 11156-11178.

[145] Li, Y., Y. Tong, and F. Peng, *Metal-free carbocatalysis for electrochemical oxygen reduction reaction: Activity origin and mechanism.* Journal of Energy Chemistry, 2020. **48**: p. 308-321.

[146] Serov, A., A.D. Shum, X. Xiao, V. De Andrade, K. Artyushkova, I.V. Zenyuk, and P. Atanassov, *Nano-structured platinum group metal-free catalysts and their integration in fuel cell electrode architectures.* Applied Catalysis B: Environmental, 2018. **237**: p. 1139-1147.

[147] Singh, S.K., K. Takeyasu, and J. Nakamura, *Active Sites and Mechanism of Oxygen Reduction Reaction Electrocatalysis on Nitrogen-Doped Carbon Materials.* Advanced Materials, 2019. **31**(13): p. 1804297.

[148] Satyapal, S., *Hydrogen and Fuel Cells Enabled through the U.S. Department of Energy, Department of Energy, 235th ECS Meeting, https://www.energy.gov/sites/prod/files/2019/06/f63/fcto-satyapal-overview-for-ecs-meeting-2019-05-27.pdf, 2019 (accessed 10 June 2020).* .

[149] Xu, Y. and B. Zhang, *Recent advances in porous Pt-based nanostructures: synthesis and electrochemical applications.* Chemical Society Reviews, 2014. **43**(8): p. 2439-2450.

[150] Chen, W., J. Huang, J. Wei, D. Zhou, J. Cai, Z.-D. He, and Y.-X. Chen, *Origins of high onset overpotential of oxygen reduction reaction at Pt-based electrocatalysts: A mini review.* Electrochemistry Communications, 2018. **96**: p. 71-76.

[151] Ghosh, S., S. Mondal, and C. Retna Raj, *Carbon nanotube-supported dendritic Pt-on-Pd nanostructures: growth mechanism and electrocatalytic activity towards oxygen reduction reaction.* Journal of Materials Chemistry A, 2014. **2**(7): p. 2233-2239.

[152] Gutowski, T.G., S. Sahni, J.M. Allwood, M.F. Ashby, and E. Worrell, *The energy required to produce materials: constraints on energy-intensity improvements, parameters of demand.* 2013. **371**(1986): p. 20120003.

[153] Xie, L. and D.W. Kirk, *Stability Comparison of Pt and Ni as Base Metal Catalysts in Anion Exchange Membrane Fuel Cells.* Journal of The Electrochemical Society, 2020. **167**(6): p. 064519.

[154] Lai, J. and S. Guo, *Design of Ultrathin Pt-Based Multimetallic Nanostructures for Efficient Oxygen Reduction Electrocatalysis.* 2017. **13**(48): p. 1702156.

[155] Tang, Y. and W. Cheng, *Key parameters governing metallic nanoparticle electrocatalysis.* Nanoscale, 2015. **7**(39): p. 16151-16164.

[156] Kawabata, S., Y. Naono, Y. Taguchi, S.H. Huh, and A. Nakajima, *Designable formation of metal nanoparticle array with the deposition of negatively charged nanoparticles.* Applied Surface Science, 2007. **253**(16): p. 6690-6696.

[157] Li, Q., L. Li, X. Yu, X. Wu, Z. Xie, X. Wang, Z. Lu, X. Zhang, Y. Huang, and X. Yang, *Ultrafine platinum particles anchored on porous boron nitride enabling excellent stability and activity for oxygen reduction reaction.* Chemical Engineering Journal, 2020. **399**: p. 125827.

[158] Gao, J.J., P. Du, Q.H. Zhang, X. Shen, F.K. Chiang, Y.R. Wen, X. Lin, X.J. Liu, and H.J. Qiu, *Platinum single atoms/clusters stabilized in transition metal oxides for enhanced electrocatalysis.* Electrochimica Acta, 2019. **297**: p. 155-162.

[159] Cherevko, S., N. Kulyk, and K.J.J. Mayrhofer, *Durability of platinum-based fuel cell electrocatalysts: Dissolution of bulk and nanoscale platinum.* Nano Energy, 2016. **29**: p. 275-298.

[160] Dolbec, R., E. Irissou, M. Chaker, D. Guay, F. Rosei, and M.A. El Khakani, *Growth dynamics of pulsed laser deposited Pt nanoparticles on highly oriented pyrolitic graphite substrates.* Physical Review B, 2004. **70**(20): p. 201406.

[161] Irissou, E., F. Laplante, S. Garbarino, M. Chaker, and D. Guay, *Structural and Electrochemical Characterization of Metastable PtAu Bulk and Surface Alloys Prepared by Crossed-Beam Pulsed Laser Deposition.* The Journal of Physical Chemistry C, 2010. **114**(5): p. 2192-2199.

[162] Adachi, H. and K. Wasa, *1 - Thin Films and Nanomaterials*, in *Handbook of Sputtering Technology (Second Edition)*, K. Wasa, I. Kanno, and H. Kotera, Editors. 2012, William Andrew Publishing: Oxford. p. 3-39.

[163] Wen, S.-B., X. Mao, R. Greif, and R.E. Russo, *Experimental and theoretical studies of particle generation after laser ablation of copper with a background gas at atmospheric pressure.* Journal of Applied Physics, 2007. **101**(12): p. 123105.

[164] Kim, M., S. Osone, T. Kim, H. Higashi, and T. Seto, *Synthesis of Nanoparticles by Laser Ablation: A Review.* KONA Powder and Particle Journal, 2017. **34**: p. 80-90.

[165] Semaltianos, N.G., *Nanoparticles by Laser Ablation.* Critical Reviews in Solid State and Materials Sciences, 2010. **35**(2): p. 105-124.

[166] Kuroda, S., S. Kaihara, Y. Fujii, T. Kinoshita, and M. Adachi, *Modeling of particle generation in laser ablation plasma.* Journal of Aerosol Science, 2012. **50**: p. 38-56.

[167] Marla, D., U.V. Bhandarkar, and S.S. Joshi, *A model of laser ablation with temperature-dependent material properties, vaporization, phase explosion and plasma shielding.* Applied Physics A, 2014. **116**(1): p. 273-285.

[168] Girault, M., J.L. Le Garrec, J.B.A. Mitchell, J.M. Jouvard, E. Carvou, J. Menneveux, J. Yu, F.X. Ouf, S. Carles, V. Potin, G. Pillon, S. Bourgeois, J. Perez, M.C. Marco de Lucas, and L. Lavisse, *Influence of the reactive atmosphere on the formation of nanoparticles in the plasma plume induced by nanosecond pulsed laser irradiation of metallic targets at atmospheric pressure and high repetition rate.* Applied Surface Science, 2016. **374**: p. 132-137.

[169] Hamoudi, Z., B. Aïssa, M.A. El Khakani, and M. Mohamedi, *Electrocatalytic Reduction of Oxygen at Binderless Carbon-Pt Nanostructured Electrodes: Effects of the Nature of the Carbon Support and the Pt Morphology.* Int. J. Electrochem. Sci. , 2012. **7**: p. 12227-12235.

[170] Jorge, L., P.-L. Girard-Lauriault, and S. Coulombe, *pH-reversible destabilization-dispersion of MWCNTs coated with functional plasma polymer films in water.* Plasma Processes and Polymers, 2017. **14**(11): p. 1700026.

[171] Hergenröder, R., *A model for the generation of small particles in laser ablation ICP-MS.* Journal of Analytical Atomic Spectrometry, 2006. **21**(10): p. 1016-1026.

[172] Poitrasson, F. and F.-X. d'Abzac, *Femtosecond laser ablation inductively coupled plasma source mass spectrometry for elemental and isotopic analysis: are ultrafast lasers worthwhile?* Journal of Analytical Atomic Spectrometry, 2017. **32**(6): p. 1075-1091.

[173] Koechner, W., *Laser Amplifier*, in *Solid-State Laser Engineering*, W. Koechner, Editor. 2006, Springer New York: New York, NY. p. 156-209.

[174] Koechner, W., *Optical Pump Systems*, in *Solid-State Laser Engineering*, W. Koechner, Editor. 2006, Springer New York: New York, NY. p. 300-422.

[175] Martis, P., B.R. Venugopal, J. Delhalle, and Z. Mekhalif, *Selective decoration of nickel and nickel oxide nanocrystals on multiwalled carbon nanotubes.* Journal of Solid State Chemistry, 2011. **184**(5): p. 1245-1250.

[176] Li, B., J. Wang, Y. Yuan, H. Ariga, S. Takakusagi, and K. Asakura, *Carbon Nanotube-Supported RuFe Bimetallic Nanoparticles as Efficient and Robust Catalysts for Aqueous-Phase Selective Hydrogenolysis of Glycerol to Glycols.* ACS Catalysis, 2011. **1**(11): p. 1521-1528.

[177] Mao, X., W.-T. Chan, M. Caetano, M.A. Shannon, and R.E. Russo, *Preferential vaporization and plasma shielding during nano-second laser ablation.* Applied Surface Science, 1996. **96-98**: p. 126-130.

[178] Perez, D. and L.J. Lewis, *Molecular-dynamics study of ablation of solids under femtosecond laser pulses.* Physical Review B, 2003. **67**(18): p. 184102.

[179] Kelly, R. and A. Miotello, *Comments on explosive mechanisms of laser sputtering.* Applied Surface Science, 1996. **96-98**: p. 205-215.

[180] Mazzi, A., F. Gorrini, and A. Miotello, *Liquid nanodroplet formation through phase explosion mechanism in laser-irradiated metal targets.* Physical Review E, 2015. **92**(3): p. 031301.

[181] Mazzi, A. and A. Miotello, *Simulation of phase explosion in the nanosecond laser ablation of aluminum.* Journal of Colloid and Interface Science, 2017. **489**: p. 126-130.

[182] Wu, M.-C., C.-L. Li, C.-K. Hu, Y.-C. Chang, Y.-H. Liaw, L.-W. Huang, C.-S. Chang, T.-T. Tsong, and T. Hsu, *Curvature effect on the surface diffusion of silver adatoms on carbon nanotubes: Deposition experiments and numerical simulations.* Physical Review B, 2006. **74**(12): p. 125424.

[183] Hergenröder, R., *Laser-generated aerosols in laser ablation for inductively coupled plasma spectrometry.* Spectrochimica Acta Part B: Atomic Spectroscopy, 2006. **61**(3): p. 284-300.

[184] Cao, A., C. Xu, J. Liang, D. Wu, and B. Wei, *X-ray diffraction characterization on the alignment degree of carbon nanotubes.* Chemical Physics Letters, 2001. **344**(1): p. 13-17.

[185] Hu, L., C. Shang, X. Wang, and G. Zhou, *Hollow Carbon Nanocubes as Oxygen Reduction Reaction Electrocatalyst.* 2020. **5**(42): p. 13300-13304.

[186] Kim, S.J., J.Y. Koo, T. Mun, M. Choi, and W. Lee, *Tailoring defect chemistry at interfaces for promoted oxygen reduction reaction kinetics.* Journal of Materials Chemistry A, 2020. **8**(44): p. 23313-23322.

[187] Aruna, I., B.R. Mehta, L.K. Malhotra, and S.M. Shivaprasad, *Size dependence of core and valence binding energies in Pd nanoparticles: Interplay of quantum confinement and coordination reduction.* 2008. **104**(6): p. 064308.

[188] Yang, D.Q., B. Hennequin, and E. Sacher, *XPS Demonstration of π−π Interaction between Benzyl Mercaptan and Multiwalled Carbon Nanotubes and Their Use in the Adhesion of Pt Nanoparticles.* Chemistry of Materials, 2006. **18**(21): p. 5033-5038.

[189] Uddin, A.S.M.I., U. Yaqoob, K. Hassan, and G.-S. Chung, *Effects of Pt shell thickness on self-assembly monolayer Pd@Pt core-shell nanocrystals based hydrogen sensing.* International Journal of Hydrogen Energy, 2016. **41**(34): p. 15399-15410.

[190] Kodama, K., A. Beniya, N. Isomura, and Y. Watanabe, *Electrochemical Observation of High Oxophilicity and its Effect on Oxygen Reduction Reaction Activity of Au Clusters Mass-Selectively Deposited on Glassy Carbon.* Electrocatalysis, 2018. **9**(4): p. 471-479.

[191] Geniès, L., R. Faure, and R. Durand, *Electrochemical reduction of oxygen on platinum nanoparticles in alkaline media.* Electrochimica Acta, 1998. **44**(8): p. 1317-1327.

[192] Zhang, L., M. Wei, S. Wang, Z. Li, L.-X. Ding, and H. Wang, *Highly stable PtP alloy nanotube arrays as a catalyst for the oxygen reduction reaction in acidic medium.* Chemical Science, 2015. **6**(5): p. 3211-3216.

[193] Alia, S.M., G. Zhang, D. Kisailus, D. Li, S. Gu, K. Jensen, and Y. Yan, *Porous Platinum Nanotubes for Oxygen Reduction and Methanol Oxidation Reactions.* 2010. **20**(21): p. 3742-3746.

[194] Pilapil, B.K., J. van Drunen, Y. Makonnen, D. Beauchemin, G. Jerkiewicz, and B.D. Gates, *Ordered Porous Electrodes by Design: Toward Enhancing the Effective Utilization of Platinum in Electrocatalysis.* 2017. **27**(36): p. 1703171.

[195] Czerwinski, A., *The Comparative Study of "Adsorbed Co" Oxidation On the Rough and Smooth Pt Electrodes.* Analytical Letters, 1989. **22**(6): p. 1547-1553.

[196] Czerwiński, A. and J. Sobkowski, *The adsorption of carbon monoxide on a platinum electrode.* Journal of Electroanalytical Chemistry and Interfacial Electrochemistry, 1978. **91**(1): p. 47-53.

[197] Hussain, S., H. Erikson, N. Kongi, A. Tarre, P. Ritslaid, M. Kook, M. Rähn, M. Merisalu, V. Sammelselg, and K. Tammeveski, *Improved ORR Activity and Long-Term Durability of Pt Nanoparticles Deposited on TiO2-Decorated Multiwall Carbon Nanotubes.* Journal of The Electrochemical Society, 2019. **166**(16): p. F1284-F1291.

[198] Molina-García, M.A. and N.V. Rees, *Effect of catalyst carbon supports on the oxygen reduction reaction in alkaline media: a comparative study.* RSC Advances, 2016. **6**(97): p. 94669-94681.

[199] Anand, A.N., K.S. Dheeraj, S. Navneet, G. Gaurav, G. Junfeng, Z. Zhigang, and J.K. Luo, *A Comparative Investigation on Various Platinum Nanoparticles Decorated Carbon Supports for Oxygen Reduction Reaction.* Current Nanoscience, 2017. **13**(2): p. 136-148.

[200] Marković, N.M. and P.N. Ross, *Surface science studies of model fuel cell electrocatalysts.* Surface Science Reports, 2002. **45**(4): p. 117-229.

[201] Cuesta, A., A. Couto, A. Rincón, M.C. Pérez, A. López-Cudero, and C. Gutiérrez, *Potential dependence of the saturation CO coverage of Pt electrodes: The origin of the pre-peak in CO-stripping voltammograms. Part 3: Pt(poly).* Journal of Electroanalytical Chemistry, 2006. **586**(2): p. 184-195.

[202] García, G. and M.T.M. Koper, *Dual Reactivity of Step-Bound Carbon Monoxide during Oxidation on a Stepped Platinum Electrode in Alkaline Media.* Journal of the American Chemical Society, 2009. **131**(15): p. 5384-5385.

[203] Hrnjić, A., F. Ruiz-Zepeda, M. Gaberšček, M. Bele, L. Suhadolnik, N. Hodnik, and P. Jovanovič, *Modified Floating Electrode Apparatus for Advanced Characterization of Oxygen Reduction Reaction Electrocatalysts.* Journal of The Electrochemical Society, 2020. **167**(16): p. 166501.

[204] Shinozaki, K., J.W. Zack, S. Pylypenko, B.S. Pivovar, and S.S. Kocha, *Oxygen Reduction Reaction Measurements on Platinum Electrocatalysts Utilizing Rotating Disk Electrode Technique.* Journal of The Electrochemical Society, 2015. **162**(12): p. F1384-F1396.

[205] Huang, Q., Y. Guo, D. Chen, L. Zhang, T.-T. Li, Y. Hu, J. Qian, and S. Huang, *Rational construction of ultrafine noble metals onto carbon nanoribbons with efficient oxygen reduction in practical alkaline fuel cell.* Chemical Engineering Journal, 2021. **424**: p. 130336.

[206] Kucernak, A.R. and E. Toyoda, *Studying the oxygen reduction and hydrogen oxidation reactions under realistic fuel cell conditions.* Electrochemistry Communications, 2008. **10**(11): p. 1728-1731.

[207] Santori, P.G., A.N. Mondal, D.R. Dekel, and F. Jaouen, *The critical importance of ionomers on the electrochemical activity of platinum and platinum-free catalysts for anion-exchange membrane fuel cells.* Sustainable Energy & Fuels, 2020. **4**(7): p. 3300-3307.

[208] Kongkanand, A. and M.F. Mathias, *The Priority and Challenge of High-Power Performance of Low-Platinum Proton-Exchange Membrane Fuel Cells.* The Journal of Physical Chemistry Letters, 2016. **7**(7): p. 1127-1137.

[209] Liu, L. and A. Corma, *Metal Catalysts for Heterogeneous Catalysis: From Single Atoms to Nanoclusters and Nanoparticles.* Chemical Reviews, 2018. **118**(10): p. 4981-5079.

[210] Subbaraman, R., D. Tripkovic, K.-C. Chang, D. Strmcnik, A.P. Paulikas, P. Hirunsit, M. Chan, J. Greeley, V. Stamenkovic, and N.M. Markovic, *Trends in activity for the water electrolyser reactions on 3d M(Ni,Co,Fe,Mn) hydr(oxy)oxide catalysts.* Nature Materials, 2012. **11**(6): p. 550-557.

[211] Feng, Y., Q. Shao, Y. Ji, X. Cui, Y. Li, X. Zhu, and X. Huang, *Surface-modulated palladium-nickel icosahedra as high-performance non-platinum oxygen reduction electrocatalysts.* 2018. **4**(7): p. eaap8817.

[212] Schröder, J., J. Quinson, J.K. Mathiesen, J.J.K. Kirkensgaard, S. Alinejad, V.A. Mints, K.M. Jensen, and M. Arenz, *A New Approach to Probe the Degradation of Fuel Cell Catalysts*

under Realistic Conditions: Combining Tests in a Gas Diffusion Electrode Setup with Small Angle X-ray Scattering. Journal of The Electrochemical Society, 2020. **167**(13): p. 134515.

[213] Ergul-Yilmaz, B., Z. Yang, M.L. Perry, K.L. More, N. Macauley, R.L. Borup, and T. Karabacak, *Microstructural Evolution and ORR Activity of Nanocolumnar Platinum Thin Films with Different Mass Loadings Grown by High Pressure Sputtering.* Journal of The Electrochemical Society, 2020. **167**(13): p. 134514.

[214] Zalitis, C.M., D. Kramer, and A.R. Kucernak, *Electrocatalytic performance of fuel cell reactions at low catalyst loading and high mass transport.* Physical Chemistry Chemical Physics, 2013. **15**(12): p. 4329-4340.

[215] Ehelebe, K., D. Seeberger, M.T.Y. Paul, S. Thiele, K.J.J. Mayrhofer, and S. Cherevko, *Evaluating Electrocatalysts at Relevant Currents in a Half-Cell: The Impact of Pt Loading on Oxygen Reduction Reaction.* Journal of The Electrochemical Society, 2019. **166**(16): p. F1259-F1268.

[216] Inaba, M., A.W. Jensen, G.W. Sievers, M. Escudero-Escribano, A. Zana, and M. Arenz, *Benchmarking high surface area electrocatalysts in a gas diffusion electrode: measurement of oxygen reduction activities under realistic conditions.* Energy & Environmental Science, 2018. **11**(4): p. 988-994.

[217] Ciureanu, M. and R. Roberge, *Electrochemical Impedance Study of PEM Fuel Cells. Experimental Diagnostics and Modeling of Air Cathodes.* The Journal of Physical Chemistry B, 2001. **105**(17): p. 3531-3539.

[218] Singh, R.K., R. Devivaraprasad, T. Kar, A. Chakraborty, and M. Neergat, *Electrochemical Impedance Spectroscopy of Oxygen Reduction Reaction (ORR) in a Rotating Disk Electrode Configuration: Effect of Ionomer Content and Carbon-Support.* Journal of The Electrochemical Society, 2015. **162**(6): p. F489-F498.

[219] Zhang, D., C. Zhang, J. Liu, Q. Chen, X. Zhu, and C. Liang, *Carbon-Encapsulated Metal/Metal Carbide/Metal Oxide Core–Shell Nanostructures Generated by Laser Ablation of Metals in Organic Solvents.* ACS Applied Nano Materials, 2019. **2**(1): p. 28-39.

[220] Kim, S.J., Y.J. Park, E.J. Ra, K.K. Kim, K.H. An, Y.H. Lee, J.Y. Choi, C.H. Park, S.K. Doo, M.H. Park, and C.W. Yang, *Defect-induced loading of Pt nanoparticles on carbon nanotubes.* 2007. **90**(2): p. 023114.

[221] Zhang, J., X. Zhang, S. Chen, T. Gong, and Y. Zhu, *Surface-enhanced Raman scattering properties of multi-walled carbon nanotubes arrays-Ag nanoparticles.* Carbon, 2016. **100**: p. 395-407.

[222] Nesselberger, M., S. Ashton, J.C. Meier, I. Katsounaros, K.J.J. Mayrhofer, and M. Arenz, *The Particle Size Effect on the Oxygen Reduction Reaction Activity of Pt Catalysts: Influence of Electrolyte and Relation to Single Crystal Models.* Journal of the American Chemical Society, 2011. **133**(43): p. 17428-17433.

[223] Shu, Q., Z. Xia, W. Wei, X. Xu, R. Sun, R. Deng, Q. Yang, H. Zhao, S. Wang, and G. Sun, *Controllable Unzipping of Carbon Nanotubes as Advanced Pt Catalyst Supports for Oxygen Reduction.* ACS Applied Energy Materials, 2019. **2**(8): p. 5446-5455.

[224] Xiang, Z., W. Li, F. Liu, F. Tan, F. Han, X. Wang, C. Shao, M. Xu, W. Liu, and X. Yang, *Catalyst with a low load of platinum and high activity for oxygen reduction derived from strong adsorption of Pt−N4 moieties on a carbon surface.* Electrochemistry Communications, 2021. **127**: p. 107039.

[225] Toh, S.Y., K.S. Loh, S.K. Kamarudin, and W.R.W. Daud, *Facile preparation of ultra-low Pt loading graphene-immobilized electrode for methanol oxidation reaction.* International Journal of Hydrogen Energy, 2018. **43**(33): p. 16005-16014.

[226] Tiwari, J.N., R.N. Tiwari, G. Singh, and K.S. Kim, *Recent progress in the development of anode and cathode catalysts for direct methanol fuel cells.* Nano Energy, 2013. **2**(5): p. 553-578.

[227] Pollet, B.G., S.S. Kocha, and I. Staffell, *Current status of automotive fuel cells for sustainable transport.* Current Opinion in Electrochemistry, 2019. **16**: p. 90-95.

[228] Rajeshkhanna, G. and G. Ranga Rao, *Micro and nano-architectures of Co3O4 on Ni foam for electro-oxidation of methanol.* International Journal of Hydrogen Energy, 2018. **43**(9): p. 4706-4715.

[229] Wang, F. and B. Fu, *4 - Anion-exchange membranes for direct methanol alkaline fuel cells*, in *Direct Methanol Fuel Cell Technology*, K. Dutta, Editor. 2020, Elsevier. p. 71-106.

[230] Higa, M., S. Mehdizadeh, S. Feng, N. Endo, and Y. Kakihana, *Cell performance of direct methanol alkaline fuel cell (DMAFC) using anion exchange membranes prepared from PVA-Based block copolymer.* Journal of Membrane Science, 2020. **597**: p. 117618.

[231] Jaggai, C., Z. Imkaraaz, K. Samm, A. Pounder, N. Koylass, D.P. Chakrabarti, M. Guo, and K. Ward, *Towards greater sustainable development within current Mega-Methanol (MM) production.* Green Chemistry, 2020. **22**(13): p. 4279-4294.

[232] Iaquaniello, G., G. Centi, A. Salladini, and E. Palo, *Chapter 22 - Methanol Economy: Environment, Demand, and Marketing With a Focus on the Waste-to-Methanol Process*, in *Methanol*, A. Basile and F. Dalena, Editors. 2018, Elsevier. p. 595-612.

[233] Aiyappa, H.B., S.N. Bhange, V.P. Sivasankaran, and S. Kurungot, *Single Cell Fabrication Towards the Realistic Evaluation of a CNT-Strung ZIF-Derived Electrocatalyst as a Cathode Material in Alkaline Fuel Cells and Metal−Air Batteries.* ChemElectroChem, 2017. **4**(11): p. 2928-2933.

[234] Ma, K.-B., S.-B. Han, S.-H. Kwon, D.-H. Kwak, and K.-W. Park, *High-performance direct ethanol fuel cell using nitrate reduction reaction.* International Journal of Hydrogen Energy, 2018. **43**(36): p. 17265-17270.

[235] Arenas, L.F., C. Ponce de León, and F.C. Walsh, *Three-dimensional porous metal electrodes: Fabrication, characterisation and use.* Current Opinion in Electrochemistry, 2019. **16**: p. 1-9.

[236] Kloke, A., F. von Stetten, R. Zengerle, and S. Kerzenmacher, *Strategies for the Fabrication of Porous Platinum Electrodes.* 2011. **23**(43): p. 4976-5008.

[237] Luo, L.-M., R.-H. Zhang, D. Chen, Q.-Y. Hu, and X.-W. Zhou, *Synthesis of 3D Thornbush-like Trimetallic CoAuPd Nanocatalysts and Electrochemical Dealloying for Methanol Oxidation and Oxygen Reduction Reaction.* ACS Applied Energy Materials, 2018. **1**(6): p. 2619-2629.

[238] Liu, Z., X. Lin, J.Y. Lee, W. Zhang, M. Han, and L.M. Gan, *Preparation and Characterization of Platinum-Based Electrocatalysts on Multiwalled Carbon Nanotubes for Proton Exchange Membrane Fuel Cells.* Langmuir, 2002. **18**(10): p. 4054-4060.

[239] Li, W., C. Liang, W. Zhou, J. Qiu, Zhou, G. Sun, and Q. Xin, *Preparation and Characterization of Multiwalled Carbon Nanotube-Supported Platinum for Cathode Catalysts of Direct Methanol Fuel Cells.* The Journal of Physical Chemistry B, 2003. **107**(26): p. 6292-6299.

[240] Tian, Z.Q., S.P. Jiang, Y.M. Liang, and P.K. Shen, *Synthesis and Characterization of Platinum Catalysts on Multiwalled Carbon Nanotubes by Intermittent Microwave*

Irradiation for Fuel Cell Applications. The Journal of Physical Chemistry B, 2006. **110**(11): p. 5343-5350.

[241] Rost, U., P. Podleschny, M. Schumacher, R. Muntean, D.T. Pascal, C. Mutascu, J. Koziolek, G. Marginean, and M. Brodmann, *Long-term Stable Electrodes Based on Platinum Electrocatalysts Supported on Titanium Sintered Felt for the Use in PEM Fuel Cells.* IOP Conference Series: Materials Science and Engineering, 2018. **416**: p. 012013.

[242] Chetty, R., K. Scott, S. Kundu, and M. Muhler, *Optimization of Mesh-Based Anodes for Direct Methanol Fuel Cells.* Journal of Fuel Cell Science and Technology, 2010. **7**(3): p. 031011-031011-9.

[243] Xue, Q., J.-K. Li, and Z.-Y. Yang, *Synergistically Improving the Activity, Antipoisonous Ability, and Long-Term Stability of Pt to Methanol Oxidation through Developing Favorable Graphene-Based Supports.* Langmuir, 2017.

[244] Satyanarayana, M., G. Rajeshkhanna, M.K. Sahoo, and G.R. Rao, *Electrocatalytic Activity of $Pd_{20-x}Ag_x$ Nanoparticles Embedded in Carbon Nanotubes for Methanol Oxidation in Alkaline Media.* ACS Applied Energy Materials, 2018. **1**(8): p. 3763-3770.

[245] Shrestha, S., Y. Liu, and W.E. Mustain, *Electrocatalytic Activity and Stability of Pt clusters on State-of-the-Art Supports: A Review.* Catalysis Reviews, 2011. **53**(3): p. 256-336.

[246] Themsirimongkon, S., T. Sarakonsri, S. Lapanantnoppakhun, J. Jakmunee, and S. Saipanya, *Carbon nanotube-supported Pt-Alloyed metal anode catalysts for methanol and ethanol oxidation.* International Journal of Hydrogen Energy, 2018.

[247] Radhakrishnan, T. and N. Sandhyarani, *Pt-Ag nanostructured 3D architectures: A tunable catalyst for methanol oxidation reaction.* Electrochimica Acta, 2019. **298**: p. 835-843.

[248] Ottakam Thotiyl, M.M., T. Ravikumar, and S. Sampath, *Platinum particles supported on titanium nitride: an efficient electrode material for the oxidation of methanol in alkaline media.* Journal of Materials Chemistry, 2010. **20**(47): p. 10643-10651.

[249] Huang, H., G. Ye, S. Yang, H. Fei, C.S. Tiwary, Y. Gong, R. Vajtai, J.M. Tour, X. Wang, and P.M. Ajayan, *Nanosized Pt anchored onto 3D nitrogen-doped graphene nanoribbons towards efficient methanol electrooxidation.* Journal of Materials Chemistry A, 2015. **3**(39): p. 19696-19701.

[250] Zhou, Y., X. Li, C. Yu, X. Hu, Y. Yin, S. Guo, and S. Zhong, *Synergistic and Durable Pt-WC Catalyst for Methanol Electro-Oxidation in Ionic Liquid Aqueous Solution.* ACS Applied Energy Materials, 2019. **2**(12): p. 8459-8463.

[251] Anjos, R.P.R., A.O. Santos, R.M. Antoniassi, O.C. Alves, E.A. Ponzio, and J.C.M. Silva, *The Effect of Tin Addition to Platinum Catalysts with Different Morphologies towards Methanol Electrooxidation in Alkaline Media.* ACS Applied Energy Materials, 2021. **4**(6): p. 6253-6260.

[252] Zhong, J.-P., C. Hou, L. Li, M. Waqas, Y.-J. Fan, X.-C. Shen, W. Chen, L.-Y. Wan, H.-G. Liao, and S.-G. Sun, *A novel strategy for synthesizing Fe, N, and S tridoped graphene-supported Pt nanodendrites toward highly efficient methanol oxidation.* Journal of Catalysis, 2020. **381**: p. 275-284.

[253] Debe, M.K., *Electrocatalyst approaches and challenges for automotive fuel cells.* Nature, 2012. **486**(7401): p. 43-51.

[254] Chakrapani, N., B. Wei, A. Carrillo, P.M. Ajayan, and R.S. Kane, *Capillarity-driven assembly of two-dimensional cellular carbon nanotube foams.* 2004. **101**(12): p. 4009-4012.

[255] Liu, C., Z. Li, P. Yu, H.-W. Wong, and Z. Gu, *Vertically Aligned and Surface Roughed Pt Nanostructured Wire Array as High Performance Electrocatalysts for Methanol Oxidation.* ACS Applied Energy Materials, 2018. **1**(8): p. 3973-3983.

[256] Wang, Z., S. Hu, A. Ali, H. Chen, and P.K. Shen, *Facile One-Pot Synthesis of a PtRh Alloy Decorated on Ag Nanocubes as a Trimetallic Core–Shell Catalyst for Boosting Methanol Oxidation Reaction.* ACS Applied Energy Materials, 2021. **4**(2): p. 1085-1092.

[257] Haisch, T., F. Kubannek, S. Baranton, C. Coutanceau, and U. Krewer, *The influence of adsorbed substances on alkaline methanol electro-oxidation.* Electrochimica Acta, 2019. **295**: p. 278-285.

[258] Yan, Q., H. Toghiani, Y.-W. Lee, K. Liang, and H. Causey, *Effect of sub-freezing temperatures on a PEM fuel cell performance, startup and fuel cell components.* Journal of Power Sources, 2006. **160**(2): p. 1242-1250.

[259] Chojak-Halseid, M., Z. Jusys, and R.J. Behm, *Methanol Oxidation Over a Pt/C Catalyst at High Temperatures and Pressure: An Online Electrochemical Mass Spectrometry Study.* The Journal of Physical Chemistry C, 2010. **114**(51): p. 22573-22581.

[260] Aricò, A.S., V. Baglio, A. Di Blasi, E. Modica, P.L. Antonucci, and V. Antonucci, *Analysis of the high-temperature methanol oxidation behaviour at carbon-supported Pt–Ru catalysts.* Journal of Electroanalytical Chemistry, 2003. **557**: p. 167-176.

[261] Chen, Y., Q. Zhong, G. Li, T. Tian, J. Tan, and M. Pan, *Electrochemical study of temperature and Nafion effects on interface property for oxygen reduction reaction.* Ionics, 2018. **24**(12): p. 3905-3914.

[262] Yan, W.-Y., S.-L. Zheng, W. Jin, Z. Peng, S.-N. Wang, H. Du, and Y. Zhang, *The influence of KOH concentration, oxygen partial pressure and temperature on the oxygen reduction reaction at Pt electrodes.* Journal of Electroanalytical Chemistry, 2015. **741**: p. 100-108.

[263] Tse, E.C.M. and A.A. Gewirth, *Effect of Temperature and Pressure on the Kinetics of the Oxygen Reduction Reaction.* The Journal of Physical Chemistry A, 2015. **119**(8): p. 1246-1255.

[264] Chung, D.Y., K.-J. Lee, and Y.-E. Sung, *Methanol Electro-Oxidation on the Pt Surface: Revisiting the Cyclic Voltammetry Interpretation.* The Journal of Physical Chemistry C, 2016. **120**(17): p. 9028-9035.

[265] Melnick, R.E. and G.T.R. Palmore, *Impedance Spectroscopy of the Electro-oxidation of Methanol on Polished Polycrystalline Platinum.* The Journal of Physical Chemistry B, 2001. **105**(5): p. 1012-1025.

[266] Xia, X.H., T. Iwasita, F. Ge, and W. Vielstich, *Structural effects and reactivity in methanol oxidation on polycrystalline and single crystal platinum.* Electrochimica Acta, 1996. **41**(5): p. 711-718.

[267] Melnick, R.E. and G.T.R. Palmore, *Time-Dependent Impedance of the Electro-oxidation of Methanol on Polished Polycrystalline Platinum.* The Journal of Physical Chemistry B, 2001. **105**(39): p. 9449-9457.

[268] Bhuvanendran, N., S. Ravichandran, W. Zhang, Q. Ma, Q. Xu, L. Khotseng, and H. Su, *Highly efficient methanol oxidation on durable Pt_xIr/MWCNT catalysts for direct methanol fuel cell applications.* International Journal of Hydrogen Energy, 2020. **45**(11): p. 6447-6460.

[269] Nouralishahi, A., Y. Mortazavi, A.A. Khodadadi, M. Choolaei, L.T. Thompson, and B.A. Horri, *Characteristics and performance of urea modified Pt-MWCNTs for electro-oxidation of methanol.* Applied Surface Science, 2019. **467-468**: p. 335-344.

[270] Xiong, W., B.A.T. Mehrabadi, S.G. Karakolos, R.D. White, A. Shakouri, P. Kasak, S.J. Zaidi, J.W. Weidner, J.R. Regalbuto, H. Colon-Mercado, and J.R. Monnier, *Enhanced Performance of Oxygen-Functionalized Multiwalled Carbon Nanotubes as Support for Pt and Pt–Ru Bimetallic Catalysts for Methanol Electrooxidation.* ACS Applied Energy Materials, 2020. **3**(6): p. 5487-5496.

[271] Prabhuram, J., T.S. Zhao, Z.K. Tang, R. Chen, and Z.X. Liang, *Multiwalled Carbon Nanotube Supported PtRu for the Anode of Direct Methanol Fuel Cells.* The Journal of Physical Chemistry B, 2006. **110**(11): p. 5245-5252.

[272] Hernández-Fernández, P., R. Nuño, E. Fatás, J.L.G. Fierro, and P. Ocón, *MWCNT-supported PtRu catalysts for the electrooxidation of methanol: Effect of the functionalized support.* International Journal of Hydrogen Energy, 2011. **36**(14): p. 8267-8278.

[273] Liu, Z., Q. Shi, F. Peng, H. Wang, H. Yu, J. Li, and X. Wei, *Enhanced methanol oxidation activity of Pt catalyst supported on the phosphorus-doped multiwalled carbon nanotubes in alkaline medium.* Catalysis Communications, 2012. **22**: p. 34-38.

[274] Akilavasan, J. and F. Marlow, *Electrochemical Impedance Spectroscopy at Redox-Type Liquid|Liquid Interfaces: The Capacitance Lag.* The Journal of Physical Chemistry C, 2020. **124**(7): p. 4101-4108.

[275] Greeley, J., I.E.L. Stephens, A.S. Bondarenko, T.P. Johansson, H.A. Hansen, T.F. Jaramillo, J. Rossmeisl, I. Chorkendorff, and J.K. Nørskov, *Alloys of platinum and early transition metals as oxygen reduction electrocatalysts.* Nature Chemistry, 2009. **1**(7): p. 552-556.

[276] Liu, S., W. Qi, S. Adimi, H. Guo, B. Weng, J.P. Attfield, and M. Yang, *Titanium Nitride-Supported Platinum with Metal–Support Interaction for Boosting Photocatalytic H2 Evolution of Indium Sulfide.* ACS Applied Materials & Interfaces, 2021. **13**(6): p. 7238-7247.

[277] Gao, C., J. Low, R. Long, T. Kong, J. Zhu, and Y. Xiong, *Heterogeneous Single-Atom Photocatalysts: Fundamentals and Applications.* Chemical Reviews, 2020. **120**(21): p. 12175-12216.

[278] Saha, N.C. and H.G. Tompkins, *Titanium nitride oxidation chemistry: An X-ray photoelectron spectroscopy study.* Journal of Applied Physics, 1992. **72**(7): p. 3072-3079.

[279] Avasarala, B. and P. Haldar, *On the stability of TiN-based electrocatalysts for fuel cell applications.* International Journal of Hydrogen Energy, 2011. **36**(6): p. 3965-3974.

[280] Tavares, J., S. Coulombe, and J.L. Meunier, *Synthesis of cubic-structured monocrystalline titanium nitride nanoparticles by means of a dual plasma process.* Journal of Physics D: Applied Physics, 2009. **42**(10): p. 102001.

[281] Dong, S., X. Chen, L. Gu, X. Zhou, H. Xu, H. Wang, Z. Liu, P. Han, J. Yao, L. Wang, G. Cui, and L. Chen, *Facile Preparation of Mesoporous Titanium Nitride Microspheres for Electrochemical Energy Storage.* ACS Applied Materials & Interfaces, 2011. **3**(1): p. 93-98.

[282] Zhou, X., C. Shang, L. Gu, S. Dong, X. Chen, P. Han, L. Li, J. Yao, Z. Liu, H. Xu, Y. Zhu, and G. Cui, *Mesoporous Coaxial Titanium Nitride-Vanadium Nitride Fibers of Core–shell Structures for High-Performance Supercapacitors.* ACS Applied Materials & Interfaces, 2011. **3**(8): p. 3058-3063.

[283] Avasarala, B. and P. Haldar, *Electrochemical oxidation behavior of titanium nitride based electrocatalysts under PEM fuel cell conditions.* Electrochimica Acta, 2010. **55**(28): p. 9024-9034.

[284] Milošv, I., H.-H. Strehblow, B. Navinšek, and M. Metikoš-Huković, *Electrochemical and thermal oxidation of TiN coatings studied by XPS.* Surface and Interface Analysis, 1995. **23**(7-8): p. 529-539.

[285] Kaskel, S., K. Schlichte, G. Chaplais, and M. Khanna, *Synthesis and characterisation of titanium nitride based nanoparticles.* Journal of Materials Chemistry, 2003. **13**(6): p. 1496-1499.

[286] Drygaś, M., C. Czosnek, R.T. Paine, and J.F. Janik, *Two-Stage Aerosol Synthesis of Titanium Nitride TiN and Titanium Oxynitride TiO_xN_y Nanopowders of Spherical Particle Morphology.* Chemistry of Materials, 2006. **18**(13): p. 3122-3129.

[287] Schramke, K.S., Y. Qin, J.T. Held, K.A. Mkhoyan, and U.R. Kortshagen, *Nonthermal Plasma Synthesis of Titanium Nitride Nanocrystals with Plasmon Resonances at Near-Infrared Wavelengths Relevant to Photothermal Therapy.* ACS Applied Nano Materials, 2018. **1**(6): p. 2869-2876.

[288] Greer, J., *Large-Area Commercial Pulsed Laser Deposition*, in *Pulsed Laser Deposition of Thin Films*. 2006. p. 191-213.

[289] Trelenberg, T.W., L.N. Dinh, B.C. Stuart, and M. Balooch, *Femtosecond pulsed laser ablation of metal alloy and semiconductor targets.* Applied Surface Science, 2004. **229**(1): p. 268-274.

[290] Bereznai, M., Z. Tóth, A.P. Caricato, M. Fernández, A. Luches, G. Majni, P. Mengucci, P.M. Nagy, A. Juhász, and L. Nánai, *Reactive pulsed laser deposition of thin molybdenum- and tungsten-nitride films.* Thin Solid Films, 2005. **473**(1): p. 16-23.

[291] Migita, T., R. Kamei, T. Tanaka, and K. Kawabata, *Effect of dc bias on the compositional ratio of WN_X thin films prepared by rf-dc coupled magnetron sputtering.* Applied Surface Science, 2001. **169-170**: p. 362-365.

[292] De Giacomo, A., V.A. Shakhatov, G.S. Senesi, O. De Pascale, and F. Prudenzano, *Plasma-assisted pulsed laser deposition for the improvement of the film growth process.* Applied Surface Science, 2002. **186**(1): p. 533-537.

[293] Rijnders, G.a.B., D. H., John Wiley & Sons, Inc., (2006). Growth Kinetics During Pulsed Laser Deposition, Pulsed Laser Deposition of Thin Films.

[294] Chou, C.-M., C.-C. Lai, C.-W. Chang, K.-H. Wen, and V.K.S. Hsiao, *Radio-frequency oxygen-plasma-enhanced pulsed laser deposition of IGZO films.* AIP Advances, 2017. **7**(7): p. 075309.

[295] Harilal, S.S., C.V. Bindhu, M.S. Tillack, F. Najmabadi, and A.C. Gaeris, *Internal structure and expansion dynamics of laser ablation plumes into ambient gases.* 2003. **93**(5): p. 2380-2388.

[296] Soundiraraju, B. and B.K. George, *Two-Dimensional Titanium Nitride (Ti_2N) MXene: Synthesis, Characterization, and Potential Application as Surface-Enhanced Raman Scattering Substrate.* ACS Nano, 2017. **11**(9): p. 8892-8900.

[297] McSkimming, B.M., C. Chaix, and J.S. Speck, *High active nitrogen flux growth of GaN by plasma assisted molecular beam epitaxy.* 2015. **33**(5): p. 05E128.

[298] Ohkawa, K., A. Ueno, and T. Mitsuyu, *Molecular-beam epitaxial growth of p- and n-type ZnSe homoepitaxial layers.* Journal of Crystal Growth, 1992. **117**(1): p. 375-384.

[299] Hong, Y.J., C.J. Nam, K.B. Song, G.S. Cho, H.S. Uhm, D.I. Choi, and E.H. Choi, *Measurement of hydroxyl radical density generated from the atmospheric pressure bioplasma jet.* Journal of Instrumentation, 2012. **7**(03): p. C03046.

[300] Xiong, Y., Y. Ma, L. Zou, S. Han, H. Chen, S. Wang, M. Gu, Y. Shen, L. Zhang, Z. Xia, J. Li, and H. Yang, *N-doping induced tensile-strained Pt nanoparticles ensuring an excellent durability of the oxygen reduction reaction.* Journal of Catalysis, 2020. **382**: p. 247-255.

[301] Feng, Q., S. Zhao, D. He, S. Tian, L. Gu, X. Wen, C. Chen, Q. Peng, D. Wang, and Y. Li, *Strain Engineering to Enhance the Electrooxidation Performance of Atomic-Layer Pt on Intermetallic Pt_3Ga.* Journal of the American Chemical Society, 2018. **140**(8): p. 2773-2776.

[302] Yang, S., D.Y. Chung, Y.-J. Tak, J. Kim, H. Han, J.-S. Yu, A. Soon, Y.-E. Sung, and H. Lee, *Electronic structure modification of platinum on titanium nitride resulting in enhanced catalytic activity and durability for oxygen reduction and formic acid oxidation.* Applied Catalysis B: Environmental, 2015. **174-175**: p. 35-42.

[303] Thotiyl, M.M.O., T.R. Kumar, and S. Sampath, *Pd Supported on Titanium Nitride for Efficient Ethanol Oxidation.* The Journal of Physical Chemistry C, 2010. **114**(41): p. 17934-17941.